Neutron and X-ray Scattering Studies of Honeycomb Iridates



Sungkyun Choi
Wolfson College
University of Oxford

A Thesis submitted for the Degree of
Doctor of Philosophy

Hilary 2014

Neutron and X-ray Scattering Studies of Honeycomb Iridates

Sungkyun Choi, Wolfson College

A Thesis submitted for the Degree of Doctor of Philosophy, Hilary 2014

This thesis presents neutron and x-ray scattering measurements on quasi-two-dimensional honeycomb antiferromagnets $\mathcal{A}_2IrO_3$ ($\mathcal{A}$=Na, Li) and the solid-solution intermediate material $(Na_{1-x}Li_x)_2IrO_3$. The aim is to study the magnetic order and excitations of $5d$ Ir^{4+} ions in a honeycomb lattice, where unusual magnetic properties have been theoretically predicted to be stabilised by the combinations of strong spin-orbit coupling and honeycomb lattice geometry with 90° Ir-O-Ir bonding.

By using an optimised setup to minimise the strong neutron absorption by Ir nuclei, inelastic neutron scattering measurements on powder sample of Na_2IrO_3 observed dispersive excitations below 5 meV with a dispersion that can be accounted for by including substantial further-neighbor exchanges that stabilize zigzag magnetic order. The onset of long-range magnetic order was confirmed by the observation of oscillations in zero-field muon-spin rotation experiments. Higher-resolution inelastic neutron data found features consistent with a spin gap of 1.8 meV and the data was parameterised by including Ising-type exchange anisotropy.

Combining single-crystal diffraction and density functional calculations, a revised crystal structure model with significant departures from the ideal 90° Ir-O-Ir bonds required for dominant Kitaev exchange was proposed. Various "idealised" crystal structures were constructed to emphasize the departures between the actual structure and structures with cubic IrO_6 octahedra.

The magnetic excitations from the isostructural Li_2IrO_3 revealed strongly dispersive magnetic excitations, qualitatively different from Na_2IrO_3. Elastic neutron diffraction detected a magnetic Bragg peak with a wavevector consistent with spiral orders. To explain the observed neutron data, the spiral H2 phase in the Heisenberg J_1-J_2-J_3 model was proposed, and a full calculation was performed with strong in-plane anisotropic interaction. A further measurement for improving the lower-energy excitation found no clear evidence for a spin gap down to $E = 0.7$ meV.

Lastly, the crystal structure of $(Na_{1-x}Li_x)_2IrO_3$ was investigated with single-crystal x-ray diffraction, revealing a site-mixing of Ir and Na ions in the honeycomb lattice and insensitivity of the refinement to the Li positions. *Ab initio* calculations suggested that up to $x = 0.25$ Li ions replaced Na in the honeycomb centre and phase separation occurred beyond that, which is consistent with the evolution of observed lattice parameters.

Acknowledgements

I would like to thank everybody who has helped me in preparing this thesis, and in enjoying life in Oxford over these years.

First and foremost, I would like to thank my supervisor, Radu Coldea, for his advice, patience and many inspiring discussions over the entire course. Without his support and guidance, this thesis would not be possible. I also appreciate Ivelisse Cabrera, Alun Biffin, Jordan Thomson, Franz Lang for reading chapters of this thesis.

During my time in Oxford, I have benefited hugely from many collaborations with Amalia Coldea for the susceptibility and torque experiments, Paolo Radaelli, Roger Johnson and Federica Fabrizi for x-ray and neutron experiments, Peter Baker, Tom Lancaster, Johannes Moeller and Stephen Blundell for muon spin relaxation experiments, Paul Goddard and Saman Ghannadzadeh for the high-pulse magnetization experiments, Igor Mazin and Aleksey Kolmogorov for *ab initio* calculations for iridate materials. I would like to thank Kang Ryoung Choi and Sang-Wook Cheong, Soham Manni, Yogesh Singh and Philipp Gegenwart for providing the samples used in experiments in this thesis. My thanks also go to Dharmalingam Prabhakaran for providing other interesting samples and support for magnetization experiments in the Clarendon laboratory, and Friedrich Wondre for technical support in using x-ray diffractometers.

I wish to thank instrumental scientists in ISIS and ILL who assisted with neutron experiments: Laurent Chapon, Winfried Kockelmann, Christopher Stock, Jon Taylor, Devashibhai Adroja, Franz Demmel and Marek Koza.

I would like to thank especially my office 106 colleagues: Jack Wright, Danielle Kaminski, Alun Biffin, David Keen, Franz Lang and Liam Collins-McIntyre for sharing stimulating academic and non-academic stories over the years. Also, I cannot forget to mention Lucian Pascut for helping me to smoothly start the course with useful advice. I also wish to thank everybody in the Quantum Matter group: Alice Tayor, Sam Blake, Amir Haghighirad, Stephen Gaw, Liam Gannon, Matthew Watson, Benjamin Williams, Natasha Perks, Alexander Hearmon, Sunil Nair, Heather Lewtas, Peter Babkevich, Graeme Johnstone, Andrew Steele, Isabel Franke, Martin Rotter, and everyone else who shared good moments at tea time and in the laboratory. I would like to mention other friends in the Korean society and college, who enriched my life in Oxford and beyond for these years.

Finally, I cannot thank my parents and brother enough for the love and support, that brought me this far. I dedicate this thesis to them.

Contents

1 Introduction **1**

2 Introduction to Magnetic Ordering and Excitations **4**

2.1 Permanent Magnetic Moments in Insulators 4

2.2 Magnetic Exchange Interactions 8

2.3 Long-Range Magnetic Ordering 10

2.4 Mean-Field and Spin-Wave Theory of Magnetism 13

2.5 Quantum Magnetism 20

2.5.1 Two-Dimensional Magnetism 20

2.5.2 Frustration Effects 20

2.6 Magnetism in the Two-Dimensional Honeycomb Lattice 22

2.7 Quantum Magnets Studied in This Thesis 22

3 Experimental Techniques **24**

3.1 Basic Properties of Neutrons 24

3.2 Theory of Neutron Scattering 27

3.2.1 Nuclear Scattering Cross-Section 30

3.2.2 Magnetic Scattering Cross-Section 33

3.3 Neutron Scattering Instrument Components 37

3.3.1 Neutron Sources 37

3.3.2 Moderators 38

3.3.3 Monochromators 39

3.3.4 Detectors 39

3.4 Neutron Instruments 40
3.4.1 Time-of-Flight Diffractometer 40
3.4.2 Time-of-Flight Inelastic Neutron Spectrometer 41
3.5 X-ray Diffraction 43
3.5.1 Theory of X-ray Diffraction 43
3.5.2 Single Crystal X-ray Diffractometer 43
3.6 Bulk Magnetic Susceptibility Measurements 45

4 Magnetic Order and Excitations of Quasi-Two-Dimensional Honeycomb Antiferromagnet Na_2IrO_3 46

4.1 Introduction 47
4.2 Magnetic Order of Na_2IrO_3 48
4.2.1 Experimental Details 48
4.2.2 Measurements and Results 49
4.3 Magnetic Excitations of Na_2IrO_3 53
4.3.1 Experimental Details 53
4.3.2 Measurements and Results 54
4.4 Linear Spin-Wave Analysis 57
4.4.1 Zigzag and Stripy Phase in the Heisenberg J_1-J_2-J_3 Model . . 57
4.4.2 Stripy Phase in the Kitaev-Heisenberg Model 66
4.4.3 Zigzag Phase in the Kitaev-Heisenberg-J_2-J_3 Model 75
4.4.4 Zigzag Phase in the Generalised Kitaev-Heisenberg Model . . 78
4.5 Magnetic Anisotropy of Na_2IrO_3 82
4.5.1 Experimental Details 82
4.5.2 Measurements and Results 84
4.6 Parameterization of the Low Energy Dispersion using Linear Spin-Wave Theory for the Heisenberg J_1-J_2-J_3 Model with Exchange Anisotropy 85
4.7 Conclusions 89

5 Revised Crystal Structure Model for Na_2IrO_3 **90**

5.1 Introduction 90

5.2 Experimental Details 92

5.3 Measurements and Results 93

5.4 Analysis 96

5.4.1 Structural Optimization Calculations using VASP 96

5.4.2 Microscopic Model of Stacking Faults 96

5.4.3 Diffraction Simulation with Stacking Faults Model 98

5.4.4 X-ray Diffraction Calculation of the C2/c and C2/m Structures 100

5.4.5 Structural Distortions in Na_2IrO_3 from Ideal Cubic Symmetry for IrO_6 Octahedra 103

5.5 Conclusions 115

6 Magnetism of Honeycomb Antiferromagnet Li_2IrO_3 **116**

6.1 Introduction 117

6.2 Thermodynamic Properties 118

6.2.1 Susceptibility 119

6.2.2 Muon Spin Rotation 120

6.3 Powder Neutron Diffraction 124

6.3.1 Experimental Details 124

6.3.2 Measurements and Results 127

6.4 Powder Inelastic Neutron Scattering 130

6.4.1 Experimental Details 130

6.4.2 Measurements and Results 131

6.5 Linear Spin-Wave Analysis of Two Spiral Phases in the Heisenberg J_1-J_2-J_3 Model 136

6.6 Discussion 157

6.7 Conclusions 157

7 Crystal Structure of $(Na_{1-x}Li_x)_2IrO_3$ **159**

7.1 Introduction 160

7.2 Experimental Details 161

7.3 Measurements and Results 162

7.3.1 Lower Li-Doped Samples 162

7.3.2 Higher Li-Doped Samples 170

7.4 Structure-Factor Calculations of the Diffraction Pattern 174

7.5 Conclusions 177

8 Concluding Remarks **179**

A Dynamical Correlation **183**

B Spherically-averaged Neutron Scattering Intensity **185**

Bibliography **187**

List of Figures

2.1 Spin-Orbital Ground State for an Ir^{4+} ion in an Octahedral Cubic Cystal Field 7
2.2 A Schematic Diagram of Superexchange between Two Transition Metal Ions Mediated by a Non-Magnetic Oxygen Ion. 9
2.3 Pictorial Concept of a Spin-Wave in 1D Ferromagnet Chain 15
2.4 Frustration in the Two-Dimensional Triangular and Honeycomb Lattices 21

3.1 Geometry of Neutron Scattering 26
3.2 Instrument Layout of the Cold Neutron Time-of-Flight Spectrometer IN6 42
3.3 Schematic Layout of the Single Crystal X-Ray Diffractometer 44
3.4 Detection of Magnetic Signal in SQUID 45

4.1 Susceptibility of Powder Na_2IrO_3 49
4.2 Muon Spin Rotation Results on Powder Na_2IrO_3 51
4.3 Effective Neutron Absorption Simulated for MARI Experiments on Na_2IrO_3 at $E_i = 18, 40$ meV 53
4.4 Powder Inelastic Neutron Scattering Data Collected using MARI on Na_2IrO_3 55
4.5 Scan through Magnetic Excitation in INS data 56
4.6 Spin-Wave Spectrum for the Zigzag and Stripy Phase in the Heisenberg J_1-J_2-J_3 Model 63
4.7 Mean-Field Phase Diagram of the Heisenberg J_1-J_2-J_3 model on the Honeycomb Lattice 64

4.8 Spherically-Averaged Magnetic Excitation Spectra Generated by Linear Spin-Wave Theory 65
4.9 Phase Diagram of KH model as a Function of Frustration Parameter α 67
4.10 Colour Contour Maps of Dispersions in the Stripy Phase in the KH model at $\alpha = 0.5$ in both the Rotated and Global Frame 69
4.11 Magnetic Excitations in the Stripy Phase in the KH model and Dynamic Correlation at $\alpha = 0.5$ in the Rotated Frame 70
4.12 Magnetic Excitations in the Stripy Phase in the KH model and Dynamic Correlation at $\alpha = 0.5$ in the Global Frame 72
4.13 Magnetic Excitation in the Stripy Phase in the KH model and Dynamic Correlation at $\alpha = 0.4$ 74
4.14 Magnetic Excitation in the Zigzag Phase in the KH-J_2-J_3 model and Dynamic Correlation 77
4.15 Generalised Phase Diagram in KH Model 80
4.16 Dispersion Relation in the KH model with AFM J_K and FM J_1 in Zigzag Phase 81
4.17 Low-Energy Magnetic Excitations Observed by Powder INS in Na_2IrO_3 83
4.18 Scans through the INS Data and Spin-Wave Calculations 84
4.19 Comparison of the Magnetic Inelastic Scattering Signal and Simulations 86
4.20 Spin-Wave Dispersion for the J_1-J_2-J_3 model with Exchange Anisotropy ε=0.05 88

5.1 Proposed Crystal Structure of Na_2IrO_3 with the C2/c Model 91
5.2 Experimental Data from Single Crystal X–ray Diffraction 93
5.3 Crystal Structure of Na_2IrO_3 Determined by Single Crystal X-ray Diffraction 95
5.4 Radial Distribution Functions for Na_2IrO_3 Structural Models 97
5.5 Stacking Order in the Layered Honeycomb Iridate 98
5.6 Simulations for Single Crystal X-ray Diffraction including Stacking Faults 99
5.7 X-ray Diffraction Intensity in the $(-3, k', l')$ Plane 102

5.8 Idealised Crystal Structure of Na_2IrO_3: the A1 and A2 Models 105
5.9 Idealised Crystal Structure of Na_2IrO_3: the A3 and A4 Models 108
5.10 Observed Crystal Structure of the A5 Model and Fully-Relaxed Structure of the A7 Model 112
5.11 Schematic Diagram of Charge Order in $AgNiO_2$ 114

6.1 Susceptibility of Powder Li_2IrO_3 119
6.2 Muon Spin Rotation Results on Powder Li_2IrO_3 122
6.3 Temperature Evolution of the Parameters from μ^+SR Spectra of Li_2IrO_3 123
6.4 Comparison of Fitted Muon Frequency and Order Parameter from WISH 125
6.5 Elastic Neutron Signal on Li_2IrO_3 126
6.6 Schematic Diagram of Two Candidate Spiral Orders for Li_2IrO_3 . . . 128
6.7 Effective Neutron Absorption Simulated for the MERLIN Experiments with Li_2IrO_3 130
6.8 Powder Inelastic Neutron Scattering on Li_2IrO_3 from MERLIN 133
6.9 Energy Scan through the Magnetic Excitation in the MERLIN Data . 134
6.10 Powder Inelastic Neutron Scattering on Li_2IrO_3 using IN6 135
6.11 Exchange Interaction Paths in the Honeycomb Lattice up to Third Nearest Neighbour 137
6.12 Mean-Field Phase Diagram of in the Heisenberg J_1-J_2-J_3 Model . . . 138
6.13 Schematic Diagram of the Transformation from Global to Local Axes in the Spiral Structure 141
6.14 Spherically-Averaged Spin-Wave Spectrum for the H2 Phase with Isotropic Exchange Couplings 148
6.15 Momentum Trajectories along High-Symmetry Direction 149
6.16 Spin-Wave Spectrum of the H2 Spiral Phase of the Isotropic J_1-J_2-J_3 Model along High-Symmetry Directions 150
6.17 Spin-Wave Spectrum in the H2 Phase of the Isotropic J_1-J_2-J_3 Model along the (0K0) Direction 151

6.18 Spherically-Averaged Spin-Wave Spectrum in the H2 Phase of the J_1-J_2-J_3 Model with Exchange Anisotropy as in Fig. 6.19 and 6.20 . . . 154
6.19 Spin-Wave Spectrum in the H2 Phase of the J_1-J_2-J_3 Model with Exchange Anisotropy ($\varepsilon = 0.4$) along High-Symmetry Directions 155
6.20 Spin-Wave Spectrum in the H2 Phase of the J_1-J_2-J_3 Model with Exchange Anisotropy ($\varepsilon = 0.4$) along the (0K0) Directions 156

7.1 X-Ray Diffraction Data for the 5 % Li-doped Sample 163
7.2 Evolution of Lattice Parameters in $(Na_{1-x}Li_x)_2IrO_3$ upon Li-doping . 172
7.3 Simulated (0KL) Diffraction Planes 175
7.4 Scans along (00L) and (02L) Directions in the Simulated Diffraction Pattern 176

Chapter 1

Introduction

In this thesis, the magnetic orders and excitations are studied using x-ray and neutron scattering measurements on quasi-two-dimensional honeycomb antiferromagnets $\mathcal{A}_2IrO_3$ ($\mathcal{A}$=Na, Li) and the solid-solution intermediate material $(Na_{1-x}Li_x)_2IrO_3$. This family of materials, with strong spin-orbit coupling and a honeycomb lattice geometry, have received much attention recently as unusual magnetic structures and excitations were predicted.

The rest of the thesis is organised as follows: Chapter 2 presents an introduction to magnetism concepts relevant for this thesis. The origin of permanent magnetic moments in insulators, magnetic exchange interactions and long-range magnetic ordering are explained. Mean-field theory is reviewed in connection with linear spin-wave theory, and is used to illustrate the semiclassical picture of magnetic excitations in one-dimensional ferromagnet and antiferromagnet chains. Relevant concepts about two dimensional quantum magnets in a honeycomb lattice geometry are outlined with a summary of the quantum magnets studied in this thesis.

In Chapter 3, the experimental techniques used throughout this thesis are described. Basic properties of the neutron are given, followed by an outline of the theory of neutron scattering with both nuclear and magnetic scattering cross-sections. Components of neutron scattering instruments are then briefly explained in relation to neutron instruments used in this thesis. X-ray diffraction theory and instrumentations as well as bulk magnetic susceptibility are introduced.

In Chapter 4, the magnetic order and excitations of Na_2IrO_3, in which edge-sharing

IrO_6 octahedra form a honeycomb lattice, are investigated. Bulk magnetic susceptibility showed a magnetic anomaly at low temperature, which was confirmed by muon spin relaxation as an onset of long-range magnetic order. Powder inelastic neutron scattering measurements were successfully performed using an optimized experimental setup to minimize the neutron absorption from iridium nuclei. It revealed dispersive magnetic excitations, which can be accounted for using linear spin-wave theory for the isotropic Heisenberg J_1-J_2-J_3 model. In a region of parameter space where the ground state has zigzag antiferromagnetic order, the magnetic spectrum of various other spin Hamiltonians were also calculated using linear spin-wave theory, and compared with the experimental data, showing the qualitative/quantitative disagreements. The upper bound of a possible Kitaev interaction in a Kitaev-Heisenberg-J_2-J_3 model with zigzag order was estimated as well. The lower-energy magnetic excitations found a tentative evidence for a spin gap (at 1.8 meV).

In Chapter 5, the crystal structure of Na_2IrO_3 is revised by combining single crystal x-ray diffraction with *ab initio* structural relaxation calculations, as well as the structure-factor simulations. In single crystal x-ray diffraction measurement, diffuse scattering due to stacking faults was reliably separated from the main peaks. Analysing the sharp Bragg peak intensity using structural refinement methods showed that the crystal structure was a monoclinic C2/m unit cell of a higher symmetry than a previously prosed C2/c model. *Ab initio* calculations confirmed the stability of the C2/m structure, and the C2/c structure was found to converge to the experimentally obtained C2/m model by releasing strong electrostatic forces between ions. A model for stacking faults was proposed and showed through direct structure-factor calculations to be consistent with the observed diffuse scattering. Various distortions from a more idealised C2/m structure with cubic octahedra were examined, revealing that the biggest distortion in the real structure is the trigonal squashing of the IrO_6 octahedra.

In Chapter 6, the magnetic order and excitations of the honeycomb Li_2IrO_3 are studied using the combined experimental techniques of magnetic bulk susceptibility, muon spin relaxation, elastic neutron diffraction and inelastic neutron scattering

experiments. Bulk magnetic susceptibility showed a signature of antiferromagnetic transition at low temperature, confirmed as the onset of long-range magnetic order by muon spin relaxation measurements. Powder elastic neutron diffraction measurements found one magnetic Bragg peak whose wavevector is much smaller than the value expected for a zigzag phase, but which could indicate a non-collinear spiral phase. Powder inelastic neutron scattering measurements showed that a strongly dispersive signal, qualitatively different from Na_2IrO_3, which stems from the wavevector that is consistent with a magnetic Bragg peak seen in neutron diffraction measurements. The inelastic neutron scattering data was analysed using linear spin-wave theory for various spin Hamiltonians. The spiral H2 order in the Heisenberg J_1-J_2-J_3 model was proposed as a candidate for the magnetic order in Li_2IrO_3, and Heisenberg exchange interactions with strong in-plane anisotropy were parameterized. The lower-energy magnetic excitations were also successfully observed, finding no clear evidence for a spin gap (down to at least 0.7 meV).

In Chapter 7, the crystal structure of Li-doped $(Na_{1-x}Li_x)_2IrO_3$ ($x = 0.05 - 0.4$) single crystals are studied by single crystal x-ray diffraction measurements. The experiments showed that site-mixing between Ir and Na (or Li) ions in the honeycomb layer becomes essential in order to refine the crystal structure. *Ab initio* calculations revealed that Li ions are preferentially substituted for Na ions in the centre of the Ir honeycomb network up to $x = 0.25$, and beyond this doping phase separation is energetically more preferable. This is consistent with the tendency observed in the lattice parameters upon Li-doping obtained from single crystal x-ray diffraction measurements. The structure-factor simulations were also performed to have a better understanding on the (in)sensitivity of the x-ray diffraction intensity to the location of Li ions and the effect of site-mixing onto the peak intensity in the x-ray data.

In Chapter 8, the key results of the previous chapters are summarized with suggestions for possible future plans to better elucidate the nature of magnetic order and excitations in these materials.

Chapter 2

Introduction to Magnetic Ordering and Excitations

This chapter provides a brief summary of the classical concepts and theories in magnetism, which will be widely used throughout this thesis. The origin of magnetic moments in insulators will first be introduced by explaining fundamental concepts in magnetism such as the magnetic moments from unpaired electrons, and a discussion of how long-range magnetic order is formed, with examples of various types of magnetic structures. The mechanisms of magnetic exchanges such as direct and superexchange interactions are then outlined. The classical notion of mean-field theory is introduced in relation to spin-wave theory, which will be used in understanding the elementary excitations in ferromagnetic and antiferromagnetic sysems with the one dimenstional ferromagnet and antiferromagnet provided as examples along with the concept of geometric frustration. Two-dimensional magnetism in the honeycomb lattice is discussed, followed by a summary of the magnetic materials studied experimentally in this thesis.

2.1 Permanent Magnetic Moments in Insulators

The understanding of solids could begin with classifying a material as belonging to a state of matter. One of the conventional ways to do so is to use conductivity, separating matter into metals, semiconductors, and insulators. In metals, the physical properties can be understood by the motion of free electrons, which are delocalised through out the material. On the other hand, in insulators the electrons are strongly

attracted to the positively charged ions, so the wavefunction is much more localised.

Magnetism in ionic solids is an intriguing subject which comes from the permanent magnetic moments of the ions and their cooperative interactions. The magnetic moment is a fundamental object in magnetism, which originates from unpaired electrons in the partially filled electronic shells. Each electron has spatial movement around the nucleus, resulting in the orbital angular momentum $\boldsymbol{l}_i$, which depends on the electronic state occupied by the electron [1]. Each also possesses intrinsic spin angular momentum $\boldsymbol{s}_i$, which is a purely quantum mechanical concept without an analogous notion in classical mechanics, thus magnetism is a quantum mechanical phenomenon. In a completely filled electronic shell, the orbital and spin angular momentum of all the electrons in that orbital cancel out due to the symmetry of these angluar momentum vectors, thus there is not a net magnetic moment. However, unfilled shells can give a finite orbital and spin angular momentum, leading to a permanent magnetic moment.

Assuming weak spin-orbit (L-S) coupling, defined as $\lambda \boldsymbol{L} \cdot \boldsymbol{S}$, places us in a regime where the total angluar momentum J of a free ion is given by the sum of the total spin S and total orbital angular momentum L of unpaired electrons. This results in a magnetic moment on a magnetic atom $\boldsymbol{J} = \boldsymbol{L} + \boldsymbol{S}$ where $\boldsymbol{L} = \sum_i \boldsymbol{l}_i, \boldsymbol{S} = \sum_i \boldsymbol{s}_i$. The effective magnetic moment obatined in susceptibility measurements as a function of temperature is given by

$$\mu_{eff} = g_J \mu_B \sqrt{J(J+1)}, \tag{2.1}$$

where μ_B is the Bohr magneton ($\frac{e\hbar}{2m_e}$), the unit of magnetic moment, and the constant g_J is known as the Landé g-factor [1],

$$g_J = \frac{3}{2} + \frac{S(S+1) + L(L+1)}{2J(J+1)}. \tag{2.2}$$

The ground state of an isolated atom is determined by Hund's rules, which minimize the energy resulting from the combination of L and S [1]. For ions placed in crystals, these rules work well for 4f ions, where the unpaired electrons lie in deep inner electronic shells inside the ion so that there are no significant interactions between magnetic electrons and other ions of the crystal environment.

For 3d ions, on the other hand, the environment around a magnetic ion affects the ground state of the magnetic ion quite strongly, because the unparied e^- are the outer electrons in 3d shell, close to the electrons in the surrounding ions, so the unpaired electrons in the magnetic ion feel the crystal electric field. For $5d$ ions the spin-orbit coupling is no longer small ($\lambda \sim Z^4$), and can be comparable with other energy scales such as electron-electron repulsion energies, crystal field energies and so on.

The crystal field is an important factor in 3d ions in determining the magnetic ground state of an ion. The origin of the crystal field is the electronic repulsion energy bewteen electrons in the magnetic ion and the electrons in the surrounding ions. The atomic orbitals occupied by the electrons in the magnetic ions have different angular dependence, thus the angluar overlap of these orbitals with those of the surrounding ions is different, depending on the symmetry of the surrouding crystal environments

For 3d ions, the crystal field is usually stronger than the spin-orbit coupling, which can be treated as a perturbation. In this case, the orbital angular momentum often becomes zero, so called 'orbital quenching' ($L = 0$), and thus it forms a singlet orbital ground state and the total magnetic moment is determined solely by the spin of the electrons unpaired. Thus the oribital angular momentum does not participate in the collective magnetic properties of these materials. The small spin-orbit interaction can be treated as a perturbative interaction, leading to a small deviation from $g = 2$.

This situation changes dramatically in the heavier transition metal ions with unfilled $4d$ and $5d$ shells. An example of the energy level splittings for an Ir^{4+} ion in a cubic octahedral oxygen environment is shown in Fig. 2.1. For IrO_6 in a $5d$ iridate system, Ir ions are surrounded by six oxygen ions (O^{-2}) located in the corner of an octahedron. As seen in Fig. 2.1, the five $5d$ orbitals which are degenerate in a spherically symmmetric environment are divided into three-fold degenerate t_{2g} (d_{xy}, d_{yz}, d_{zx}) orbitals, which point out between x, y and z axes and two fold degenerate e_g ($d_{z^2}, d_{x^2-y^2}$) orbitals which are pointing toward these axes in the octahedral oxygen cage. Since t_{2g} orbitals points out between x, y and z axes, they have lower energy by avoiding strong electron repulsion with electrons in the oxygen ions.

Then the spin-orbit interaction $\lambda \boldsymbol{L} \cdot \boldsymbol{S}$ further splits the t_{2g} orbitals into J_{eff}=1/2

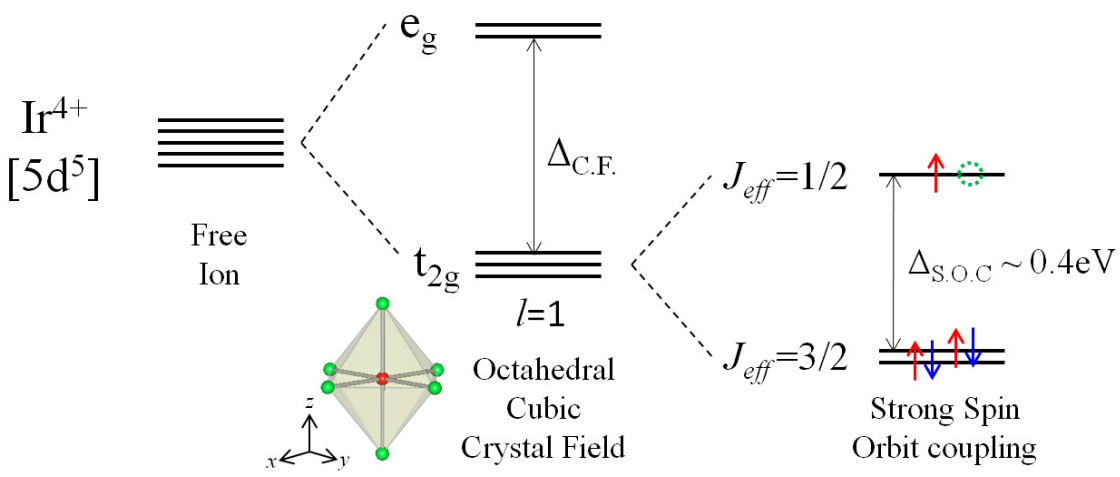


Figure 2.1: Spin-Orbital Ground State for an Ir^{4+} ion in an Octahedral Cubic Cystal Field. Splitting of one-electron energy levels by the octahedral environment lead to a lower orbtial triplet further splits this into J_{eff}=1/2 and 3/2 states with effective orbital angular momentum l=1.

doublets and J_{eff}=3/2 quadruplets, and the J_{eff}=3/2 orbital is completely filled by four electrons, leaving one electron to occupy the J_{eff}=1/2 orbital. This J_{eff}=1/2 wavefunction of the ground state is spin-orbit entangled. In order to show that this is indeed the crystal field structure of iridates, one needs to observe the transitions from the J_{eff}=3/2 to J_{eff}=1/2 state by spectroscopy tools, such as resonant inelastic x-ray scattering [2].

This J_{eff}=1/2 spin-orbit coupled ground state is quite different from a pure S=1/2 state say in a 3d ion, where the orbital momentum is zero, as the exchange ineteraction between neighbouring sites can be considerably more complex with spin anisotropy in the exchange linked to the orientation of the bond [3, 4] in contrast to exchange between S=1/2 moment which lead to the near isotropic of the Heisenberg form $\boldsymbol{S}_1 \cdot \boldsymbol{S}_2$. On certain lattice geometries such as honeyocmb, the strongly anisotropic interactions between J_{eff}=1/2 moments have been predicted to stabilise novel magnetic phases and dynamics such a Kitaev spin liqud and search for such physics is part of the motivation for experimentally exploring the magentism in the layered iridates Na_2IrO_3 and Li_2IrO_3 in this thesis.

2.2 Magnetic Exchange Interactions

Magnetic moments in solids order usually below a critical temperature T_c, where the thermal energy becomes similar to the strength of the interaction such that at lower temperatures the ordered phase more favourable than the paramagnetic phase. Thermodynaically, this can be understood using $F = E - TS$, where the free energy (F) becomes lower when the magnet orders to have a lower entropy (S) at the critical temperature ($T=T_c$), and at $T>T_c$ the paramagnetic (disordered phase) is more favourable. Here E is the internal energy.

Many materials order at high T_c, for instance Fe orders a ferromagnetically below $T_c \simeq 1000$ K. Since the typical energy scale of the dipolar interaction is an order of a few Kelvin, it cannot exaplain the long-range magnetic order temperatures which are much higher than a few Kelvin.

The exchange interaction originates from the combined effect of the Pauli exclusion principle and Coulomb interaction (the electrostatic interaction) between electrically charged particles. As an illustration, let's consider a simple model with the two electrons localised an neighbouring ions with orbitals φ_a, φ_b with some overlap. To satisfy the Pauli exclusion principle, the total wavefunction which made up of the spatial and spin state of electrons should be antisymmetric. Thus, when two spins (1 and 2) align in an anti-parallel way (a singlet state), they can occupy the same orbital ground state. The total wavefunction is then [1]

$$\Psi = \frac{1}{\sqrt{2}}\chi_S[\varphi_a(1)\varphi_b(2) + \varphi_a(2)\varphi_b(1)], \tag{2.3}$$

where χ_S is the singlet spin function $\frac{1}{\sqrt{2}}(|\uparrow\downarrow\rangle - |\downarrow\uparrow\rangle)$. On the other hand, when the two spins are aligned parallel (a triplet state), the orbital states can be antisymmetric, so the total wavefuction is

$$\Psi = \frac{1}{\sqrt{2}}\chi_T[\varphi_a(1)\varphi_b(2) - \varphi_a(2)\varphi_b(1)], \tag{2.4}$$

where χ_T is the triplet spin function, sand one of $|\uparrow\uparrow\rangle$, $|\downarrow\downarrow\rangle$ and $\frac{1}{\sqrt{2}}(|\uparrow\downarrow\rangle + |\downarrow\uparrow\rangle)$ states. The Coulomb interactions (V_C) between two electrons,

$$V_C = \frac{e^2}{4\pi\varepsilon_0|\boldsymbol{r}_1 - \boldsymbol{r}_2|}, \tag{2.5}$$

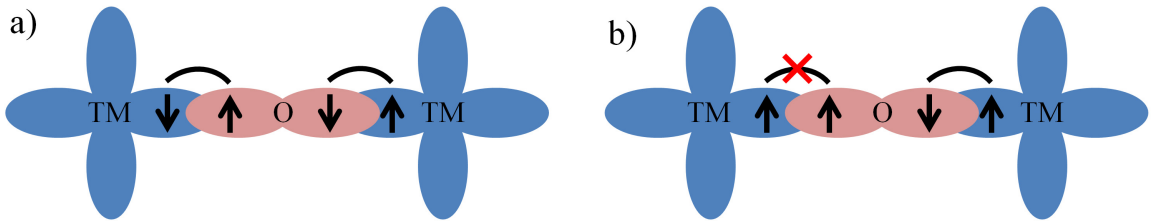


Figure 2.2: A Schematic Diagram of Superexchange between Two Transition Metal Ions Mediated by a Non-Magnetic Oxygen Ion. a) Antiferromagnetic and b) ferromagnetic alignment of the TM ions. The excited state, where electrons have an overlapping orbitals, is available for a) whereas it is not allowed for b) due to the violation of the Pauli principle.

where $\boldsymbol{r}_i$ is the position of the i-th electron, is lower when the electrons are far apart as V_C is inversely proportional to the distance between two electrons.

This difference between the singlet and triplet spin states (E_S, E_T) can be written as

$$\mathcal{H}_{1,2} = E_0 - (E_S - E_T)\boldsymbol{S}_1 \cdot \boldsymbol{S}_2 \tag{2.6}$$

where E_0 is a constant energy offset and E_S (E_T) is the singlet (triplet) energy. This could be generalised for the nearest neighbour coupling between all ions in the system, negleting a constant energy offset E_0 and summing over all electrons in the system, we have the isotropic Heisenberg Hamiltonian,

$$\mathcal{H} = \sum_{ij} J_{ij}\boldsymbol{S}_i \cdot \boldsymbol{S}_j, \tag{2.7}$$

where $J(= -(E_S - E_T))$ is the isotropic exchange constant between the spins at sites i, j. By definition, positive J stabilises anti-parallel alignment of spins (antiferromagnetic alignment), whereas negative J_{ij} favours a parallel (ferromagnetic).

Since the exchange interaction depends on orbital overlap, it is intrinsically short-range, so it decreases quickly with increasing distance between the two magnetic ions. Thus the direct exchange due to the direct overlap of electron density of two magnetic ions is usually weak when electrons are localised such as for 4f rare earth and 3d transition metal ions. In addition to the direct exchange, the exchange coupling between magnetic ions can also be mediated by an intemediate non-magnetic ion.

This is so called superexchange and it is usually antiferromagnetic. An example is illustrated in Fig. 2.2 for a 180° configuration between two transition metal (TM) ions and one oxygen ion. For AFM alignment of the spins at the TM ions in Fig. 2.2a), all e^- can hop on neighbouring sites such that the electron wavefunction is spread out, resulting in a lower energy (analogy to particle in a box, lower confinement energy for a bigger box), making it energetically favourable. In the ferromagnetic case, on the other hand, spins in the transition metal (TM) ions are not allowed to hop by the Pauli exclusion principle since two parallel spins would occupy the same orbital in the overlapped region between the TM ions and the intermediate oxygen ion as seen in Fig. 2.2b), so this state cannot gain energy from e^- delocalisation, thus it is higher in energy than the AF alignment.

If the magnetic ions have a non-zero orbital angular momentum, the magnetic moment also has a contribution from the orbital motion of electrons. This combined with crystal field effects, which tend to have a prefered orinetation for $\boldsymbol{L}$, can lead to a preferred orientation for the total magnetic moment $\boldsymbol{J}$, in order to minimise the spin-orbit interaction, $\lambda \boldsymbol{L} \cdot \boldsymbol{S}$, giving rise to a magnetic anisotropy.

For the materials studied in this thesis, $\mathcal{A}_2\mathrm{IrO}_3$ ($\mathcal{A}$=Na, Li), the strong spin-orbit interaction at the Ir^{4+} is potentially a key factor in understanding the magnetic properties. The magnetic anisotropy in $\mathrm{Na_2IrO_3}$ (discussed in Sec. 4.5) could be easy-axis with the collinear zigzag magnetic structure, whereas it could be the easy-plane anisotropy in $\mathrm{Li_2IrO_3}$ (discussed in Sec. 6.4)with a spiral order potentially.

2.3 Long-Range Magnetic Ordering

Materials can be classified by their response to an external magnetic field, which can generate an induced magnetic moment. This response is described by two quantities, magnetization and magnetic susceptibility.

All materials show very weak diamagnetism [1] with a negatively induced magnetic moment in an applied field, which comes from the orbital motion of electrons in closed electronic shells. Paramagnetism results in a positive magnetic susceptibility due to

aligned unpaired electrons, but moments are randomly oriented without an applied field because the interaction between them is too weak to form long-range order.

Some magnetic materials do possess long-range magnetic order even without an applied magnetic field. This magnetic order can be seen in different structures such as collinear ferromagnetic (FM), antiferromagnetic (AFM) and the non-collinear spiral order. In the collinear ferromagnet, the magnetic moments in one domain are all aligned in parallel whereas in an AFM the magnetic moments on neighbouring sites are anti-parallel. This can be parametised using the exchange coupling in a Heisenberg exchange model as in Eq. (2.7). If J in Eq. (2.7) is negative, the magnetic moments are energetically favoured to be aligned in a parallel way whereas when J is positive, it is energetically favoured that they align in an anti-parallel way between nearest neighbours. In an AFM, the antiferrmagnetic arrangement of spin sites enables us to separate the system into two sublattices.

Unlike the most studied structures such as the collinear FM and AFM, non-collinear magnetic order can be formed by competing exchange interactions, where all exchange interactions are not simultaneously satisfied on the given lattice geometry. This is the case for the spiral order, where the magnetic moment changes their directions at each subsequent magnetic site, with a larger periodicity than that of the structural unit cell. This means that the propagation wavevector ($\boldsymbol{Q}$), which is the periodicity of the magnetic unit cell in reciprocal space, is located between the nuclear Brillouin zone centre (the Bragg peak positions of the crystal lattice) and Brillouin zone boundary (those of two-sublattice AFM).

Both geometry and competing interactions could also play a role in stabilising an unusual magnetic structure in the layered honeycomb iridate [5, 6, 7]. With only nearest neighbour antiferromagnetic exchange (J_1), conventional Néel order [8] is expected to occur, whereas unusual zigzag magnetic ordering (see Fig. 4.4b)) has been seen in Na_2IrO_3 (discussed in Chapter 4). Extended Heisenberg exchange interactions beyond the first nearest neighbour couplings are thought to be the cause of this unexpected magnetic order. Also a non-collinear spiral order is expected to be realised in Li_2IrO_3 (discussed in Chapter 6).

It is useful to introduce how the magnetic structure is described in terms of the propagation wavevector in the most general non-collinear order, where the collinear phase is a limit where the rotation angle between neighbouring unit cells is 0 or π. For the case of a crystallographic solid with one magnetic ion per unit cell with spins that lie in a plane $(\hat{\boldsymbol{u}}, \hat{\boldsymbol{v}})$, the ordered magnetic moment by

$$\boldsymbol{m}_l = m_0[\cos(\boldsymbol{Q}\cdot\boldsymbol{R}_l + \phi)\hat{\boldsymbol{u}} + \sin(\boldsymbol{Q}\cdot\boldsymbol{R}_l + \phi)\hat{\boldsymbol{v}}], \tag{2.8}$$

where m_0 is the magnitude of the magnetic moment, $\boldsymbol{Q}$ is the propagation wavevector, $\boldsymbol{R}_l$ is the position of the l-th unit cell, ϕ is an arbitrary phase, and $\hat{\boldsymbol{u}}$ and $\hat{\boldsymbol{v}}$ are the orthogonal unit vectors to define the spin rotating plane. This equation implies that the moment rotates by an angle $\boldsymbol{Q}\cdot(\boldsymbol{R}_l - \boldsymbol{R}_{l'})$ when moving from unit cell l' to l. If the plane of spin rotation is perpendicular to the the direction of propagation, the structure is called helix. This is experimentally seen in the rare-earth metals and presented in detail in Ref. [9]. On the other hand, if the plane of the spin rotation contains the propagation wavevector, it is called cycloidal order. Such spiral order may be the ground state in Li_2IrO_3, where the magnetic moments rotate in the plane (see Figs. 6.6(a-b) in Chapter 6). Since the periodicity of the spiral magnetic structure depends only on the ratio of relative exchange couplings, it is in general incommensurate with respect to the periodicity of the underlying crystal structure. Furthermore the direction of the magnetic moment can be fixed by the magnetic anisotropy, which could confine the spin to the crystallographic $\boldsymbol{ac}$-plane in the monoclinic Li_2IrO_3 with the unique eaxis along $\boldsymbol{b}$.

Magnetic order can be determined by neutron diffraction experiments, which rely on the observation of magnetic Bragg peaks, the contructive interference of coherently scattered neutrons from the magentic order. Theoretical approaches for the elastic magnetic cross-section are introduced in Sec. 3.2.2 (See Eq. (3.41)) with an explanation of neutron diffraction experiments in Sec. 3.4.1.

2.4 Mean-Field and Spin-Wave Theory of Magnetism

Magnetic ions develop long-range correlations at a critical temperature T_c, below which the magnetic interactions are stronger than any thermal agitation. In mean-field theory, it is assumed that the fluctuations of magnetic moments around an averaged value are small, so this variation can be treated as negligible. Since thermal fluctuations are only taken into account, fluctuation is absent at zero temperature in the mean-field approximation. The mean-field at the position of each magnetic ion is determined by the averaged magnetic field generated by surrounding magnetic ions. The mean-field approximation is used to study the stability of the zigzag and spiral magnetic order relevant for in Na_2IrO_3 (See Chapter 4) and Li_2IrO_3 (See Chapter 6) respectively.

Linear spin-wave theory is a well-established technique to calculate the elementary excitations of a magnetically ordered spin system. It gives a basic understanding of the dynamics of the ordered state. The theory adopts the mean-field approximation of the ordered state, and calculates the low-energy exictations arising from small collective oscillations of the ordered magnetic moments around their mean-field equilibrium directions.

The spin-wave spectrum for the isotropic ferromagnet is good example to understand the spin-wave theory and the resultant excitation features [10]. The spin Hamiltonian for an isotropic Heisenberg spin model is given by

$$\mathcal{H} = \sum_{\langle i,j \rangle} J \boldsymbol{S}_i \cdot \boldsymbol{S}_j \tag{2.9}$$

where J is negative for ferromagnetic nearest neighbour exchange between the i and j-th ions, $\langle i, j \rangle$ indicates each ij bond counted once.

For illustration the FM one-dimensional chain is considered below. Here the ground state has the magnetic moments fully aligned along with a spontanously chosen spin quantization direction, interacting with each other by the exchange in-

teraction J as illustrated in Fig. 2.3a). Eq. (2.9) can then be decomposed into

$$\boldsymbol{S}_i \cdot \boldsymbol{S}_j = S_i^z S_j^z + \frac{1}{2}(S_i^+ S_j^- + S_i^- S_j^+), \tag{2.10}$$

where the first term in the right-hand side is the longitudinal interaction and the terms inside the parenthesis are the transverse part, which flips spin. One may think that a single spin-flip state, where one of spins is flipped might be the lowest energy excited state, but this is not an eigenstate of the Hamiltonian in Eq. (2.10) as it does not give the same state after applying the Hamiltonian, thus not an eigenstate. The true lowest energy excited state is formed by a linear combination of spin-flipped states over the delocalised at different atomic sites [1].

When the spin is large, the semi-classical method can be used to solve for the excitations using the Holstein-Primakoff transformation [11],

$$\begin{aligned} S_i^z &= S - a_i^\dagger a_i \\ S_i^+ &= S_i^x + iS_i^y \simeq \sqrt{2S} a_i \\ S_i^- &= S_i^x - iS_i^y \simeq \sqrt{2S} a_i^\dagger \end{aligned} \tag{2.11}$$

where $a_i^\dagger(a_i)$ creates (annihilates) a spin derivation at the site i, and a_i and $a_i^\dagger$ are Boson operators. Here fully aligned spins are moved out of alignment by the transverse spin operators to make quantized excited state, a magnon. For the ferromagnet, the ground state is an exact eigenstate of the Hamiltonian with no quantum fluctuations, and the one-magnon wavefuction is also an exact eigenstate with $\Delta S^z = -1$ that can be excited by a neutron spin-flip scattering process. In the multi-magnon prcess, neutron scatterings are disallowed for a ferromagnet as they would violate the spin conservative rule, $\Delta S^z = 0, \pm 1$ for the neutron scatterings.

Excluding higher than quadratic terms, after substituting Eq. (2.11) into Eq. (2.10) leads to

$$\mathcal{H} \simeq NE_{MF} + JS \sum_{i,j} (a_i a_j^\dagger + a_i^\dagger a_j - a_i^\dagger a_i - a_j^\dagger a_j) \tag{2.12}$$

where the mean-field ground state energy $E_{MF} = (1/2)JzS^2$, a factor of $(1/2)$ is used to avoid double counting and N is the total number of sites in the spin system.

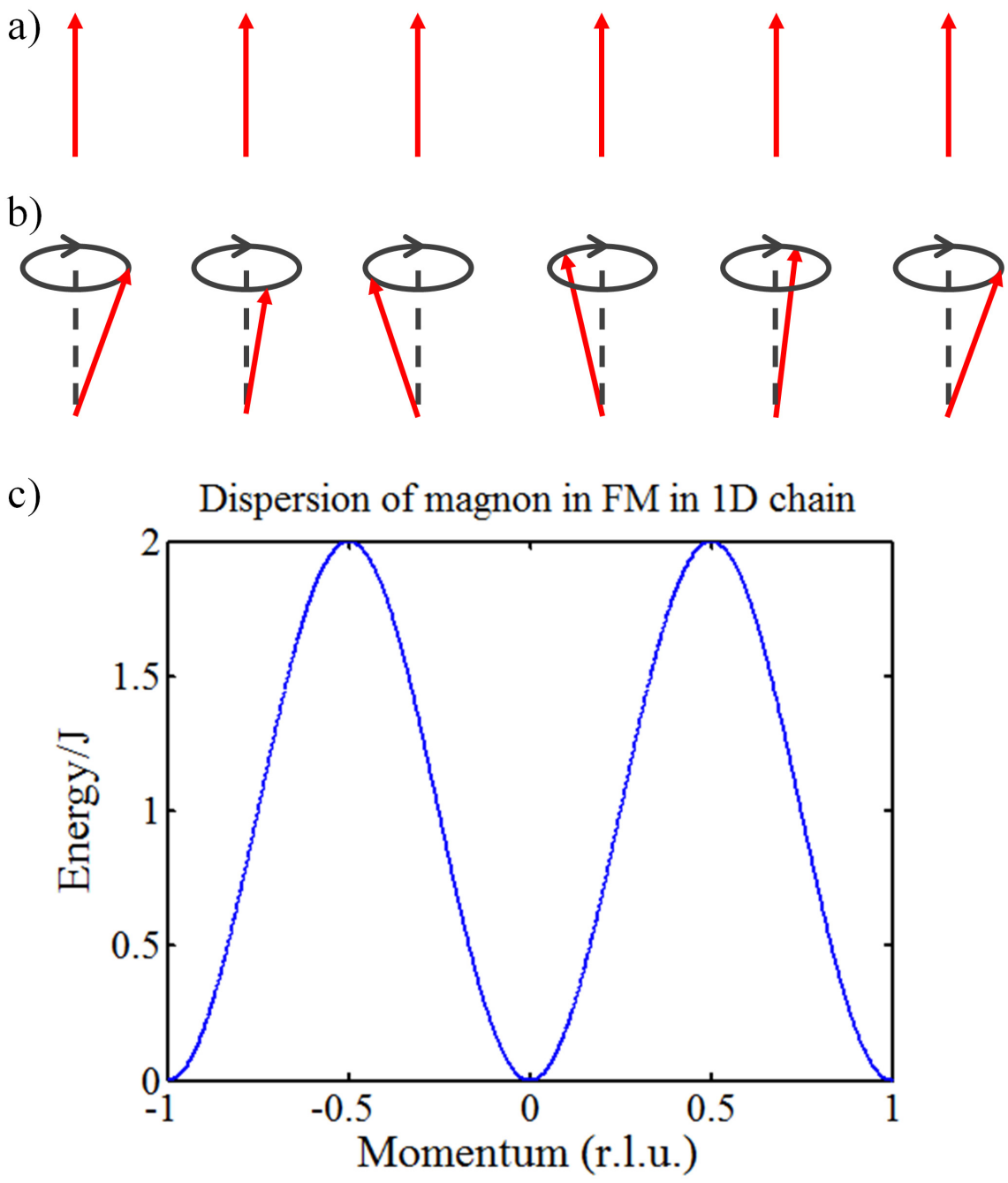


Figure 2.3: Pictorial Concept of a Spin-Wave in 1D Ferromagnet Chain. a) The fully saturated magnetic moments in one-dimensional ferromagnet with ordering direction along z-axis. b) The precessing spins after applying the spin deviation operators. c) The magnon dispersion, corresponding to the semi-classical picture in b).

Because the excitations can be described as well-defined magnons, it is more useful to express the spin Hamiltonian in momentum space using the Fourier transformation

$$a_i = \frac{1}{\sqrt{N}} \sum_{\boldsymbol{k}} a_{\boldsymbol{k}} e^{-i\boldsymbol{k}\cdot\boldsymbol{r}_i} \qquad\qquad a_i^\dagger = \frac{1}{\sqrt{N}} \sum_{\boldsymbol{k}} a_{\boldsymbol{k}}^\dagger e^{+i\boldsymbol{k}\cdot\boldsymbol{r}_i} \tag{2.13}$$

where $a_k^\dagger$ (a_k) creates (annihilates) a magnon with wavevector $\boldsymbol{k}$, inside the first Brillouin zone of the nuclear unit cell. This allows the spin Hamiltonian Eq. (2.12) to be expressed as a linear combination of magnon operators in momentum space. The second-order term in momentum space is expressed as

$$\mathcal{H}_2 = JzS \sum_{\boldsymbol{k}} (\gamma_{-\boldsymbol{k}} a_{\boldsymbol{k}} a_{\boldsymbol{k}}^\dagger + \gamma_{\boldsymbol{k}} a_{\boldsymbol{k}}^\dagger a_{\boldsymbol{k}} - 2 a_{\boldsymbol{k}}^\dagger a_{\boldsymbol{k}}) \tag{2.14}$$

and

$$\gamma_{\boldsymbol{k}} = z^{-1} \sum_{\boldsymbol{\delta}} e^{i\boldsymbol{k}\cdot\boldsymbol{\delta}} \tag{2.15}$$

where $\boldsymbol{r}_j = \boldsymbol{r}_i - \boldsymbol{\delta}$ and z is the number of neighbours of an magnetic ion. Since magnons are bosonic operators, the bosonic commutation relation satisfies $[a_{\boldsymbol{k}}, a_{\boldsymbol{k}}^\dagger] = 1$, and $\sum_{\boldsymbol{k}} \gamma_{\boldsymbol{k}} = 0$. When there is an inversion symmtery in the crystal structure, $\gamma_{\boldsymbol{k}} = \gamma_{-\boldsymbol{k}}$ and Eq. 2.14 is reformulated as

$$\mathcal{H}_2 = \sum_{\boldsymbol{k}} \omega(\boldsymbol{k}) a_{\boldsymbol{k}}^\dagger a_{\boldsymbol{k}}. \tag{2.16}$$

The dispersion relation is given by

$$\omega(\boldsymbol{k}) = JzS(\gamma_{\boldsymbol{k}} - 1), \tag{2.17}$$

where the structure factor $\gamma_{\boldsymbol{k}}$ depends on the lattice geometry. For the 1D chain as described in Fig. 2.3a), $\gamma_{\boldsymbol{k}}$=$(1/2)z\cos(2\pi h)$ and z=2. The dispersion relation is shown in Fig. 2.3c) with a pictorial visualisation of atomic magnetic moments in the real space in Fig. 2.3b). As expected from the dispersion relation in Eq. (2.17), the dispersion has a simple sinusoidal form. Also since it does not have an energy gap at $\boldsymbol{k} = 0$, excitations with long-wavelength could emerge from the ground state at very small $\boldsymbol{k}$ in the limit of zero energy cost, and these are called Goldstone bosons [1]. As

can be seen in Fig. 2.3c), the dispersion is softened at zero momentum transfer, which is the magnetic ordering wavevector of the ferromagnetic ground state, because the excitations appear from the ground state. Based on the form of Fourier transformation in Eq. (2.13), it is clear that the eigenstate is a superposition of plane-waves. For a given J value, the dispersion energy increases upon momentum wavevector toward the zone boundary at h=0.5 since more energy is required to maintain a coherent phase relation with a larger phase difference between spins in neighbouring ions. It is therefore natural that the bandwidth of the dispersion is proportional to the magnitude of exchange coupling as shown in Eq. (2.17).

When it comes to the antiferromagnet [10], the relevant spin Hamiltonian is given by Eq. (2.9) with positive J ensuring the antiferromagnetic arrangement of magnetic moments. In this case, sites can be decomposed into two interpenetrating sublattices of up and down spins. To cause fluctuations in the aligned spins, Holstein-Primakoff transformation is used with two sublattices.

$$\begin{aligned} S_i^z &= S - a_i^\dagger a_i & S_j^z &= -S + b_j^\dagger b_j \\ S_i^+ &= S_i^x + iS_i^y \simeq \sqrt{2S}a_i & S_j^+ &= S_j^x + iS_j^y \simeq \sqrt{2S}b_j^\dagger \\ S_i^- &= S_i^x - iS_i^y \simeq \sqrt{2S}a_i^\dagger & S_j^- &= S_j^x - iS_j^y \simeq \sqrt{2S}b_j. \end{aligned} \tag{2.18}$$

where a_i (b_j) is an annihilation operator which removes a spin deviation and $\mathrm{a}_i^\dagger$ ($\mathrm{b}_j^\dagger$) is a creation operator which generates a spin deviation in the spin system on the a (b)-sublattice. From Eq. (2.18), it is evident that the tranformation for the b-sublattice is opposite to that of the a-sublattice since they are aligned in anti-parallel. Quantum fluctations called the zero-point motion are now existent because Néel antiferromagnetic state is not an exact eigenstate of the Hamiltonian. There are two types of magnons, degenerate in energy for the same $\boldsymbol{k}$ with $\Delta S^z = \pm 1$. Neutrons can scatter by exciting a single magnon, as well as by exciting simultaneously two magnons with opposite spins $\Delta S^z = +1$ and $\Delta S^z = -1$, and this process occurs in the longitudinal correlation $S^{zz}(\boldsymbol{k}, \omega)$, whereas the 1-magnon process happens in the transverse correlations $S^{xx}, S^{yy}(\boldsymbol{k}, \omega)$.

It is convenient to use the concept of well-defined quasi-particle magnons in momentum space by adopting the Fourier transformation with corresponding operators

$$\begin{aligned} a_i &= \frac{1}{\sqrt{N}} \sum_{\boldsymbol{k}} a_{\boldsymbol{k}} e^{-i\boldsymbol{k}\cdot\boldsymbol{r}_i} \qquad b_j = \frac{1}{\sqrt{N}} \sum_{\boldsymbol{k}'} b_{\boldsymbol{k}'} e^{-i\boldsymbol{k}'\cdot\boldsymbol{r}_j} \\ a_i^\dagger &= \frac{1}{\sqrt{N}} \sum_{\boldsymbol{k}} a_{\boldsymbol{k}}^\dagger e^{+i\boldsymbol{k}\cdot\boldsymbol{r}_i} \qquad b_j^\dagger = \frac{1}{\sqrt{N}} \sum_{\boldsymbol{k}'} b_{\boldsymbol{k}'}^\dagger e^{+i\boldsymbol{k}'\cdot\boldsymbol{r}_j} \end{aligned} \tag{2.19}$$

where N is the total number of spins on each sublattice, a_i ($a_i^\dagger$) annihilates (creates) a spin deviation on the a-sublattice (up-spins) and b_i ($b_i^\dagger$) behaves similarly for the b-sublattice (down-spins).

The spin Hamiltonian of magnon operators up to a quadratic order becomes

$$\mathcal{H} \simeq 2NE_{MF} + JzS \sum_{\boldsymbol{k}} \left[(\gamma_{-\boldsymbol{k}} a_{\boldsymbol{k}} b_{-\boldsymbol{k}} + \gamma_{\boldsymbol{k}} a_{\boldsymbol{k}}^\dagger b_{-\boldsymbol{k}}^\dagger) + (a_{\boldsymbol{k}}^\dagger a_{\boldsymbol{k}} + b_{-\boldsymbol{k}}^\dagger b_{-\boldsymbol{k}}) \right] \tag{2.20}$$

where E_{MF} is the mean-field ground state energy, and $2N$ is the total number of spins on the two sublattices. The sum extends over all wavevectors $\boldsymbol{k}$ in the first magnetic Brillouin zone.

The quadratic terms in Eq. (2.20) can be rearranged as

$$\mathcal{H}_2 = \sum_{\boldsymbol{k}} \mathsf{X}^\dagger \mathsf{H} \mathsf{X} \tag{2.21}$$

by using the operator basis of

$$\mathsf{X}^\dagger = \left[a_{\boldsymbol{k}}^\dagger \ , \ b_{-\boldsymbol{k}} \right] \tag{2.22}$$

where $a_{\boldsymbol{q}}^\dagger$ ($a_{\boldsymbol{q}}$) creates (annihilates) a plane-wave magnon mode on the a-sublattice and so on. The Hamiltonian matrix in Eq. (2.21) is

$$\mathsf{H} = \begin{bmatrix} A_{\boldsymbol{k}} & B_{\boldsymbol{k}} \\ B_{-\boldsymbol{k}} & A_{\boldsymbol{k}} \end{bmatrix} \tag{2.23}$$

where

$$\begin{aligned} A_{\boldsymbol{k}} &= JzS \\ B_{\boldsymbol{k}} &= JzS\gamma_{\boldsymbol{k}} \\ \gamma_{\boldsymbol{k}} &= z^{-1} \textstyle\sum_{\boldsymbol{\delta}} e^{i\boldsymbol{k}\cdot\boldsymbol{\delta}} \end{aligned}$$

Diagonalisation of the Hamiltonian by conventional techniques [12] gives normal magnon modes created by $\alpha_{\boldsymbol{k}}^{\dagger}$ and $\beta_{\boldsymbol{k}}^{\dagger}$ operators with the Hamiltonian

$$\mathcal{H}_2 = \sum_{\boldsymbol{k}} \omega(\boldsymbol{k})(\alpha_{\boldsymbol{k}}^{\dagger}\alpha_{\boldsymbol{k}} + \beta_{\boldsymbol{k}}^{\dagger}\beta_{\boldsymbol{k}}) + E_0, \tag{2.24}$$

and the dispersion relation

$$\omega(\boldsymbol{k}) = JzS\sqrt{1-\gamma_{\boldsymbol{k}}^2}, \tag{2.25}$$

where E_0 is the zero-point fluctuation energy, which comes from the uncertainty of the two antiferromagnetic ground state configuration. Eq. (2.24) gives a doubly degenerate mode, stemming from two sublattices in the generic antiferromagnetic system. The magnon excitations of the antiferromagnet shows qualitatively distinct feature compared to that of a ferromagnetic system; for instance, in the one-dimensional antiferromagnetic system, $\gamma_{\boldsymbol{k}}$=(1/2)$z$cos(2πh), z=2 and the dispersion is

$$\omega(\boldsymbol{k}) = JzS|\sin(2\pi h)|, \tag{2.26}$$

where $\sin(2\pi h) \sim 2\pi h$ for small h, thus the dispersion is linear at low energies above the magnetic Bragg peaks. Linear dispersion from the softening point is a general feature of antiferromagnetic interaction due to the sine function in Eq. (2.26).

Neutron scattering technique can measure magnetic excitation experimentally (See Sec. 3.2.2), which can then be compared with the calculated spin-wave spectra. Using key features such as the bandwidth and minima of the excitation, and the relative intensity of the spectra, one can propose the microscopic Hamiltonian and parameterize the exchange interactions.

In linear spin-wave theory, the spin deviation operators deviate fully aligned spins based on the Holstein-Primakoff tranformation. The excitation is a well-defined quasiparticle, which depends on the wavevector $\boldsymbol{k}$ according to the dispersion relation $\omega(\boldsymbol{k})$. Linear spin-wave theory works particularly well for large spins where the spin deviation is still small compared to the total spin, such that the expectation value of the quantum mechanical spin operators is almost the same as in the classical case.

Linear spin-wave theory is used to verify the proposed Hamiltonians and parameterise the exchange interactions in a connection with the measurement of the exci-

tations in the antiferromagnetic honeycomb magnets Na_2IrO_3 (See Chapter 4) and Li_2IrO_3 (See Chapter 6).

2.5 Quantum Magnetism

The quantum mechanical properties of magnetism come from cooperative magnetic order and dynamical phenomena, which are enhanced by frustrating geometry and low dimensionality of magnetic interactions.

2.5.1 Two-Dimensional Magnetism

The Mermin-Wagner theorem [13] states that there is no long-range ordering at the finite temperature in a two-dimensional Heisenberg antiferromagnet with short-range interactions. In reality, most samples show long-range magnetic ordering since there is a small interlayer coupling which has an impact, leading to the build up of magnetic order at a temperature where the thermal fluctuation energy is lower than the effective interlayer coupling energy.

Although the systems studied in this thesis, $\mathcal{A}_2IrO_3$ ($\mathcal{A}$=Na, Li) with a layered structure show long-range magnetic order at a finite temperature, the interlayer spacing is rather large and it is justified to assume in a first approximation that the magnetic excitations can be effectively decribed by two-dimensional magnetic interaction.

2.5.2 Frustration Effects

Geometric frustration occurs when the magnetic interactions cannot all be simultaneously stabilized due to the geometry of the lattice. As an illustration, Ising antiferromagnetic exchange on the two-dimensional isotropic triangular lattice does not give conventional magnetic order as shown in Fig. 2.4a), but a spin liquid is proposed [14]. Antiferromagnetic interaction on the honeycomb lattice provides a special playground for geometric frustration. The honeycomb lattice is not a Bravais lattice, and it is made up of two sublattices, thus when only considering the first nearest neighbours, simple antiferromagnetic order is not frustrated. However, strong inter-

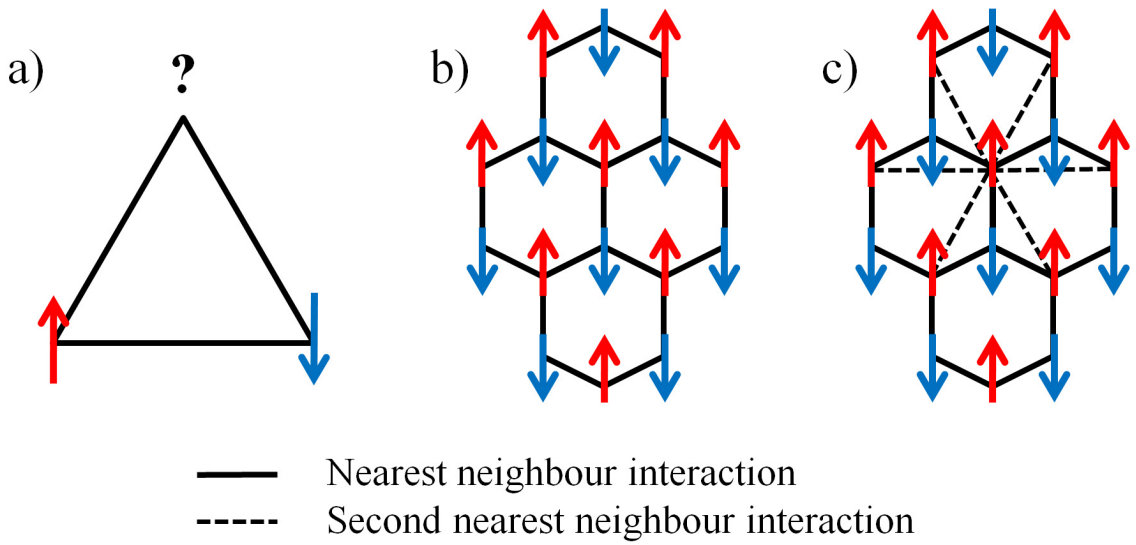


Figure 2.4: Frustration in the Two-Dimensional Triangular and Honeycomb Lattices. a) Geometric frustration on the isotropic triangular lattice with the antiferromagnetic nearest-neighbour interaction. The magnetic moment direction of the third corner ion cannot be determined. b) Simple antiferromagnetic order with nearest neighbour antiferromagnetic coupling on a bipartite honeycomb lattice. c) The magnetism starts to be frustrated with the inclusion of antiferromagnetic next nearest neighbour coupling (dashed line).

actions beyond the first nearest neighbour cannot be simultaneously satisfied by the conventional antiferromagnetic Néel order.

In the isotropic Heisenberg J_1-J_2-J_3 model where J_i is the i-th nearest neighbour exchange interaction, various magnetic orders are predicted by the mean-field theory, depending on the relative exchange interactions [5, 6, 7]. The outcome of these competing exchange interactions is various distinct magnetic orders (See Fig. 4.7) including collinear orders such as stripy and zigzag phases, as well as the non-collinear spiral phases. Two-dimensional magnetism in the honeycomb lattice is the central subject of this thesis.

2.6 Magnetism in the Two-Dimensional Honeycomb Lattice

Among the phases predicted in Fig. 4.7), the magnetic structure and excitations of the conventional Néel order on the honeycomb lattice have been previously studied by neutron scattering experiments. For instance, the magnetic spectra of $MnPS_3$ [15] shows a good agreement with linear spin-wave theory predictions basded on a method of dominant nearest neighbour exchange interaction.

The introduction of anisotropic exchange interaction induced by strong spin-orbit coupling could alter the nature of the magnetic order predicted for this model. A system with strong spin-orbit coupling is an interesting subject since the magnetism on a honeycomb lattice of such ions has been predicted to exhibit various exotic magnetic phenomena quantum spin liquids [3], field-induced topological order [16]. Spin-orbit coupling is often neglected in magnetic studies of 3d compounds as it is small. However, it is much stronger in ions with $5d$ orbitals due to the larger number of electrons, because it is proportional to Z^4, where Z is the number of electrons in the ion, whereas Coulomb repulsion weakens in $5d$ orbitals since it is more spatially extended. This new energy hierarchy leads to an unusual spin-orbital entangled ground state with J_{eff}=1/2. The magnetic interactions of $5d$ ions on the honeycomb lattice combined with a CEF environment of edge-sharing octahedra may stabilise Kitaev interaction, bond-dependent Ising exchange, which are explained in detail in Section 4.4.

2.7 Quantum Magnets Studied in This Thesis

In this thesis, the cooperative magnetism in the two-dimensional honeycomb antiferromagnets $\mathcal{A}_2IrO_3$ ($\mathcal{A}$=Na, Li) and the intermediate material (solid solution) $(Na_{1-x}Li_x)_2IrO_3$, which are all candidates to display novel magnetism stabilized by strong relativistic spin-orbit coupling of the $5d$ Ir ions, are explored using various techniques.

In Chapter 4, the magnetic order and excitations of the compound Na_2IrO_3, in

which edge-sharing IrO_6 octahedra form a honeycomb lattice are investigated using bulk susceptibility, muon spin rotation and inelastic neutron scattering techniques, and the neutron data is analysed using linear spin-wave theory.

In Chapter 5, the crystal structure of Na_2IrO_3 is revised using the combined techniques of single crystal x-ray diffraction and ab-initio calculations as well as the diffraction simulations.

In Chapter 6, the magnetic order and excitations of the compound Li_2IrO_3 are studied using bulk susceptibility, muon spin rotation and inelastic neutron scattering experiments, modelled using linear spin-wave theory.

In Chapter 7, the crystal structure of Li-doped $(Na_{1-x}Li_x)_2IrO_3$ at various dopings is examined with single crystal diffractometry and structure factor diffraction simulations.

Chapter 3

Experimental Techniques

This Chapter outlines the experimental methods used in this thesis. The properties of neutrons will be first explained and compared with complementary x-ray scattering techniques in Sec. 3.1. The theory of neutron scattering will be then introduced in Sec. 3.2, followed by the nuclear and magnetic scattering cross-section in Sec. 3.2.1 and 3.2.2, respectively. The instrument components for neutron scattering are briefly explained in Sec. 3.3 whose combinations lead to the neutron instruments used in this thesis, explained in Sec. 3.4. X-ray diffraction techniques are presented in Sec. 3.5 with the theory in Sec. 3.5.1 and the explanations of the instruments used in this thesis in Sec. 3.5.2. Susceptibility measurements for studying the bulk magnetism will be outlined in Sec. 3.6.

3.1 Basic Properties of Neutrons

Neutron and x-ray scattering are complementary techniques that allows us to obtain information about physical properties in solids at the atomic scale. In this section, the properties of neutrons are introduced and compared with that of x-rays.

One of the unique characteristics of a neutron is that it interacts with the atomic nucleus, as opposed to x-rays, which are scattered by the electron cloud and thus the x-ray scattering cross-section increases with the total number of electrons. The nuclear-sensitive neutron scattering technique can in principle distinguish more easily neighbouring atoms in the periodic table. It can also distinguish isotopes of the same

atom, so the deuteration of specific atoms affects the neutron scattering cross-section (e.g., the hydrogen atom is a strong neutron scatterer, whereas deuterium is a weak scatterer; therefore, substitution of hydrogen by deuterium in the material of interest allows us to suppress the uninteresting strong scattering from hydrogen. Thus, neutron scattering is a powerful technique to study, for example organic materials which are made up of hydrogen and other light atoms.

Since the neutron interacts weakly with matter, it produces a small perturbation in the sample. The scattering matrix element is very well known. Therefore, interpretation of results can be made very quantitatively.

The basic properties of the neutron are summarised in Table. 3.1. Because the neutron does not have charge, it is not affected by the Coulomb field from electrons, thus it can penetrate deeply inside the sample, and interact with the bulk. In combination with extreme sample environment such as high magnetic and electric fields, or hydrostatic pressure, they make the neutron scattering a very powerful technique of the microscopic physics under such extreme conditions.

Coincidentally, thermal neutrons can have energies compatible with elementary excitations of matter and wavelengths compatible with typical interatomic distances ($\sim$Å). By measuring coherent scattering of thermal neutrons the diffraction technique, the structure of solids can be determined. The energy of thermal neutrons can be as low as a few meV (See Table. 3.1), and their energy range is adequate to probe elementary excitations in solids, such as phonons and magnons, and up to 50 $\sim$ 100 meV becomes suitable to probe transition between crystal field levels of magnetic ions. The neutron has a spin $S = 1/2$, therefore it can interact with the magnetic field distribution of the unpaired electrons in the sample. These unique properties make the neutron scattering a unique technique to probe both the nuclear and magnetic structure of a system as well as their excitations (dynamics).

Table 3.1: Basic properties of the neutron. m_p refers to the proton's mass.

Property	Value
charge	0
mass, m_n	1.675×10^{-27} kg $\approx m_p$
spin, S	1/2
thermal neutron E, λ	$\sim$ 25 meV, $\sim$ 1.81 Å
magnetic dipole moment, μ_n	-1.913 μ_N ($\mu_N = e\hbar/2m_p$)

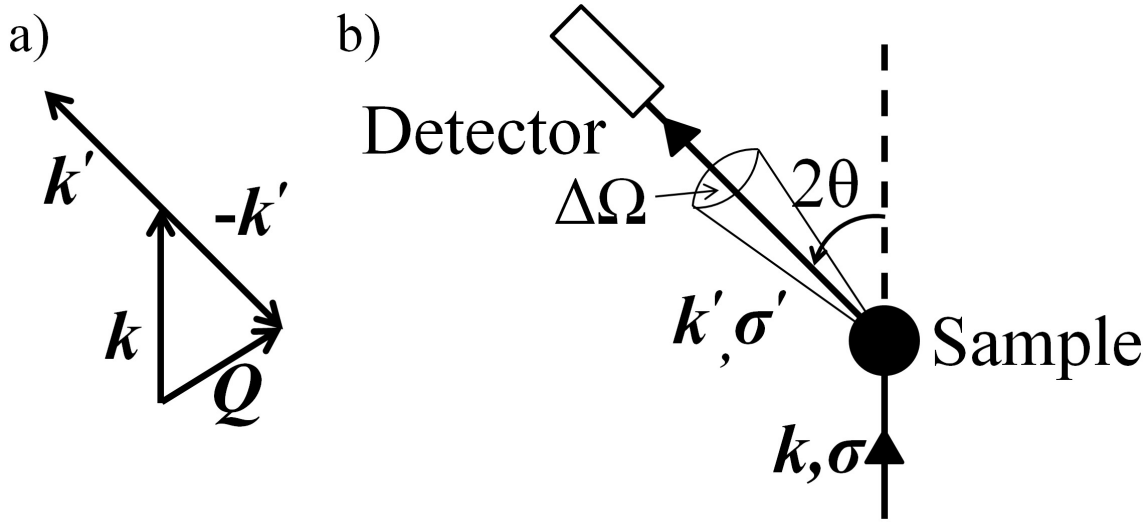


Figure 3.1: Geometry of Neutron Scattering. a) The scattering triangle $\boldsymbol{k} - \boldsymbol{k}' = \boldsymbol{Q}$. b) A schematic diagram of a neutron scattering experiment.

3.2 Theory of Neutron Scattering

This section gives an outline of the theory of neutron scattering as discussed in more detail in Refs. [17, 18, 19].

A neutron scattering experiment consists of an incoming neutron beam incident on a sample, a detector measuring the spectrum of the scattered neutrons. The typical geometry of a neutron scattering experiment is illustrated in Fig. 3.1. Quantitatively, the neutron scattering probability can be described by the partial differential cross-section, defined

$$\frac{d^2\sigma}{d\Omega dE'} = \frac{\text{total number of neutrons scattered per second with energy interval } dE' \text{ into a solid angle } d\Omega}{\Psi_0 \Delta\Omega \Delta E'}, \tag{3.1}$$

with units of area (per energy per unit solid angle). Here E' is the final energy of neutrons, Ψ_0 is the incident flux of neutrons (i.e., the number of neutrons passing through the an area perpendicular to the beam direction per unit time). In an actual experiment, the neutron count rate in a detector (i.e., the total number of neutrons scattered toward the specific direction (2θ)) (See Fig. 3.1), is related to the the partial differential cross-section by

$$I = \eta \Psi_0 \frac{d^2\sigma}{d\Omega dE'} \Delta\Omega \Delta E'. \tag{3.2}$$

$\Delta\Omega$ is the total solid angle subtended by the detector, detector efficiency is η, $\Delta E'$ is the energy window, and E' is the final energy of the scattered neutrons. By measuring I, the partial differential cross-section $d^2\sigma/d\Omega dE'$ is experimentally determined based on the pre-determined instrumental parameters, and it is compared with theoretical calculations based on various scattering models.

When the range of the scattering potential is much smaller than the neutron wavelength, the scattering can be considered to be spherically symmetric and therefore can be expressed by a plane wave with characteristic wavevector $\boldsymbol{k}$. During the scattering process, the neutron changes wavevectors from $\boldsymbol{k}$ to $\boldsymbol{k}'$ at an angle 2θ with respect to $\boldsymbol{k}$, and the spin state of neutrons changes from σ to σ', leading to a change of state of the sample system from λ to λ'. The transferred energy is determined by the energy

conservation rule as

$$\begin{aligned}\hbar\omega &= E - E' \\ &= \frac{\hbar^2 k^2}{2m} - \frac{\hbar^2 k'^2}{2m} \\ &= \frac{\hbar^2 (k^2 - k'^2)}{2m},\end{aligned} \tag{3.3}$$

where m is the mass of the neutron and $\hbar = h/2\pi$, where h is Plank's constant. Since the total momentum is also conserved, the transferred wavevector $\boldsymbol{Q}$ is given by

$$\boldsymbol{Q} = \boldsymbol{k} - \boldsymbol{k'}, \tag{3.4}$$

illustrated in Fig. 3.1. The magnitude of the wavevector transfer Q is then obtained as

$$Q^2 = k^2 + k^{'2} - 2kk' \cos(2\theta). \tag{3.5}$$

In the case of elastic scattering, the energy transfer is zero ($\hbar\omega = 0$, $k = k'$), and Eq. (3.5) converges into the Bragg condition $Q = 2k \sin(2\theta)$. In the case inelastic scattering, the energy transfer is non-zero ($\hbar\omega \neq 0$, $k \neq k'$).

When the interaction potential V between the incident neutron and the sample is small enough, the scattering can be treated as a perturbation and the transition rate of the sample state can be expressed by first-order perturbation theory using Fermi's Golden rule as

$$W_{|\lambda \boldsymbol{k}\sigma\rangle \to |\lambda' \boldsymbol{k}'\sigma'\rangle} = \frac{2\pi}{\hbar} |\langle \lambda' \boldsymbol{k}' \sigma' | V | \lambda \boldsymbol{k} \sigma \rangle|^2 \ \rho_{\boldsymbol{k}'}, \tag{3.6}$$

where the unprime (prime) variables indicate the initial (final) neutron state, and $\rho_{\boldsymbol{k}'}$ is the number of momentum states in the solid angle $d\Omega$ per energy range dE' in the final state $\boldsymbol{k}'$.

The partial differential cross-section is obtained by summing Eq. (3.6) over all final states λ' of the sample and weighting all initial states λ with the probability distribution p_λ, and is given by

$$\frac{d^2\sigma}{d\Omega dE'} = \frac{k'}{k} \Big(\frac{m}{2\pi\hbar^2} \Big)^2 \sum_{\lambda\lambda'} p_\lambda \sum_{\sigma\sigma'} p_\sigma |\langle \boldsymbol{k}' \lambda' \sigma' | \hat{V} | \boldsymbol{k} \lambda \sigma \rangle|^2 \delta(\hbar\omega + E_{\lambda'} - E_\lambda). \tag{3.7}$$

where the summation over the initial neutron spin states σ appears with the normalised weight p_σ. The factor k'/k arises from the density of the final neutron states ($\rho_{\boldsymbol{k}'}$) divided by the incident neutron flux, and the delta function ensures the conservation of total energy.

If the interacting potential is not a function of momentum but only neutron position and spin, the potential would not be perturbed by the neutron's momentum (i.e., neutrons of specific momentum will not excite the state of the potential). In this case, the wavevector of neutrons can be treated as a separable variable in the wavefunction such as $|\lambda\boldsymbol{k}\sigma\rangle = |\boldsymbol{k}\rangle|\lambda\sigma\rangle$ (before scattering) and $|\lambda'\boldsymbol{k}'\sigma'\rangle = |\boldsymbol{k}'\rangle|\lambda'\sigma'\rangle$ (after scattering). The wavevector part in the wavefunction in Eq. (3.6) can be combined with the potential as $|\langle\lambda'\sigma'|V(\boldsymbol{Q})|\lambda\sigma\rangle|$ where $V(\boldsymbol{Q})$ is the Fourier transform of the potential energy in real space, and given by

$$V(\boldsymbol{Q}) = \int d\boldsymbol{r} V(\boldsymbol{r}) e^{i\boldsymbol{Q}\cdot\boldsymbol{r}}, \tag{3.8}$$

where the integration runs over the neutron coordinate $\boldsymbol{r}$ and the scattering wavevector is defined as $\boldsymbol{Q} = \boldsymbol{k} - \boldsymbol{k}'$. Now, Eq. (3.7) can be expressed with $V(\boldsymbol{Q})$ as

$$\frac{d^2\sigma}{d\Omega dE'} = \frac{k'}{k}\Big(\frac{m}{2\pi\hbar^2}\Big)^2 \sum_{\lambda\lambda'} p_\lambda \sum_{\sigma\sigma'} p_\sigma |\langle\lambda'\sigma'|V(\boldsymbol{Q})|\lambda\sigma\rangle|^2 \delta(\hbar\omega + E_{\lambda'} - E_\lambda). \tag{3.9}$$

which is called the first Born approximation to the cross-section, and its consequence is that the nuclear scattering amplitude depends on $\boldsymbol{Q} = \boldsymbol{k} - \boldsymbol{k}'$ rather than some other functions of $\boldsymbol{k}, \boldsymbol{k}'$ [18]. The origin of V can be nuclear via the strong nuclear force (nuclear scattering in Section 3.2.1), or magnetic via the dipole-dipole interaction (magnetic scattering in Section 3.2.2).

The change of neutron spin state σ is irrelevant for unpolarized neutron scattering, and when the potential is independent of the neutron spin,

$$\langle\sigma'|V(\boldsymbol{Q})|\sigma\rangle = \delta_{\sigma,\sigma'} V. \tag{3.10}$$

Here the Kronecker delta function comes from the orthogonality of different spin states of neutrons. The spin dependence in the scattering amplitude disappears in Eq. (3.9) for unpolarised neutrons, which is the type of technique used for all experiments in

this thesis. Therefore, the scattering theory based on the first Born approximation, Eq. (3.9), will be derived for unpolarised neutrons.

3.2.1 Nuclear Scattering Cross-Section

In this Subsection, the nuclear scattering cross-section [17, 18, 19] will be derived based on the interaction of neutrons with the atomic nucleus. In this kind of scattering, the typical wavelength of thermal neutrons used is of the order of 10^{-10} m ($\sim$ Å) whereas the interaction range is about 10^{-15} m. Therefore, the range of the force is much smaller than the wavelength of thermal neutrons, and the first Born approximation in Eq. (3.9) applies. In this case, the potential V is an essentially isotropic delta-function, due to a short-ranged nature, with the Fermi pseudo-potential

$$V(\mathbf{r}) = \frac{2\pi\hbar^2}{m} \sum_l b_l \delta(\mathbf{r} - \boldsymbol{R}_l), \tag{3.11}$$

where m is the neutron mass, $\boldsymbol{R}_l$ is the nuclear position of the l-th atom, and b_l is the nuclear scattering length, which depends on the type of nucleus, the isotope and the relative orientation of the nuclear and neutron spins.

Inserting Eq. (3.11) and Eq. (3.8) into Eq. (3.9) for unpolarised neutrons leads to

$$\frac{d^2\sigma}{d\Omega dE'} = \frac{k'}{k} \sum_{\lambda'\lambda} p_\lambda \left| \langle \lambda' | \sum_l b_l \exp(i\boldsymbol{Q} \cdot \boldsymbol{R}_l) | \lambda \rangle \right|^2 \delta(\hbar\omega + E_{\lambda'} - E_\lambda) \tag{3.12}$$

where p_λ represents the probability of the system to be in the state $|\lambda\rangle$ given by $\exp(-E_\lambda/k_BT)/Z$, where $Z = \sum_\lambda \exp(-E_\lambda/k_BT)$. Eq. (3.12) can be reformulated as

$$\begin{aligned} \frac{d^2\sigma}{d\Omega dE'} = \frac{k'}{k} \sum_{\lambda'\lambda} p_\lambda \sum_{l,l'} \overline{b_{l'}^* b_l} \langle \lambda | \exp(-i\boldsymbol{Q} \cdot \boldsymbol{R}_{l'}) | \lambda' \rangle \\ \times \langle \lambda' | \exp(i\boldsymbol{Q} \cdot \boldsymbol{R}_l) | \lambda \rangle \ \delta(\hbar\omega + E_{\lambda'} - E_\lambda) \end{aligned} \tag{3.13}$$

where $\overline{b_{l'}^* b_l}$ is the average of $b_{l'}^* b_l$ over a random nuclear spin orientation and isotope distribution in a large number of nuclei. Assuming no correlation between the b values of different nuclei, it is described by

$$\overline{b_{l'}^* b_l} = |\bar{b}|^2 + \delta_{l,l'}(\overline{|b|^2} - |\bar{b}|^2), \tag{3.14}$$

where the bar denotes an average over all nuclei in the target system, and Eq. (3.14) becomes $|\bar{b}|^2$ at $l' \neq l$ and $\overline{|b|^2}$ at $l' = l$. Note that for the more general case where types are multiple of nuclei in the target system, $\bar{b} = \sum_i f_i b_i$ and $\overline{|b|^2} = \sum_i f_i |b_i|^2$, where f_i is the relative probability that a nucleus is of type i with scattering length b_i with the normalisation condition $\sum_i f_i = 1$ [17]. Substituting Eq. (3.14) into Eq. (3.13), the cross-section can be split into two parts denoting the coherent and incoherent scattering,

$$\frac{d^2\sigma}{d\Omega dE'} = \frac{d^2\sigma_c}{d\Omega dE'} + \frac{d^2\sigma_i}{d\Omega dE'} = \frac{k'}{k}\frac{1}{4\pi}[\sigma_c S_c(\boldsymbol{Q},\omega) + \sigma_i S_i(\boldsymbol{Q},\omega)]. \tag{3.15}$$

The total cross-sections and the dynamic correlation functions in the integral form are given by [17]

$$\sigma_c = 4\pi|\bar{b}|^2, \tag{3.16}$$

$$\sigma_i = 4\pi[\overline{|b|^2} - |\bar{b}|^2], \tag{3.17}$$

$$S_c(\boldsymbol{Q},\omega) = \frac{1}{2\pi\hbar}\int_{-\infty}^{\infty} dt e^{-i\omega t}\sum_{l,l'}\langle e^{-i\boldsymbol{Q}\cdot\boldsymbol{R}_{l'}(0)} e^{i\boldsymbol{Q}\cdot\boldsymbol{R}_l(t)}\rangle, \tag{3.18}$$

$$S_i(\boldsymbol{Q},\omega) = \frac{1}{2\pi\hbar}\int_{-\infty}^{\infty} dt e^{-i\omega t}\sum_{l}\langle e^{-i\boldsymbol{Q}\cdot\boldsymbol{R}_{l}(0)} e^{i\boldsymbol{Q}\cdot\boldsymbol{R}_l(t)}\rangle, \tag{3.19}$$

where $\langle ... \rangle$ denotes a statistical average over the initial states of the system. $\boldsymbol{R}_j(t)$ is the position of the j-th nucleus at time t, which is the time-dependent position operator in the Heisenberg representation and linked to the Schrödinger representation by $\boldsymbol{R}_l(t) = e^{i\mathcal{H}t/\hbar}\boldsymbol{R}_l e^{-i\mathcal{H}t/\hbar}$, where $\mathcal{H}$ is the Hamiltonian.

From Eq. (3.18) and Eq. (3.19), it is now evident that the two contributions have different features. The coherent scattering in Eq. (3.18) is proportional to the correlation between the same nucleus at different times and the different nucleus at different times, which gives an interference effect. On the other hand, the incoherent scattering depends on the correlation between the same nucleus at different times, thus only give a mere background signal in a neutron scattering experiment. This background is proportional to the variance of neutron scattering lengths coming from different cross-sections of multiple different atoms and nuclear spins. The physical interpretation of the coherent scattering is that it represents the correlation from the averaged

scattering length $|\bar{b}|$ over the all mixed scattering lengths from different nuclei, and the incoherent scattering is the actual deviated scattering from the averaged value. $S(\boldsymbol{Q},\omega)$ represents the nuclear-nuclear correlation function in reciprocal space that is obtained by the Fourier transformation of the density correlation function $G(\boldsymbol{r},t)$ in real space, ($\langle ...\rangle$ in Eq. (3.18)).

When considering a single crystal composed of N atoms, assuming a Bravais crystal with only one atom per unit cell for simplicity, the atomic position $\boldsymbol{R}$ can be expressed by

$$\boldsymbol{R} = \mathrm{r}_1\mathbf{a}_1 + \mathrm{r}_2\mathbf{a}_2 + \mathrm{r}_3\mathbf{a}_3, \tag{3.20}$$

where $\mathbf{a}_i$ ($i = 1, 2, 3$) is a lattice vector in the unit cell and r_i ($i = 1, 2, 3$) are integers. The volume of the unit cell is

$$\nu_0 = \mathbf{a}_1 \cdot [\mathbf{a}_2 \times \mathbf{a}_3]. \tag{3.21}$$

The reciprocal lattice vectors are defined as

$$\boldsymbol{\tau}_1 = \frac{2\pi}{\nu_0}[\mathbf{a}_2 \times \mathbf{a}_3], \quad \boldsymbol{\tau}_2 = \frac{2\pi}{\nu_0}[\mathbf{a}_3 \times \mathbf{a}_1], \quad \boldsymbol{\tau}_3 = \frac{2\pi}{\nu_0}[\mathbf{a}_1 \times \mathbf{a}_2], \tag{3.22}$$

in order to satisfy $\mathbf{a}_i \cdot \boldsymbol{\tau}_j = 2\pi\ \delta_{i,j}$. The volume of unit cell of the reciprocal lattice is

$$\boldsymbol{\tau}_1 \cdot [\boldsymbol{\tau}_2 \times \boldsymbol{\tau}_3] = \frac{(2\pi)^3}{\nu_0}. \tag{3.23}$$

The coherent scattering cross-section from a single crystal sample gives nuclear Bragg peaks at reciprocal lattice vectors $\boldsymbol{\tau}$, which are perpendicular to families of atomic planes. At $t \to \infty$ in Eq. (3.18), the time-dependence of the correlation function in the definition of the Heisenberg operator disappears, giving an elastic neutron scattering cross-section ($k = k'$, $\lambda = \lambda'$, $E = E'$). Then, the correlation function in Eq. (3.18) is simplified as

$$\sum_{l,l'} \langle e^{-i\boldsymbol{Q}\cdot\boldsymbol{R}_{l'}(0)} e^{i\boldsymbol{Q}\cdot\boldsymbol{R}_l(t)} \rangle = N \sum_l e^{i\boldsymbol{Q}\cdot\boldsymbol{R}_l}, \tag{3.24}$$

where for simplicity $l' = 0$ because the correlation between the positions of the nuclei l and l' depends only on the difference $l - l'$ in the Bravais lattice [17]. From the periodicity of the crystal, $\Sigma_l \exp(i\boldsymbol{Q}\cdot\boldsymbol{R}_l) = \frac{(2\pi)^3}{\nu_0}\Sigma_{\boldsymbol{\tau}}\delta(\boldsymbol{Q} - \boldsymbol{\tau})$ where the sum runs over

all reciprocal lattice vectors $\boldsymbol{\tau}$ [17, 18]. The nuclear elastic scattering cross-section becomes

$$\frac{d\sigma_N}{d\Omega}(\boldsymbol{Q}) = N\frac{(2\pi)^3}{\nu_0}|\bar{b}|^2\sum_{\boldsymbol{\tau}}\delta(\boldsymbol{Q}-\boldsymbol{\tau}). \tag{3.25}$$

This is generalised to the case with more than one atom per unit as [19]

$$\frac{d\sigma_N}{d\Omega}(\boldsymbol{Q}) = N\frac{(2\pi)^3}{\nu_0}\sum_{\boldsymbol{\tau}}|F_N(\boldsymbol{Q})|^2\delta(\boldsymbol{Q}-\boldsymbol{\tau}), \tag{3.26}$$

where the sum extends over all wavevectors $\boldsymbol{\tau}$ of the reciprocal lattice of the crystal N in the numbers of unit cells, and the nuclear structure factor is given by

$$F_N(\boldsymbol{Q}) = \sum_l b_l e^{i\boldsymbol{Q}\cdot\boldsymbol{R}_l}e^{-W_l}, \tag{3.27}$$

where the sum extends over all nuclei at positions $\boldsymbol{R}_l$ in the nuclear unit cell. For multiple isotopes of the same nucleus or for the multiple nuclei, b_l is replaced by the average scattering length. The Debye-Waller factor e^{-W_l} corrects for the fact that the atoms oscillate around their equilibrium positions due to thermal motion, decreasing the nuclear structure factor, and it is usually small at low temperatures much lower than room temperature.

3.2.2 Magnetic Scattering Cross-Section

The starting point to derive the magnetic scattering cross-section is the partial differential cross-section in Eq. (3.7)

$$\frac{d^2\sigma}{d\Omega dE'} = \frac{k'}{k}\Big(\frac{m}{2\pi\hbar^2}\Big)^2\sum_{\lambda\lambda'}p_\lambda\sum_{\sigma\sigma'}p_\sigma|\langle\boldsymbol{k}'\lambda'\sigma'|V_m|\boldsymbol{k}\lambda\sigma\rangle|^2\delta(\hbar\omega+E_{\lambda'}-E_\lambda). \tag{3.28}$$

where the magnetic form of the potential (V_m) is determined by the interaction between the magnetic dipole moment of the neutron ($\boldsymbol{\mu}$) and the magnetic field ($\boldsymbol{B}$) generated by the unpaired electrons in the sample

$$V_m = -\boldsymbol{\mu}\cdot\boldsymbol{B}, \qquad \boldsymbol{\mu} = -\gamma\mu_N\boldsymbol{\sigma}, \tag{3.29}$$

where γ is a positive constant (≈ 1.9132), μ_N is the nuclear magneton ($= e\hbar/2m_p$), and σ is the Pauli spin operator of the neutron (with eigenvalues ± 1). The magnetic

field ($\boldsymbol{B}$) created by an electron with spin $\boldsymbol{s}$ and momentum $\boldsymbol{p}$ at a distance $\boldsymbol{R}$ away is

$$\boldsymbol{B} = \boldsymbol{B}_s + \boldsymbol{B}_L = \frac{\mu_0}{4\pi}\left[-\boldsymbol{\nabla}\times\left(2\mu_B\frac{\boldsymbol{s}\times\boldsymbol{R}}{R^3}\right) - \frac{2\mu_B}{\hbar}\frac{\boldsymbol{p}\times\boldsymbol{R}}{R^3}\right], \tag{3.30}$$

where the first term is the dipolar magnetic field of the spin moment, and the second term is the field due to the orbital motion of the electron. Inserting Eq. (3.30) into Eq. (3.29) causes the magnetic potential to become

$$V_m = -\frac{\mu_0}{4\pi}\gamma\mu_N 2\mu_B\boldsymbol{\sigma}\cdot(\boldsymbol{W}_s + \boldsymbol{W}_L), \tag{3.31}$$

where

$$\boldsymbol{W}_s = \boldsymbol{\nabla}\times\left(\frac{\boldsymbol{s}\times\hat{\boldsymbol{R}}}{R^2}\right), \boldsymbol{W}_L = \frac{1}{\hbar}\frac{\boldsymbol{p}\times\hat{\boldsymbol{R}}}{R^2}. \tag{3.32}$$

The matrix element $\langle\boldsymbol{k}'|\boldsymbol{W}|\boldsymbol{k}\rangle$ where $\boldsymbol{W} = \boldsymbol{W_s} + \boldsymbol{W_L}$ with V_m in Eq. (3.31) yields

$$\langle\boldsymbol{k}'|\boldsymbol{W}|\boldsymbol{k}\rangle = 4\pi\mathbf{M}'_{\perp} \tag{3.33}$$

with

$$\mathbf{M}'_{\perp} = \hat{\boldsymbol{Q}}\times\left[-\frac{1}{2\mu_B}\mathbf{M}(\mathbf{Q})\times\hat{\boldsymbol{Q}}\right], \mathbf{M}(\mathbf{Q}) = \mathbf{M_s}(\mathbf{Q}) + \mathbf{M_L}(\mathbf{Q}) \tag{3.34}$$

where $\mathbf{M}'_{\perp}$ is the perpendicular component of the effective magnetization $-\frac{1}{2\mu_B}\mathbf{M}(\mathbf{Q})$, coming from the Fourier transformation of the electron's spin and orbital magnetization with respect to the scattering wavevector $\boldsymbol{Q} = \boldsymbol{k} - \boldsymbol{k}'$, and $\hat{\boldsymbol{Q}}$ is the unit vector along $\boldsymbol{Q}$. The physical interpretation of Eq. (3.34) is that the magnetic neutron scattering occurs from the interaction of the magnetic moment of the neutron and the magnetic moment of the electron's spin and orbital moment. Geometrically, Eq. (3.34) means that the neutrons can only detect the perpendicular component of the magnetic moment with respect to $\boldsymbol{Q}$.

Combined with Eq. (3.31) and Eq. (3.33), the partial differential cross-section in Eq. (3.28) for unpolarised neutrons becomes

$$\frac{d^2\sigma}{d\Omega dE'} = (\gamma r_o)^2\frac{k'}{k}\sum_{\lambda\lambda'}p_\lambda|\langle\lambda'|\mathbf{M}'_{\perp}|\lambda\rangle|^2\delta(\hbar\omega + E_{\lambda'} - E_\lambda) \tag{3.35}$$

where r_o is the classical radius of the electron analytical formula 2.82×10^{-15} m. For polarised neutrons, the matrix element of the magnetic potential should be considered

with the spin dependence since Eq. (3.32) also contains the spin component $\boldsymbol{\sigma}$. Using the relation $\mathbf{M'}_{\perp}^{\dagger} \cdot \mathbf{M'}_{\perp} = \sum_{\alpha\beta}(\delta_{\alpha\beta} - \hat{Q}_{\alpha}\hat{Q}_{\beta}){M'}_{\alpha}^{\dagger}{M'}_{\beta}$, Eq. (3.35) can be stated with the completeness relation $\sum_{\lambda'} |\lambda'\rangle\langle\lambda'| = 1$ as

$$\frac{d^2\sigma}{d\Omega dE'} = (\gamma r_o)^2 \frac{k'}{k} \sum_{\alpha\beta}(\delta_{\alpha\beta} - \hat{Q}_{\alpha}\hat{Q}_{\beta}) \sum_{\lambda\lambda'} p_{\lambda}\langle\lambda|{M'}_{\alpha}^{\dagger}|\lambda'\rangle\langle\lambda'|{M'}_{\beta}|\lambda\rangle\delta(\hbar\omega + E_{\lambda'} - E_{\lambda}). \tag{3.36}$$

For spin-only scattering, where the orbital magnetic moment is quenched by the strong crystal field, the partial differential cross-section for unpolarized neutrons becomes

$$\frac{d^2\sigma}{d\Omega dE'} = (\gamma r_o)^2 \frac{k'}{k} \Big[\frac{1}{2} g f(\boldsymbol{Q})\Big]^2 \exp(-2W(\boldsymbol{Q})) \sum_{\alpha\beta}(\delta_{\alpha\beta} - \hat{Q}_{\alpha}\hat{Q}_{\beta}) S^{\alpha\beta}(\boldsymbol{Q},\omega), \tag{3.37}$$

where g is the Landé g-factor, $f(\boldsymbol{Q})$ is the magnetic form factor of the ion, and its dependence of $\boldsymbol{Q}$ stems from the real space distribution of the electronic wavefunctions. The $g = 2$ for the spin only scattering. The Debye-Waller factor, $\exp(-2W(\boldsymbol{Q}))$, is caused by the thermal motion of the ions around their equilibrium position and usually falls off less rapidly than $f(\boldsymbol{Q})$ with increasing Q. Therefore, it is usually neglected when the magnetic scattering is considered. $\delta_{\alpha\beta}$ is the Kronecker delta function where α and β stand for x,y and z. $\hat{Q}$ is the unit vector along $\boldsymbol{Q}$, and $\hat{Q}_{\alpha}$ is the unit vector along the α direction.

The dynamical correlation function $S^{\alpha\beta}(\boldsymbol{Q},\omega)$ in Eq. (3.37), which is the space and time Fourier transform of the time-dependent spin-spin correlation function, and is

$$S^{\alpha\beta}(\boldsymbol{Q},\omega) = \frac{1}{2\pi\hbar N} \sum_{ll'} e^{i\boldsymbol{Q}\cdot(\boldsymbol{R}_l - \boldsymbol{R}_{l'})} \int_{-\infty}^{+\infty} dt e^{-i\omega t} \langle S_{l'}^{\alpha}(0) S_{l}^{\beta}(t)\rangle, \tag{3.38}$$

where $S_{l'}^{\alpha}(0)$ is the α-component of the spin at site l' and at time 0, and $\langle ...\rangle$ denotes a statistical averaged value of the spin-spin correlation in real space. At $T = 0$ K, all states are ground state, which are only excited. The statistical averaged value in Eq. (3.38) is then replaced by the expectation value in the ground state, which simplifies the dynamic correlation function into

$$S^{\alpha\alpha}(\boldsymbol{Q},\omega) = \sum_{\lambda} |\langle\lambda|S^{\alpha}(\boldsymbol{Q})|0\rangle|^2 \delta(\hbar\omega + E_0 - E_{\lambda}), \tag{3.39}$$

where the sum runs over all eigenstates $|\lambda\rangle$ with the energy E_λ, which are excited from the ground state $|0\rangle$ with the energy E_0. $S^\alpha(\boldsymbol{Q})$ is the Fourier transformed magnetic moment along the α-direction, and is given by

$$S^\alpha(\boldsymbol{Q}) = \frac{1}{\sqrt{N}} \sum_i e^{i\boldsymbol{Q}\cdot\boldsymbol{R}_i} S_i^\alpha. \tag{3.40}$$

The iridate systems studied in this thesis are expected to contain both spin and orbital angular momenta as the crystal field energy is smaller than the spin-orbit coupling energy, so a spin-orbit entangled ground state is expected to form. For this case in Eq. (3.37), $\frac{1}{2}gf(\boldsymbol{Q})$ now includes the approximate orbital contribution based on the dipole approximation which applies when $|\boldsymbol{Q}|^{-1}$ is large compared to the mean radius of the orbital wavefunctions of the unpaired electrons [17], and g deviates from 2 by containing the orbital components. Also, $S^{\alpha\beta}(\boldsymbol{Q},\omega)$ refers to scattering from $\boldsymbol{J}$ rather than the $\boldsymbol{S}$ moment, where $\boldsymbol{J}$ is the total angular momentum operator.

When the magnetic moments order periodically in the lattice, magnetic Bragg peaks appear by the mechanics that nuclear Bragg peaks are due to periodic arrangement of atoms in a lattice. The partial differential cross-section for elastic magnetic scattering is

$$\frac{d\sigma_M}{d\Omega}(\boldsymbol{Q}) = (\frac{\gamma r_o}{2\mu_B})^2 N_m \frac{(2\pi)^3}{\nu_{0,m}} \sum_{\boldsymbol{\tau}_m} |F_{M\perp}(\boldsymbol{Q})|^2 \delta(\boldsymbol{Q}-\boldsymbol{\tau}_m), \tag{3.41}$$

where N_m is the number of the magnetic unit cells, $\nu_{0,m}$ is the volume of the magnetic unit cell. $\delta(\boldsymbol{Q}-\boldsymbol{\tau}_m)$ indicates that magnetic Bragg peaks are only detected at the magnetic reciprocal lattice vectors $\boldsymbol{\tau}_m$. The magnetic structure factor is given by

$$\boldsymbol{F}_M(\boldsymbol{Q}) = \sum_l \boldsymbol{m}_l f_l(\boldsymbol{Q})\ e^{-i\boldsymbol{Q}\cdot\boldsymbol{r}_l}\ e^{-W_l} \tag{3.42}$$

where $\boldsymbol{m}_l$ is the magnetic moment at the l-th atom. The elastic magnetic scattering is temperature-dependent since $\boldsymbol{m}_l$ becomes zero above the magnetic ordering transition temperature.

3.3 Neutron Scattering Instrument Components

This chapter reviews the components of a neutron scattering experiment, which are explained in detail in Ref. [20] and [21].

In the neutron scattering experiment, ensuring enough neutron flux is an important factor for obtaining more confident data. An attempt to increase the flux is one of the key efforts when developing neutron scattering, and there are two methods for producing neutron: reactor and spallation sources, which are compared in the Subsection 3.3.1. In both methods, neutrons are generated from high-energy nuclear reactions. Therefore, neutrons needs to be cooled for practical uses in condensed matter physics through the use of moderators, as explained in the Subsection 3.3.2. These cooled neutron beams contain polychromatic wavelengths, which need to be monochromatised. In some cases, this is accomplished by either time-of-flight techniques or single crystals monochromators, which are discussed in the Subsection 3.3.3. The scattered neutrons are measured by detectors, which are discussed in the Subsection 3.3.4.

3.3.1 Neutron Sources

Nuclear reactors produce neutrons from fission of fissile materials. The most frequently used fissile material is ^{235}U, with the reaction of

$$^{235}\mathrm{U} + \mathrm{n} = 2.7\mathrm{n} + \text{fission fragments} + 190\mathrm{MeV} \tag{3.43}$$

where n is the number of neutrons. The excess neutrons can cause further fission events or escape the reactor. To maximize the luminosity of neutrons, in neutron scattering experiments, users seek to focus on as many neutrons as possible in a small volume. Unlike spallation source (to be discussed later), the neutron beams from nuclear reactors are more suitable for experiments with relatively low neutron energy due to the moderate temperature of reactors. Nuclear reactor sources are continuous, so traditionally the triple-axis instrumentation is incorporated with a reactor source. However, it is not uncommon to use time-of-flight techniques with a

reactor source. For instance, the IN6 beamline at the Institut Laue-Langevin (ILL) in Grenoble, France, is a time-of-flight instrument on a reactor source, and was used for experiments reported in this thesis.

Spallation sources are relatively newer than reactor sources. Here, negatively charged Hydrogen ions are initially produced and accelerated by a linear accelerator up to kinetic energies in the GeV range, then the electrons are stripped off at the end of a linear accelerator, leading to a proton beam. The accumulated protons form a single high intensity proton pulse is accelerated in a circular synchrotron before colliding it with a target material, made of a heavy element (tantalum at ISIS or liquid mercury at SNS).

After the collision, large number of nuclei become highly excited nuclei. When the excited nuclei decay, they emit neutrons. The whole process takes place within a pulse repetition rate, suitable for the use of the time-of-flight technique. One of the big advantages of using a spallation source is that it provides a larger neutron flux ($\sim 10^{18}$ neutrons/cm^2·s) compared to that of reactors sources ($\sim 10^{15}$ neutrons/cm^2·s). The spallation source used in this thesis is ISIS at the Rutherford Appleton Laboratory in Oxford, the United Kingdom.

3.3.2 Moderators

The typical energy spectrum of neutrons generated at a source is the order of MeV, whereas a range of 0.1 to 100 meV is required for scattering experiments. Thus, the energy is decreased by using moderators, made up of light atoms such as H_2O. The moderator is maintained at a constant temperature and neutrons reach thermal equilibrium by passing through it. The temperature of the moderator determine the distribution of neutron energies, which can be described by Maxwell's distribution, such that the energy corresponding to the maximum number of neutrons increases with the moderator's temperature. Typical experiments are made with neutrons at room temperature around 300 K, called thermal neutrons. For experiments which need cold or hot neutrons, cold (D_2O at T $\geq$ 20 K) or hot (a graphite block at T $\leq$ 2000 K) moderators can also be used by shifting the energy spectrum of neutrons to

lower or higher energies, respectively. In the experiments of this thesis, cold neutrons with lower incident neutron energies of less than 5 meV were used an IN6 at ILL, France.

3.3.3 Monochromators

To get a monochromatic neutron beam from a white beam containing a wide range of energies, two methods are usually used: the single crystal monochromator and Fermi chopper. The single crystal monochromator diffracts the polychromatic neutron beam by an angle 2θ into a monochromatic beam by satisfying the diffraction condition $2d\sin(\theta) = n\lambda$, where d is the d-spacing of the atomic family of planes scattering the neutron beam. Higher orders ($n \geq 2$) are also diffracted and need to be screened by a filter. One of the best materials for this purpose is a Be filter, which has a cutoff of 5 meV (4 Å) and 3.8 meV (4.6 Å), and it passes all lower energies than this cutoff value, so that it is suitable for cold neutron experiments. In this thesis, the cold neutron beamline IN6 in ILL equipped with a Be filter was used for studying low energy excitations, and the schematic diagram of IN6 beamline is illustrated in Fig. 3.2.

In the time-of-flight instrument on a spallation source, a Fermi chopper is used to select monochromatic neutron. This is made up of a series of curved sheets of alternating neutron absorbing and transparent materials, which rotates along the cylindrical axis with a chosen frequency and phase. When the transmitting slit is parallel to the neutron beams, incident neutrons with a specific energy range can go through, and a faster spinning of the Fermi chopper allows a narrower range of neutron energies to pass. This method is used in experimental beamlines at ISIS such as MARI and MERLIN, used in experiments reported in this thesis.

3.3.4 Detectors

Since Neutrons do not have an electric charge, they have the advantage of weakly interacting with matter and penetrating deeply inside the sample, but they are also difficult to detect. The most common way to detect scattered neutrons from a sample

is to use their nuclear reaction with ^{3}He gas:

$$^1_0\mathrm{n} + ^3_2\mathrm{He} = ^3_1\mathrm{H} + ^1_1\mathrm{H} + \gamma(0.77\mathrm{MeV}) \tag{3.44}$$

where the electrons produced by the ionizing particles by a photon (0.77 MeV) are accelerated towards the anode, giving an electric signal.

Neutron instruments also need a beam monitor to probe the incident neutron flux, which should detect only a small amount of incoming neutrons, such that the majority of neutrons are used for the experiment.

3.4 Neutron Instruments

The instrument components introduced in the Section 3.3 can be put together in various ways to produce the specific properties of a neutron scattering instrument. Instruments can be divided into diffractometers (elastic neutron scattering) and spectrometers (inelastic neutron scattering). With neutron spectrometers, the dynamics of the nuclear and magnetic order are probed via inelastic scattering with a non-zero energy transfer. In this Section, the layout of each instrument utilized for the experiments in this thesis is discussed. A good introduction of instruments including those covered here can be found in Ref. [20].

3.4.1 Time-of-Flight Diffractometer

The aim of doing a neutron diffraction experiment is to detect the Bragg peaks, which results from the coherent interference of neutrons scattered from the ordered ions, to determine the system's structure. In diffraction experiments, since the energy transfer is zero ($\hbar\omega = 0$), the dynamical correlation function $S(\boldsymbol{Q}, \omega)$ reduces to the static case of $S(\boldsymbol{Q})$. The diffractometer can be used to determine the nuclear and magnetic structures of a system.

In time-of-flight diffraction, the incident neuron beam is polychromatic, which means that neutrons with different energies travel with different velocities, but they scattered elastically, and the scattering angle (2θ) is fixed. According to the Bragg

law

$$2d\sin(\theta) = \lambda, \tag{3.45}$$

by determining the wavelength (λ) the d-spacing of the crystalline plane can be calculated. To achieve this, pulsed neutrons are tracked via a total travel time (t) for the total path (L) during the scattering process, which gives the relation

$$\frac{2\pi}{\lambda} = \frac{mL}{\hbar t}. \tag{3.46}$$

where m is the mass of a neutron. Based on the measured total time of flight for neutrons to reach the detectors, the wavelength can be determined. In general, a longer flight path L is preferable for a better resolution $\Delta t/t$. The pulse width Δt is determined by other instrumental components such as moderators, Fermi chopper and so on. The backscattering configuration is used for ensuring a longer L for the better resolution. The drawback is the fact that a backscattering geometry gives access to larger wavevectors ($\boldsymbol{Q}$), so detecting magnetic Bragg peaks is difficult due to the sharp fall-off of the magnetic form factor of the ions ($f(\boldsymbol{Q})$ in Eq. (3.42)) upon increasing $|\boldsymbol{Q}|$.

The instrument used here is the Wide angle In a Single Histogram (WISH) diffractometer at ISIS. WISH provides a wide range of wavelengths ($1.5 \sim 15$ Å), which is preferable for studying complex magnetic order with magnetic Bragg peaks at very low Q. This is the case for Li_2IrO_3 discussed in Chapter 6. The technical details of the WISH diffractometer are discussed online [22] and the reference paper [23].

3.4.2 Time-of-Flight Inelastic Neutron Spectrometer

The time-of-flight technique can be used for measuring the dynamical correlation function $S(\boldsymbol{Q}, \omega)$, the energy spectrum of the exited states as a function of momentum transfer $\boldsymbol{Q}$, and energy transfer $\hbar\omega$. The scattered neutrons which induced excitations in the sample will lose some energy, thus they travel more slowly. By measuring the time and position of detected neutrons in a series of detectors, the energy and momentum of the excited spectra can be calculated. Since the neutron flux at the detectors is usually low, it is important to have large detector banks extending from

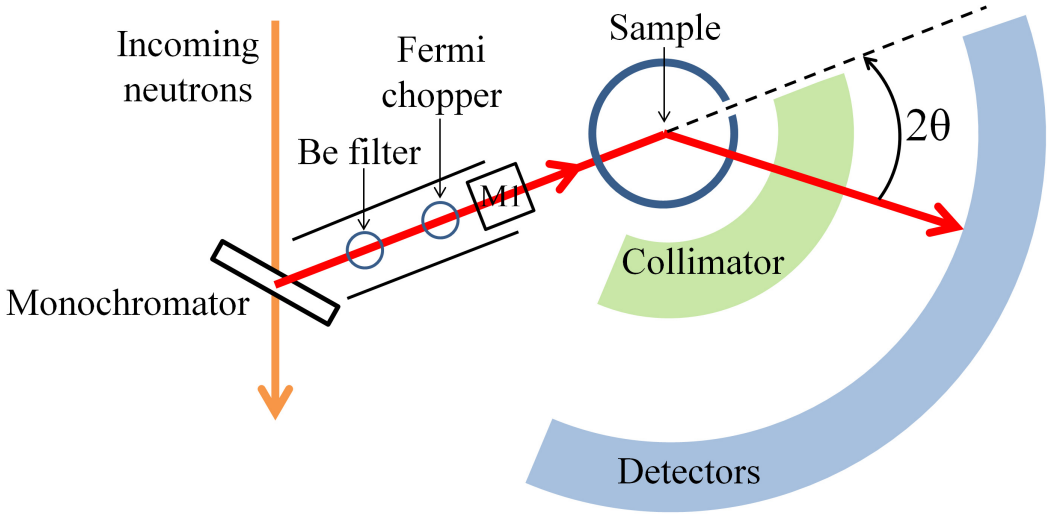


Figure 3.2: Instrument Layout of the Cold Neutron Time-of-Flight Spectrometer IN6 [24]. Important instrumental components are described.

lower to higher scattering angles to cover a wide solid angle. This is the advantage of time-of-flight inelastic neutron spectrometer: it covers a wide range of $S(\boldsymbol{Q},\omega)$ in a single measurement, whereas the triple-axis spectrometer can only detect a single point in $S(\boldsymbol{Q},\omega)$ in one measurement.

The time-of-flight spectrometer can be of two types: the direct and indirect geometries. The direct geometry setup uses a selected incident neutron energy by the chopper and measures the varying energies of the scattered neutrons. On the other hand, the indirect geometry utilises an initial polychromatic neutron beam and only counts the neutrons with a fixed final energy in the scattered beam by using analyzer crystals. Only the direct geometry instruments are used in experiments discussed in this thesis, such as MARI for Na_2IrO_3 (see Section 4.3) and MERLIN for Li_2IrO_3 (see Section 6.4) both at ISIS.

The layout of the cold neutron time-of-flight spectrometer IN6 instrument in ILL is shown in Fig. 3.2 as an example. An incoming polychromatic neutron beam is reflected by the monochromator, leading to a monochromatic beam, which passes through a Be filter to eliminate the higher order λ neutrons. It becomes a pulsed neutron beam by the Fermi chopper. M1 is the monitor detector to count the incident

neutrons to normalise the neutron flux. The pulsed incident neutron beam scatters from the target sample, mounted in the sample chamber, go through the collimator, and are measured by the detector bank. The sample chamber and detectors are evacuated during the experiment to minimise the scattering of neutrons by air.

3.5 X-ray Diffraction

3.5.1 Theory of X-ray Diffraction

X-Ray Diffraction (XRD) is a complementary technique of neutron diffraction to examine the crystal structure of solids. The advantage of XRD is the fact that an x-ray source can be generated in the home laboratory and is easy to handle compared to a neutron source which is only available in large scale facilities such as ISIS and ILL, discussed in the previous Section. The underlying principle to determine the crystal structure in XRD is the same as the one used in neutron diffraction: to make use of Bragg's law (See Eq. (3.45)), which is the coherent interference of the scattered x-ray beam from the atomic planes, giving rise to nuclear Bragg peaks. The instrumental details of XRD experiments used in this thesis are explained in the next Subsection.

3.5.2 Single Crystal X-ray Diffractometer

X-ray diffraction experiments on materials discussed in this thesis were performed using a Mo-source Oxford Diffraction Supernova diffractometer installed at the Clarendon laboratory in Oxford, the United Kingdom. The schematic view of the instrument is illustrated in Fig. 3.3. The sample is mounted at the end of a goniometer, controlled by four angles: phi, kappa, omega, and theta, to have access to a wide region of wavevectors transfer in reciprocal space. A Mo x-ray beam ($\lambda \sim 0.711$ Å) is produced by a generator with typical voltages of 50 kV and current of 0.8 mA, and it is emitted by the source tube. The x-ray beam diffracted from the sample is detected by charge coupled device (CCD) detectors by identifying an incoming x-ray photons, followed by a conversion to electric charges, enabling signal to be measured.

The shape of the x-ray beam is circular with a diameter of about 250 μm, and

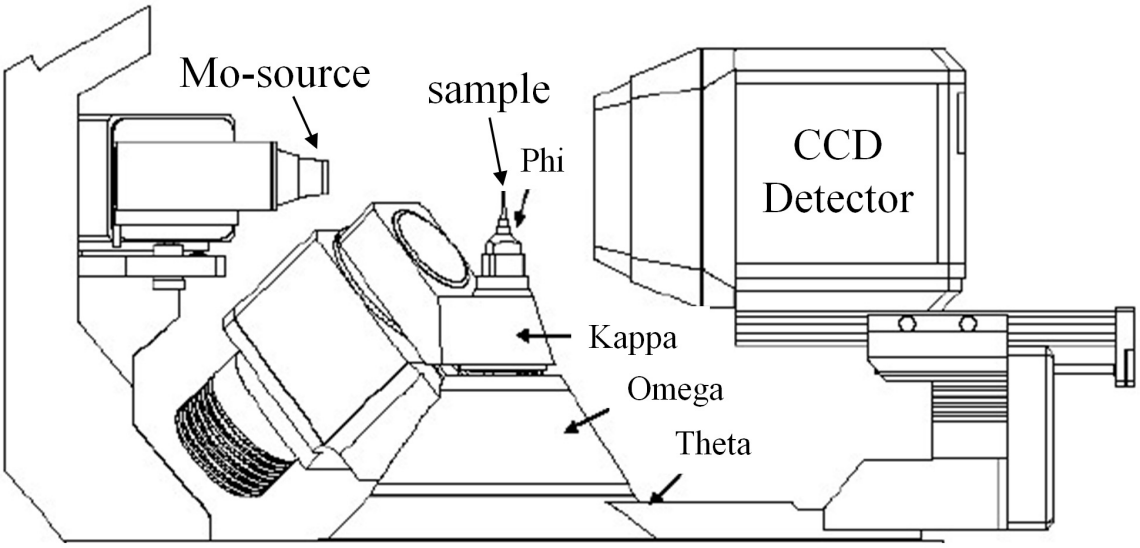


Figure 3.3: Schematic Layout of the Single Crystal X-Ray Diffractometer [25]. The sample is mounted at the end of a goniometer, whose position is manipulated by the four angles to cover a wide range of momentum space. The incident x-ray beam from the Mo source tube is diffracted by the sample, and detected by the CCD detector.

the optimal size of a sample is to have a diameter of about 100 μm to ensure that not only the whole volume of the sample is covered by the x-ray beam, but also that enough signal from the sample is detected. During the experiments, the larger samples (a few mm) had been initially tested with multiple measurements at different x-ray hitting points on the sample to verity the sample quality before breaking it into small pieces for the more accurate measurements. Typical counting times for the preliminary experiments were 1 or 2 hours, followed by longer measurements for the structure refinement with the selected samples for $5 \sim 20$ hours.

The measured nuclear Bragg peaks are integrated in three dimensional momentum space, and the data is further manipulated by applying absorption corrections with a face-defined sample model in the CrysAlisPro software package [26]. The list of nuclear Bragg peaks obtained from this process is used for determining the crystal structure and further refinement of atomic positions was performed using a combined software packages of Sir-92 and Shelx [27, 28].

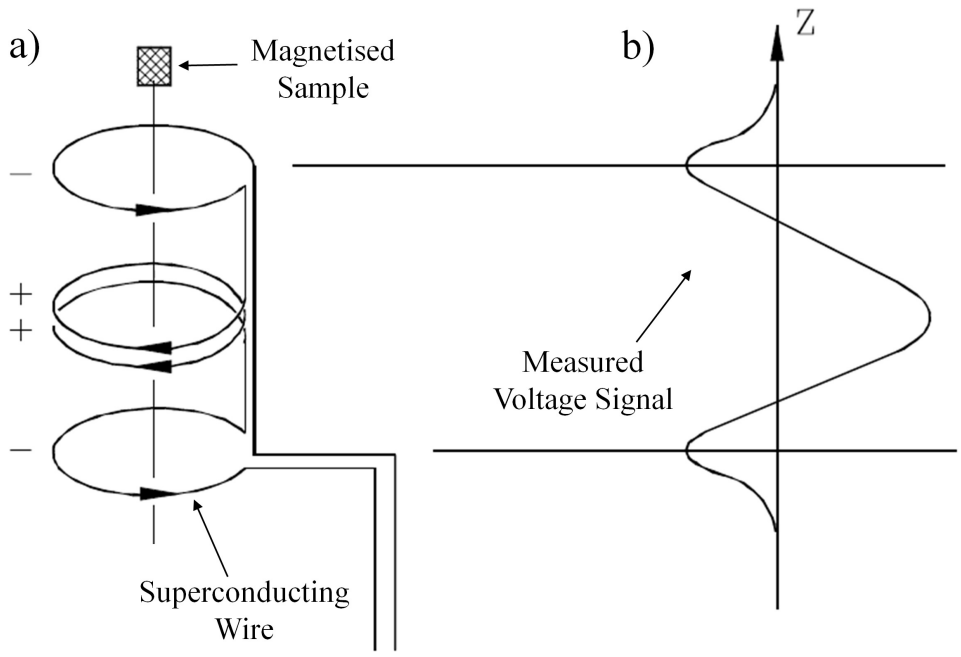


Figure 3.4: Detection of Magnetic Signal in SQUID [29]. a) A detection coil. b) Magnetic signal measured when the magnetised sample go through the coil.

3.6 Bulk Magnetic Susceptibility Measurements

Bulk magnetic susceptibility measurements were performed with a Superconducting quantum interference device (SQUID) in the Clarendon laboratory, Oxford. In the experiments, the sample was mounted in a weak diamagnetic capsule inside a plastic straw which is then placed in a helium cryostat. A very weak magnetic field must be externally applied in order to magnetise the sample and induce a magnetic moment. When the magnetised sample moves through the coil, the net magnetization inside the sample induces a current which is measured as output voltage as shown in Fig. 3.4. It is then fitted assuming an ideal dipole magnetic moment, and the amplitude of the fitted curve yields the induced sample magnetization and the integrated area of the curve is the magnetic moment. The average value of magnetic moment and its standard deviation are obtained by multiple cycles of measurements. The measurements in this thesis were typically made in the temperature range of 2 to 300 K.

Chapter 4

Magnetic Order and Excitations of Quasi-Two-Dimensional Honeycomb Antiferromagnet Na_2IrO_3

This chapter investigates the magnetic properties of the ground and excited state of quasi-two-dimensional honeycomb antiferromagnet Na_2IrO_3, a candidate for the realisation of the Kitaev spin model. Susceptibility measurements observed an anomaly below $T_N = 15.3$ K, confirmed to be the onset of the long-range antiferromagnetic order by the observation of oscillations of the muon polarization in zero-field muon-spin rotation experiments. Inelastic neutron scattering measurements on powder samples was performed successfully using an optimised setup to minimize the neutron absorption from Ir. A magnetic inelastic signal has been observed with a sinusoidal dispersion emerging from $Q \sim 0.67$ $\AA^{-1}$ extend up to 5 meV and this signal damped at 55 K, which confirmed its magnetic character. To understand the origin of the observed magnetic spectra, linear spin-wave analysis was used for various spin Hamiltonians. The measured dispersions could be accounted for by a further neighbour antiferromagnetic Heisenberg model with zigzag order. An upper bound of a possible Kitaev interaction was estimated in the zigzag phase in the Kitaev-Heisenberg-J_2-J_3 model. An alternative model with AFM Kitaev and FM Heisenberg model was also considered, and in principle it can also be quantitatively compatible with the data. To explore the effects of magnetic anisotropy, the lower energy excitations was also measured with

high-resolution inelastic neutron scattering experiments, which observed a decrease in inelastic signal below 1.8 meV that could be indicative of a spin gap. The data was captured quantitatively with linear spin-wave calculation in the gapped zigzag phase in the Heisenberg J_1-J_2-J_3 model with easy-axis (Ising) exchange anisotropy.

4.1 Introduction

The compounds $\mathcal{A}_2IrO_3$ ($\mathcal{A}$=Li, Na) [30, 31], in which edge-sharing IrO_6 octahedra form a honeycomb lattice, have been predicted to display novel magnetic states for composite spin-orbital moments coupled via frustrated exchanges. A series of recent theoretical papers have proposed that this material may realize an exotic quantum spin model with bond-directional "Kitaev" exchanges, which under certain conditions can stabilize novel forms of cooperative magnetism in two dimensions, including "stripe-ordered" antiferromagnetism or a "Kitaev quantum spin liquid" with exotic excitations, "Majorana fermions", not realized experimentally before. However, in spite of many theoretical studies [16, 3, 32, 33, 34, 35, 36, 37, 38] only a few experimental results are available for $\mathcal{A}_2IrO_3$ [30, 31, 39]. Therefore, a investigation of the magnetism in these compounds from an experimental side is essential.

The Kitaev exchange was proposed for Ir^{4+} magnetic ions in the honeycomb lattice geometry [3, 4]. The essential ingredient for realizing this physics is the $J_{eff} = 1/2$ spin-orbit coupled magnetic ground state, explained in Section 2.1. In addition to the bond-dependent Kitaev superexchange interactions, the direct exchange (isotropic Heisenberg form) can also exist, which leads to the phase diagram (in Fig. 4.9) in the Kitaev-Heisenberg model discussed in Section 4.4.2. In this phase diagram, the Néel and spin liquid phases are not compatible with resonant x-ray magnetic diffraction experiments, which found a magnetic Bragg peak at $(0, 1, 11/2)$ equivalent to $(0, 1, 1/2)$ [39], but a stripy phase is compatible with this observation. The more conventional spin Hamiltonians, the Heisenberg J_1-J_2-J_3 model [7] predict stripy and zigzag phases (See Fig. 4.7) which are both compatible with the observed magnetic Bragg peak. Therefore, in this study, the powder inelastic neutron scattering mea-

surements were performed to understand the nature of magnetic excitations as well as to distinguish different magnetic ground state candidates.

This chapter presents various experimental studies of the magnetic properties of powder samples of Na_2IrO_3 using susceptibility, muon-spin rotation and inelastic neutron scattering experiments, which allow us to experimentally characterise the magnetic ground state and excitations. Linear spin-wave theory is used to calculate the dispersion relation and extract the exchange couplings.

The rest of this Chapter is organised as follows. The next Section 4.2 describes bulk magnetic susceptibility and muon-spin rotation experiments are shown in Subsection 4.2.1, followed by the measurements and results in Subsection 4.2.2 with relevant discussions. Section 4.3 presents the powder inelastic neutron scattering results that detect the magnetic excitations with experimental details in Section 4.3.1 and the results and discussions in Section 4.3.2. The measured sinusoidal magnetic dispersion modelled by linear spin-wave theory presented in Section 4.4 based on various spin Hamiltonian models and ground states: zigzag and stripy phases in the Heisenberg J_1-J_2-J_3 model in Section 4.4.1, a stripy phase in the Kitaev-Heisenberg model in Section 4.4.2, a zigzag phase in the Kitaev-Heisenberg-J_2-J_3 model in Section 4.4.3 and a zigzag phase in the generalised Kitaev-Heisenberg model in Section 4.4.4. Presence of a spin gap due to magnetic anisotropy and consequences for powder neutron scattering experiments is discussed in Section 4.5. The conclusion of this Chapter is summarized in Section 4.7 with a discussion of possible future directions of research.

4.2 Magnetic Order of Na_2IrO_3

4.2.1 Experimental Details

High quality powder crystalline Na_2IrO_3 samples were obtained from the Philipp Gegenwart group at Georg-August-Universität in Göttingen, Germany. Bulk susceptibility experiments were made with the Quantum Design magnetic property measurement systems (MPMS) in with a Superconducting Quantum Interference Device (SQUID) magnetometer in the Clarendon laboratory. The mass of powder sample

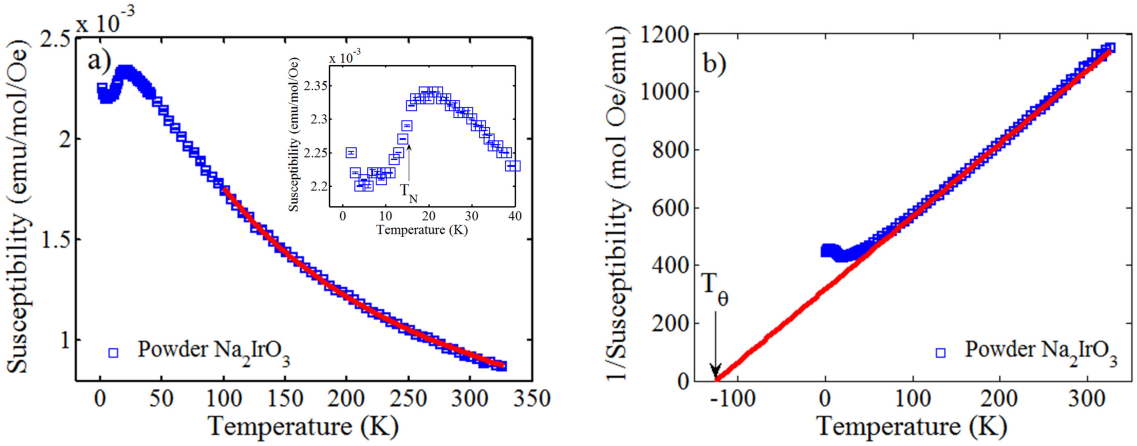


Figure 4.1: Susceptibility of Powder Na_2IrO_3. a) Zero-field cooled magnetic susceptibility probed by SQUID as a function of temperature. The red line is fitted curve with a Curie-Weiss from in Eq. (4.1). The inset indicates AFM-like magnetic anomaly around 15 K, reproducing previously reports [30]. b) Inverse of susceptibility to a Curie-Weiss form for T>100 K (red solid line).

was about 51.4 mg which was stacked into a weak diamagnetic plastic capsule, and the measurement was made in 100 Oe external magnetic field.

Zero field (ZF) μ^+SR measurements were also made by the group of Tom Lancaster and Stephen Blundell group from Oxford at the Swiss Muon Source (Sμ^+S), Paul Scherrer Institut, CH using the GPS spectrometer and the results are included here for reference. For the measurement a 250 mg powder sample of Na_2IrO_3 from the same batch used for inelastic neutron scattering measurement (See Fig. 4.3.2) was packed inside a silver foil with a thickness of 25 μm, and mounted on a silver sample holder.

4.2.2 Measurements and Results

Two batches of powder Na_2IrO_3 samples were tested with SQUID and the better powder sample was selected which showed the less steeper upturn of susceptibility near the base temperature of 2 K, possibly due to the smaller amount of isolated magnetic impurity ions inside the sample. The susceptibility data of the better sample is shown in Figs. 4.1(a-b). It shows a Curie-Weiss behaviour at high temperatures before revealing a magnetic anomaly at around 15 K with a sudden drop of the sus-

ceptibility, indicative of an AFM magnetic transition. When magnetic moments align antiferromagnetically below T_N, the magnetic susceptibility is suppressed, leading to a drop in the effective magnetic moment. Figure 4.1b) illustrates the inverse susceptibility with a fitted red solid line, which intersects the x-axis at the Curie-Weiss (CW) temperature (θ) of around -125 K.

$$\chi = \frac{C}{T+\theta} + \chi_0, \tag{4.1}$$

where χ_0 is a temperature-independent value and

$$C = \frac{n\mu_0\mu_{eff}^2}{3k_BT}, \tag{4.2}$$

where n is number of magnetic moments per mole and

$$\mu_{eff} = g_J\mu_B\sqrt{J_{eff}(J_{eff}+1)}. \tag{4.3}$$

By fitting the data to Eq. (4.1), the Curie-Weiss constant (C) and θ can be obtained. They can be marginally varying, depending on the choice of fitting range for the Curie-Weiss fit, thus values obtained here should be taken as representative parameters. The Curie-Weiss constant (C) can be used to obtain the experimental effective magnetic moment (μ_{eff}) using Eq. (4.2), which is compared with the theoretical value from Eq. (4.3) [1] assuming $g_J = 2$. The effective magnetic moment for $J_{eff} = 1/2$ is 1.74 μ_B, which is close to an experimental results of 1.77 μ_B obtained from C= 0.39 emuK/mol in Fig. 4.1, which also agrees with reported results earlier [31]. Moreover, since θ is proportional to the sum of the magnetic interactions, it can be used to determine the exchange interactions in relation to the neutron data and spin-wave analysis examined in Section 4.4 in detail. The measured powder sample was also used for the muon-spin rotation and powder inelastic neutron scattering experiments (See Section 4.3).

Magnetic order of the Ir spins was directly detected by zero-field (ZF) muon-spin rotation (μ^+SR) on a powder sample of Na_2IrO_3. The raw spectra are shown in Fig. 4.2a). At temperatures below $T_N = 15.3$ K, clear oscillations in the time-

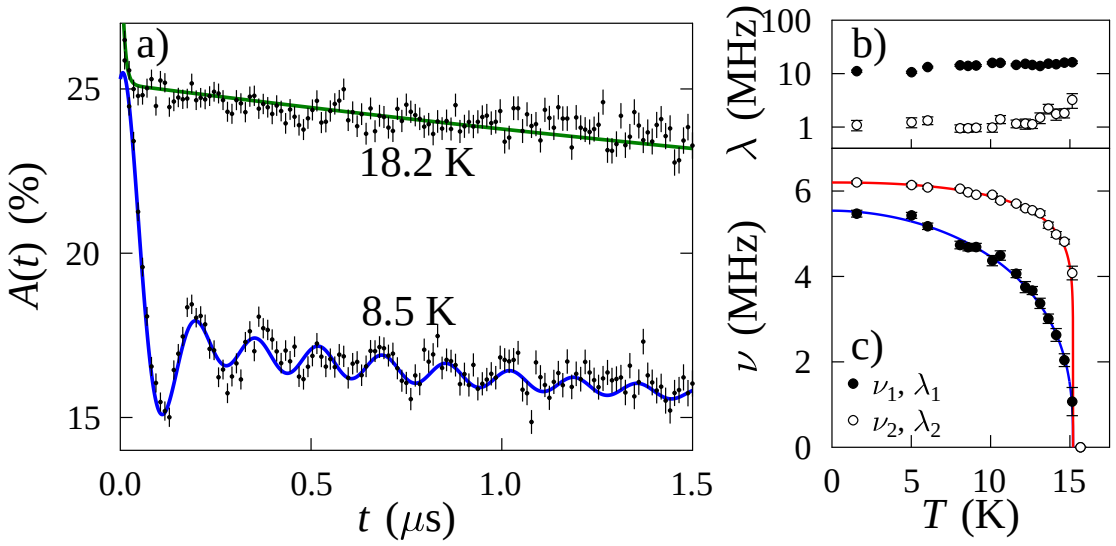


Figure 4.2: a) ZF μ^+SR spectra [40] on a polycrystalline sample of Na_2IrO_3 above and below T_N. Solid lines are (top) guide to the eye and (bottom) a fit described in the text. b, c) Fitted parameters as a function of temperature.

dependence of the muon polarization, characteristic of quasi-static local magnetic fields at the muon stopping site is observed. The full spectra was fitted to the form

$$A(t) = A_1 e^{-\lambda_1 t}\cos(2\pi\nu_1 t + \phi_1) + A_2 e^{-\lambda_2 t}\cos(2\pi\nu_2 t + \phi_2) + A_3 e^{-\Lambda t} + A_{\mathrm{bg}} \qquad (4.4)$$

where the last two terms account for muons polarized parallel to the local magnetic fields, and muons stopping in the sample holder (or cryostat tail), respectively. Fits of the data to Eq. (4.4) reveal the evolution of ν_i and λ_i with temperature, as shown in Figs. 4.2(b-c).

Unusually, the frequencies do not vary in fixed proportion, although they do tend to zero at the same temperature. The low-amplitude, higher frequency component ν_2 drops off far more dramatically than the large amplitude, lower frequency ν_1. It is worthwhile mentioning that many magnetic systems tends to have more than one (two is common) muon site so that multiple precession frequencies are in fact not unusual. The muon-spin precession frequency observed for a particular site reflects the local coupling to the magnetic order parameter which is particular for that site, but one usually finds that though the frequency scale varies between sites because

of differences in coupling, and they have an identical temperature dependence since they track the same magnetic order parameter. The present case is rather unusual because the two classes of muon site observed have substantially different magnetic environments as reflected in the different temperature dependence of the frequency and the magnitude of the relaxation rates of the precession signals (see Fig. 4.2a)). This implies that the two sites are qualitatively different in their properties.

In order to quantify this behavior, the frequencies were fitted to the phenomenological function

$$\nu_i(T) = \nu_i(0)\left[1 - (T/T_{\mathrm{N}})^{\alpha_i}\right]^{\beta_i} . \tag{4.5}$$

A common value of $T_{\mathrm{N}} = 15.3(1)$ K was identified from fitting to this function. It was found that $\alpha \approx 2$ for both cases. The parameter β can be interpreted as an order parameter exponent. The other fit parameters are $\nu_1(0) = 5.54(1)$ MHz, $\beta_1 = 0.36(1)$, $\nu_2(0) = 6.20(3)$ MHz and $\beta_2 = 0.11(1)$. It is noted that λ_1 is an order of magnitude larger than λ_2, implying either that the distribution of fields is broader in the majority site or, assuming the fast fluctuation limit, that the fluctuation rate is smaller. The lower frequency oscillation, accounting for ≈ 90 % of the muon sites in the material, has a β value suggestive of the behavior of a three-dimensional (3D) system (for 3D Heisenberg $\beta = 0.367$ and 3D Ising $\beta = 0.326$), while the minority muon site has an exponent value more similar to that expected for a 2D Ising system (for which $\beta = 0.125$). These seem to quantitatively suggest that the magnetic fluctuations have a rather different character at the two muon sites as well.

The relative weight of the second frequency component suggests that it may come from muon sites implanted near stacking fault planes, as such sites also occur in a similar proportion of 9 % (discussed in detail in Section 5.4.2 and 5.4.3). The value for $T_{\mathrm{N}} = 15.3$ K is consistent with susceptibility measurements on the same batch, which indicated a clear anomaly of the sharp downturn near T_N as reported previously [30, 31].

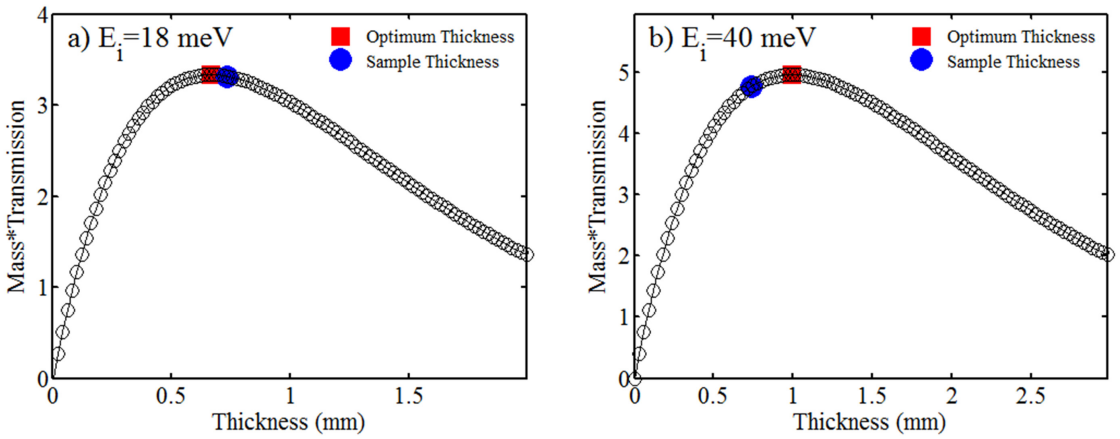


Figure 4.3: Effective Neutron Absorption Simulated for MARI Experiments on Na_2IrO_3 at E_i=18, 40 meV. For a given dimension of an annular can, the effective neutron absorption (defined as mass × absorption) is shown as a function of the thickness of the annular can.

4.3 Magnetic Excitations of Na_2IrO_3

4.3.1 Experimental Details

The magnetic excitations were probed by powder inelastic neutron scattering (INS) using the direct-geometry time-of-flight spectrometer MARI in ISIS, UK. The biggest challenge to do INS experiment on any iridate material is that iridium ions heavily absorb neutrons, i.e. absorption cross-section for iridium for 2200 m/s neutrons velocity at thermal energy ($E \sim 25$ meV) is $\sigma_{abs} = 425$ barns/Ir, whereas scattering cross-section for 1 μ_B magnet is $\sigma_s = 4\pi(\gamma r_0)^2 = 3.2$ barns. Thus roughly speaking, 1 out of 100 neutrons would only be scattered. To the best of our knowledge, inelastic neutron scattering studies on magnetic excitation of any iridate materials have not yet been reported, so it has been considered that INS experiments on iridate system are not feasible. Therefore the key issue to succeed in INS experiment on Na_2IrO_3 is to minimise the neutron absorptions, which has been resolved with an optimized setup. The optimized mass of powder sample was found by using the absorption calculation for an annular can as shown in Fig. 4.3.

About 10 g sample of Na_2IrO_3 powder was spread out in a very thin layer ($\lesssim 1$ mm) inside of an annular can of outer diameter of 40 mm and height of 50 mm. A small

wrap of Aluminum-coil was placed below the sample sachet as a support to prevent the sample for falling down during the experiment. Several incident energies were tested 40, 18 meV and the latter was selected for high statistics counting as it was found to cover the range where the strongest magnetic signal was observed. Measurements with even higher incident energy of E_i = 400, 800, 1000, 1300, 1500 meV were made in an attempt to observe excitations related to the spin-orbit gap, 500 meV, but no clear magnetic inelastic signal was observed at those high energy transfer. The instrumental energy resolution for E_i = 18 meV was 0.67(1) meV (FWHM) on the elastic line. Counting times for the data in Figs. 4.4(e-f) were 28 and 7 hours, respectively at an average proton current of 150 μAmps.

4.3.2 Measurements and Results

The collected INS data is shown in Figs. 4.4(e-f) at T= 1.5 K and 55 K respectively. Fig. 4.4e) shows the raw neutron scattering intensity as a function of wavevector ($Q = |\boldsymbol{Q}|$) and energy transfer deep in the ordered phase at T= 1.5 K. An inelastic signal with a sinusoidal-like dispersive boundary below a maximum near 5 meV is clearly observed at low Q. A gap, if present, is smaller than 2 meV which the current experiment cannot resolve. The magnetic character of the scattering is confirmed by the broad, damped-out signal observed in the paramagnetic phase at 55 K shown in Fig. 4.4f). Interestingly, the dispersion boundary extrapolates at the lowest energies to a wavevector Q much smaller than that expected for conventional Néel order, $Q_{(020)} = 1.34$ Å^{-1}, so this magnetic order can be ruled out. Similarly, this is much smaller than that of the first phonon peak position at about $Q_{(001)} = 1.12$ Å^{-1}, which excluded the possibility of an acoustic phonon. In fact, Q is close to the expected location of the first magnetic Bragg peak for both zigzag or stripy order, $Q_{(010)} = 0.67$ Å^{-1} (See Fig. 4.4d)).

In the next Section, various models proposed for the magnetic phase will be tested to determine the magnetic ground state and understand the excitations within linear-spin wave theory.

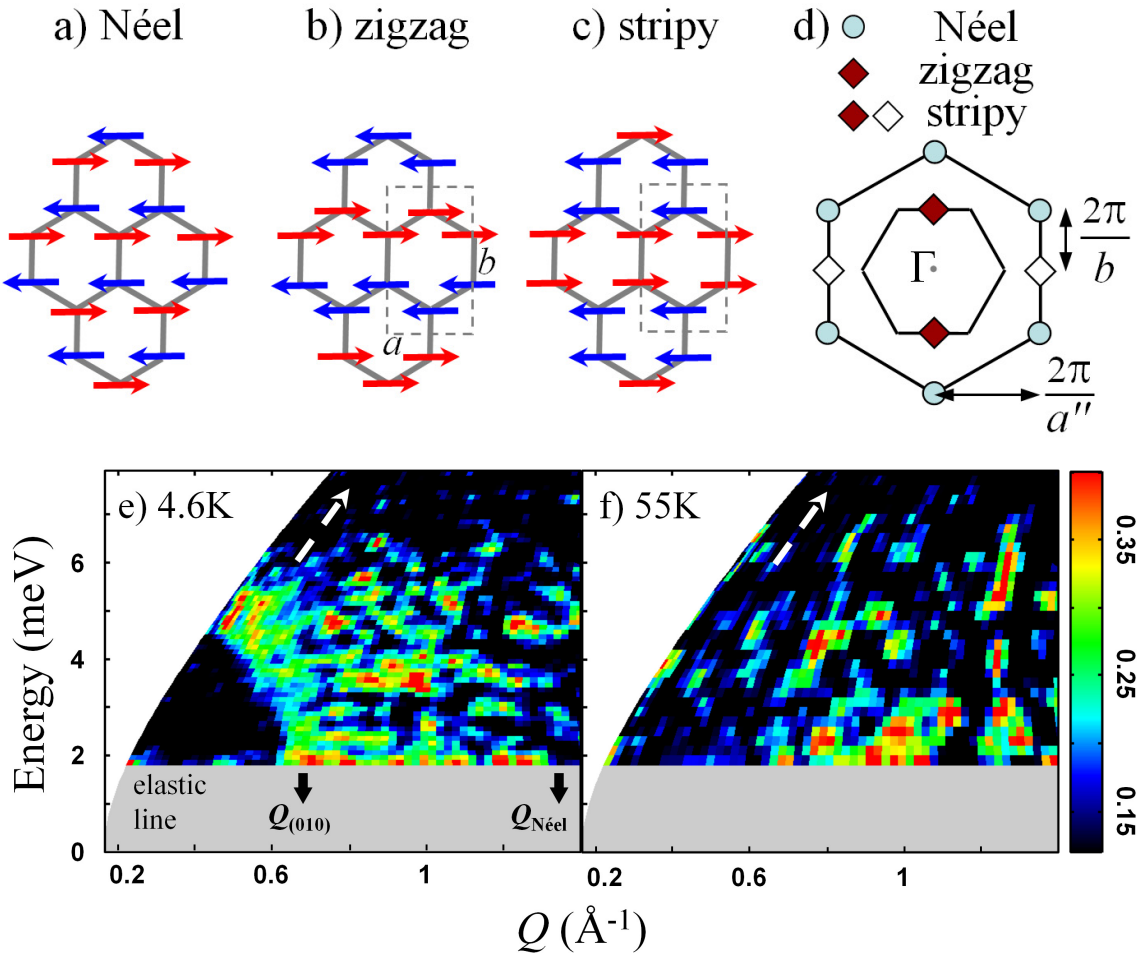


Figure 4.4: Powder Inelastic Neutron Scattering Data Collected using MARI on Na_2IrO_3. Diagram of a) Néel, b) zigzag and c) stripy order. d) Reciprocal space diagram showing locations of magnetic Bragg peaks for various magnetic phases (inner hexagon shows first Brillouin zone of the honeycomb lattice). e) Powder inelastic neutron scattering data. The notable well-defined feature is the sharp lower boundary of the scattering at low Q (filled magenta symbols in Fig. 4.8, associated with a sinusoidal spin wave dispersion). This signal becomes damped out in the paramagnetic phase in f). Slanted thick dashed arrow shows the scan direction in Fig. 4.5. Gray shading marks the inaccessible region close to the elastic line dominated by incoherent elastic scattering. Note that in d) $a'' = a \sin \beta$.

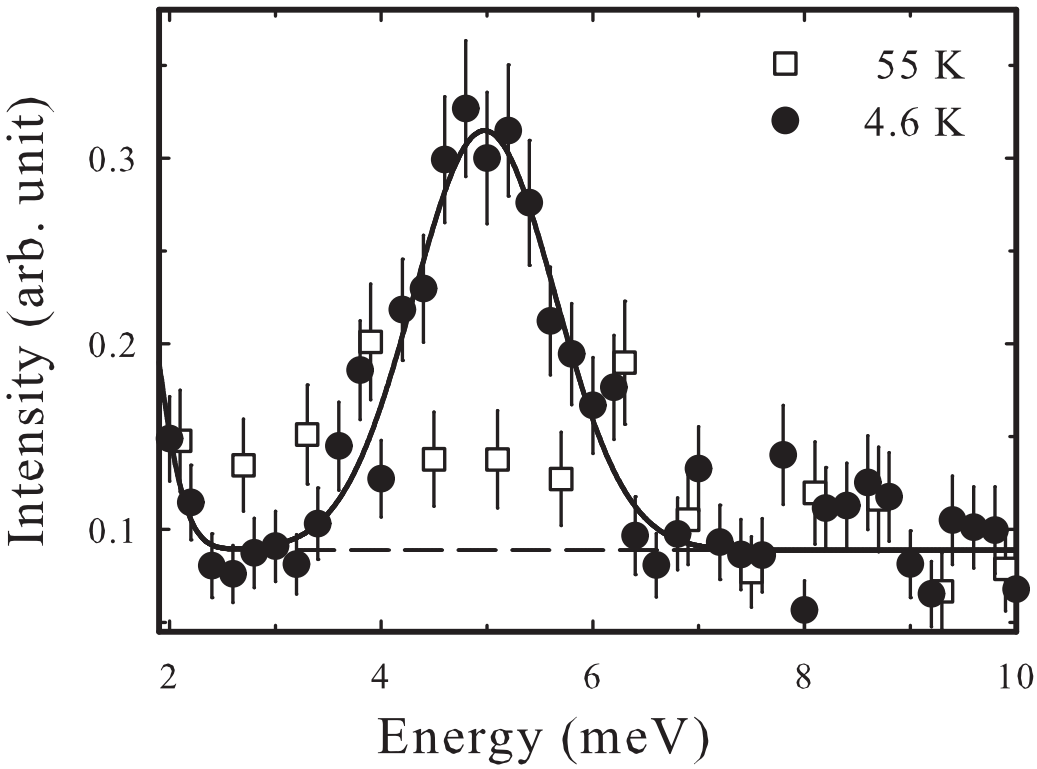


Figure 4.5: A representative cut to see the signal of magnetic excitation and background for the scan direction illustrated with a slanted thick dashed arrow in Fig. 4.4.

4.4 Linear Spin-Wave Analysis

This Section outlines the derivation of the linear spin wave dispersion relations and dynamical structure factors relevant for neutron scattering for the zigzag and stripy phases of spin Hamiltonians on the honeycomb lattice, and both phases have same ordering wavevector seen in RXS [39] and where excitations soften in INS data (See Fig. 4.4e)). For the Heisenberg model with up to 3rd neighbour exchanges, the previous results on the dispersion relations [5] are extended to include also the dynamical structure factors. For the Kitaev-Heisenberg model, the spin-wave spectrum including 1/S quantum corrections has been studied previously in a special "rotated" reference frame [3]. Here in Subsection 4.4.2 the dynamical structure factors as well as the dispersion relations in the experimentally-relevant, un-rotated reference frame are explicitly derived. For the Kitaev-Heisenberg-J_2-J_3 models in Subsection 4.4.3, both the dispersion relations and dynamical structure factors, have not been studied before, are derived here explicitly. Furthermore, a more recently proposed zigzag phase in the generalised Kitaev-Heisenberg model will be examined in Subsection 4.4.4.

4.4.1 Zigzag and Stripy Phase in the Heisenberg J_1-J_2-J_3 Model

This Subsection deals with the isotropic Heisenberg (HB) model on the honeycomb lattice with exchanges with up to 3rd nearest-neighbor, so called the J_1-J_2-J_3 model with Hamiltonian

$$\mathcal{H} = \sum_{1\text{NN}} J_1 \boldsymbol{S}_i \cdot \boldsymbol{S}_j + \sum_{2\text{NN}} J_2 \boldsymbol{S}_i \cdot \boldsymbol{S}_k + \sum_{3\text{NN}} J_3 \boldsymbol{S}_i \cdot \boldsymbol{S}_l \tag{4.6}$$

where 1-, 2-, and 3NN indicate summing over all 1st, 2nd and 3rd nearest-neighbor pairs with couplings J_1, J_2 and J_3 [paths indicated in Fig. 4.6a)], where positive values correspond to antiferromagnetic exchanges. Depending on the relative ratio of the couplings there are seven distinct types of mean-field ground states [7], which include the two candidate magnetic orders for Na_2IrO_3, the zigzag and stripy AFM orders shown in Figs. 4.6(a-b) (labelled II and IV, respectively in Fig.2 [6]). Both of those magnetic structures have four magnetic sublattices (labelled $A - D$) and

can be described by a rectangular magnetic unit cell (dashed box in Figs. 4.6(a-b)), which coincides with the in-plane chemical unit cell $a \times b$ of Na_2IrO_3. Within a single layer, the Ir honeycomb lattice is very close to be ideal ($b/a \simeq \sqrt{3}$) in spite of the 3D monoclinic crystal structure, so the ideal 2D honeycomb lattice with three-fold symmetry is considered in the calculation. In this case the magnetic order can have three spatial domains. One such domain is shown for both structures in Figs. 4.6(a-b), and the other two magnetic domains are obtained by $\pm 60°$ rotation around the direction normal to the plane.

Eq. (4.6) can be decomposed into

$$\begin{aligned}\mathcal{H} =& \sum_{1\text{NN}} J_1[S_i^z S_j^z + \frac{1}{2}(S_i^+ S_j^- + S_i^- S_j^+)] + \sum_{2\text{NN}} J_2[S_i^z S_k^z + \frac{1}{2}(S_i^+ S_k^- + S_i^- S_k^+)] \\ &+ \sum_{3\text{NN}} J_3[S_i^z S_l^z + \frac{1}{2}(S_i^+ S_l^- + S_i^- S_l^+)],\end{aligned} \tag{4.7}$$

where z-axis defines the equilibrium direction of the spin in the ground state, and the fluctuations along x and y-axis give the spin dynamics.

Using a standard Holstein-Primakoff transformation in the large-S limit the Hamiltonian becomes (to leading order) a quadratic form of magnon operators

$$\mathcal{H} = \sum_{\boldsymbol{q}} \mathsf{X}^\dagger \mathsf{H} \mathsf{X} + N(1 + 1/S) E_{MF} \tag{4.8}$$

where higher than quadratic terms are neglected. Here E_{MF} is the mean-field ground state energy (per spin) and N is the total number of spin sites. The sum extends over all wavevectors $\boldsymbol{q}$ in the first magnetic Brillouin zone.

For the zigzag order in Fig. 4.6a), the defined operator basis is

$$\mathsf{X}^\dagger = \left[a_{\boldsymbol{q}}^\dagger \ , \ d_{\boldsymbol{q}}^\dagger \ , \ c_{-\boldsymbol{q}} \ , \ b_{-\boldsymbol{q}}\right], \tag{4.9}$$

where $a - d$ label operators on sublattice $A - D$, i.e. $a_{\boldsymbol{q}}^\dagger$ ($a_{\boldsymbol{q}}$) creates (annihilates) a plane-wave magnon mode on sublattice A and so on.

The spin Hamiltonian in Eq. (4.8) can be rewritten as

$$\mathcal{H} = \sum_{\boldsymbol{q}} \begin{bmatrix} a^\dagger_{\boldsymbol{q}} , & d^\dagger_{\boldsymbol{q}} , & c_{-\boldsymbol{q}} , & b_{-\boldsymbol{q}} \end{bmatrix} \begin{bmatrix} A & B & C & D^* \\ B^* & A & D & C \\ C & D^* & A & B \\ D & C & B^* & A \end{bmatrix} \begin{bmatrix} a_{\boldsymbol{q}} \\ d_{\boldsymbol{q}} \\ c^\dagger_{-\boldsymbol{q}} \\ b^\dagger_{-\boldsymbol{q}} \end{bmatrix} + \text{constant} \quad (4.10)$$

$$= \sum_{\boldsymbol{q}} A a^\dagger_{\boldsymbol{q}} a_{\boldsymbol{q}} + B a^\dagger_{\boldsymbol{q}} d_{\boldsymbol{q}} + C a^\dagger_{\boldsymbol{q}} c^\dagger_{-\boldsymbol{q}} + D^* a^\dagger_{\boldsymbol{q}} b^\dagger_{-\boldsymbol{q}} + ... \ , \quad (4.11)$$

where

$$\begin{aligned} A &= S\ \{-J_1 + 2J_2 + 3J_3 + 2J_2\cos(2\pi h)\} \\ B &= 2SJ_1\eta\cos(\pi h) \\ C &= 2SJ_2\{\cos[\pi(h+k)] + \cos[\pi(h-k)]\} \\ D &= S\ \{J_1\eta^2 + J_3[\eta^{-4} + 2\eta^2\cos(2\pi h)]\} \\ \eta &= e^{k\pi i/3}. \end{aligned}$$

Here (h, k) are components of the wavevector $\boldsymbol{q}$ in units of the reciprocal lattice of the $a \times b$ rectangular unit cell shown in Fig. 4.6a). By periodicity the above expressions are valid for any momentum, not necessarily restricted to the 1st magnetic Brillouin zone. The close examination of Eq. (4.11) gives an understanding on the exchange interactions such as ferromagnetic coupling between A and D sublattices and antiferromagnetic couplings between A and B and so on, based on the zigzag magnetic ground state described in Fig. 4.6a) with the four magnetic sublattices, $A - D$.

Diagonalisation of the Hamiltonian by standard techniques [12, 41] to obtain the normal magnon modes gives two doubly-degenerate dispersions

$$\begin{aligned} (\omega^\pm_{\boldsymbol{q}})^2 &= A^2 + BB^* - C^2 - DD^* \\ &\quad \pm\sqrt{4|AB - CD^*|^2 - |B^*D^* - BD|^2}. \end{aligned} \quad (4.12)$$

I have explicitly verified that Eq. (4.12) agrees with earlier results (Eq. (5.21) in Ref. [5]) for the same model (Eq. (4.6)). The spin-wave intensity in neutron scattering is proportional to the dynamical structure factor (expressed as $S^{xx}(\boldsymbol{Q}, \omega)$ for spin fluctuations along the x-direction and similarly for y-direction), and an analytical

expression for a 4×4 Hamiltonian matrix as in Eq. (4.10) was derived in the earlier result (See Eq. (A3) in Ref. [41]), and is included explicitly in Appendix A.

The obtained spin-wave dispersions and intensities are shown in Fig. 4.6e). As expected, the acoustic magnon, ω^-, is gapless with a linear dispersion at the magnetic Bragg peak at the Y point, is also linear and gapless at the X point, but has zero intensity because the structure factor for magnetic Bragg peaks cancels at this position. Furthermore, the dispersions soften and appear gapless at the M point and other points of the quartet $(\pm 1/2, \pm 1/2)$, which are Bragg peaks for the other two magnetic domains rotated by $\pm 60°$. This softening is a general feature of linear spin-wave dispersions for a multi-domain magnetic ground state [41]. However, the fact that the gap closes at those points is not protected by any symmetry, but is an artefact of the linear spin-wave approximation; by analogy with related spin-wave models for other multi-domain structures [42] it is expected that the dispersions become gapped at the softening points when quantum fluctuations to 1st order in $1/S$ are included.

A spherical-average of the spin-wave spectrum of the zigzag phase, including various prefactors listed in Eq. (B1) in Appendix B, is shown in Fig. 4.8b). The dominant contribution to the low-Q dispersive edge of the strong signal near the first softening point ($Q = 0.67$ Å^{-1}) is due to acoustic magnons on the $\omega^-_{\boldsymbol{k}}$ branch emerging out of the Y point and dispersing in the Y→ Γ direction [see Fig. 4.6e)] and also magnons on the $\omega^+_{\boldsymbol{k}}$ branch emerging out of the M-point and dispersing in the M→ Γ direction. To reproduce the observed low-Q dispersion in the powder data, the constraint of the zone-boundary energy of the lowest branch on the Γ-Y line is imposed, which reproduces the observed maximum of the low-Q dispersion, i.e. $\omega^-\left(0, \frac{1}{2}\right) = 5$ meV. This constraint together with the condition that the exchanges reproduce the observed Curie-Weiss constant (θ) cannot determine all three exchange values J_1, J_2 and J_3 independently,

$$\theta = -S(S+1)(J_1 + 2J_2 + J_3)/k_{\mathrm{B}} = -125 \text{ K} \tag{4.13}$$

However, it allows for a one-dimensional family of solutions located on a curve in

the parameter space $(J_2/J_1, J_3/J_1)$ (the dotted line in region II in Fig. 4.7). All sets of exchange values part of this family are broadly consistent with the data. The level of agreement is illustrated in Fig. 4.8b) for one representative solution (red star in Fig. 4.7), chosen as it comes closest to reproducing also the intensity distribution at the lowest Q.

For the stripy order shown in Fig. 4.6b), spin-wave operator basis can be defined as

$$\mathsf{X}^\dagger = \left[a^\dagger_{\boldsymbol{q}} \ , \ b^\dagger_{\boldsymbol{q}} \ , \ c_{-\boldsymbol{q}} \ , \ d_{-\boldsymbol{q}}\right], \tag{4.14}$$

then the Hamiltonian reduces to the same form as in Eq. (4.8) with the same 4×4 Hamiltonian matrix in Eq. (4.10) such that

$$\mathcal{H} = \sum_{\boldsymbol{q}} \left[\ a^\dagger_{\boldsymbol{q}} \ , \ b^\dagger_{\boldsymbol{q}} \ , \ c_{-\boldsymbol{q}} \ , \ d_{-\boldsymbol{q}} \ \right] \begin{bmatrix} A & B & C & D^* \\ B^* & A & D & C \\ C & D^* & A & B \\ D & C & B^* & A \end{bmatrix} \begin{bmatrix} a_{\boldsymbol{q}} \\ b_{\boldsymbol{q}} \\ c^\dagger_{-\boldsymbol{q}} \\ d^\dagger_{-\boldsymbol{q}} \end{bmatrix} + \text{constant} \tag{4.15}$$

$$= \sum_{\boldsymbol{q}} A a^\dagger_{\boldsymbol{q}} a_{\boldsymbol{q}} + B a^\dagger_{\boldsymbol{q}} b_{\boldsymbol{q}} + C a^\dagger_{\boldsymbol{q}} c^\dagger_{-\boldsymbol{q}} + D^* a^\dagger_{\boldsymbol{q}} d^\dagger_{-\boldsymbol{q}} + ... \ , \tag{4.16}$$

where the expressions for the $A - D$ parameters are

$$\begin{aligned} A &= S\left\{J_1 + 2J_2 - 3J_3 + 2J_2\cos(2\pi h)\right\} \\ B &= S\left\{J_1\eta^{-2} + J_3\left[\eta^4 + 2\eta^{-2}\cos(2\pi h)\right]\right\} \\ C &= 2SJ_2\{\cos\left[\pi(h+k)\right] + \cos\left[\pi(h-k)\right]\} \\ D &= 2SJ_1\eta^{-1}\cos(\pi h) \\ \eta &= e^{k\pi i/3}. \end{aligned}$$

The same form of magnon dispersions is also given by Eq. (4.12) for the stripy phase since the form of the 4×4 Hamiltonian matrix in Eq. (4.15) is set to be same for both magnetic orders. Eq. (4.16) reveals that the A sublattice couples ferromagnetically with A and B, and antiferromagnetically with C and D, and these couplings stem from the stripy order described in Fig. 4.6b).

The resulting spin-wave dispersions and intensities for representative exchange values are plotted in Fig. 4.6d). In contrast to the zigzag phase, for the stripy phase

the acoustic magnon ω^- is gapless with a linear dispersion and finite intensity at both the X and Y points, as both are magnetic Bragg peaks with non-zero structure factor: X is four times stronger intensity than Y. Again, due to the three domain structure there is softening of the dispersion with an artificial gapless point at M, which is expected to become gapped when quantum fluctuations beyond the linear spin-wave approximation are included, as discussed earlier.

A spherical averaging of the spin-wave spectrum in Fig. 4.6d) is shown in Fig. 4.8b), here the strongest signal at low energies is due to scattering from acoustic magnons near the X-point ($Q = 1.16$ Å^{-1}) with weaker scattering from magnons near Y ($Q = 0.67$ Å^{-1}) and intensity decreasing rapidly for magnons with smaller momentum, which cannot explain the data.

To summarize, the calculated spin-wave spectra in the zigzag phase (Fig. 4.8b)) is qualitatively consistent with the observed dispersion at low-Q (filled symbols) (Fig. 4.8a)), whereas the stripy phase (Fig. 4.8b)) cannot account for the strong low-Q dispersive signal and predicts stronger scattering at larger-Q's which is not seen in the INS data. A minimal model of the zigzag phase in the Heisenberg J_1-J_2-J_3 model also predicts the distribution of magnetic scattering in broad overall agreement with the data up to some intensity modulations (shown in Fig. 4.8b)) and requires substantial couplings up to 3rd neighbors, which stabilize the zigzag magnetic order.

There is a possibility that the zone-boundary energy of 5 meV observed in the experiment could come from another high-symmetry direction from $\Gamma(0,0)$ to $(1/4,1/4)$ point. Thus, the simulations were also considered in this case for the zigzag phase in HB J_1-J_2-J_3 model. The simulations did not qualitative change the current picture and also the parameterised couplings were similar to the currently presented values, which means the zone-boundary energy of two directions are comparable.

It was also confirmed that spin-wave spectra maintained their key features when the small interlayer exchange interaction up to 0.417 meV (10 % of J_1) was taken into account since affected only on the boundary of the magnetic scattering near at the low Q, showing that the simulated spherically-averaged magnetic spectrum was qualitatively similar.

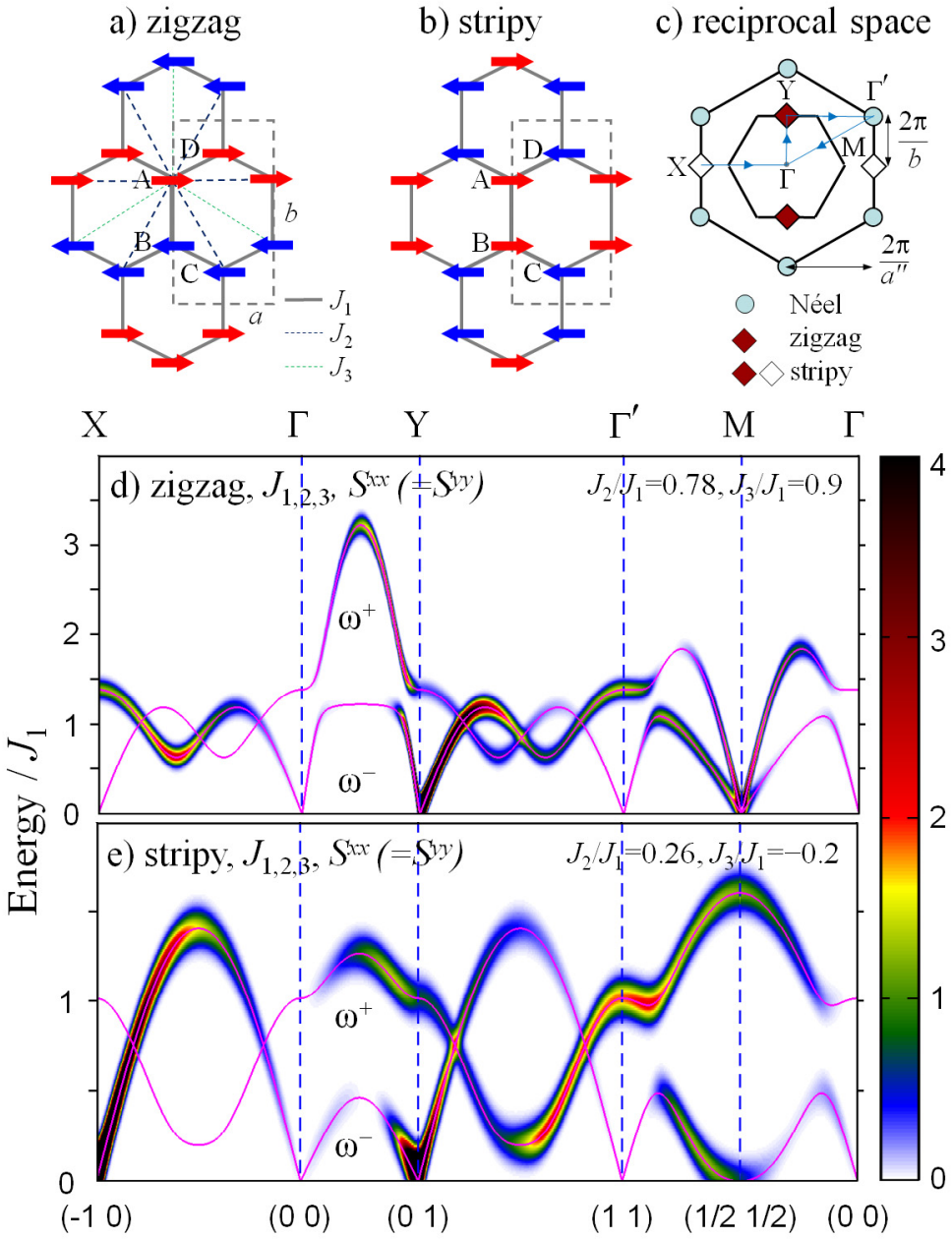


Figure 4.6: Spin-Wave Spectrum for the Zigzag and Stripy Phase in the Heisenberg J_1-J_2-J_3 Model. a) Zigzag order. Dashed rectangular box of size $a \times b$ shows the magnetic unit cell containing four sublattices A-D. b) Stripy order. c) 2D reciprocal space showing magnetic Bragg peak positions for various magnetic orders. d-e) Spin-wave dispersions along symmetry directions in reciprocal space (arrowed path in c)) for the Heisenberg J_1-J_2-J_3 model with d) zigzag, and e) stripy order for exchange values and magnetic orders listed in the legends. Wavevectors $\boldsymbol{Q}$ are expressed in reciprocal lattice units of the rectangular magnetic unit cell. Colour is the dynamical structure factor (convolved with a Gaussian in energy for visualization, full width at half maximum $= 0.15J_1$).

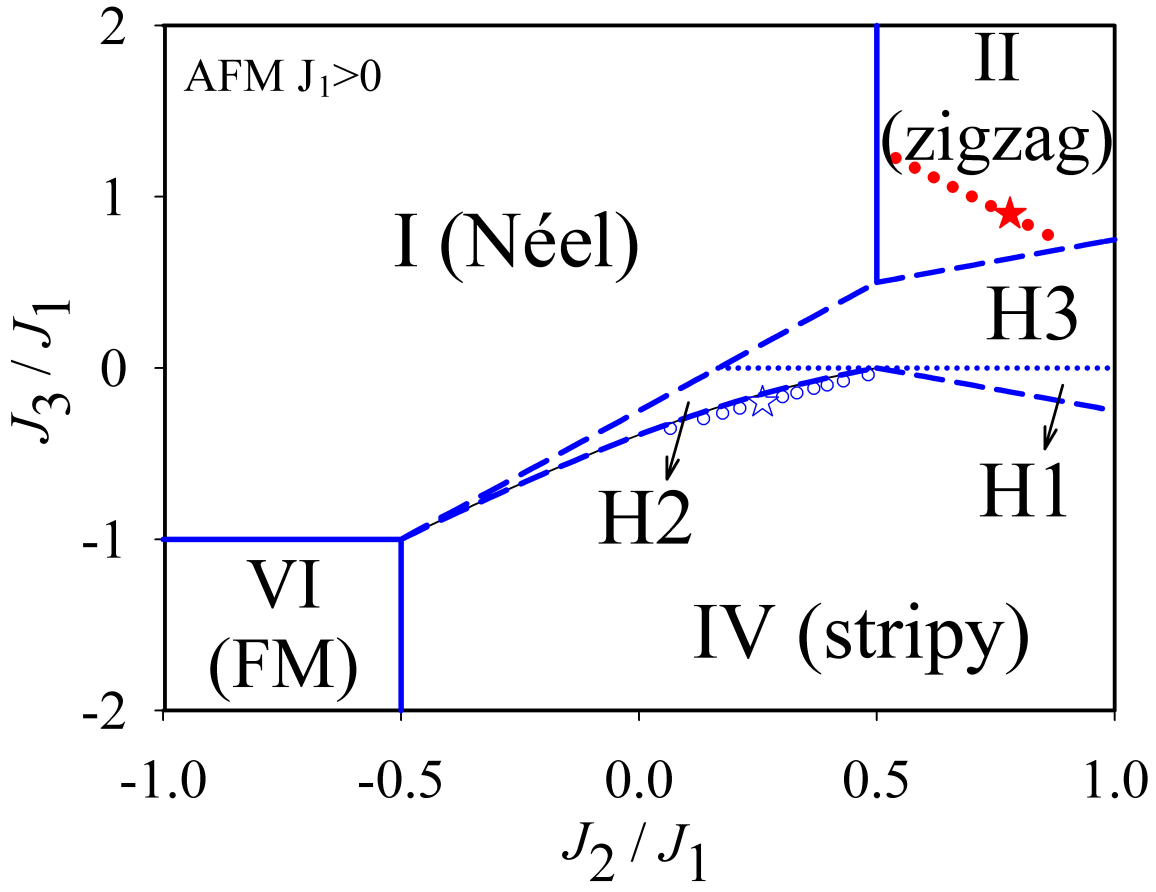


Figure 4.7: Mean-Field Phase Diagram of the Heisenberg J_1-J_2-J_3 model on the Honeycomb Lattice. Eq. (4.6) from Ref. [6] shows the regions of stability for the zigzag (II) and stripy order (IV). For dominant J_1, the collinear two-sublattice Néel order (I) is stable. H1, H2 and H3 are incommensurate helical phases, and solid lines are phase boundaries [7]. The red dotted line inside the zigzag phase indicates possible solutions for a minimal model to describe the spin dynamics in Na_2IrO_3 obtained by imposing the constraints described in the text (the red star is a representative solution for which the full spectrum is shown in Fig. 4.6d)). The blue star corresponds to the condition used for the spectrum shown in Fig. 4.6e) with other candidates that satisfy Curie-Weiss temperature marked by blue circles.

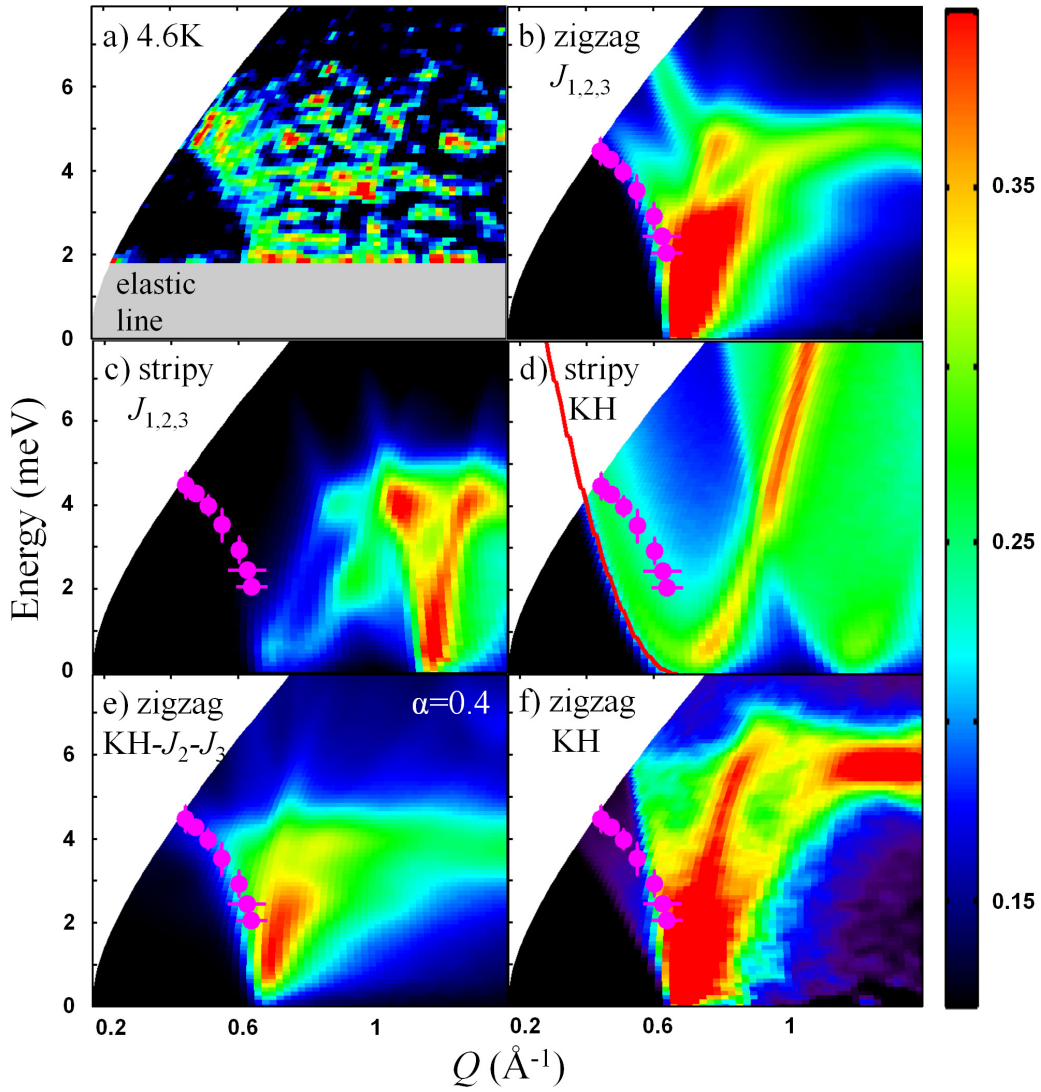


Figure 4.8: Spherically-Averaged Magnetic Excitation Spectra Generated by Linear Spin-Wave Theory. a) the INS data, b) zigzag phase, c) stripy phase in the Heisenberg J_1-J_2-J_3 model, d) stripy phase in KH model, e) zigzag phase in KH-J_2-J_3 model, f) zigzag phase in the generalised KH model. Solid magenta circles are data points obtained from fits to the boundary of the observed sinusoidal magnetic signal in a). The calculation includes the convolution with the instrumental resolution, and the spherical average was done using random Monte-Carlo points, more than 500 points uniformly distributed on the sphere.

4.4.2 Stripy Phase in the Kitaev-Heisenberg Model

In this Subsection, the Kitaev-Heisenberg (KH) model is considered, where the bond-selective anisotropic Kitaev coupling is added such that Kitaev interaction is strong enough to change the magnetic ground state and excitation spectra. In this model, the exchange between neighboring Ir moments (called $\boldsymbol{S}_{i,j}$, S=1/2) is proposed to be [3]

$$\mathcal{H}_{ij} = -J_{\mathrm{K}} S_i^{\gamma} S_j^{\gamma} + J_1 \boldsymbol{S}_i \cdot \boldsymbol{S}_j, \tag{4.17}$$

where $J_{\mathrm{K}} > 0$ is an Ising ferromagnetic (FM) term arising from superexchange via the Ir-O-Ir bond, and $J_1 > 0$ is the antiferromagnetic (AFM) Heisenberg exchange via direct Ir-Ir $5d$ overlap. Due to the strong spin-orbital admixture the Kitaev term J_{K} couples only the components in the direction γ, normal to the plane of the Ir-O-Ir bond [3, 4]. For each of the three bonds coming out of a honeycomb lattice site the Kitaev term J_{K} couples different spin components x, y, z expressed in terms of an orthogonal (cubic) reference frame. This is oriented with the cubic [111] axis normal to the honeycomb plane with the projections of the $\hat{\boldsymbol{x}}$, $\hat{\boldsymbol{y}}$ and $\hat{\boldsymbol{z}}$ axes in the plane making 120° as shown in Fig. 4.12a) inset. Each bond is labelled with the type of the spin component for the moments at the two bond ends coupled by the Kitaev term, i.e. the z-bond AB stands for exchange $-J_{\mathrm{K}} S_A^z S_B^z$ and x-bond AD stands for $-J_{\mathrm{K}} S_A^x S_D^x$ and so on.

This anisotropy leads to the strongly-frustrated Kitaev-Heisenberg (KH) model [3], which has the conventional Néel order (see Fig. 4.9a)) for large J_1, a stripy collinear AFM phase (see Fig. 4.9b)) for $0.4 \lesssim \alpha \lesssim 0.8$ (with an exact ground state at $\alpha = 1/2$) and a quantum spin liquid with Majorana fermion excitations [43] at large J_{K} ($\alpha \gtrsim 0.8$) (see Fig. 4.9c)), where α is defined as the relative strength of J_K and J_1 expressed as

$$\alpha = J_{\mathrm{K}} / \left(J_{\mathrm{K}} + 2J_1 \right) \tag{4.18}$$

Following Ref. [3], to see the hidden symmetry in the model leading to the exact ground state at α=1/2, one can solve the ground state in a "rotated" frame. This

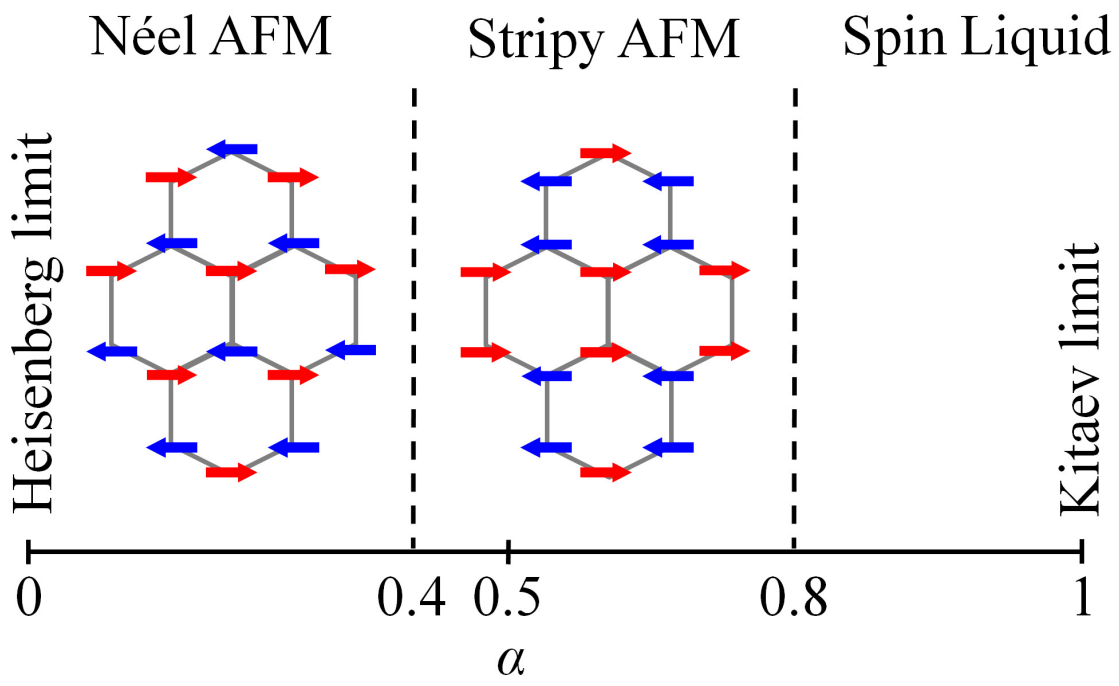


Figure 4.9: Phase Diagram of KH model as a Function of Frustration Parameter α. Néel ordered antiferromagnet (AFM) at smaller alpha value, intermediate stripy AFM and spin liquid phases in the limit of a dominant bond-selective Ising interactions.

is constructed starting from the honeycomb lattice divided into four-sublattices seen in Fig. 4.12a). In the rotated frame, one of sublattices maintain the sign of the spin operators such as $\tilde{\boldsymbol{S}}=\boldsymbol{S}$ whereas the other three sublattices differs from the original $\boldsymbol{S}$ by the sign of two appropriate spin components depending on the bonds [3, 4]. Then, in the "rotated" frame, Eq. (4.17) can also be represented by

$$\mathcal{H}_{ij} = -2(2\alpha - 1)\tilde{S}_i^{\gamma}\tilde{S}_j^{\gamma} - (1-\alpha)\tilde{\boldsymbol{S}}_i \cdot \tilde{\boldsymbol{S}}_j, \tag{4.19}$$

where it is clear that the Kitaev interaction is absent at α=1/2. (the model is equivalent to a HB FM, a special point where there are no quantum fluctuation as it is intrinsically a ferromagnetic Heisenberg where the fully aligned state is an exact ground state)

Due to the anisotropic nature of the Kitaev exchange more coupling terms between magnon operators on the 4 different magnetic A - D sublattices are generated as compared to the Heisenberg J_1-J_2-J_3 model. Thus, one needs to use the full 8-term

operator basis

$$\mathsf{X}^\dagger = \left[a_{\boldsymbol{q}}^\dagger\ ,\ b_{\boldsymbol{q}}^\dagger\ ,\ c_{\boldsymbol{q}}^\dagger\ ,\ d_{\boldsymbol{q}}^\dagger\ ,\ a_{-\boldsymbol{q}}\ ,\ b_{-\boldsymbol{q}}\ ,\ c_{-\boldsymbol{q}}\ ,\ d_{-\boldsymbol{q}}\right] \tag{4.20}$$

for which the Hamiltonian expressed in terms of magnon operators to leading order still has the quadratic form Eq. (4.8) with the matrix H given by

$$\mathsf{H} = \frac{1}{2}\begin{bmatrix} A & B & 0 & C & 0 & 0 & 0 & D \\ B^* & A & C^* & 0 & 0 & 0 & D^* & 0 \\ 0 & C & A & B & 0 & D & 0 & 0 \\ C^* & 0 & B^* & A & D^* & 0 & 0 & 0 \\ 0 & 0 & 0 & D & A & B & 0 & C \\ 0 & 0 & D^* & 0 & B^* & A & C^* & 0 \\ 0 & D & 0 & 0 & 0 & C & A & B \\ D^* & 0 & 0 & 0 & C^* & 0 & B^* & A \end{bmatrix} \tag{4.21}$$

where

$$\begin{aligned} A &= S\left(J_1 + J_{\mathrm{K}}\right) \\ B &= SJ_1\eta^{-2} \\ C &= -SJ_{\mathrm{K}}i\sin\left(\pi h\right)\eta \\ D &= S\left(2J_1 - J_{\mathrm{K}}\right)\cos\left(\pi h\right)\eta \\ \eta &= e^{k\pi i/3}. \end{aligned}$$

Diagonalisation to get the normal magnon modes [12] gives four dispersion relations

$$\begin{aligned} &\omega_{1,2}^2(\boldsymbol{q}) = A^2 - DD^* + |B - C|^2 \\ &\pm\sqrt{4A^2|B-C|^2 - |D^*(B-C) - D(B^* - C^*)|^2} \\ &\omega_{3,4}^2(\boldsymbol{q}) = A^2 - DD^* + |C + B|^2 \\ &\pm\sqrt{4A^2|B+C|^2 - |D^*(B+C) - D(B^* + C^*)|^2}. \end{aligned} \tag{4.22}$$

The dynamic correlations were solved by digonalising Eq. (4.21) numerically following a process proposed in Ref. [44]. Referring to the Q vector where the magnetic signal softens in the INS data, both conventional Néel order and spin liquid phase were eliminated, then the only remaining candidate within a KH model could be the stripy phase in the phase diagram in Fig. 4.9.

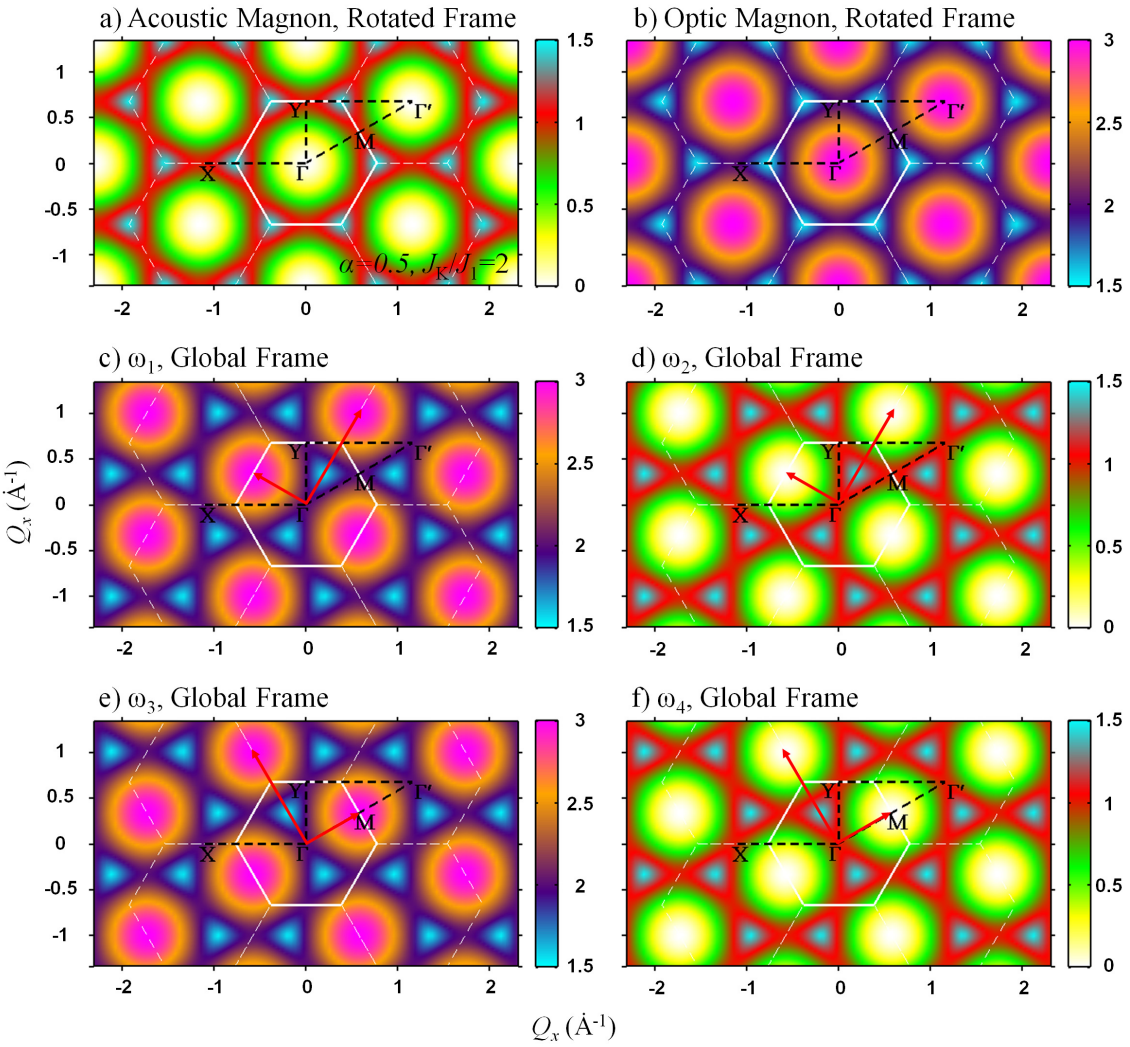


Figure 4.10: Colour Contour Maps of Dispersions in the Stripy Phase in the KH model at $\alpha = 0.5$ in both the Rotated and Global Frame. a-b) Acoustic and optic magnons in the *ab*-plane in the rotated frame. c-f) four dispersion modes in the global frame splitted from two branches in the rotated frame in a-b). The softening points are shifted by red arrows noted in c-f) in the global frame explained in the text. The black dotted line is the momentum path used in one-dimensional dispersion plots shown in Fig. 4.11 and 4.12.

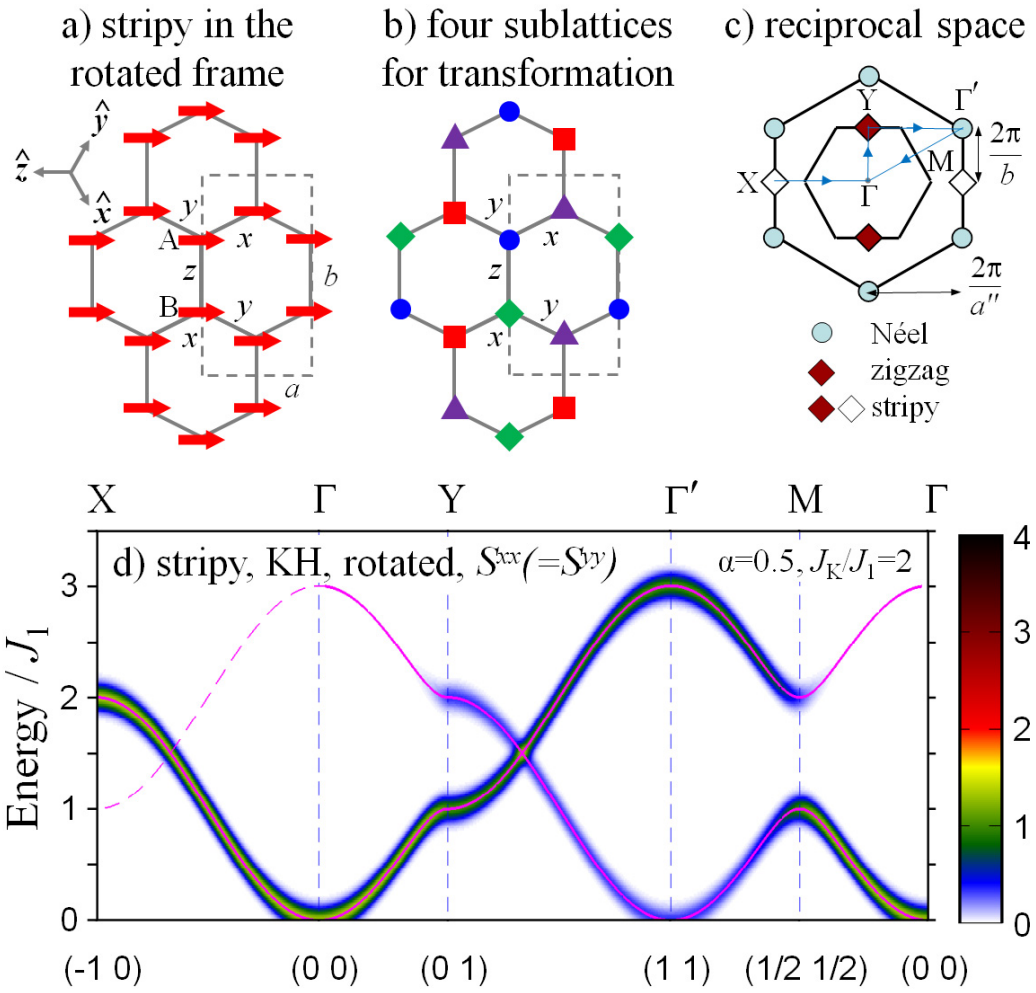


Figure 4.11: Magnetic Excitations in the Stripy Phase in the KH model and Dynamic Correlation at $\alpha = 0.5$ in the Rotated Frame. a) FM phase in the rotated frame converted from stripy order. b) Four sublattices to transform stripy phase into FM phase. c) 2D reciprocal space showing magnetic Bragg peak positions for various magnetic orders. Note that magnetic Bragg peaks for FM order occur at Γ and Γ' positions, whereas for the Néel order occur at Γ' positions only. d) Spin-wave dispersions along symmetry directions in reciprocal space (arrowed path in c)) for the KH Hamiltonians for exchange values and magnetic orders listed in the legends.

The overall feature of the spectrum of the stripy order can then be understood by a representative example at $\alpha = 0.5$, where in the rotated frame the system is equivalent to pure Heisenberg ferromagnet. At this special point, the Ising term in the Hamiltonian (the first term in Eq. (4.19)) completely vanishes leaving only the Heisenberg ferromagnetic part.

Dynamic correlations for the Heisenberg ferromagnetic order on the honeycomb in the rotated frame is shown in Fig. 4.11. It shows the same dispersion form as tight-binding model for electron bands in graphene such that two branches of optic and acoustic magnons exist, meeting at the same k-point as seen in Fig. 4.10. The transformation was performed with four sublattice illustrated in Fig. 4.11b) by keeping the corresponding spin component along the specific bond in the honeycomb lattice constant, and rotating two other spin components. Transformation from the rotated frame to the laboratory frame means that the dynamic correlations are shifted in wavevectors, S^{xx} by $(1/2, 1/2)$ and S^{yy} by $(-1/2, 1/2)$ (See Fig. 4.10 and 4.12), whereas S^{zz} (Bragg peaks) by $(0, 1)$. The resulting spectrum in the global frame along the high-symmetry direction is shown in Fig. 4.12, obtained directly by explicitly diagonalising the Hamiltonian in Eq. (4.21).

The dispersion curves are plotted for $\alpha = 0.4$ in Figs. 4.13(c-d), where the colour represents the dynamical structure factor, plotted separately for the spin fluctuations along x and y-axes, which are non-equivalent because of the presence of Kitaev bond-directional exchanges. The structure factors were obtained from the eigenvectors of the Hamiltonian matrix H in Eq. (4.21), using a numerical implementation of a general algorithm to diagonalise a quadratic form of boson operators proposed in Ref. [44]. Changing the relative strength of the Kitaev term, for example $\alpha = 0.4$ compared to 0.5, does not change the spectrum qualitatively only introduces a weak dispersion in the gapped $\omega_{1,2}$ modes, compare Figs. 4.12(c-d).

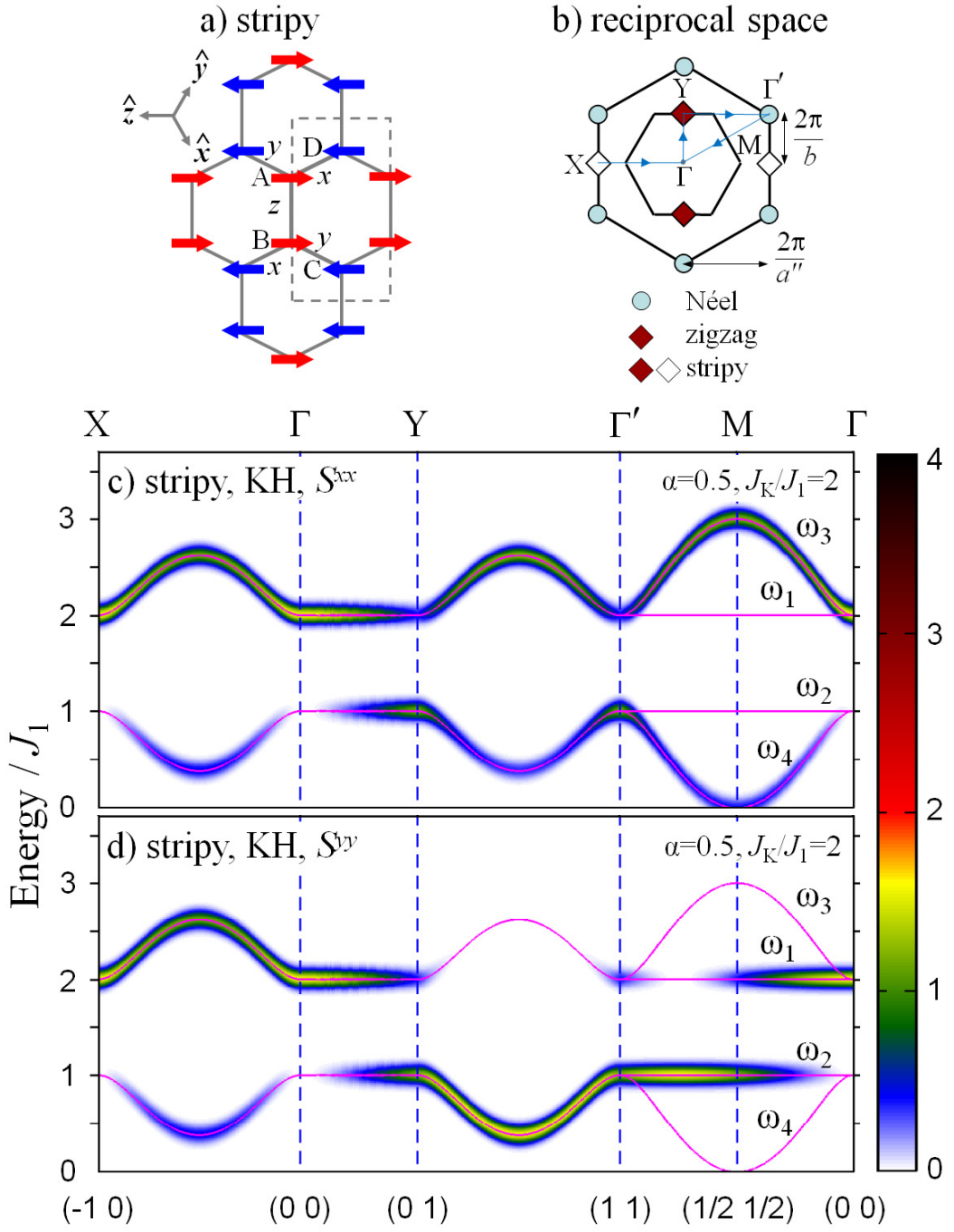


Figure 4.12: Magnetic Excitations in the Stripy Phase in the KH model and Dynamic Correlation at $\alpha = 0.5$ in the Global Frame. a) Stripy order. Dashed rectangular box of size $a \times b$ shows the magnetic unit cell containing four sublattices A-D. Bond labels x, y, z refer to the components of the spins at the two bond ends coupled by the Kitaev term. Inset show projection of the (cubic) $\hat{\boldsymbol{x}}$, $\hat{\boldsymbol{y}}$ and $\hat{\boldsymbol{z}}$ axes onto the honeycomb plane. b) 2D reciprocal space showing magnetic Bragg peak positions for various magnetic orders. c-d) Spin-wave dispersions along symmetry directions in reciprocal space (arrowed path in b)) for the KH Hamiltonians for exchange values and magnetic orders listed in the legends. Wavevectors $\boldsymbol{Q}$ are expressed in reciprocal lattice units of the rectangular magnetic unit cell. Colour is the dynamical structure factor (convolved with a Gaussian in energy for visualization, full width at half maximum = $0.15J_1$).

The dispersions show many distinct features compared to the case when the same stripy ground state was stabilized instead by isotropic Heisenberg exchanges shown in Fig. 4.6d). Notably there is no longer a gapless mode at the Γ point and at the Bragg peak positions (X and Y). The lowest mode softens at the M point as in the J_1-J_2-J_3 model due to the three-domain structure of the stripy ground state. The dispersion is gapless at this point in the linear spin-wave approximation and a gap is predicted to open up when quantum fluctuations to 1st order in $1/S$ are included for any general α, except for the exactly solvable point $\alpha = 0.5$ where due to an exact cancellation the spectrum is gapless [3].

The CW temperature in the KH model is obtained as

$$\Theta = -S(S+1)(J_1 - J_K/3)/k_B, \tag{4.23}$$

where J_1 (J_K) is the nearest neighbour Heisenberg (Kitaev) interaction.

For the direct comparison with INS data, the spherically-averaged spin-wave spectrum was calculated (including both the S^{xx} and S^{yy} dynamical structure factors), and are compared with the INS data shown in Fig. 4.8d). The exchange parameter for the KH model with stripy order was selected as $J_1 = 25.85$ meV at $\alpha = 0.4$ for a representative plot. The lower boundary of the scattering at low Q (emphasized the red solid line) is due to scattering off magnons on the ω_4 Γ-M dispersion branch near the M point. It is predicted to have a quadratic shape near the first softening point, a robust feature for any α throughout the whole range of the stripy phase. This is in contrast to the INS data where the dispersion boundary (marked by filled symbols) has a distinctly different, sinusoidal-like shape with a curvature in the opposite way. In addition, a different distribution of scattering weight to higher energies is predicted, but not seen in the data. Therefore, it is concluded that the KH model in the stripy phase has a qualitatively different spin-wave spectrum compared to the INS data.

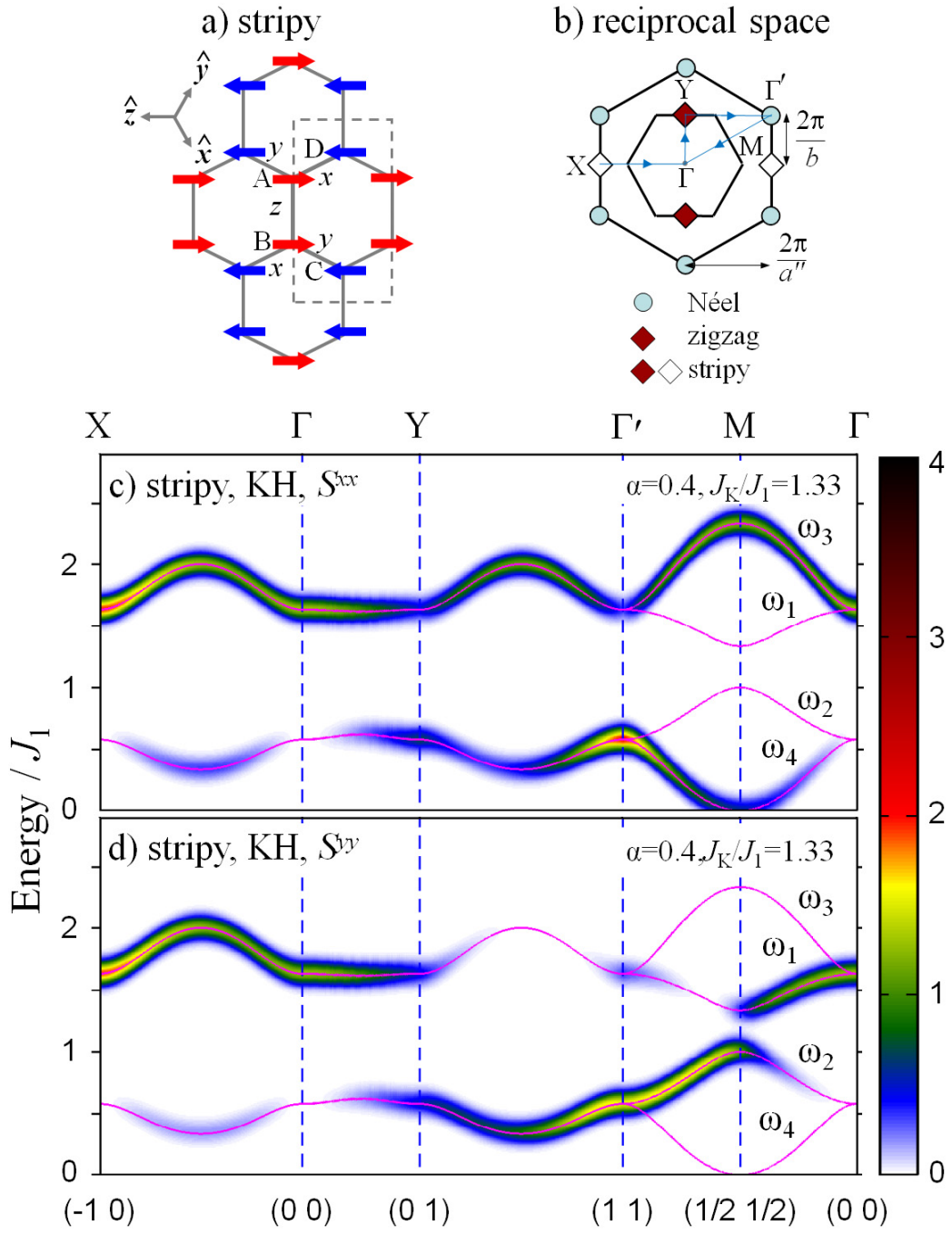


Figure 4.13: Magnetic Excitation in the Stripy Phase in the KH model and Dynamic Correlation at $\alpha = 0.4$. The outline is the same as Fig. 4.12 at $\alpha = 0.5$.

4.4.3 Zigzag Phase in the Kitaev-Heisenberg-J_2-J_3 Model

The possibility to have the Kitaev exchange interaction in the Heisenberg J_1-J_2-J_3 model has also been considered since the zigzag phase has been shown to be stable for a range of J_K values [35]. With this model, the upper bound of α value was aimed to be estimated by comparing with the INS data. The upper bound value is chosen when the calculated spectrum starts to be qualitatively different from the observed INS data.

In this Section, the effects of adding a small Kitaev interaction J_K to the J_1-J_2-J_3 Hamiltonian when the ground state order is maintained as the zigzag phase is considered. The spin-wave Hamiltonian matrix in this model is given by combining the Hamiltonian in Eq. (4.10) and (4.21) such as

$$\mathsf{H} = \frac{1}{2}\begin{bmatrix} A & B & 0 & C & 0 & D & E & F \\ B^* & A & C^* & 0 & D^* & 0 & F^* & E \\ 0 & C & A & B & E & F & 0 & D \\ C^* & 0 & B^* & A & F^* & E & D* & 0 \\ 0 & D & E & F & A & B & 0 & C \\ D^* & 0 & F^* & E & B^* & A & C^* & 0 \\ E & F & 0 & D & 0 & C & A & B \\ F^* & E & D^* & 0 & C^* & 0 & B^* & A \end{bmatrix} \tag{4.24}$$

where

$$\begin{aligned} A &= S\,\{-J_1 + 2J_2 + 3J_3 + 2J_2\cos(2\pi h) + J_K\} \\ B &= (-1/2)SJ_K\eta^{-2} \\ C &= S\,\{2J_1\cos(\pi h) - (1/2)J_K\zeta\}\eta \\ D &= S\,\{J_1\eta^{-2} + J_3\,[\eta^4 + 2\eta^{-2}\cos(2\pi h)] - J_K\eta^{-2}/2\} \\ E &= 2SJ_2\{\cos\,[\pi(h+k)] + \cos\,[\pi(h-k)]\} \\ F &= (1/2)SJ_K\zeta\eta \\ \zeta &= e^{h\pi i} \\ \eta &= e^{k\pi i/3}. \end{aligned}$$

Diagonalisation to obtain the normal modes leads to four dispersion branches

$$\begin{aligned}\omega^2_{1,2}(\boldsymbol{q}) &= A^2 - E^2 + |B-C|^2 - |D-F|^2 \\ &\pm\sqrt{4|A(B-C)+E(D-F)|^2 - \delta_-^2} \\ \omega^2_{3,4}(\boldsymbol{q}) &= A^2 - E^2 + |B+C|^2 - |D+F|^2 \\ &\pm\sqrt{4|A(B+C)-E(D+F)|^2 - \delta_+^2}\end{aligned} \tag{S8}$$

where $\delta_\pm = |(B \pm C)(D^* \pm F^*) - (B^* \pm C^*)(D \pm F)|$.

The resultant dispersions and intensities are plotted in Figs. 4.14(c-d) for $\alpha = 0.4$ ($J_K/J_1 = 4/3$), $J_2/J_1 = 0.23$ and $J_3/J_1 = 0.51$. So as to discuss the key features of the spectrum, it is helpful to visualize the degeneracies associated with the magnetic order. The magnetic structure is the zigzag pattern shown in Fig. 4.14a) but where the spin direction can be either along the $\hat{\boldsymbol{x}}$ direction to satisfy the Kitaev term on the x-type AD bond, or along the $\hat{\boldsymbol{y}}$ direction to satisfy the Kitaev exchange on the y-type BC bond. At the classical level any in-between direction, i.e. in the $\hat{\boldsymbol{x}}\hat{\boldsymbol{y}}$ plane, also has the same energy, so one expects a gapless mode associated with rotations in this "easy" plane. Indeed Fig. 4.14d) shows that the dispersion is gapless at the Y point and with strong intensity for fluctuations in this easy-plane (along the $\hat{\boldsymbol{y}}'$ normal to the ordered direction labelled $\hat{\boldsymbol{x}}'$), and gapped for fluctuations along $\hat{\boldsymbol{z}}$ out of the easy plane, see Fig. 4.14c). Furthermore, due to the honeycomb lattice geometry the magnetic structure is degenerate with the other two domains rotated by $\pm 60^\circ$ around the axis normal to the plane, so the spectrum is gapless at the Bragg peak positions of those other two domains, at points equivalent to M. The Hamiltonian however does not poses any continuous rotational symmetry in the presence of the Kitaev term, so one might expect that small gaps would open at both Y and M points when quantum fluctuations are included so the spectrum would be fully gapped. For completeness the Curie-Weiss temperature for this model is given as

$$\theta_{\rm CW} = -S(S+1)(J_1 + 2J_2 + J_3 - J_K/3)/k_B = -125 \text{ K}. \tag{4.25}$$

Spherically-averaged spin-wave dispersions are compared with data (see Fig. 4.8e)) and a Kitaev term is estimated, if present, it is smaller than an upper bound corresponding to $\alpha \lesssim 0.40(5)$, and beyond this value the spectrum starts to be qualitatively different from the INS data.

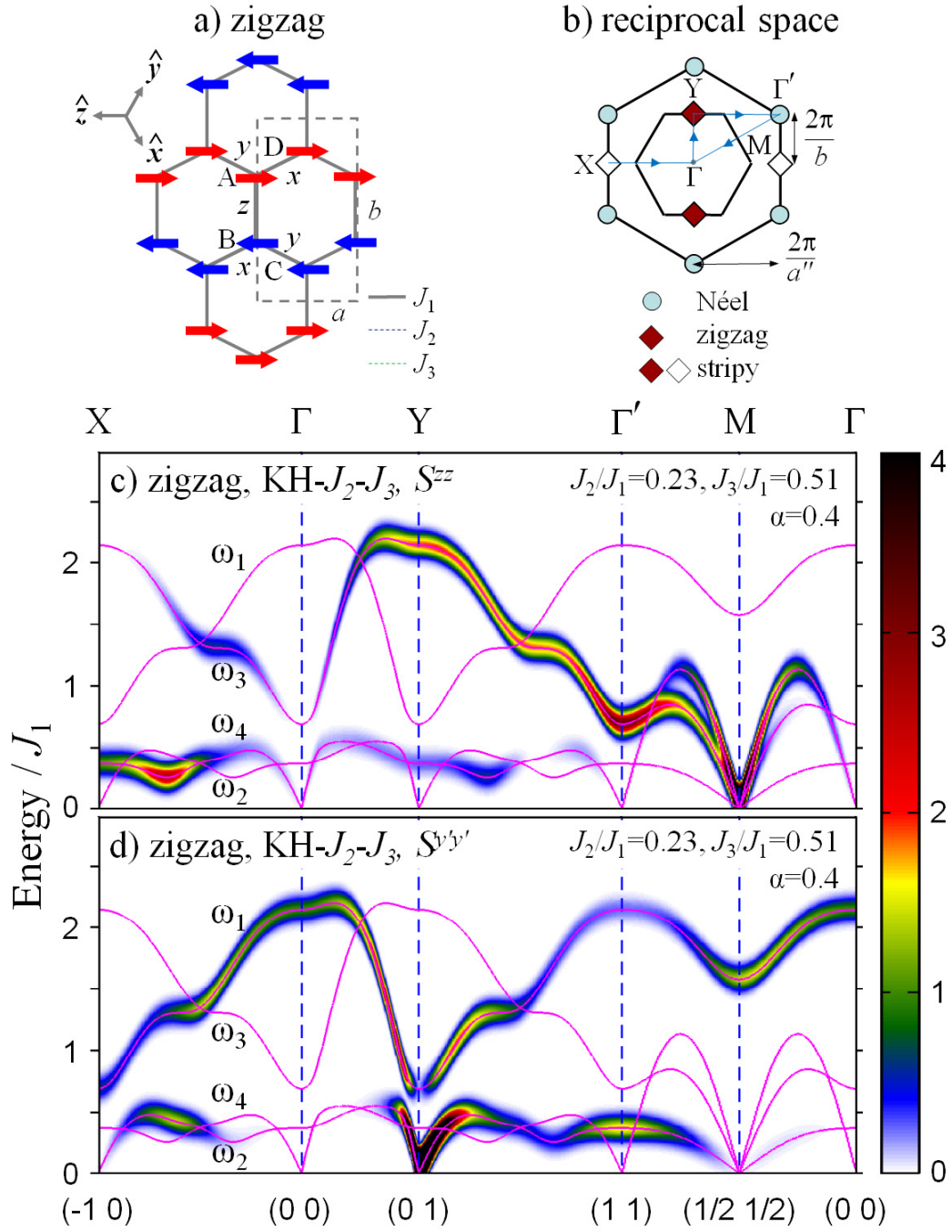


Figure 4.14: Magnetic Excitation in the Zigzag Phase in the KH-J_2-J_3 model and Dynamic Correlation. a) Zigzag order. Dashed rectangular box of size $a \times b$ shows the magnetic unit cell containing four sublattices A-D. b) 2D reciprocal space showing magnetic Bragg peak positions for various magnetic orders. c-d) Spin-wave dispersions along symmetry directions in reciprocal space (arrowed path in b)) for the Kitaev-Heisenberg-J_2-J_3 model with zigzag phase shown in a) for exchange values and magnetic orders listed in the legends. Wavevectors $\boldsymbol{Q}$ are expressed in reciprocal lattice units of the rectangular magnetic unit cell. Colour is the dynamical structure factor (convolved with a Gaussian in energy for visualization, full width at half maximum $= 0.15J_1$).

4.4.4 Zigzag Phase in the Generalised Kitaev-Heisenberg Model

The KH model has been recently generalised to account for more stable phases including a zigzag order [45]. In this scheme, the KH model in Eq. (4.17) is redefined as [45]

$$\mathcal{H}_{ij} = 2K\ S_i^\gamma S_j^\gamma + J_1 \boldsymbol{S}_i \cdot \boldsymbol{S}_j, \tag{4.26}$$

which can be rewritten in the form

$$\mathcal{H}_{ij} = A\ (2\sin\varphi\ S_i^\gamma S_j^\gamma + \cos\varphi \boldsymbol{S}_i \cdot \boldsymbol{S}_j) \tag{4.27}$$

by introducing the energy scale $A = \sqrt{K^2 + J_1^2}$ and the angle φ via $K = A\sin\varphi$ and $J_1 = A\cos\varphi$. If the "phase" angle φ is allowed to vary from 0 to 2π, additional phases can occur in the model such as the zigzag order, spin liquid states [45]. The generalised phase diagram is shown in Fig. 4.15.

In this extended phase diagram [45], it has been suggested that the zigzag phase could be stabilised, AFM Kitaev and FM Heisenberg interactions. The theory predicted the exchange parameters of $J_1 = -4$ meV and $K = 10.5$ meV [45] ($J_K = -21$ meV in the notation in Eq. (4.17)).

For the consistency, the same form of spin Hamiltonian for the generalised Kitaev-Heisenberg model for the zigzag order (illustrated in Fig. 4.16a)) is given by

$$\mathcal{H}_{ij} = -J_{\mathrm{K}} S_i^\gamma S_j^\gamma + J_1 \boldsymbol{S}_i \cdot \boldsymbol{S}_j. \tag{4.28}$$

The corresponding Hamiltonian matrix is

$$\mathsf{H} = \frac{1}{2}\begin{bmatrix} A & 0 & 0 & B & 0 & C & 0 & D \\ 0 & A & B^* & 0 & C^* & 0 & D^* & 0 \\ 0 & B & A & 0 & 0 & D & 0 & C \\ B^* & 0 & 0 & A & D^* & 0 & C^* & 0 \\ 0 & C & 0 & D & A & 0 & 0 & B \\ C^* & 0 & D^* & 0 & 0 & A & B^* & 0 \\ 0 & D & 0 & C & 0 & B & A & 0 \\ D^* & 0 & C^* & 0 & B^* & 0 & 0 & A \end{bmatrix} \tag{4.29}$$

where

$$\begin{aligned} A &= S\ \{-J_1 - J_{\mathrm{K}}\} \\ B &= S\ \{2J_1 - J_{\mathrm{K}}\}\cos(\pi h)\eta \\ C &= S\ \ J_1\eta^{-2} \\ D &= S\ \{-J_{\mathrm{K}} i \sin(\pi h)\eta\} \\ \eta &= e^{k\pi i/3}. \end{aligned}$$

Diagonalisation to obtain the normal modes leads to four dispersion modes

$$\begin{aligned} \omega^2_{1,2}(\boldsymbol{q}) &= A^2 + |B|^2 - |C-D|^2 \\ &\quad \pm\sqrt{2|B|^2(2A^2 - |C-D|^2) + B^2(C^* - D^*)^2 + B^{*2}(C-D)^2)} \\ \omega^2_{3,4}(\boldsymbol{q}) &= A^2 + |B|^2 - |C+D|^2 \\ &\quad \pm\sqrt{2|B|^2(2A^2 - |C+D|^2) + B^2(C^* + D^*)^2 + B^{*2}(C+D)^2)}. \end{aligned} \tag{4.30}$$

The spin-wave dispersions (Eq. (4.30)) and intensities (obtained from the structure factors based on a numerical algorithm proposed in Ref. [44]) are shown in Fig. 4.16, reproducing the reported results [45].

The calculation reproduces several important qualitative features of the data, namely, the presence of a kinematically disallowed region at low Q, and steep dispersion out of the Q vector - (010) corresponding to the zigzag order. Qualitatively the shape of the dispersion is steeper than in the data (compare Fig.4.8f)) the edge of strong scattering intensity and the boundary points in the data, however, potential other terms that might exist in the real material (such as symmetry allowed J^{xy} term) might improve the agreement.

One clear way to qualitatively distinguish between this and the Heisenberg J_1-J_2-J_3 model would be to measure the magnetic spectra at the Γ point where the KH model shows a large and strong intensity whereas the HB model is gapless with zero intensity. This region might be accessible by the other techniques such as resonant inelastic x-ray scattering (recent work in this regard is reported in Ref. [2]) or TeraHertz (THz) spectroscopy.

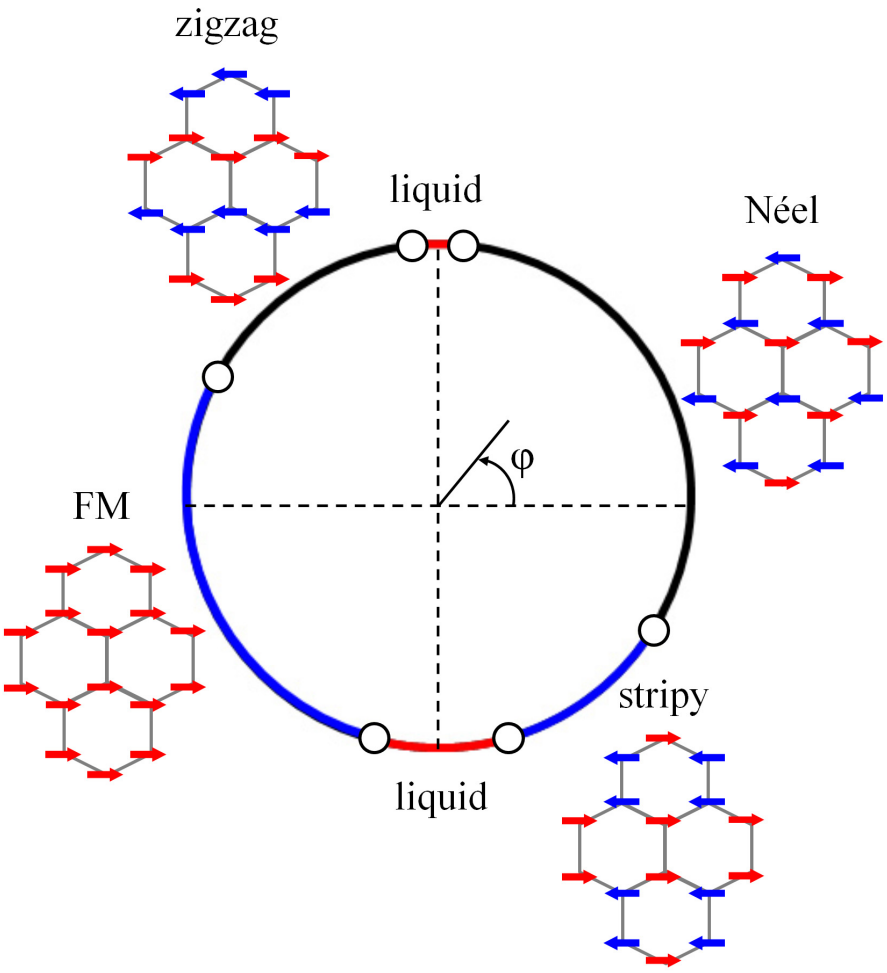


Figure 4.15: Generalised Phase Diagram in the KH Model [45]. The phase φ is the relative strength of Kitaev interaction compared to Heisenberg interaction defined as $K = A\sin\varphi$ and $J_1 = A\cos\varphi$.

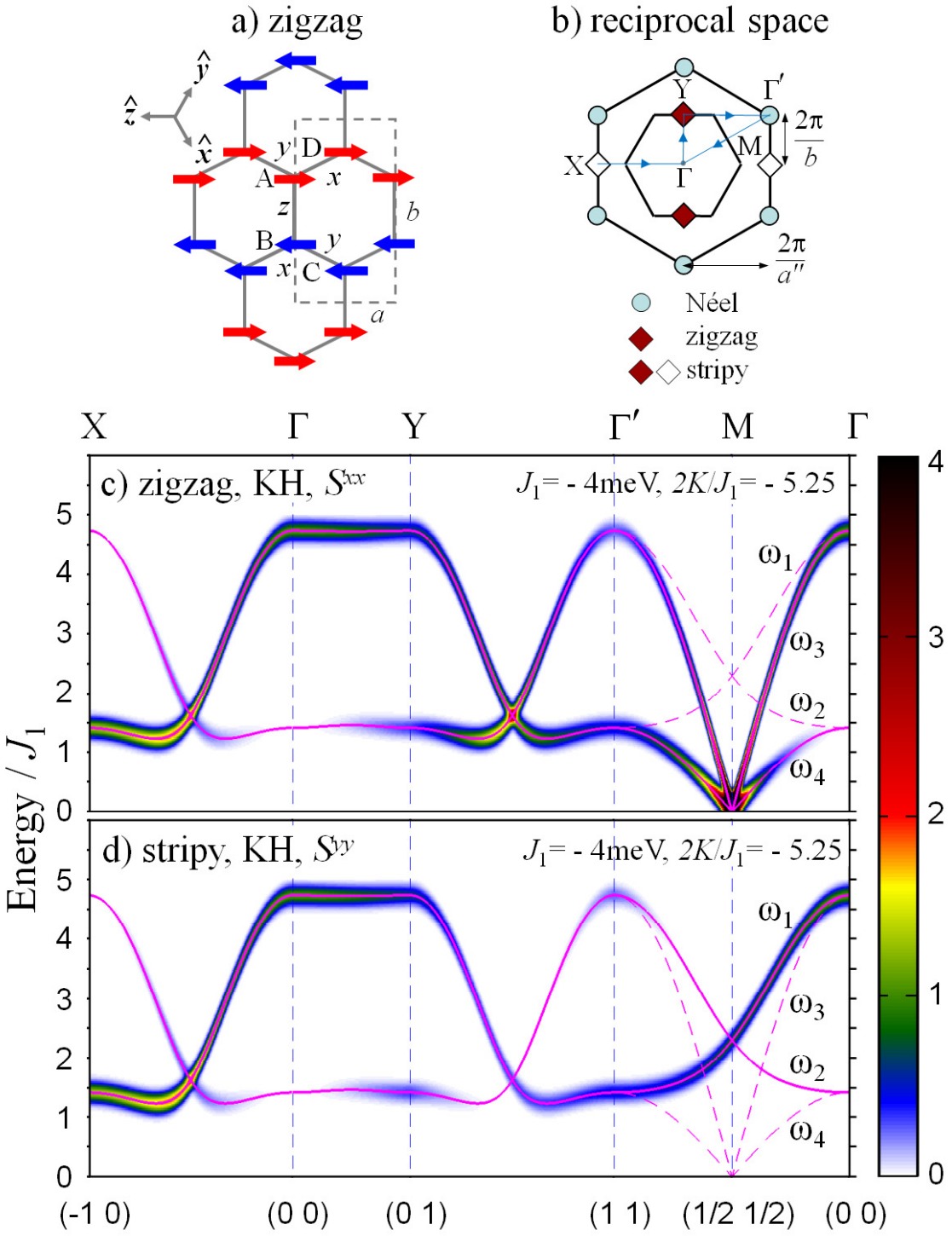


Figure 4.16: Dispersion Relation in the KH model with AFM J_K and FM J_1 in Zigzag Phase. a) Zigzag order. Bond labels x, y, z refer to the components of the spins at the two bond ends coupled by the Kitaev term. Inset show projection of the (cubic) $\hat{\boldsymbol{x}}$, $\hat{\boldsymbol{y}}$ and $\hat{\boldsymbol{z}}$ axes onto the honeycomb plane. b) 2D reciprocal space showing magnetic Bragg peak positions for various magnetic orders. c-d) Spin-wave dispersions along symmetry directions in reciprocal space (arrowed path in b)) for exchange values listed in the legend. Note that the presence of four non-degenerate modes at a general wavevector k, matching the dispersions ω_1-ω_4 to the analytical expressions given in Eq. (4.30).

4.5 Magnetic Anisotropy of Na_2IrO_3

The INS measurements discussed in the earlier section were successful in obtaining key features of the low energy dispersions of magnetic excitations in Na_2IrO_3. However, no information on a possible gap at very low energy could be obtained due to the tail of elastic line due to the limitation of the energy resolution (see Fig. 4.4e)). Following the inelastic magnetic signal down to the lowest energies and searching for the presence of a spin gap will be a sensitive test for the presence of anisotropy, which are important to understand the stability of the zigzag order. In this Section experimental INS data on the lower energy down to 1 meV is presented, followed by an analysis using linear spin-wave theory in the zigzag phase in the Heisenberg J_1-J_2-J_3 model with exchange anisotropy.

4.5.1 Experimental Details

In order to explore the very low-energy magnetic excitations and the possible existence of a spin gap, INS experiments have been performed with the cold neutron time-of-flight spectrometer IN6 in ILL. This experiment has been very challenging since iridium ions absorption cross-section increases as $1/v$ to become even higher for cold neutrons, and the magnetic inelastic signal is weak. To overcome this difficulty, the optimized mass of polycrystalline sample ($\sim$ 5.29 g) was placed in a thin ($\sim$ 1 mm) aluminium flat circular can angled at 45° to the incident beam. Measurements were made in transmission mode to access the small scattering vector Q where the magnetic scattering is strong. Three incident neutron energies of $4.77, 3.83$ and 3.12 meV have been used to probe the full range of 1 to 4 meV energy transfers, whose energy resolutions on the elastic line are $170, 120$ and 70 μeV, respectively. Neutron beam-size at the sample is about 3×5 cm^2. Typical counting times were around 1.5 days per setting measured at 1.5 K, 20 K (just above $T_N = 15.3$ K) and 50 K in the paramagnetic region to confirm the magnetic origin of the detected scattering. Empty-can and vanadium-can data were also collected to do the quantitative subtraction of the background from the aluminium-can and the normalization of the scattering intensity between detectors, respectively.

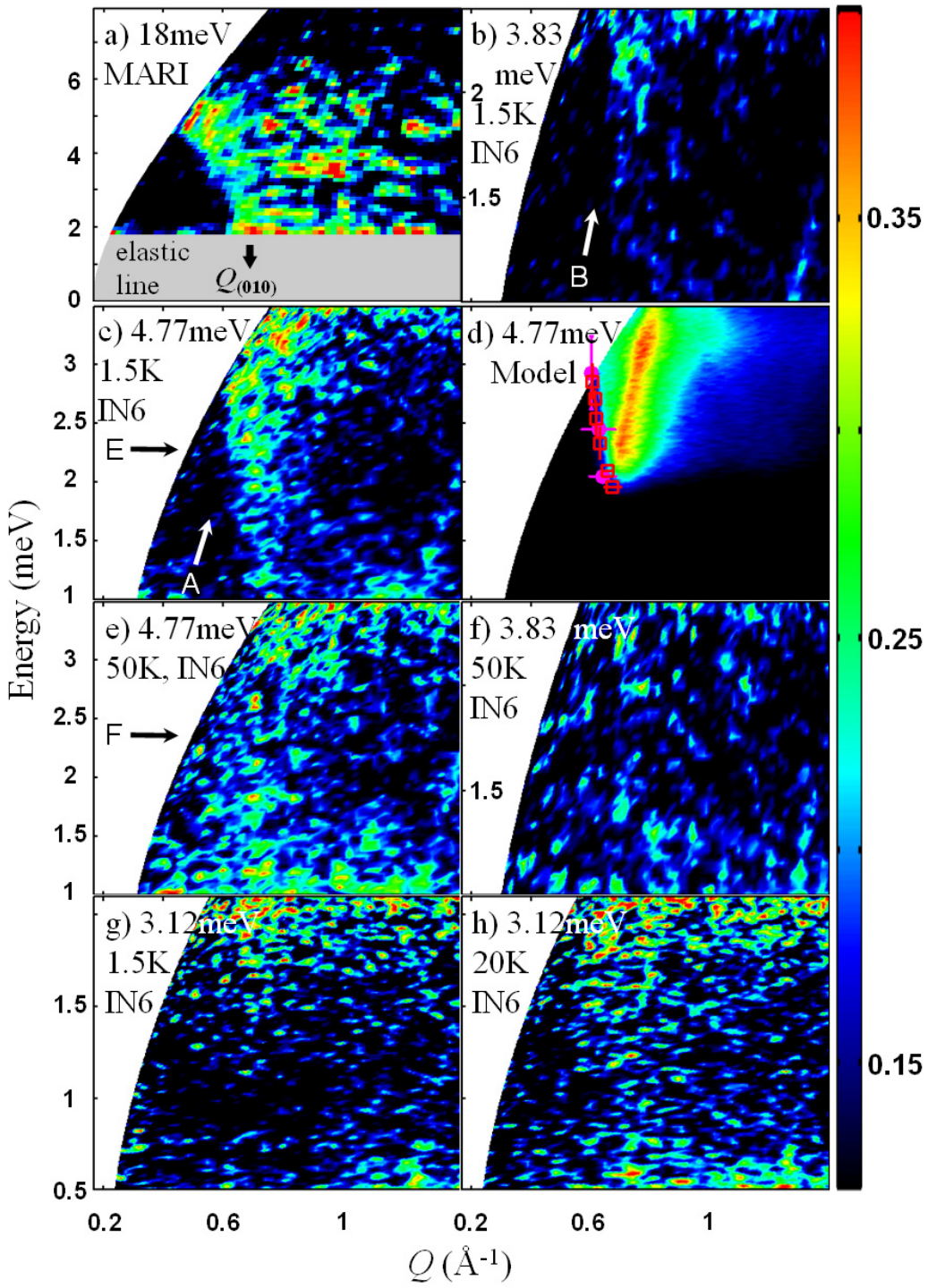


Figure 4.17: Low-Energy Magnetic Excitations Observed by Powder INS in Na_2IrO_3. Data with a) $E_i = 18$ meV at 4.6 K. b) $E_i = 3.83$ meV and c) $E_i = 4.77$ meV at 1.5 K. Higher temperature data in the paramagnetic phase at 50 K with e) $E_i = 4.77$ meV, f) $E_i = 3.83$ meV is shown respectively, revealing evidence for magnetic scattering at such low energy transfer. Another search for a possible spin gap is attempted with the lowest incident energy $E_i = 3.12$ meV at g) 1.5 K and h) 20 K. Enhanced magnetic scattering due to increasing antiferromagnetic fluctuation just above $T_N = 15.3$ K is shown in h) along the arrow. d) Simulation with the incident energy of 4.77 meV with overlapping of boundary of the dispersions extracted from (a) and (c).

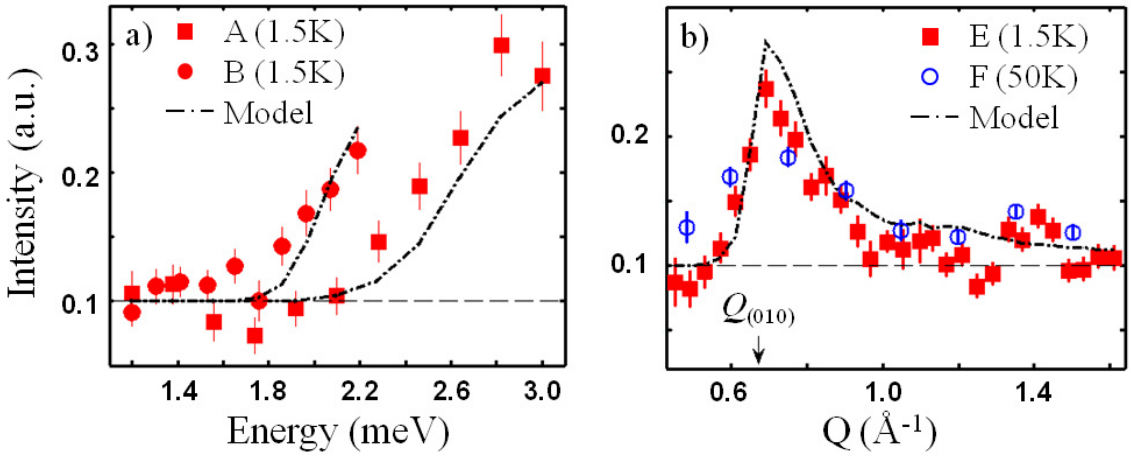


Figure 4.18: Scans through the INS Data and Spin-Wave Calculations. a) Energy scans along the A and B directions in Figs. 4.17(b,c). Scan B gives an onset of the scattering at about 1.8 meV for a Q-vectors near $\boldsymbol{Q}_{(010)}$. This sudden onset in intensity in both cuts at 1.5 K are reproduced by the model calculations. b) Momentum scans integrated over the broad energy range from 1.8 to 2.5 meV at $E_i = 4.77$ meV incident energy. A clear peak of magnetic origin is observed at 1.5 K (red rectangles), suppressed at 50 K. The dashed line is an estimated background.

The sample used in this measurement is from the same powder batch used in the previous INS experiment on MARI and well characterized with magnetic susceptibility and zero-field muon-spin rotation experiments, which confirmed well-formed magnetic order below $T_N = 15.3$ K [40].

4.5.2 Measurements and Results

Although the magnetic scattering is very weak, using the optimized experimental set-up, we have achieved a noticeable signal to noise ratio (for instance, ~ 1.5 at an incident energy of 3.83 meV, see Figs. 4.17b and 4.18c)).

Fig. 4.17c) shows inelastic neutron scattering observed for an incident energy of 4.77 meV, which allowed access to the widest energy transfer range and a clear overlap with the previous MARI data [40] (compare Figs. 4.17a,c)).

A "V-shape" spectra of strong intensity with a clearly delineated low-Q edge was observed centred around $Q\sim 0.67$ Å^{-1}, which overlaps with the higher energy data in Fig. 4.17a), this scattering is of magnetic origin as it becomes spread-out in Q

at higher temperature in Fig. 4.17e). Constant-energy cut at 2.2 meV is shown in Fig. 4.18b). The scattering is clearly peaked near $Q\sim$ 0.67 Å^{-1} (010), and becomes broad upon increasing temperature. Moving toward lower energies, the magnetic signal appeared to be lower in intensity and a possible gap was able to be extracted from E_i = 4.77 meV data. The higher resolution measurement showed a tentative evidence for a pronounced suppression below 1.8 meV, which could be consistent with a spin gap and the data in even higher resolution tested could not see any signal below 1.5 meV.

The dispersive spectrum and spin gap in the paramagnetic state at 50 K smeared out (see Figs. 4.17(e-f)), which confirms the magnetic character of the V-shaped signal observed at low temperature. The lowest excited spectrum turns out to be gapped with about 1.8 meV, which fills up at higher temperature (see Figs. 4.17b,f)), indicating a clear evidence for the presence of the spin gap. This is more evident in energy scans shown in Fig. 4.18c). Furthermore, using the lowest incident energy of 3.12 meV having the narrowest elastic line, the enhanced magnetic scattering below the spin gap was observed at 20 K (Fig. 4.17h)) and attributed to the presence of the strong magnetic critical fluctuation near T_N = 15.3 K. This signal further weakens upon increasing temperature in the paramagnetic phase at 300 K (see Fig. 4.18d)).

4.6 Parameterization of the Low Energy Dispersion using Linear Spin-Wave Theory for the Heisenberg J_1-J_2-J_3 Model with Exchange Anisotropy

In this Section, linear spin-wave theory (LSWT) is used to parameterize a possible spin gap in Na_2IrO_3 in terms of exchange anisotropy (easy-axis Ising type). In Section 4.4, LSWT for the 2D Heisenberg model with up to 3rd neighbor exchanges J_1-J_2-J_3 in the zigzag phase (See Fig. 4.8b)) qualitatively agreed with the INS data shown in Fig. 4.8a), and a representative set of parameters was proposed (J_1 = 4.17 meV, J_2/J_1 = 0.78, J_3/J_1 = 0.9) with the visualization of exchange path in Fig. 4.20a). In addition to these dominant exchange couplings,the exchange

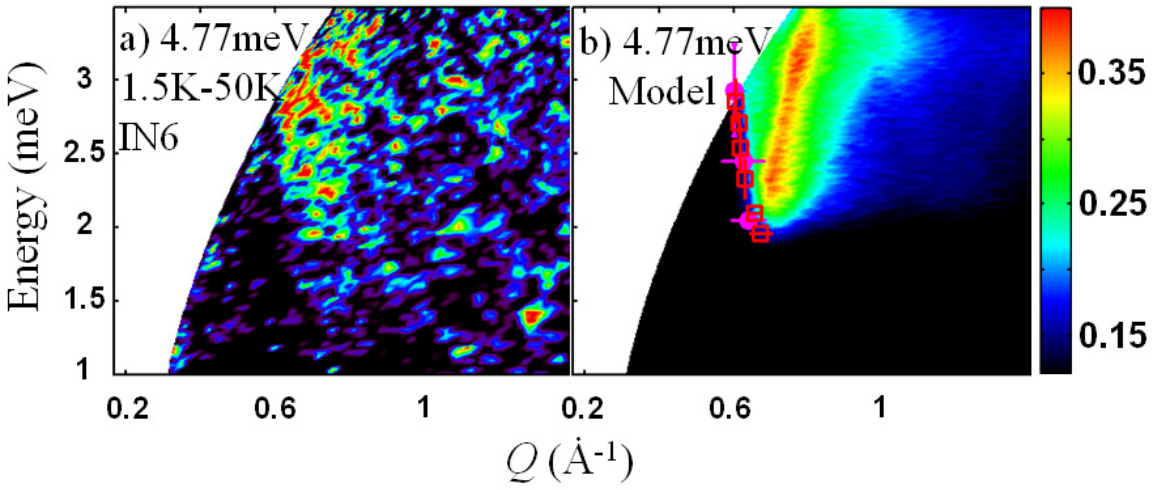


Figure 4.19: Comparison of the Magnetic Inelastic Scattering Signal and Simulations. a) Pure magnetic signal at 1.5 K with the 50 K data subtracted off. b) Simulations based on the model explained in the text.

anisotropy could be determined by a constraint to reproduce a possible spin gap of ∼1.8 meV.

To model the Ising anisotropy, one can generalise the Heisenberg model in Eq. (4.6) with an exchange $J(1+\varepsilon)$ between the S^z spin components, slightly larger than the exchange $J(1-\varepsilon)$ between the S^x (and S^y) spin components, where J stands for any of the three exchanges J_1, J_2 and J_3, such as the Hamiltonian reads

$$\begin{aligned}\mathcal{H} = &\sum_{1\text{NN}} J_1[(1+\varepsilon)S_i^z \cdot S_j^z + (1-\varepsilon)(S_i^x \cdot S_j^x + S_i^y \cdot S_j^y)] \\ &+ \sum_{2\text{NN}} J_2[(1+\varepsilon)S_i^z \cdot S_k^z + (1-\varepsilon)(S_i^x \cdot S_k^x + S_i^y \cdot S_k^y)] \\ &+ \sum_{3\text{NN}} J_3[(1+\varepsilon)S_i^z \cdot S_l^z + (1-\varepsilon)(S_i^x \cdot S_l^x + S_i^y \cdot S_l^y)],\end{aligned} \tag{4.31}$$

where S= 1/2 and 1-, 2-, and 3NN stands for summing over 1st, 2nd and 3rd nearest-neighbor pairs with corresponding exchange interactions J_1, J_2 and J_3 (paths visualized in Fig. 4.20a)). A small anisotropy $\varepsilon > 0$ opens a spin gap in the magnetic spectrum, but leaves the high energy scattering largely unchanged.

Based on Section. 4.4.1, the dispersion relations is obtained as

$$\begin{aligned}(\omega_{\boldsymbol{q}}^{\pm})^2 &= A^2 + BB^* - C^2 - DD^* \\ &\pm\sqrt{4|AB - CD^*|^2 - |B^*D^* - BD|^2}.\end{aligned} \tag{4.32}$$

where

$$\begin{aligned}A &= S\ \{(-J_1 + 2J_2 + 3J_3)(1+\varepsilon) + 2J_2(1-\varepsilon)\cos(2\pi h)\} \\ B &= 2SJ_1(1-\varepsilon)\eta\cos(\pi h) \\ C &= 2SJ_2(1-\varepsilon)\{\cos[\pi(h+k)] + \cos[\pi(h-k)]\} \\ D &= S\ \{J_1(1-\varepsilon)\eta^2 + J_3(1-\varepsilon)\left[\eta^{-4} + 2\eta^2\cos(2\pi h)\right]\} \\ \eta &= e^{k\pi i/3}.\end{aligned}$$

The spin wave dispersions in Eq. (4.32) (and the intensity dependence) for the zigzag phase with non-zero anisotropy are plotted for representative exchange values $J_1 = 4.17$ meV, $J_2/J_1 = 0.78$, $J_3/J_1 = 0.9$, $\varepsilon = 0.05$ in Fig. 4.20c). The spectrum is gapped both at ordering wavevector Y as well as the softening point M.

A spherical average of the spin-wave spectrum with all relevant pre-factors for the neutron scattering cross-section (see Appendix B for details) is shown in Fig. 4.19b). This calculated spectrum compares well to the experimental data in Fig. 4.19a). The edge of dispersive magnetic scattering (from Figs. 4.17(a,c)) are extracted and overlapped on the spherically-averaged simulated spectrum in Fig. 4.19b), clearly defining the boundary of magnetic scattering predicted by the simulation. The small exchange anisotropy of 5 % of all couplings, $\varepsilon = 0.05$ reproduces the probed size of the spin gap, ~ 1.8 meV as seen in comparison scans shown in Fig. 4.18a).

To summarize, the low energy spin dynamics was successfully probed via powder inelastic neutron scattering in honeycomb iridate Na_2IrO_3, and revealed evidence for a possible spin gap below 1.8 meV. This enables us to directly extract exchange anisotropy parameterized via a linear spin-wave model. The observation of a spin gap could be an important constraint in testing future theoretical models for the microscopic exchange interactions in Na_2IrO_3.

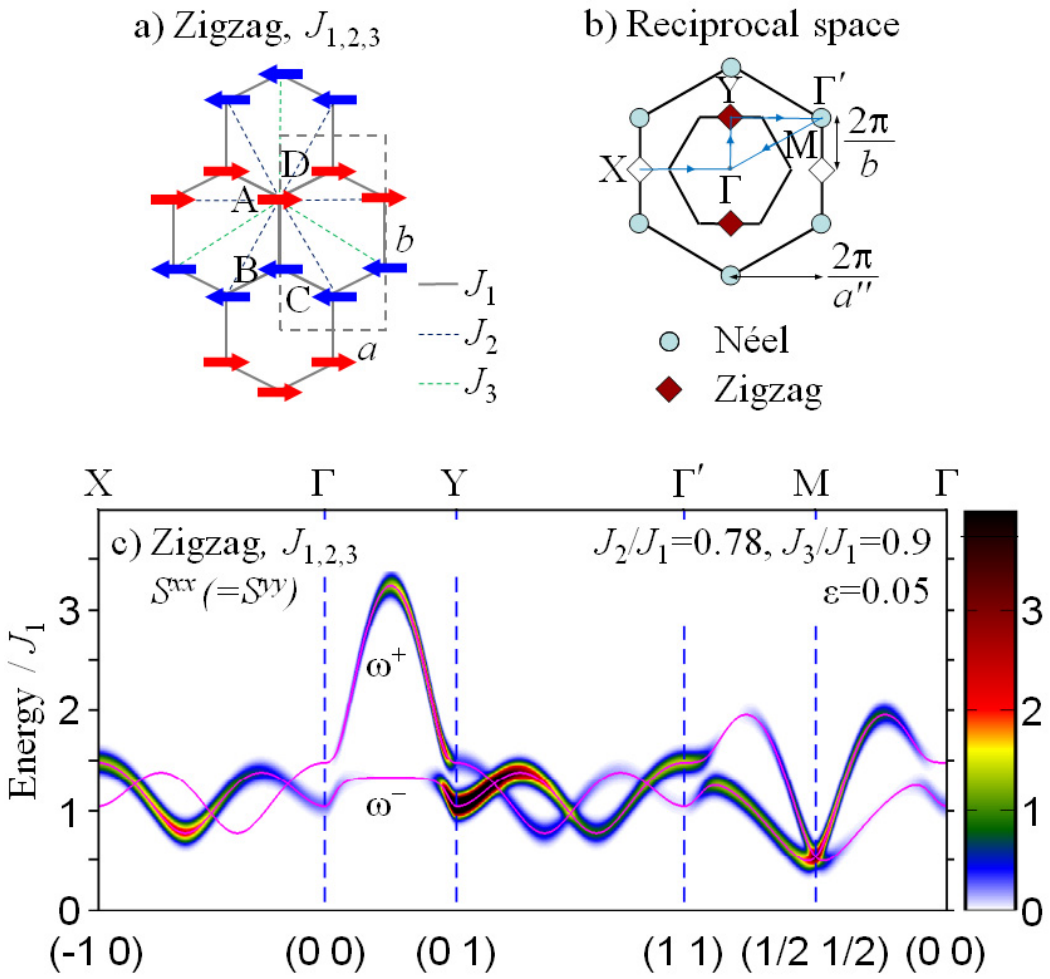


Figure 4.20: Spin-Wave Dispersion for the J_1-J_2-J_3 model with Exchange Anisotropy $\varepsilon = 0.05$. a) Zigzag magnetic ground state. Dashed rectangular box of size $a \times b$ shows the magnetic unit cell containing four sublattices A-D with three types of exchange interactions (J_1, J_2 and J_3). b) 2D reciprocal space showing magnetic Bragg peak positions for zigzag state. For reference, the location of magnetic Bragg peaks (blue circles) for a simple Néel phase are also shown. c) Spin wave dispersions along high symmetry directions in reciprocal space (arrowed path in a)) for zigzag J_1-J_2-J_3 Hamiltonians for exchange values and anisotropy listed in the legend. Wavevectors $\boldsymbol{Q}$ are expressed in reciprocal lattice units of the rectangular magnetic unit cell. Colour is the dynamical structure factor (convolved with a Gaussian in energy for visualization, full width at half maximum = $0.15J_1$), ($S^{xx}(\boldsymbol{Q},\omega) = S^{yy}(\boldsymbol{Q},\omega)$). This spectrum has been used in producing the spherically-averaged spin-wave spectrum shown in Fig. 4.17f).

4.7 Conclusions

In this Chapter, the magnetic order and excitations of Na_2IrO_3 have been studied using SQUID magnetization, zero-field muon-spin rotation and powder inelastic neutron scattering. The onset of long-range magnetic ordering occurring below $T_N = 15.3$ K was confirmed by the observation of oscillations in the relaxation of implanted muons, also consistent with anomaly in SQUID data. Powder inelastic neutron scattering measurements detected magnetic excitations, which is the first observation of dispersive spin wave excitations in any iridium-based material to our knowledge. Such measurements are technically extremely challenging because iridium is a notoriously strong neutron absorber, but was overcome by using an optimized setup to minimize neutron absorption. The results demonstrate the proof of principle that such measurements are possible with an optimised setup and open up a new opportunity to study the spectra of magnetic excitation in other potentially exotic iridium materials, not explored so far by inelastic neutron scattering due to the common belief that such measurements are not feasible.

The neutron scattering spectrum was quantitatively compared with the spin dynamics of various spin Hamiltonians calculated using linear spin-wave theory. The candidates considered were the Kitaev-Heisenberg and Heisenberg J_1-J_2-J_3 models in the stripy and zigzag ordered phases. The best agreement was found for the Heisenberg J_1-J_2-J_3 model in the zigzag phase. Another possibility could be the generalised KH model with AFM Kitaev and FM Heisenberg terms, however, the quantitative agreement was better with the HB J_1-J_2-J_3 model. Additional interactions may need to be added to the generalised KH model to give as good an agreement as the HB J_1-J_2-J_3 model.

To study the magnetic anisotropy, the experiments have searched for a spin gap in the low energy excitation spectrum, finding an evidence for a 1.8 meV spin gap which can be parameterized by including a small exchange anisotropy in the Heisenberg J_1-J_2-J_3 model.

Chapter 5

Revised Crystal Structure Model for Na_2IrO_3

This chapter revises the crystal structure previously proposed based on powder x-ray diffraction on Na_2IrO_3, a monoclinic $C2/c$ structure, obtained from a sample containing numerous stacking faults. In the current work, by using single crystal x-ray diffraction, only integrating the nuclear Bragg peaks in momentum space and excluding the diffuse scattering intensity, a more accurate crystal structure model is found. A more symmetric $C2/m$ structure is obtained with a less distorted honeycomb backbone and more isotropic IrO_6 octahedra, further confirmed by density functional calculations. The revised crystal structure shows a significant departure from the ideal 90 ° Ir-O-Ir bonds required for dominant Kitaev exchange, which could explain why no evidence for the strong Kitaev interactions was found by analysing the inelastic neutron scattering data in Chapter 5.

5.1 Introduction

The magnetism of transition-metal oxides have been extensively studied with $3d$ ion compounds, which spin-orbit interaction is weaker than other energy scales such as Couloumb interaction, crystal field energy and so on, so it is often negligible. However, $5d$ transition-metal ions have much stronger spin-orbit coupling whereas the Couloumb interaction weakens due to the extended nature of $5d$ orbitals. This new balance of energy scales is considered as a key factor to lead to novel electronic

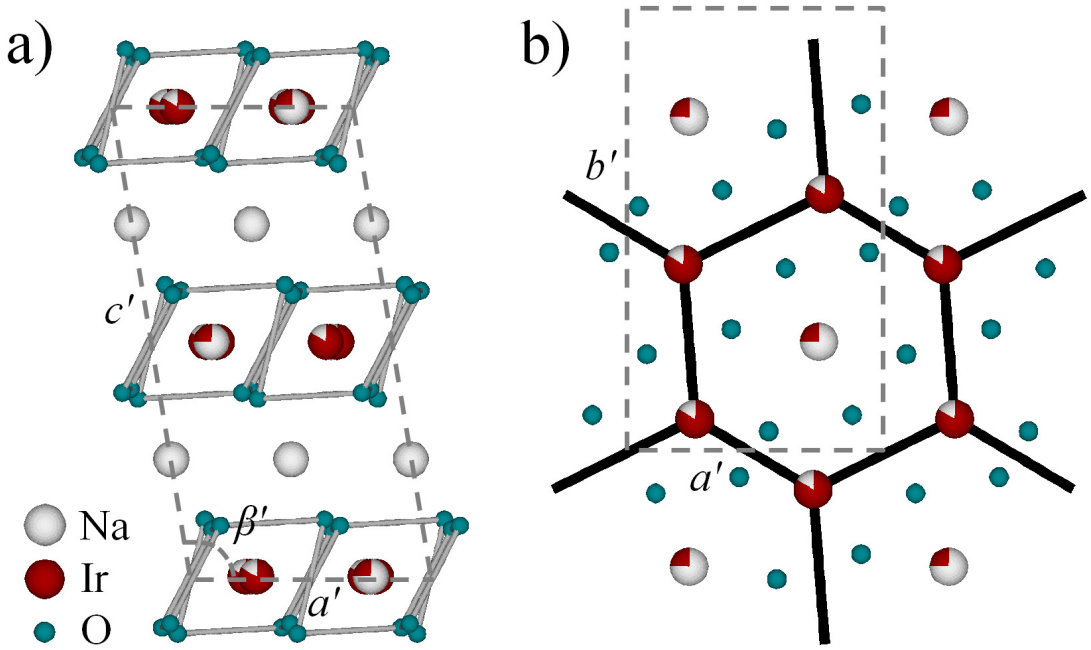


Figure 5.1: Proposed Crystal Structure of Na_2IrO_3 with the C2/c Model [30]. a) Layer stacking along the monoclinic $\boldsymbol{c}$-axis with an in-plane offset along $\boldsymbol{a}$-axis (dashed box is the C2/c unit cell). b) Basal layer ($z = 0$) showing the Ir honeycomb lattice with the artificial site-mixing between Ir and Na ions in the plane. The lattice parameters are expressed in the primed notation in C2/c space group. Note that the z-coordination of Ir1 (0.2726, 0.0781, 0.0005) ion in the honeycomb lattice was shifted to $z = 0$ for the purpose of the visualisation.

states. Particular interests lies in the honeycomb antiferromagnet iridate Na_2IrO_3 [30, 31], in which IrO_6 composes a honeycomb network. An exotic magnetic ground state is suggested to be stabilized in the bulk by competing couplings (magnetic superexchange Ir-O-Ir and direct exchange Ir-Ir) for the mixed spin-orbital ground state doublet for Ir^{4+} with effective $J_{eff} = 1/2$ [3]. The magnetic properties in this material is considered to have a close link to the crystal structure, thus in this Chapter, we revise the crystal structure of Na_2IrO_3.

The previous study on the crystal structure of Na_2IrO_3 with x-ray powder diffraction showed [30] that it is formed of an alternating arrangement of rather distorted $Na_{1/3}Ir_{2/3}O_2$ honeycomb layers and NaO_2 hexagonal layers in the C2/c space group as illustrated in Fig. 5.1. Powder x-ray diffraction patterns also presented the anisotropic

lineshapes and reduced intensities of peaks with $2\theta = 20 \sim 35^\circ$ which was explained as an effect of the disorder induced by stacking faults [30] based on a simulation of diffraction peaks from a model containing stacking faults in Li_2MnO_3 [46]. In order to imitate this effect in the powder data, rather sizeable site-mixing between Ir and Na in the honeycomb layer was artificially assumed, however this could hinder the accurate determination of the crystal structure due to the suppression of the large contrast between Ir and Na ions in the honeycomb layer. The suppressed intensity of peaks and anisotropic lineshapes due to a sizeable stacking faults in the powder XRD data will make the refinement of the crystal structure less reliable. Thus the exclusion of the diffuse scattering needs to be done for a more accurate determination of the underlying crystal structure. However, this issue cannot be resolved with the powder diffraction data as the various contribution from the crystal defects, site mixing and stacking faults cannot easily be disentangled in analysing the powder data. Therefore, in this study single crystal x-ray diffraction was used in order to separate the diffuse scattering intensity and other impurity peaks from the main peaks which were used in the analysis to determine the crystal structure, using a high-quality single crystal with a minimal level of stacking faults and impurities.

5.2 Experimental Details

X-Ray Diffraction (XRD) was performed in the Clarendon Laboratory using a Mo-source Oxford Diffraction Supernova diffractometre on a single crystal of Na_2IrO_3 of approximate size $220\times150\times10$ μm^3 (see Fig. 5.3a)), which was chosen from over 30 single crystals grown via the flux method [30]. The complete x-ray data was collected by covering up to the maximum momentum space that the equipment can reach for around 1 hour at room temperature, and more than 1000 peaks were detected. The single crystals were grown in the Philipp Gegenwart group at Georg-August-Universität in Göttingen, Germany.

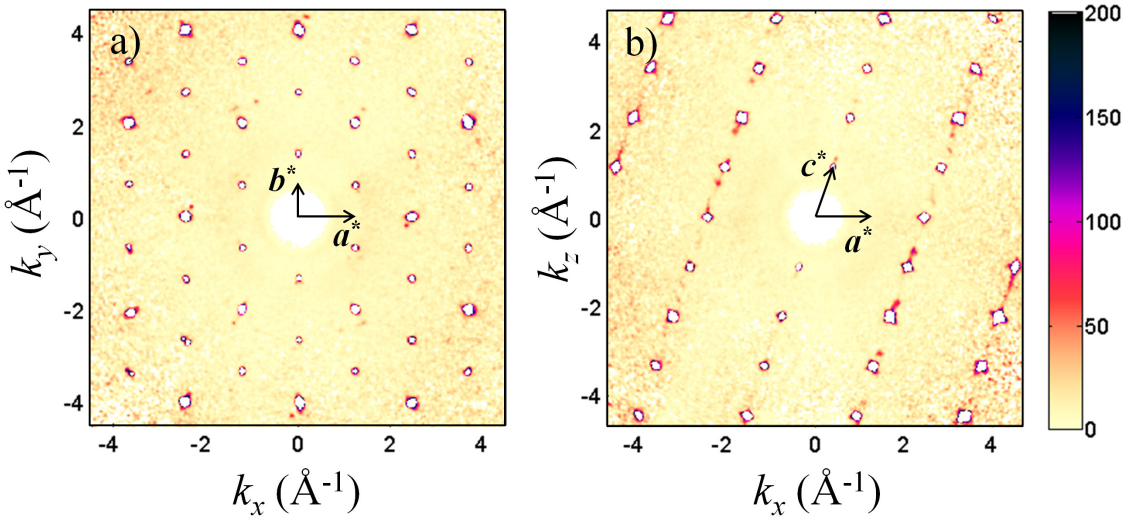


Figure 5.2: Experimental Data from Single Crystal X–ray Diffraction. a) (HK0) plane, b) (H0L) plane. A small amount of impurity peaks are also present.

5.3 Measurements and Results

The diffraction pattern showed sharp Bragg peaks which could be indexed by a monoclinic unit cell (96% of over 1000 peaks) (see Fig. 5.3b)) derived from a parent rhombohedral structure with an ideal repeat every three honeycomb layers. The monoclinic distortion leads to an in-plane shift of successive Ir honeycombs differing by 1.2 % from the ideal value ($-c\cos\beta$ compared to $a/3$, see Fig. 5.3b)), well above the instrumental resolution which allowed us to determine that the sample was a single structural monoclinic domain. This was also confirmed by attempts to index the peaks with a cell rotated by $\pm 60°$ in the ab-plane, which failed (could only account for 33, 63 % of the peaks). Typical diffraction planes collected by the experiment are shown in Fig. 5.2. In Fig. 5.2a) a hexagonal peak pattern is obtained in the (HK0) plane, and in Fig. 5.3a) a monoclinic feature inclined by 19° in (H0L) is seen, which is the angle between $\boldsymbol{a}^*$ and $\boldsymbol{c}^*$ in the reciprocal unit cell.

Using x-ray diffraction with representative plots shown in Fig. 5.2, a detailed refinement was performed using both the previously published C2/c (the space group No. 15) unit cell with 15 refined atomic positions leading to values somewhat similar to Ref. [30], and an alternative, higher-symmetry C2/m (No. 12) model with half

the unit cell volume shown in Figs. 5.3(b-c) (as found for the related Li_2IrO_3 [47]), with only 7 refined atomic positions. The refined crystal structure in the C2/m model is listed in Table 5.1. Other structural motifs reported for "213" honeycomb oxides [48, 49, 50] including Na_2PtO_3, Li_2TeO_3, Na_2TbO_3 were also tried but did not provide a good fit. Ir/Na site admixing has also been tested but this did not improve the agreement with data - the refinement became only marginally better for up to 8.6% site-mixing and worse beyond this proportion. Two standard softwares packages - SIR-92 [27] and SHELX [28] - were used for testing the various structures and further refinements of the crystal structures in both space groups. $R_{\rm int}$ and $R_{\rm sigma}$ are defined as follows [51].

$$R_{\rm int} = \frac{\sum |F_o^2 - F_o^2({\rm mean})|}{\sum F_o^2},$$
$$R_{\rm sigma} = \frac{\sum \sigma(F_o^2)}{\sum F_o^2}, \qquad (5.1)$$

where both summations in $R_{\rm int}$ are done for all input reflections for which more than one symmetry equivalent is averaged, and $R_{\rm sigma}$ is calculated over all reflections in the merged list. Refinements parameters are defined [51] as

$$wR2 = \Big(\frac{\sum[w(F_o^2 - F_c^2)^2]}{\sum[w(F_o^2)^2]}\Big)^{1/2},$$
$$R1 = \frac{\sum ||F_o| - |F_c||}{\sum |F_o|},$$
$$S = \frac{\sum[w(F_o^2 - F_c^2)^2]}{(n-p)}, \qquad (5.2)$$

where w is the weighting factor, F_o^2 is the observed intensities of peaks, F_c^2 is the calculated intensities of peaks, n is the number of reflections and p is the total number of parameters refined.

Interestingly, the C2/c structure can be described as a "supercell" obtained from the C2/m structure by small displacements of atoms (of order a few % of the unit cell dimensions) leading to a doubled unit cell volume. Although C2/m and C2/c gave comparable agreement with the main Bragg peaks, the larger C2/c unit cell should be manifested experimentally by the appearance of new "superstructure" peaks at positions such as (odd, odd, half-integer) in the small unit cell description (C2/m).

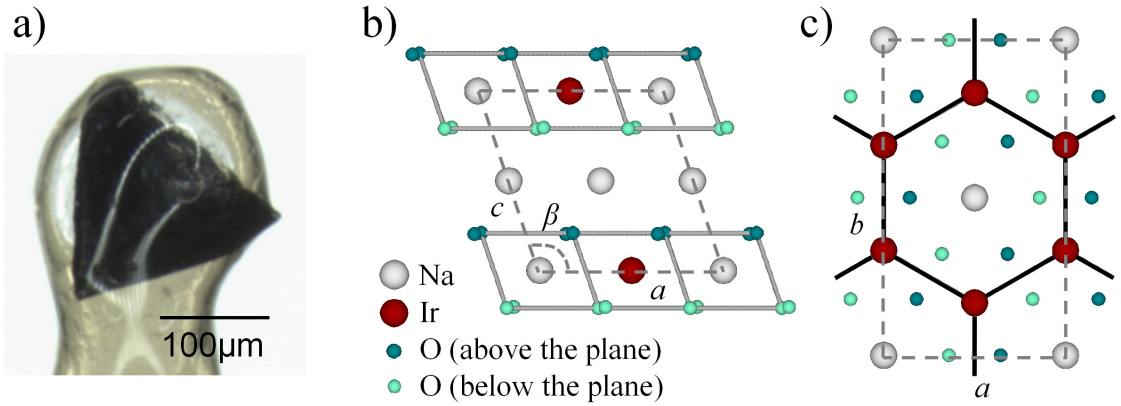


Figure 5.3: Crystal Structure of Na_2IrO_3 Determined by Single Crystal X-ray Diffraction. a) Microscopic image of the single crystal of Na_2IrO_3 used for the diffraction measurement. b) Layer stacking along the monoclinic $\boldsymbol{c}$-axis with an in-plane offset along $\boldsymbol{a}$-axis (dashed box is the C2/m unit cell). c) Basal layer ($z = 0$) showing the Ir honeycomb lattice.

Table 5.1: Structural parameters extracted from single-crystal x-ray data at 300 K. (C2/m space group, $a = 5.427(1)$ Å, $b = 9.395(1)$ Å, $c = 5.614(1)$ Å, $\beta = 109.037(18)°$, $Z = 4$). All sites are fully occupied. U is the isotropic displacement. The goodness-of-fit (S) was 2.887, $wR2 = 0.3111$, $R1 = 0.1346$ ($R_{\text{int}} = 0.1247$, $R_{\text{sigma}} = 0.0584$). Definitions of parameters for refinements are defined in the text.

Atom	Site	x	y	z	U(Å^2)
Ir	4g	0.5	0.167(1)	0	0.001(1)
Na1	2a	0	0	0	0.001(6)
Na2	2d	0.5	0	0.5	0.009(7)
Na3	4h	0.5	0.340(2)	0.5	0.009(6)
O1	8j	0.748(6)	0.178(2)	0.789(6)	0.001(6)
O2	4i	0.711(7)	0	0.204(7)	0.001(7)

These superlattice peaks, however, were not observed in the data, ruling out the C2/c model which is explained in more details in Sec. 5.4.4. Furthermore, in structural optimization calculations using VASP [52, 53] (see Sec. 5.4.1) it was found that the C2/c structural model was unstable in its asymmetrically-distorted IrO_6 octahedra: (i) the forces on the oxygen ions are very large, exceeding 3 eV/A for the published C2/c cell [30] and (ii) when the structure is allowed to relax the oxygens move such as to recover the more symmetric C2/m structure with the Ir-O distances converging to within 1.1 % of the experimentally refined values in Table 5.1. The IrO_6 octahedra are much more symmetric in the C2/m model with Ir-O distances and Ir-O-Ir bond angles ranging from 2.06 to 2.08 Å, and 98 to 99.4°, respectively, compared to the wider ranges of 1.99 to 2.43 Å, and 91 to 98° proposed previously [30].

5.4 Analysis

5.4.1 Structural Optimization Calculations using VASP

To quantitatively verify the stability of the C2/m crystal structure, the structural optimization calculations using VASP [52, 53] were performed by Aleksey Kolmogorov, now in Binghamton University, USA. The radial distribution functions calculated from the relaxation is shown in Fig. 5.4, indicating that in the experimental C2/m structure the atomic distances are more isotropic than its C2/c counterpart. The relaxed C2/m structure with atoms free to move inside a unit cell with lattice parameters fixed by experiments show a better agreement with the experimental C2/m model. It was also proved that the energy cost of a stacking fault is extremely small, below 0.1 meV/Å^2, explaining why such stacking faults are very likely to occur. All technical details are given in Ref. [40] and its supplementary materials.

5.4.2 Microscopic Model of Stacking Faults

In addition to sharp Bragg peaks, visible diffuse "rods" of scattering were also observed (see Fig. 5.6a)). The periodicity of this diffuse scattering along $\boldsymbol{c}^*$ leads to the selection rule $h + k = 2n$ and $k = 3m + 1$ or $3m + 2$ (n, m integers). This

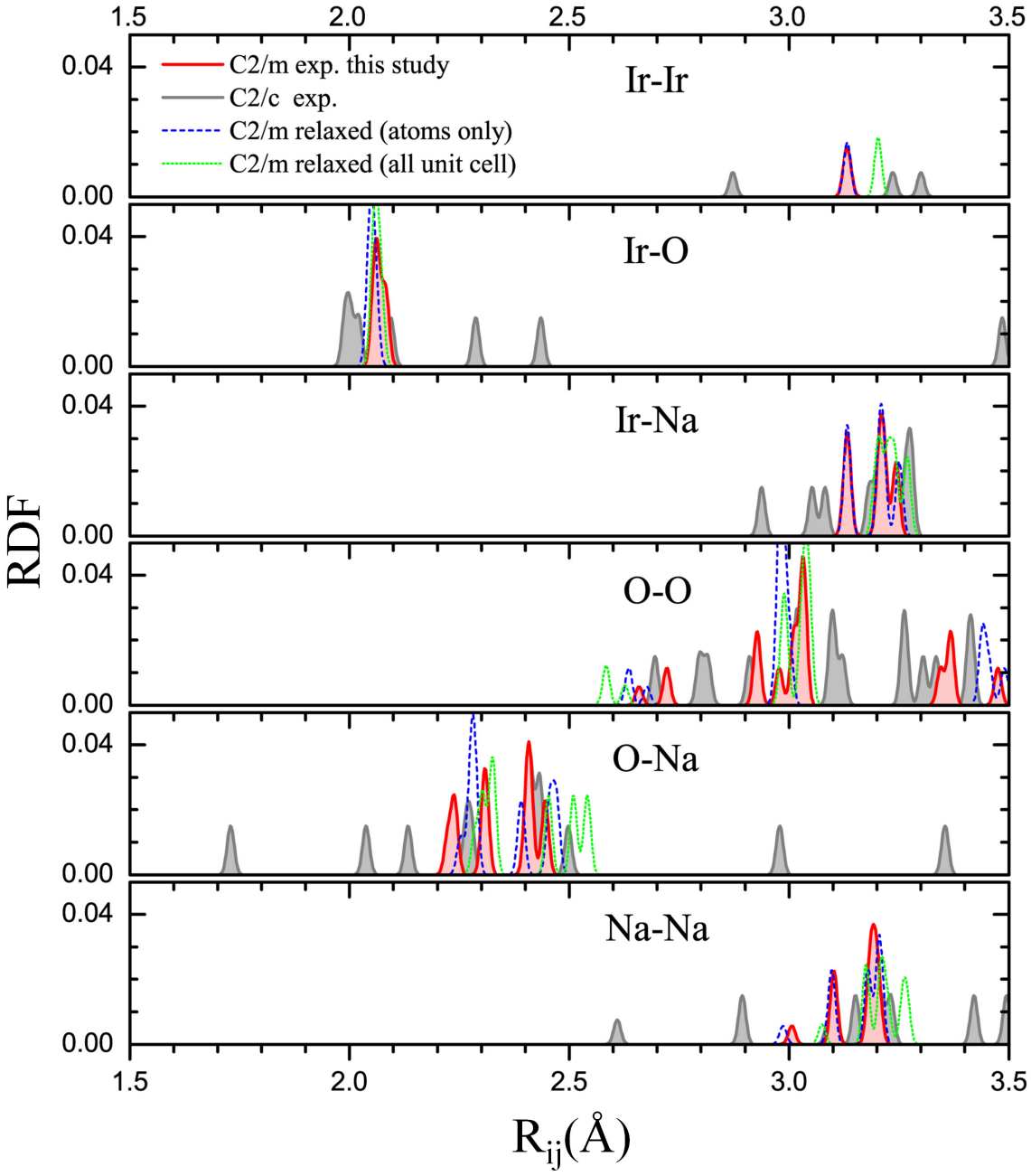


Figure 5.4: a) Radial distribution functions (RDFs) showing the difference in the local atomic environments for the previously reported C2/c structure [30] and the C2/m structure proposed in this study. In the C2/m case, the RDFs are plotted for the unit cell extracted from the experiment (red solid line), the unit cell with atomic positions relaxed in the DFT (blue dashed line), and the unit cell fully relaxed in the DFT (green dotted line). Note that a small Gaussian smearing (σ = 0.008 Å) was used in the calculation of the RDFs.

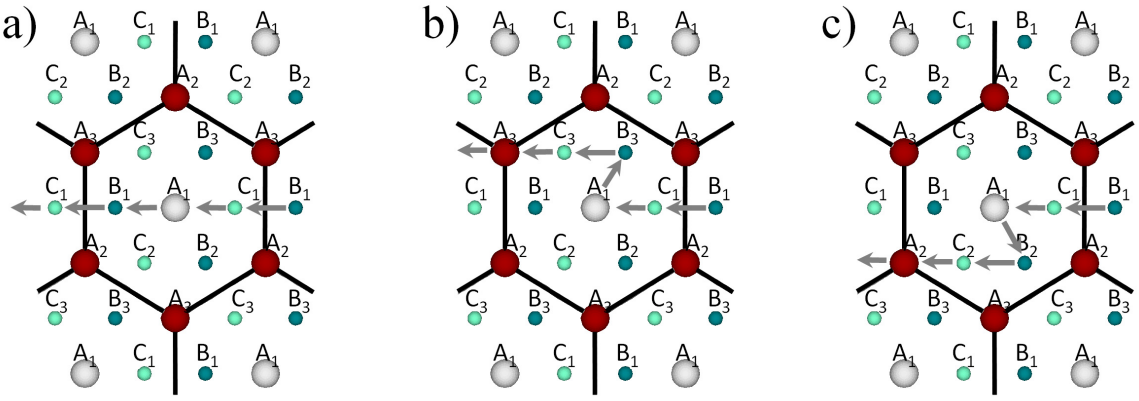


Figure 5.5: Stacking Order in the Layered Honeycomb Iridate. Diagram to illustrate a) the layer stacking of the honeycombs for the ideal case, b-c) with two simple stacking faults drawn with arrows.

diffuse scattering can be well explained by a model of occasional faults in the stacking sequence of honeycomb layers along the ***c***-axis. Such a model was first discussed for the related material Li_2MnO_3 [46]. In Fig. 5.5, A defines a nominal hexagonal lattice (made up of three triple-cell sublattices A_1-A_3), and B and C are also hexagonal lattices, positioned in the center of triangles of the A lattice. The atomic stacking is always in the ABC sequence to minimize the interlayer Coulomb energy, i.e. Ir-O-Na-O-Ir-O is A_1-B-C-A-B_1-C. Only Ir layers have a sublattice index, indicating the position of the Na at the honeycomb center, as the other atomic layers are full hexagonal lattices. However, if neighboring Ir layers are only weakly interacting (as they are separated by a hexagonal NaO_2 layer) then the second Ir layer could be shifted to another position on the B-lattice, say B_2 (thick arrows in Fig. 5.5c)) or B_3 (Fig. 5.5b)), with only minimal energy cost, as that would not affect the bonding with the fully hexagonal NaO_2 layers below and above.

5.4.3 Diffraction Simulation with Stacking Faults Model

In order to visualise the effect of containing stacking faults in the diffraction patterns, XRD diffraction planes were simulated numerically by direct structure-factor calculations using the DISCUS package [54] as shown in Fig. 5.6b). A “crystal”

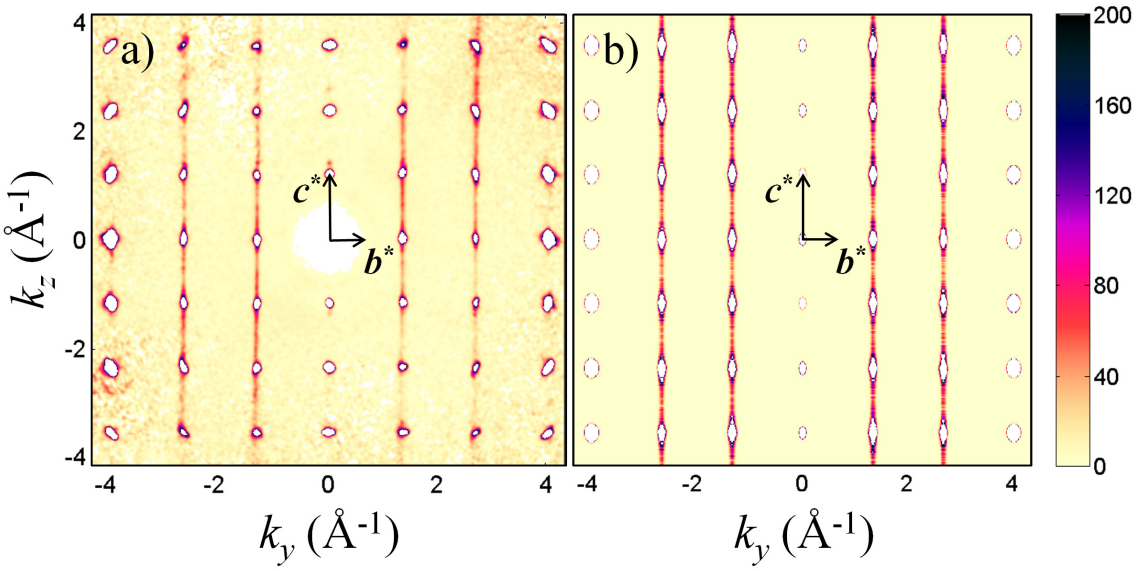


Figure 5.6: Simulations for Single Crystal X-ray Diffraction including Stacking Faults. a) X-ray diffraction intensity in the $(0, k, l)$ plane showing rods of diffuse scattering in between structural Bragg peaks along $\boldsymbol{c}^*$-axis with selection rule $h + k = 2n$ and $k = 3m+1$ or $3m+2$ (n, m integers) modelled in b) by frequent in-plane translational stacking faults of the type shown by the thick arrows in Figs. 5.5(b-c).

of $200a \times 200b \times 4000c$ unit cells of Na_2IrO_3 ($C2/m$) was built up for the simulation. To include the effect of stacking faults it was assumed that each Ir layer had a choice with probability $1-p$ to keep in-stacking-sequence with the layer below and $p/2$ to be shifted to either of the other two sublattice positions (translated in-plane by $(0, 1/3, 0)$ or $(1/2, 1/6, 0)$), (See Figs. 5.5(b-c)) with $p = 0$ for perfect stacking and $p = 1/3$ for a completely uncorrelated layer stacking sequence. The calculated scattering for such a microscopic model indeed reproduces well the selection rule for the occurrence of diffuse scattering in Figs. 5.6(a-b). In particular there is no diffuse scattering along $(00l)$, as this corresponds to adding all layers in phase irrespective of their in-plane translations. Also there is no diffuse scattering along $(0, 6n, l)$ (n integer), as again layers add in phase because the two allowed in-plane translations have a phase factor equal to a multiple of 2π.

In order to estimate the probability of stacking faults, we compared the integrated intensity of a Bragg peak with diffuse scattering in the experimental x-ray data.

Specifically, the strength of the diffuse scattering integrated between (020) and (021) relative to the intensity of the (020) peak (to have a similar absorption factor), was obtained experimentally as $\simeq 0.42$, for which it was estimated that the probability for stacking faults is $p \simeq 9\%$. This means that on average one fault occurs every $1/p \simeq 10$ layers. Over 30 crystals measured from a batch all showed diffuse scattering, suggesting that this is a common structural feature.

Therefore, by comparing the data with calculation in Fig. 5.6b), the diffuse scattering due to the stacking faults could be quantitatively understood in terms of a structural model that allows for the possibility of faults in the stacking sequence along the $\boldsymbol{c}$-axis.

5.4.4 X-ray Diffraction Calculation of the C$2/c$ and C$2/m$ Structures

The most direct way to distinguish different structures is to identify the relation between unit cells, thus recognising unique selection rule which only exists in one type of structure. Close examination reveals that the two unit cells are related by $\boldsymbol{a}' = -\boldsymbol{a}$, $\boldsymbol{b}' = -\boldsymbol{b}$, $\boldsymbol{c}' = \boldsymbol{a} + 2\boldsymbol{c}$, $c' = \sqrt{a^2 + 4c^2 + 4ac\cos\beta}$, $\sin\beta' = \frac{2c}{c'}\sin\beta$, and in terms of the reciprocal lattice components $h' = -h$, $k' = -k$, $l' = h + 2l$, where primed values refer to the C$2/c$ model. Starting from the larger unit cell (C$2/c$) and slightly displacing the atoms to some "ideal" positions one recovers the higher-symmetry structure described by the smaller unit cell C$2/m$. The distinction between these two models is entirely due to such small atomic displacements, the presence of which is manifested in finite intensity diffraction peaks at (h', k', l') positions with h' odd, k' odd and l' even, which disappear when atoms are displaced to the "ideal" positions and then the structure recovers the C$2/m$ symmetry. This is illustrated by the calculated diffraction pattern in the $(-3, k', l')$ plane where the "extra" peaks expected in the larger cell model C$2/c$ shown in Fig. 5.7c) are not seen in the data plotted in Fig. 5.7a), which is however fully consistent with the pattern expected for the higher-symmetry C$2/m$ model shown in Fig. 5.7b). This is also apparent in Fig. 5.7d) showing a scan along the $(-3, 1, l')$ line with extra peaks (triangles) predicted for $l' = 0, 2$, not seen in the

data (filled symbols). For completeness a shift of the fractional atomic coordinates in the C2/c unit cell is applied (in the notation adopted in [30]) by (-1/4,-3/4,0) before converting them into fractional atomic coordinates of the C2/m cell (in the notation used in Table. 5.1), due to the different origin positions of the two space groups. The calculated intensity of the expected supercell peaks in the lower-symmetry (C2/c) model is shown in Figs. 5.7(c-d) (filled red triangles, peaks at $l' = 0, 2$). The single-crystal x-ray data had more than enough sensitivity to see even much weaker intensity peaks, however the predicted supercell peaks were not detected, instead they were replaced by diffuse scattering along $\boldsymbol{c}^*$. Furthermore, effect of site-mixing was tested in the single-crystal x-ray diffraction calculation with the C2/c model [30], but the intensities of superlattice peaks are even stronger whereas the main peaks are weaker, which is in even stark contrast to the x-ray data in Fig. 5.7a), therefore ruling out this scenario.

To summarize, the diffraction planes were simulated and compared with the data, found that extra sharp peaks along $\boldsymbol{c}^*$ half-way between the main peaks were expected in the C2/c model (See Fig. 5.7c)), but they were not observed in the data. Instead of them, diffuse rods of scattering along $\boldsymbol{c}^*$ in Fig. 5.7a) from frequent faults in the stacking sequence of layers along $\boldsymbol{c}$ were seen in the data. This absence of the superlattice peaks in the real data supports the idea that the crystal structure has in fact higher-symmetry and the most relevant structural defects is faults in the stacking sequence along $\boldsymbol{c}$. Therefore, the more suitable structural model for Na_2IrO_3 is the C2/m model given in Table. 5.1.

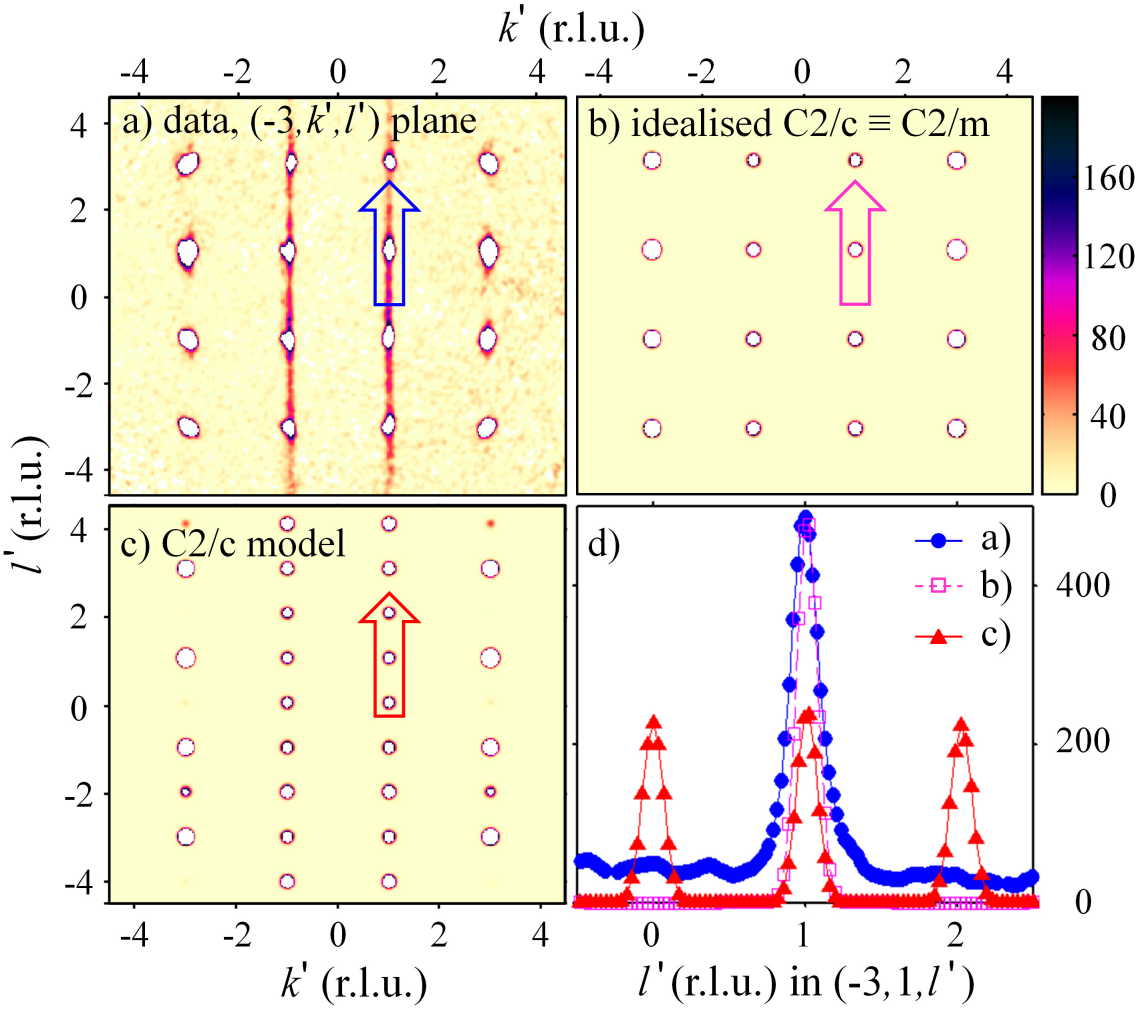


Figure 5.7: X-ray Diffraction Intensity in the $(-3, k', l')$ Plane: a) data, b) calculation for the "idealised" C2/c structure with atoms at special positions, equivalent to the C2/m model in Table. 5.1, c) calculation for the distorted C2/c model in Ref. [30] (assuming no Ir/Na site mixing in the honeycomb $Ir_{2/3}Na_{1/3}$ layers). Notice the series of sharp peaks predicted in c) at $(-3, 1$,even) positions, which however are not present in the data in a). d) Scan along the $(-3, 1, l')$ line (arrowed direction in a-c)) comparing data (solid circles) and calculation for the two models (triangles-C2/c and squares-C2/m). The calculated diffraction intensities have been multiplied by an overall scale factor and have been convolved with a finite width Gaussian in momentum space to visualise the effects of the instrumental resolution.

5.4.5 Structural Distortions in Na_2IrO_3 from Ideal Cubic Symmetry for IrO_6 Octahedra

The interest in explaining experimentally Na_2IrO_3 from a correlated electron physics point of view stem from the theoretical proposal that for ideal cubic IrO_6 octahedra in an edge-sharing connectivity, the dominant magnetic exchange could be strongly anisotropic, Ising-like with the easy axis normal to the Ir-O-Ir bond plane. In a honeycomb lattice, they would lead to reciprocally orthogonal spin directions being coupled along the three bonds emerging out of each site, which would be strongly frustrated and lead to exotic magnetic states, the Kitaev quantum spin liquid. The x-ray diffraction analysis in the previous section established that IrO_6 octahedra in Na_2IrO_3 are in fact not cubic but distorted, and the angle Ir-O-Ir departs significantly from the ideal 90°. The purpose of this Section is to construct various virtual crystal structural models for Na_2IrO_3 starting from the most symmetric with locally cubic symmetry and lowering symmetry in four steps to the "real" crystal structure. This is done such that *ab initio* calculation of the exchange interaction could be performed for the various structures to gain insight into what the most important distortions are and what structural features to look for to maximise the Kitaev interaction.

All structures discussed here are described in the same (C2/m) space group of the experimentally determined structure, and they differ only in slight displacements of the atoms and in lattice parameters. The main structural motif is the edge-sharing octahedra of NaO_6 and IrO_6 forming alternating hexagonal NaO_2 and honeycomb $Na_{1/3}Ir_{2/3}O_2$ layers stacked along the $\boldsymbol{c}$-axis. Based on this backbone, one can construct the most symmetric structure where all O_6 octahedra are regular (ideal, cubic) with all Ir-O and Na-O bonds of equal length, and angles of O-Ir-O and O-Na-O inside octahedra all 90°, and all Ir-O-Ir bond angles also 90°. One can choose to have the right Ir-Ir bond length (3.1325 Å) or the right Ir-O bond length (2.068 Å), which both are the averaged values in the actual crystal structure respectively, but not both simultaneously because the constraint for 90° Ir-O-Ir bonds is Ir-Ir = $\sqrt{2}\times$Ir-O, so they are inter-dependent. This ideal structure can also be described in relation to a

rhombohedral structural motif, so then by transforming to the C2/m setting one can understand how all coordinates acquire rational values, and the ideal values for the β angle and $\boldsymbol{c}$-axis lattice parameter can be derived analytically in a transparent way.

By choosing the right Ir-Ir bond length, the most idealised structure (the A1 model) is shown in Figs. 5.8(a-b)) (See also Table. 5.2 for the structural parameters). Here Ir-O distances are larger and Na-O distances smaller than in the actual structure and all octahedra are ideal and edge sharing with 90° Ir-O-Ir bonding. The A1 model might be too idealised to be realistic in Na_2IrO_3, but could be present in other honeycomb systems.

From A1 one can construct the A2 model by having the c-lattice parameters expand to the actual value 5.614 Å while keeping the honeycomb $Na_{1/3}Ir_{2/3}O_2$ layers unchanged (i.e. cubic IrO_6 with 90° Ir-O-Ir bonds and Ir-O bond lengths are unchanged as 2.215 Å) but their inter-layer spacing (Na2,3 layers) is adjusted to the right value such that Na2,3-O distances are increased to 2.274 Å, Na3-O-Na3 angles are changed to 87°. The model A2 is described in Figs. 5.8(c-d).

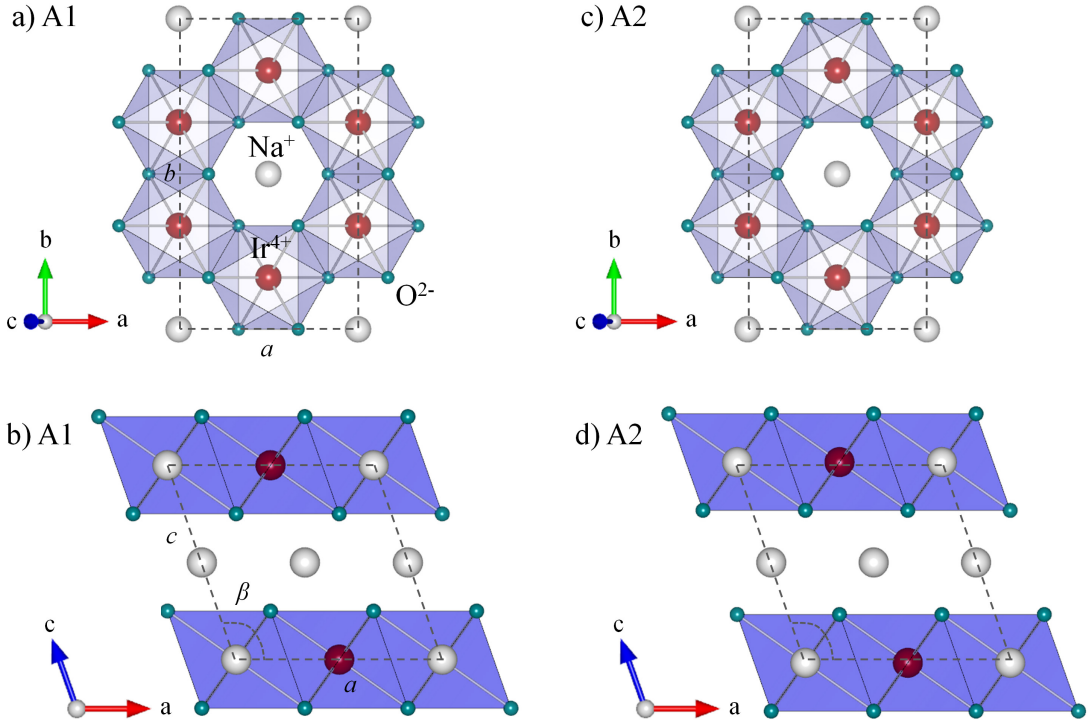


Figure 5.8: Idealised Crystal Structure of Na_2IrO_3: the A1 and A2 Models. (a-b) In the A1 model, the ideal edge-sharing octahedra are constructed by choosing the lattice parameter a to reproduce the Ir-Ir distance with all octahedra ideal and edge sharing with 90° Ir-O-Ir bonding. (c-d) The A2 model is obtained from the A1 model by stretching the $\boldsymbol{c}$-axis to the average value in the experimental structure.

Table 5.2: Structural Parameters of the A1 Model. The lattice parameters are $a = 5.42565$ Å, $b = 9.3975$ Å, $c = 5.42565$ Å, $\beta = 109.4712°$, $Z = 4$ (C2/m space group). All sites are fully occupied.

Atom	Site	x	y	z	Occ
Ir1	4g	0.5	0.16667	0	1
Na1	2a	0	0	0	1
Na2	2d	0.5	0	0.5	1
Na3	4h	0.5	0.33333	0.5	1
O1	8j	0.75	0.16667	0.75	1
O2	4i	0.75	0	0.25	1

Table 5.3: Structural Parameters of the A2 Model. The lattice parameters are $a = 5.42565$ Å, $b = 9.39750$ Å, $c = 5.61400$ Å, $\beta = 108.7930°$, $Z = 4$ (C2/m space group). All sites are fully occupied.

Atom	Site	x	y	z	Occ
Ir1	4g	0.5	0.16667	0	1
Na1	2a	0	0	0	1
Na2	2d	0.5	0	0.5	1
Na3	4h	0.5	0.33333	0.5	1
O1	8j	0.75313	0.16667	0.75938	1
O2	4i	0.74687	0	0.24062	1

To arrive at the A3 model (See Figs. 5.9(a-b) and Table. 5.4), one can squash the honeycomb layer to make the average Ir-O-Ir angles and Ir-O distances what they should be (and keep the *c*-parameter unchanged at the right value). In detail, the IrO_6 octahedra are trigonally squashed from the A2 model while preserving the local three-fold symmetry clearly seen in Fig. 5.9b), and the Ir-O bonds are shortened to the averaged experimental value (2.0681Å), and the Ir-O-Ir angles increased to a value close to the mean experimental value (98.45°). This leads to an increase in the height of NaO_6 octahedra with the increased Na2-O and Na3-O distances (2.45 Å) and Na3-O-Na3 angle being close to the actual value (79.4°). The A3 model is the most symmetric structure with distances and bond angles near the average of their experimental values, where all IrO_6 octahedra are squashed along their cubic $\langle 111 \rangle$ family axis, the local environment (i.e. the oxygen ions' positions) around each Ir (and Na) is symmetric following a three-fold rotation around the normal to the *ab*-plane, and all Ir-Ir bonds are equivalent (3.1325 Å). The effect of inserting the largest Na^+ ions between the honeycomb layers could be understood physically such that the hexagonal layer composed of the biggest Na_6 ions pushes the honeycomb layers, which could be responsible for the expansion of the *c*-lattice parameter from the A1 to A2 model and the squeezing of the honeycomb layers from the A2 to A3 model.

On the other hand, the A3 model has some shortcomings as the NaO_6 and IrO_6 octahedra in the honeycomb layers are the same size, obviously this is not realistic as the honeycomb and centre ions have different charges, Ir^{4+} and Na^+ and ionic radii (Na^+ bigger). This artificial constraint could be released by allowing the rotation of oxygen atoms for a symmetric expansion of the NaO_6 octahedron in the centre. In more detail, the A4 model (See Figs. 5.9(c-d) and Table. 5.5) is obtained from the A3 model by keeping the Ir-O distances unchanged and moving each of the oxygen ions away from the closest Na1 to increase the Na1-O distances. This is achieved by moving the oxygen ions on a circle (normal to the *ab*-plane) that is the intersection of two spheres of constant radius Ir-O centred at the adjacent Ir sites. This means that the top oxygen triangle lifts up a bit, becomes smaller and rotates, and the bottom triangle moves symmetrically opposite, i.e. moves away from the *ab*-plane, becomes slightly

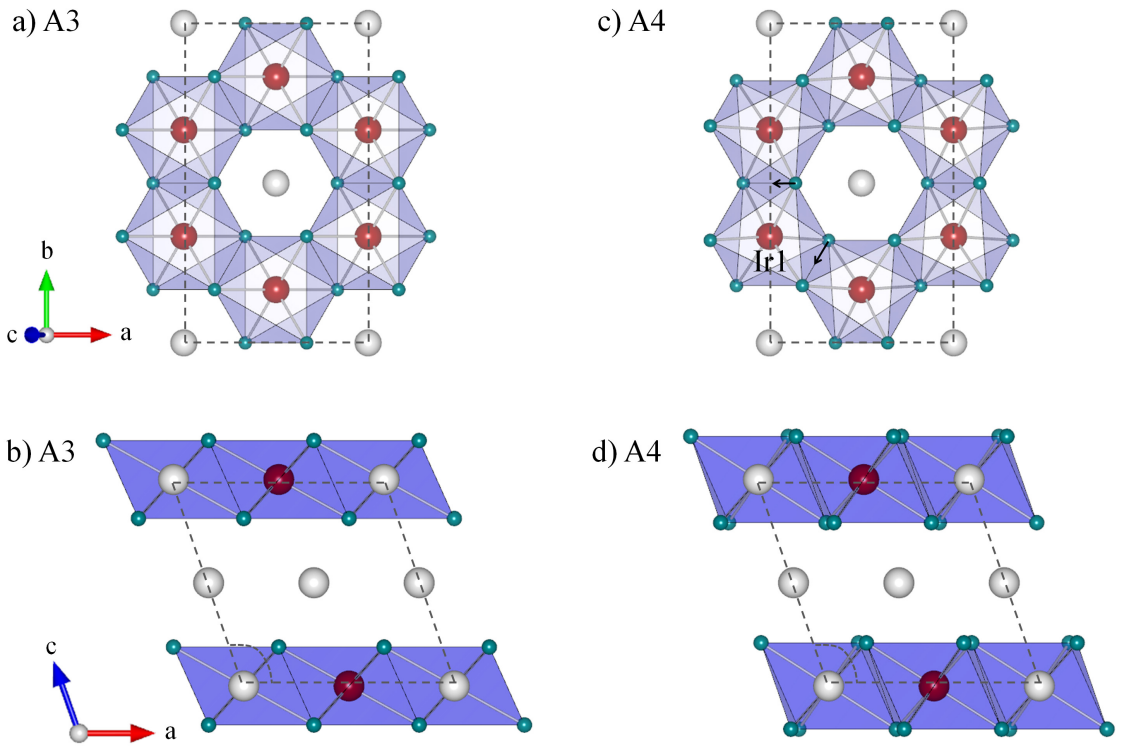


Figure 5.9: Idealised Crystal Structure of Na_2IrO_3: the A3 and A4 Models. The A3 model is obtained from the A2 model by trigonal squashing in IrO_6 octahedra, resulting in the expansion of Na-layers seen in b). In the a) *ab*-plane, Ir ions still have the local three-fold symmetry with shortened Ir-O distances and increased Ir-O-Ir bond angles. The A4 model is obtained from the A3 model by expanding the NaO_6 octahedra in the centre of the Ir honeycomb (See Fig 5.9c)). This leads to counter-rotation of the oxygen triangles for each IrO_6 octahedra, i.e., top O_3 triangle for Ir1 rotated counter-clockwise and bottom O_3 triangle rotate clockwise.

smaller and rotates in the opposite sense around the normal to the *ab*-plane. The process gives the A4 model, with alternating short and long O-O bonds upon going round an IrO_6 octahedron as shown in Figs. 5.9c). This phenomenon is reminiscent of the emergence of the oxygen displacement triggered by charge disproportionation between Ni ions in the triangular layer experimentally seen in $AgNiO_2$ [55, 56] (See Fig. 5.11).

Table 5.4: Structural Parameters of the A3 Model. The lattice parameters are $a = 5.42565$ Å, $b = 9.39750$ Å, $c = 5.61400$ Å, $\beta = 108.7930°$, $Z = 4$ (C2/m space group). All sites are fully occupied.

Atom	Site	x	y	z	Occ
Ir1	4g	0.5	0.16667	0	1
Na1	2a	0	0	0	1
Na2	2d	0.5	0	0.5	1
Na3	4h	0.5	0.33333	0.5	1
O1	8j	0.77042	0.16667	0.81125	1
O2	4i	0.72958	0	0.18875	1

Table 5.5: Structural Parameters of the A4 Model. The lattice parameters are $a = 5.42565$ Å, $b = 9.39750$ Å, $c = 5.61400$ Å, $\beta = 108.7930°$, $Z = 4$ (C2/m space group). All sites are fully occupied.

Atom	Site	x	y	z	Occ
Ir1	4g	0.5	0.16667	0	1
Na1	2a	0	0	0	1
Na2	2d	0.5	0	0.5	1
Na3	4h	0.5	0.33333	0.5	1
O1	8j	0.75119	0.17917	0.79107	1
O2	4i	0.71131	0	0.20893	1

From here slight displacements of the oxygen ions and marginal changes in the a, b-lattice parameters, β-angle and y-coordination of Ir, Na3, O1 ions take us to the structure determined experimentally, the A5 model (See Figs. 5.10(a-b) and Table. 5.6). The A6 and A7 models were found using the VASP code. The A6 model relaxes atomic positions only by keeping lattice parameters fixed at experimental values, while the A7 model relaxes also the lattice parameters with the result that the rotation of O_3 triangles is more significant in the A6 model (and even more so in the A7 model) than in the A5 model. Since the detailed structural information of the A6 and A7 models are similar, here only the A7 model (See Figs. 5.10(c-d) and Table. 5.7) is compared with the A5 model in Fig. 5.10.

It is interesting to point out that the structural model for Na_2IrO_3 proposed by the Oak Ridge group [57] predicted a more symmetric structure which did not have a sizeable relative rotation of the top and bottom O_3 triangles, however it seemed that this was not a real effect since this more symmetric pattern was not reproduced in *ab initio* calculations in the A7 model. It is possible that the Oak Ridge structure becomes more symmetric due to the significant site-mixing of Ir^{4+} and Na^{+}, which reduces the contrast of octahedra inside the honeycomb planes.

This series of idealised structures could be further used for *ab initio* calculations to identify the nature of the exchange couplings concerning the magnetic excitation observed in the experiment. For instance, the A1 and A2 models are good structures to test if the Ir-Ir exchange interactions are of the form AFM Heisenberg + FM Kitaev [4, 3] or FM Heisenberg + AFM Kitaev [45] or a bond dependent off-diagonal exchange [58]. In this case, with the A1 and A2 models, the Heisenberg part will be calculated quantitatively at the correct Ir-Ir distance but the Kitaev strength will be computed for a slightly larger Ir-O bond length than that in the actual structure. Contrasting the A1 and A2 models also tells us whether the crystal environment away from the honeycomb layer is important for the exchanges or not. The A3 model is the simplest structure that contains the two main departures from the idealised model in Ref. [4, 3], namely trigonal squashing of the IrO_6 octahedra and Ir-O-Ir bond angles different from 90°, so it would be useful to contrast the A2 and A3 models to see

what effects those departures have on the exchange couplings. The A4 model would test the effects of rotation of the oxygen triangles below and above the honeycomb plane. Since up to the A4 model all Ir-Ir bonds are equivalent, the A5 model would test final effects of the minor distortions such as a tiny monoclinic distortion in the honeycomb lattice (b-lattice parameter), the remaining small displacements of ions and the angle β.

Based on this underlying idea, the group of Jeroen van den Brink in IFW Dresden, Germany have performed *ab initio* quantum chemistry calculations [59] on the A2 (using the experimental c-lattice parameter), A5 models, finding out that the nearest-neighbor exchange is highly anisotropic with a dominant ferromagnetic Kitaev part, whereas the Heisenberg contribution is significantly weaker and antiferromagnetic. The calculations further reveal that the exchange interactions show a very strong sensitivity to structural distortions such as the trigonal distortion from the A2 to A3 model.

To summarize, the distortions implied by the experimentally observed structure have been studied in detail by considering different levels of idealised crystal structures. The actual structure was also compared with the relaxed structures from *ab initio* simulation as well as the idealised structures. This shows that the major distortion in the real structure is the trigonal squashing of the IrO_6 octahedra along the cubic $\langle 111 \rangle$ direction with smaller honeycomb and monoclinic distortions. This trigonal squashing of the honeycomb layer and the departure from the ideal length of c-lattice parameter is due to the hexagonal layer of the largest Na^+ ions. The asymmetry of octahedra in the Ir honeycomb layers could be understood due to the charge inequality of Ir^{4+} and Na^+ in that plane, which is confirmed by *ab* initio calculations.

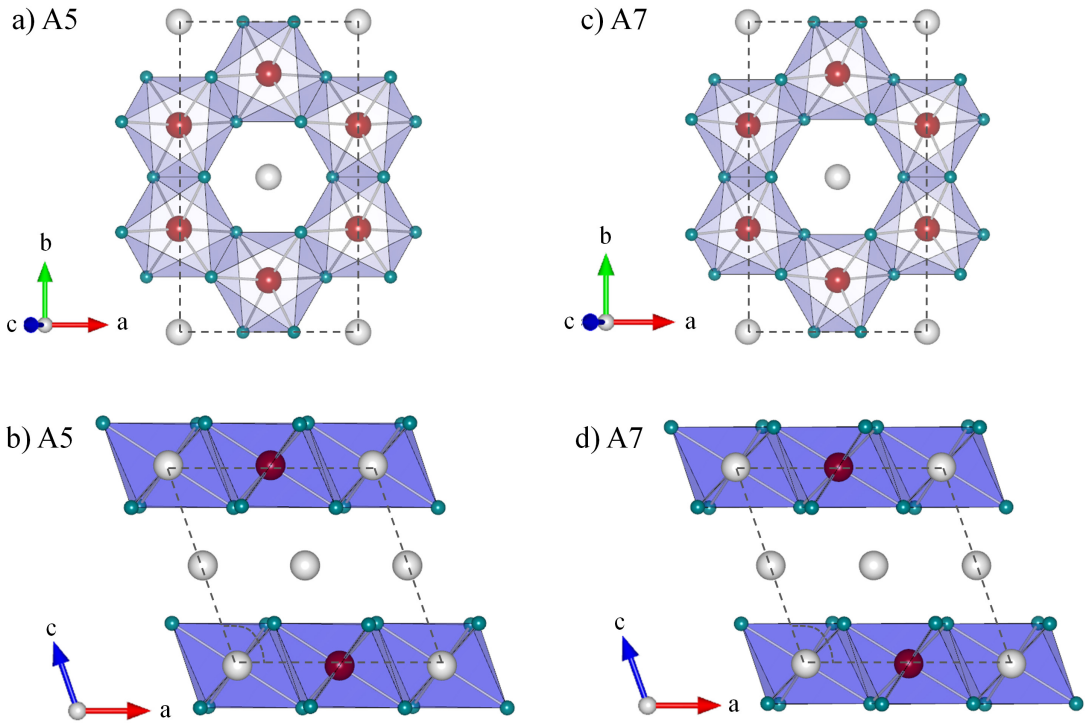


Figure 5.10: Observed Crystal Structure of the A5 Model and Fully-Relaxed Structure of the A7 Model. The experimentally determined structure is shown in a) *ab*-plane and b) *ac*-plane with only minor displacement of the oxygen ions from positions in the A4 model, the β angle increases, b becomes slightly different from the ideal value of $\sqrt{3}a$, and thus Ir-Ir distances split into two types of non-equivalent bonds. For comparison, the fully-relaxed structure with released atomic positions and lattice parameters is shown in c) *ab*-plane and d) *ac*-plane. The asymmetry of octahedra in the honeycomb plane observed experimentally in a) is well-reproduced in the calculation in c). Note that the relaxed lattice parameters as well as atomic positions are very similar to those observed in the experiment.

Table 5.6: Structural Parameters of the A5 Model. The lattice parameters are $a = 5.42565$ Å, $b = 9.395$ Å, $c = 5.61400$ Å, $\beta = 109.0370°$, $Z = 4$ (C2/m space group). All sites are fully occupied.

Atom	Site	x	y	z	Occ
Ir1	4g	0.5	0.167	0	1
Na1	2a	0	0	0	1
Na2	2d	0.5	0	0.5	1
Na3	4h	0.5	0.340	0.5	1
O1	8j	0.74800	0.17800	0.78900	1
O2	4i	0.71100	0	0.20400	1

Table 5.7: Structural Parameters of the A7 Model. The lattice parameters are $a = 5.55602$ Å, $b = 9.59269$ Å, $c = 5.63500$ Å, $\beta = 109.6360°$, $Z = 4$ (C2/m space group). All sites are fully occupied.

Atom	Site	x	y	z	Occ
Ir1	4g	0.5	0.16691	0	1
Na1	2a	0	0	0	1
Na2	2d	0.5	0	0.5	1
Na3	4h	0.5	0.33972	0.5	1
O1	8j	0.74504	0.18580	0.79684	1
O2	4i	0.70072	0	0.20642	1

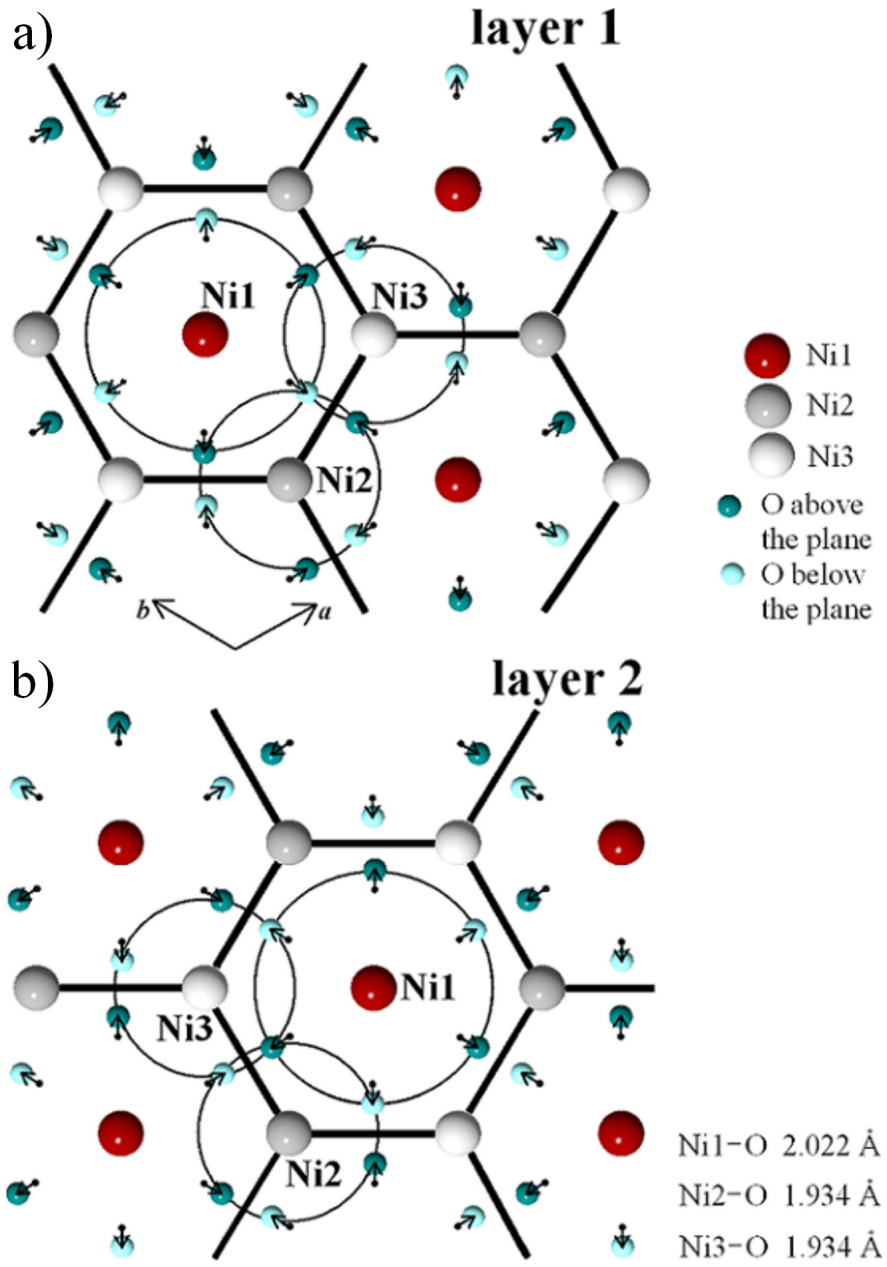


Figure 5.11: Schematic Diagram of Charge Order in $AgNiO_2$ [56]. a) Schematic diagram of the NiO_2 layer at $z = \frac{1}{4}$ showing how the displacements (small arrows) of the oxygen ions (small balls) lead to a periodic arrangement of expanded (large circle, Ni1) and contracted (small circles, Ni2, 3) NiO_6 octahedra. Thick hexagonal contour shows the honeycomb network of contracted sites. The origin of the coordinate system is at the circled Ni2 site. b) The expanded site Ni1 has a staggered zigzag arrangement between even and odd layers stacked along the $\boldsymbol{c}$-axis.

5.5 Conclusions

This chapter described a revised crystal structure of the honeycomb iridate material Na_2IrO_3 using single crystal x-ray diffraction complemented by band-structure calculations and diffraction simulations, which found a different crystal structure model (C2/m) compared to the previously published structural model (C2/c) [30]. Single crystal x-ray diffraction patterns collected from high-quality sample showed that superlattice peaks predicted in C2/c space group were not detected.

Also, a periodic pattern of diffuse rods of scattering along $\boldsymbol{c}^*$ was observed, which could be quantitatively accounted for by a model of structural stacking faults. Analysing separately the sharp Bragg peaks from the diffuse scattering enabled a robust determination of the crystal structure. It was found that the structure is better described by a more symmetric unit cell with space group C2/m, which has more isotropic honeycomb network and more symmetric IrO_6 octahedra. This refined structure quantified substantial departures from the ideal 90° Ir-O-Ir bonds required for dominant Kitaev interactions as IrO_6 octahedra were squeezed along the $\langle 111 \rangle$ cubic direction parallel to the $\boldsymbol{c}^*$-axis in the unit cell.

To better understand the departure from the ideal structure, four idealised crystal structures were constructed and compared with the experimental model, and with the fully-relaxed structure obtained from *ab initio* calculation with unconstrained atomic positions and lattice parameters. The squashing of the honeycomb layers could possibly be due to the interlayer of hexagonal Na ions which have a larger ionic radius. The asymmetry of octahedra in the honeycomb lattice could also be understood due to the charge inequality of Ir^{4+} and Na^{+} inside the honeycomb plane. These key features of the actual structure are well-reproduced in the relaxed crystal structure. All those distortions are important departures from the ideal scenario for which dominant Kitaev interactions were predicted.

Chapter 6

Magnetism of Honeycomb Antiferromagnet Li_2IrO_3

This chapter outlines the magnetic properties of the ground and excited states of the layered honeycomb antiferromagnetic Li_2IrO_3, which was theoretically proposed to have more significant Kitaev interactions. Susceptibility measurements revealed an antiferromagnetic long-range order below 15 K, confirmed by zero-field muon-spin rotation measurements. Neutron diffraction identified the magnetic order below 15 K, finding out a magnetic Bragg peak at 0.41 $Å^{-1}$, which indicates a much larger magnetic unit cell compared to Na_2IrO_3. Inelastic neutron scattering measurements on a powder sample was successfully performed with an optimized setup, revealing qualitatively distinct magnetic excitation features compared to Na_2IrO_3. A sharply dispersing signal was observed to emerge from the scattering wavevector of the elastic magnetic Bragg peak, and extend up to at least 12 meV with a particularly stronger intensity at about 2.5 meV. The whole spectrum broadened and features disappeared at 150 K, supporting their magnetic origin. Pulsed-field magnetization experiments found an anomaly indicating a transition in a magnetic field of about 25 T, which could match the 2.5 meV magnetic excitation gap. Furthermore, linear spin-wave theory was used to try to reproduce the observed magnetic excitation spectrum based on a spiral model in the Heisenberg J_1-J_2-J_3 model. The measured magnetic excitations cannot be completely captured using an isotropic Heisenberg interactions, but significant anisotropic exchange needs to be incorporated to get closes to the data. In order to explore a

possible spin gap concerning the magnetic anisotropy, the low energy excitations have been measured with higher-resolution inelastic neutron scattering experiments, which did not find any clear spin gap (down to at least 0.7 meV).

6.1 Introduction

In this Chapter, a comprehensive study of the magnetic order and excitations of Li_2IrO_3 is presented. Like Na_2IrO_3, Li_2IrO_3 is a layered honeycomb system, where novel ground states are proposed to be stabilized by frustrated interactions. Strong spin-orbit coupling at the Ir^{4+} ion has been predicted to stabilize composite spin-orbital moments, and this combined with the honeycomb lattice geometry could potentially lead to strongly-frustrated interactions that could stabilize exotic ground states, very different from the conventional two-sublattice Néel order, including collinear stripe order and a so-called Kitaev quantum spin liquid with spinon excitations, none of which have been realized experimentally before.

Li_2IrO_3 has been proposed to have more ideal IrO_6 octahedra than Na_2IrO_3, which could be more favourable for the presence of Kitaev interactions, and is a candidate for more exotic ground states than Na_2IrO_3.

Resonant Inelastic X-ray Scattering (RIXS) study [2] on both compounds Na_2IrO_3 and Li_2IrO_3 showed that the crystal field splitting due to non-cubic crystal fields, manifested in a splitting of the J_{eff}=3/2 quadruplet, is much smaller than the spin-orbit energy scale in iridates, suggesting that the ground state could be described by a J_{eff}=1/2, with experimental observations supported by quantum chemical and density functional theory calculations [2]. Those studies proposed that Li_2IrO_3 was potentially closer in parameter space to a situation where crystal field effects are weaker and spin-orbit coupling effects stronger than Na_2IrO_3, possibly closer to the Kitaev limit in the exchange parameter space, with potentially a different ground state from the zigzag phase in Na_2IrO_3.

The energy transfer measured in RIXS was about a few eV to observe the d-d transitions from occupied t_{2g} states into the empty e_g and t_{2g} levels. However, RIXS

did not have enough resolution to detect the low-energy magnetic excitations originating from the magnetic ground state. Also magnetic susceptibility measurements probe the bulk properties. In contrast, neutron scattering is a suitable experimental probe to measure the spin dynamics at low energy transfer over a wide range of momentum space, including the zero energy transfer (elastic line) with good energy resolution.

This Chapter presents neutron scattering measurements of the magnetic excitations of powder Li_2IrO_3 samples together with results from the bulk magnetic susceptibility, muon spin rotation and powder neutron diffraction measurements, which give further insight in the magnetic behaviour of this system and the balance between the different competing exchange interactions, and their outcome for the magnetic ordering wavevector and excitations.

The rest of this chapter is organised as follows. Section 6.2 presents the thermodynamic measurements: SQUID (Sec. 6.2.1) and muon spin rotation (Sec. 6.2.2). Powder neutron diffraction experiments are discussed and candidate magnetic orders are suggested in Sec. 6.3, followed by reports of powder inelastic neutron scattering results of the magnetic excitations in Sec. 6.4. Section 6.5 gives an introduction to linear spin-wave theory in a candidate spiral structure, which is then applied to calculate the dispersion relations for two spiral phases in the Heisenberg J_1-J_2-J_3 model, modified to allow for in-plane anisotropy exchange. The experimental data and calculations are discussed along with suggestion for future works in Sec. 6.6, followed by the conclusions summarized in Sec. 6.7.

6.2 Thermodynamic Properties

Single crystals of Li_2IrO_3 are not currently available due to the technical challenges in the growth process. Thus all measurements in this chapter have been performed on a high-quality single phase powder sample.

The powder sample used in the SQUID measurements comes from the same batch used for the muon-spin rotation, high-field magnetization and powder inelastic neu-

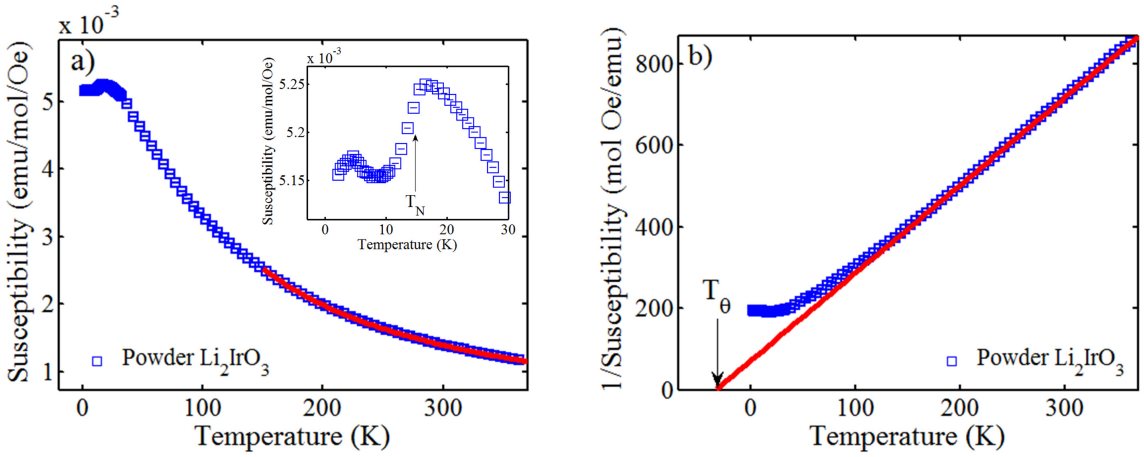


Figure 6.1: Susceptibility of Powder Li_2IrO_3. a) Zero-field cooled magnetic susceptibility probed by SQUID as a function of temperature. The red line is fitted curve with the Curie-Weiss form in Eq. (4.1). The inset indicates the AFM-like magnetic anomaly around 15 K. b) Inverse susceptibility with a fitted linear dependence (red solid line) in the range 150 K to 370 K.

tron scattering experiments. A similar quality powder sample was also tested with SQUID, and was used for the neutron diffraction experiments.

6.2.1 Susceptibility

Bulk susceptibility experiments on high-purity powder crystalline Li_2IrO_3 samples grown by the Philipp Gegenwart group in Georg-August-Universität in Göttingen, Germany, were performed using a Quantum Design Superconducting Quantum Interference Device (SQUID) magnetometer in the Clarendon Laboratory. 56.5 mg of power sample was placed inside a weak diamagnetic plastic capsule, and the measurement was performed in a 1000 Oe external magnetic field.

Susceptibility data of polycrystalline Li_2IrO_3 is illustrated in Fig. 6.1. In Fig. 6.1a), the susceptibility reveals a typical Curie-Weiss behaviour at high temperatures with an increase in the magnetization when the temperature cools. There is a sharp decrease at about 15 K, indicative of an antiferromagnetic transition, further confirmed by μ^+SR experiments in Sec. 6.2.2. Fig. 6.1b) shows inverse susceptibility with the fitted straight line (red colour), which intersects the temperature axis at a Curie-

Weiss temperature (T_θ) at about -33.77 K, comparable to the reported value of -33 K in the literature [31]. Curie-Weiss constant (C) in the fit is 0.465 emu K/mol that is also compatible with the referential value 0.42 emu K/mol [31]. Based on Eq. (4.1) and Eq. (4.2), Curie-Weiss constant (C) and T_θ can be obtained from the fitted high-temperature susceptibility, which are used for obtaining the effective magnetic moment and the strength of magnetic interactions respectively. The effective magnetic moment obtained with a fit is $\mu_{eff} = 1.93\ \mu_B$, which is close to 1.73 μ_B in the $J_{eff} = 1/2$ picture (assuming $g = 2$).

It is interesting to note that SQUID data showed another weak anomaly near 4.7 K with a small hump in susceptibility data (See inset in Fig. 6.1a)), which was also weakly observed in earlier heat capacity data [31]. From this data alone, it is unclear if this might indicate the change of the magnetic structure, so this will be further discussed with μSR results in Section 6.2.2.

6.2.2 Muon Spin Rotation

Zero-field muon-spin rotation (ZF μ^+SR) measurements [60] were made on a polycrystalline sample using the GPS instrument at the Swiss Muon Source (SμS), Paul Scherrer Institut, Villigen, Switzerland by the group of Tom Lancaster and Stephen Blundell in Oxford, and their results are included here for reference. In a μ^+SR experiment [60] spin polarized muons are implanted into the sample. The quantity of interest is the asymmetry A(t), which is proportional to the spin polarization of the muon ensemble. The raw data of ZF μ^+SR spectra are shown in Fig. 6.2. Below $T_N = 15$ K, a heavily damped oscillation in the muon asymmetry with a single frequency ν was found out, characteristic of long range magnetic order throughout the bulk of the material. As the temperature is increased a relaxing component is seen to grow in amplitude at the expense of the oscillating component. The measured data could be fitted for all $T < 15$ K with the function

$$A(t) = A_0 + A_1 e^{-\lambda_1 t} \cos(2\pi\nu_1 t + \phi_1) + A_2 e^{-\Lambda t} \tag{6.1}$$

The amplitude A_0 is a non-relaxing component accounting for a small fraction of muons that stop in the sample mount along with those muons whose spin components lie along the direction of the quasistatic local magnetic field. A nonzero phase $\phi = -\pi/4$ was found to best fit the data. It is notable that this value is often indicative of an incommensurate component in the magnetic ordering [61]. For the fits to total relaxing amplitude was fixed at 26.6 % and the relaxation rate of the oscillations was found to take a constant value of $\lambda = 7.0$ MHz.

The evolution of the parameters in Eq. (6.1) are shown in Fig. 6.1. The frequency of the oscillations is shown in Fig. 6.3a) and is well described by the phenomenological function

$$\nu_i(T) = \nu_i(0)\,[1 - (T/T_{\mathrm{N}})^{\alpha_i}]^{\beta_i}\,, \tag{6.2}$$

with $\nu(0) = 2.39(2)$ MHz, $\alpha = 2.5$, $\beta = 0.35(2)$ and $T_N = 15$ K. The amplitude of the components that reflect long range magnetic order A_0 and A_1 are generally seen to decrease across the temperature range (Fig. 6.3b)) with the purely relaxing component A_2 increasing in their place, which is indicative of disordered regions increasing in volume within the sample with increasing temperature.

In conclusion, the picture from the muon measurements is of long-range magnetic order at the lowest temperatures throughout the sample. Above $T \approx 4.7$ K regions of dynamically fluctuating magnetic disorder appear and grow in volume continuously with temperature. The remaining long-range magnetic order vanishes above the phase transition at $T_N = 15$ K.

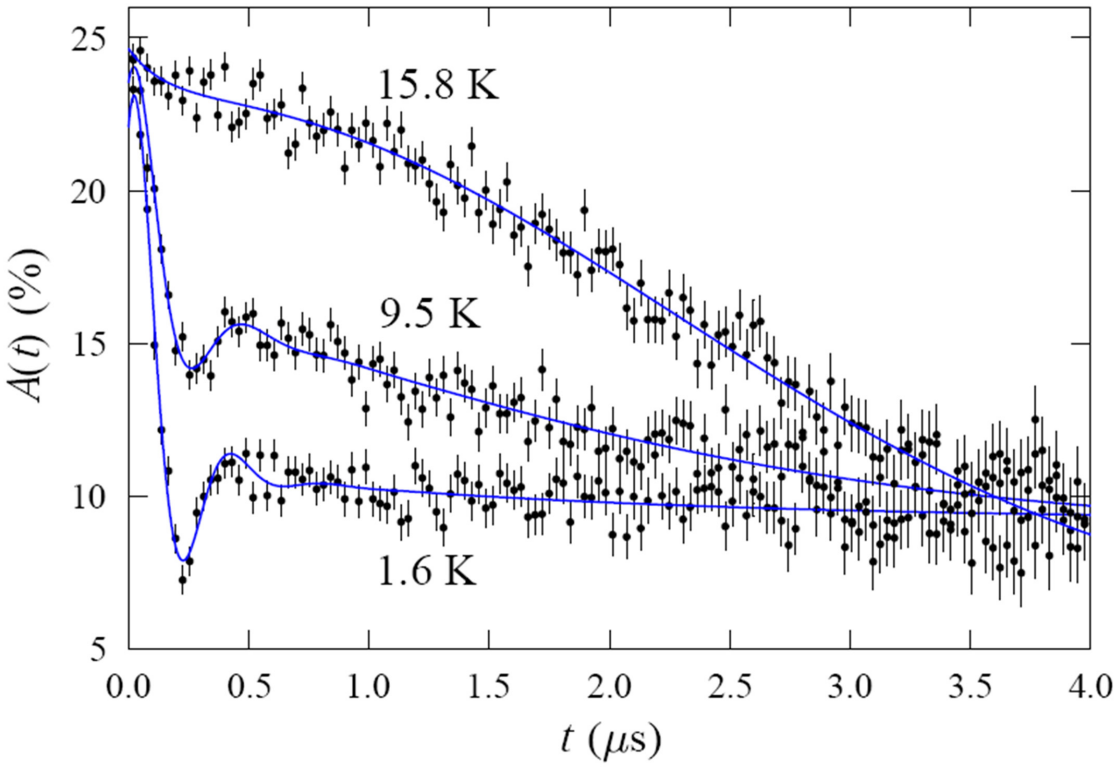


Figure 6.2: Muon Spin Rotation Results on Powder Li_2IrO_3. Zero-field μ^+SR spectra measured at several temperatures.

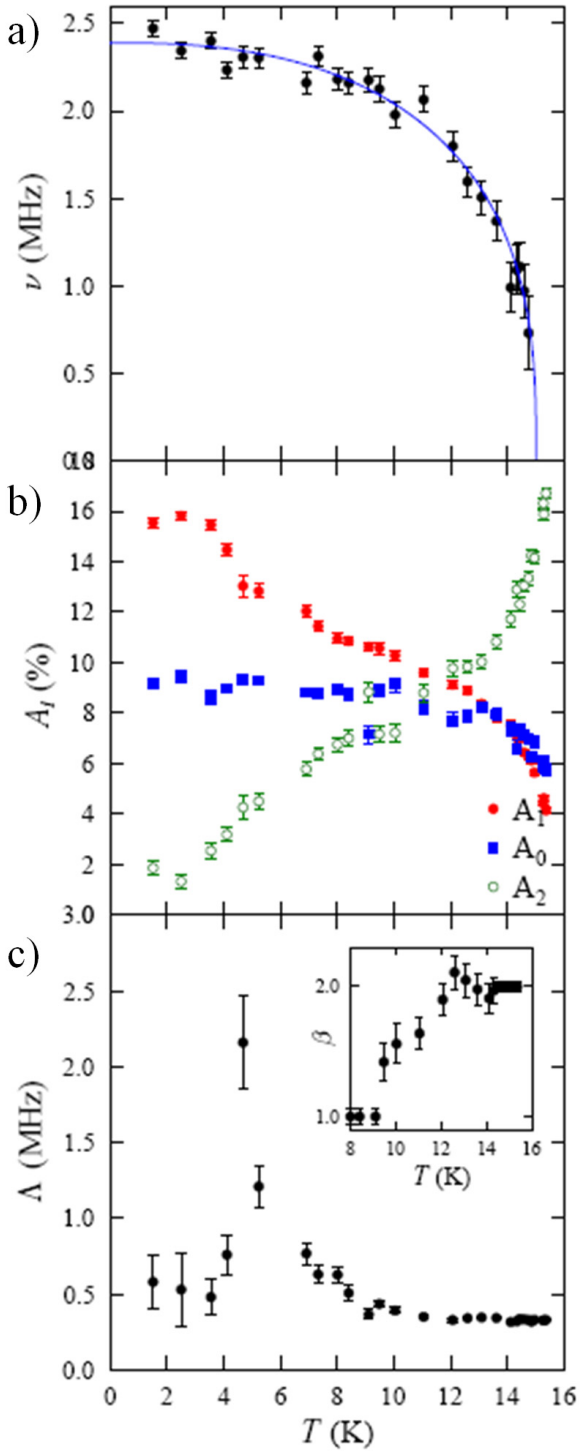


Figure 6.3: Temperature Evolution of the Parameters from μ^+SR Spectra of Li_2IrO_3. Temperature evolution of the parameters were extracted from fits to the μSR data. a) The precession frequency ν. b) The amplitudes A_0, A_1 and A_2. c) The relaxation rate Λ and (inset) the stretching factor β.

6.3 Powder Neutron Diffraction

6.3.1 Experimental Details

Neutron diffraction experiments on iridates are challenging due to the huge neutron absorption by iridium nuclei. The sample is also air-sensitive, so that when the sample is exposed to air, it absorbs moisture and the sample degrades [62]. This results in a large elastic background from the hydrogen ions in the neutron scattering experiments. Therefore a careful handling and treatment during the sample preparation was pursued with the optimized experimental setup. In order to minimize the exposure time of the sample in the air, it was delivered to the experimental beamline by placing it inside a sealed quartz ampule with an inert gas (Ar) to further prevent any unwanted chemical reaction. The sample for the neutron diffraction measurement was mounted inside a glove box with Helium gas; it was put in an aluminium sachet in a sample-can suitable for neutron measurements. It was then transferred into a furnace to be annealed at $\sim$110°C with a pump on, measuring a vacuum down to 10^{-5} bar for over 48 hours to remove any possible moisture remaining in the powder sample just before the experiments. This played an important role in reducing the incoherent scattering background from the hydrogen, which leads to an improvement on the signal to noise ratio of the magnetic Bragg peak. This method has proved to be effective working with Na_2IrO_3 to remove the absorbed moisture. To further reduce the background in the region of low Q, where the first and second magnetic Bragg peaks are expected, a Closed Cycle Refrigerator (CCR) was used to gain the advantage of the lower background from the thinner shielding compared to the orange Helium cryostat. The total mass was about 1.21 g, and the dimension of a cylindrical sample vanadium can was 4 cm high and 1.08 cm wide (diameter).

Neutron diffraction measurements were carried out using the high-resolution powder diffraction instrument WISH in ISIS, UK. The data have been collected for 10 and 8 hours in Fig. 6.5a) at 5.8 K (the base temperature of CCR) and 30 K respectively, at an average proton current of 40 μAmps.

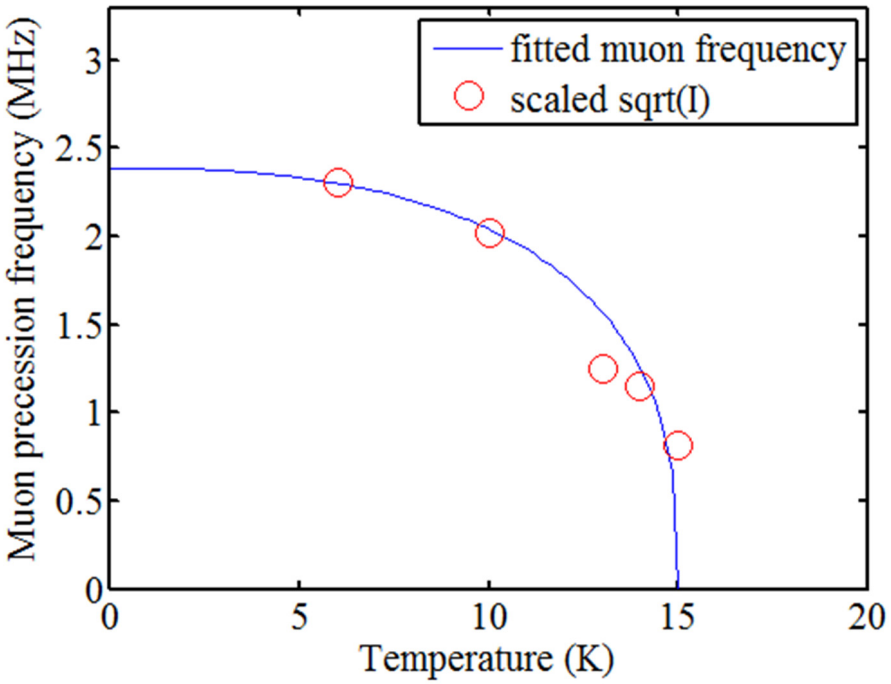


Figure 6.4: Comparison of Fitted Muon Frequency and Order Parameter from WISH. The overlap of the fitted muon frequency in a) and the order parameter extracted from neutron diffraction data in b) is good. Scaling of I values was done with respect to that at T= 6 K. I is the integrated area of the first magnetic Bragg peak.

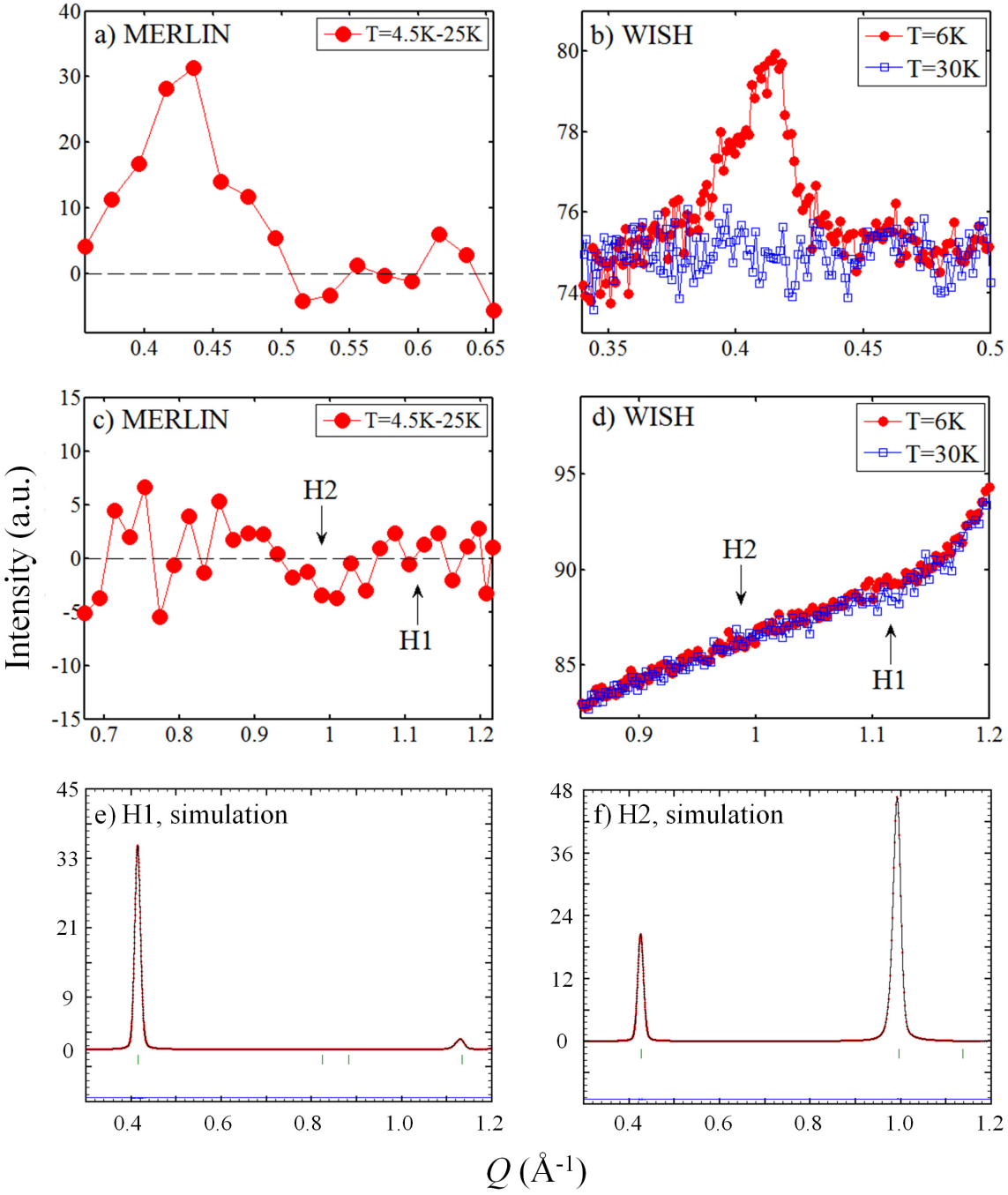


Figure 6.5: Elastic Neutron Signal on Li_2IrO_3. Elastic line data from MERLIN are given in a) and c) to show an additional contribution at low temperatures. WISH diffraction data in b) observes the identical magnetic Bragg peak. The marked arrows in c) and d) indicate the expected wavevector positions of the second magnetic Bragg peak in the H1 and H2 phases based on the simulations shown in e) and f). Note that $Q = (0.32, 0, 0)$ is used in e) for a more accurate comparison with the data.

6.3.2 Measurements and Results

A clear first magnetic Bragg peak at very low $Q \sim 0.41$ Å^{-1} (See Fig. 6.5a)) was seen at base temperature of 6 K, and then the peak disappeared above 15 K, in agreement with the presence of an anomaly around this temperature in heat capacity [31] and susceptibility measurements (See Fig. 6.1 and [31] and μSR measurements). The diffraction data was from the bank 1 of detectors in the range of around 0.23 to 6.55 Å^{-1} which allowed access to very low scattering vectors Q ($Q = |\boldsymbol{Q}|$).

Figure 6.4 shows the comparison between the fitted muon frequency to a scaled square root of the integrated area of the first magnetic Bragg peak. The Bragg peak intensity measured with neutrons is the square of the ordered magnetic moment as noted in Eq. (3.42). In Fig. 6.4, the red circle marks were extracted from WISH data by doing the square root of the intensity of the first magnetic Bragg peak in a gaussian fitting, which were further normalized by the muon frequency at T= 6 K. As expected, the data appears to agree very well with the muon frequency fitting results, which is proportional to the order parameter. Thus, the neutron diffraction data showed clearly an order parameter of the long-range magnetic order.

More magnetic Bragg peaks were attempted to be detected, but no clear evidence for new peaks could be detected even after counting a long time (10 hours) as seen in Fig. 6.5d). In Fig. 6.5d), the relevant Q range for the expected wavevector of the second magnetic Bragg peak in two spiral (helical) phases H1 and H2 (to be discussed later) are indicated with marked arrows. With experimental accuracy, no signal is detected at the H2 position and probably there may be a very weak signal at the H1 position. The absence of a sufficiently strong second magnetic Bragg peak could possibly be because the magnetic signal was simply too low to be detected.

Additional evidence that the signal near $Q \sim 0.41$ Å^{-1} is a magnetic Bragg peak comes from powder inelastic neutron scattering experiments performed at MERLIN, ISIS (See Sec. 6.4), which found a magnetic Bragg peak on the same positions in $|\boldsymbol{Q}|$ on the elastic line, very close to the wavevector where the magnetic excitations softened as shown in Fig. 6.5a). The MERLIN experiment could also not detect a second magnetic Bragg peak as shown in Fig. 6.5c).

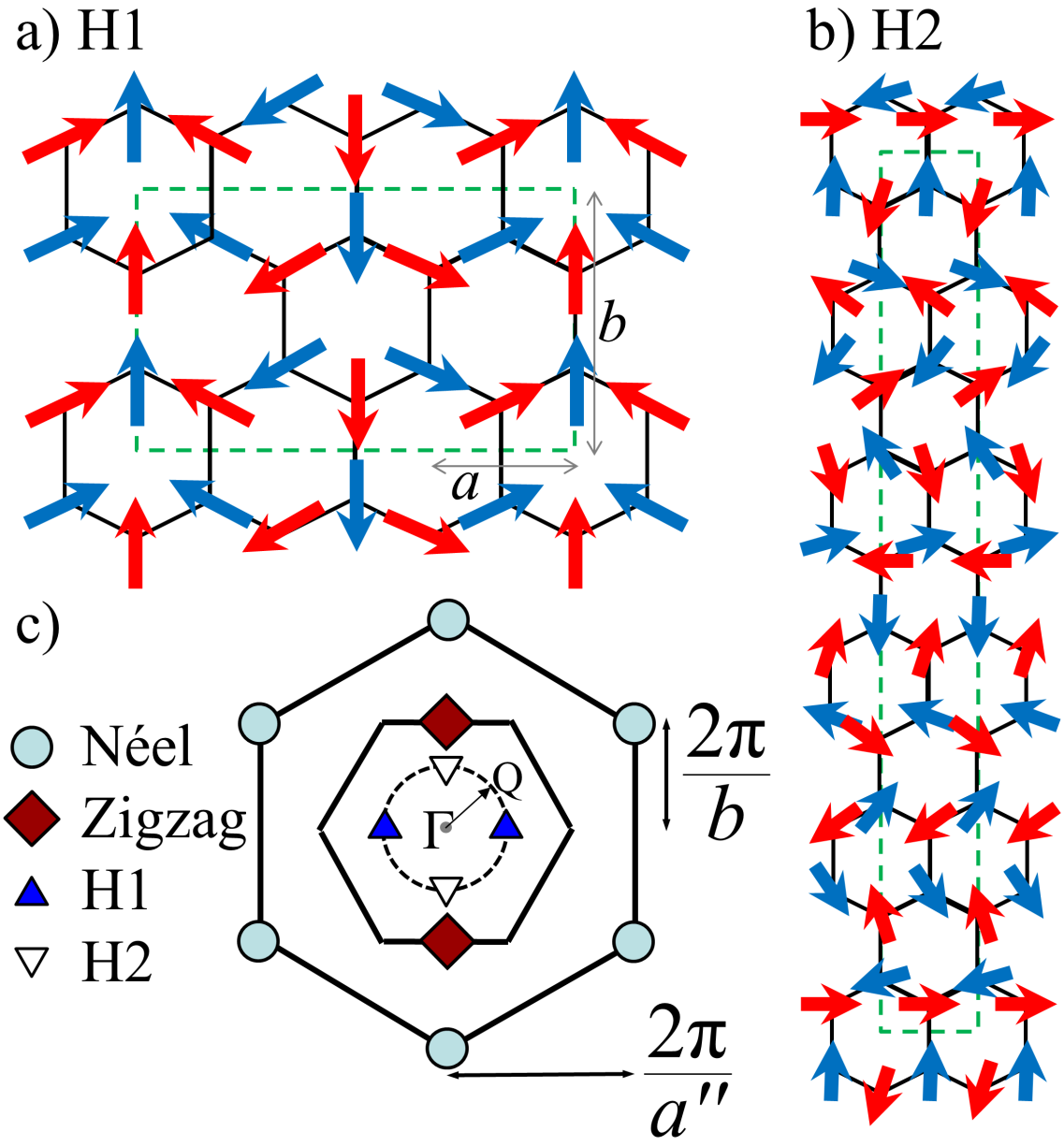


Figure 6.6: Schematic Diagram of Two Candidate Spiral Orders for Li_2IrO_3. a) H1 and b) H2 order (for the same exchange parameters as the spin-wave spectrum in Fig. 6.14 and Fig. 6.18 with exchange anisotropy) Dashed rectangular box of size $3a \times b$ and $a \times 5b$ show the closet commensurate magnetic unit cells. Red and blue arrows show the spins of the A and B sublattices of the honeycomb lattice. c) Reciprocal space diagram showing locations of magnetic Bragg peaks for various magnetic phases with the inner hexagon showing the first Brillouin zone of the honeycomb lattice. For the purpose of illustration, the spiral plane is projected in the ab-plane, in fact the spiral spins rotating in the ac-plane. In general, any positions with the same magnitude of Q, described by a dotted circle in reciprocal space, satisfy an experimentally observed magnetic Bragg peak. Note that $a''= a \sin \beta$.

The magnitude of the observed elastic peak at $Q \sim 0.41$ Å^{-1}, is surprising since this wave-vector is very different from expectations based on theoretical studies of the Kitaev-Heisenberg model on the honeycomb lattice [3, 45] or the zigzag phase seen in Na_2IrO_3 [63, 57]. This observed wavevector indicates a large magnetic unit cell, and compatible wavevectors along high symmetry directions could be close to $(1/3, 0, 0)$ or $(0, 0.6, 0)$ in reciprocal lattice units (r.l.u.) (See Fig. 6.6c)), and in general any positions with the same magnitude of Q on the surface of a sphere in reciprocal space.

The phase diagram for the Heisenberg J_1-J_2-J_3 model on the honeycomb lattice can indeed accommodate such long-period magnetic structures in the form of spiral (helical) phases H1 to H3 as shown in Fig. 6.12. The difference between them is the orientation of the $\boldsymbol{k}$ vector (along a or b) and the phase offset between the spins on the two sublattices of the honeycomb lattice.

Fig. 6.6a) shows the candidate H1 phase with $\boldsymbol{k}$-vector, $(1/3, 0, 0)$. It is the helical phase where the magnetic moments rotate along the crystallographic $\boldsymbol{a}$ direction with zero phase difference α, between the two sublattices (A and B) of the honeycomb lattice. Group theory analysis shows that such a structure is compatible with the C2/m space group if spins rotate in the ac-plane. This is because the b-axis is a unique two-fold axis with an orthogonal mirror plane. This can be described as a 60° zigzag spiral order.

Another candidate is the H2 phase with a magnetic propagation vector along the $\boldsymbol{b}$-axis, $(0, 0.6, 0)$ with a finite phase offset between A and B sublattices. In terms of the neutron diffraction pattern, the H2 phase predicts a sizeable intensity of the second Bragg peak near 0.996 Å^{-1} (indexed as $(0, \pm 1.4, 0)$) which however was not observed (See Fig. 6.5d)), whereas the H1 phase predicts a much smaller second Bragg peak at 1.134 Å^{-1} (indexed as $(\pm 2/3, \pm 1, 0)$), so the H1 phase is more compatible with the diffraction data. However, with the HB J_1-J_2-J_3 model, the H1 phase cannot give an antiferromagnetic Curie-Weiss temperature whereas the H2 phase can. Thus, the H2 candidate model will be considered in detail using linear spin-wave calculations in the following Section 6.5.

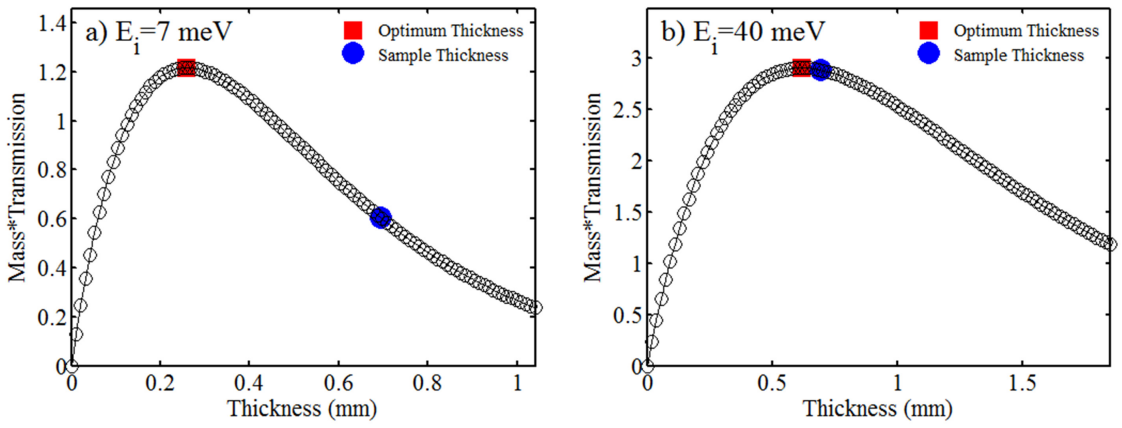


Figure 6.7: Effective Neutron Absorption Simulated for the MERLIN Experiments with Li_2IrO_3. With a given dimension of an annular can, effective neutron absorption (mass $\times$ absorption) is shown as a function of the thickness of the annular can for a fixed sample mass of 8.9 g.

To summarize, the neutron diffraction measurements have observed a magnetic Bragg peak at $Q \sim 0.41$ Å^{-1}, which is also detected consistently in inelastic neutron scattering experiments. The magnetic Bragg peak is incompatible with all of currently proposed magnetic orders in the Kitaev-Heisenberg model, and it indicates a much larger magnetic unit cell, possibly an incommensurate helical order.

6.4 Powder Inelastic Neutron Scattering

Measurements of the spin excitations as a function of momentum and energy with inelastic neutron scattering is the direct way to obtain the spin dynamics, and one can extract the underlying exchange interactions based on candidate spin Hamiltonians. In this Section, the INS measurements performed on powder samples of Li_2IrO_3 are presented and qualitative differences with the spectra of Na_2IrO_3 are discussed.

6.4.1 Experimental Details

Similar to the experimental setup used for Na_2IrO_3 (See Sec. 4.3.1), the large neutron absorption from iridium ions was a challenge. Li_2IrO_3 has even stronger neutron absorption than Na_2IrO_3 since lithium also absorbs neutrons (70.5 barns for

2200 m/s neutrons) compared to sodium ions (0.53 barns for 2200 m/s neutrons). The powder sample of mass 8.9 g was placed in an Al-sachet to form an annular shape in a sample can 40 mm high and 35 mm wide. The absorption simulation in this configuration is shown in Fig. 6.7.

The high-energy INS experiments was conducted using the time-of-fight direct geometry chopper spectrometer MERLIN at ISIS in the UK. Incident neutron energies of 7, 15, 40, 80 meV were used to search for the relevant energy range to detect magnetic excitations, and incident energies of 7, 15 meV were found to cover most of the magnetic scattering range, and were subsequently collected with high statistics to obtain a good dataset. The instrumental energy resolution, FWHM on the elastic line at 7 and 15 meV were 0.58 and 1.1 meV, respectively. Counting times for the data in Figs. 6.8(a,c) were 20 and 13 hours, respectively, at an average proton current of 150 μAmps.

Additional low-energy INS measurements were performed using the time-of-flight IN6 instrument at ILL in France. The incident energy of neutrons were chosen as E_i = 4.77 meV and 3.12 meV to search for a possible spin gap, and the data was collected at both 1.5 K (base temperature) and 150 K. Counting times for the data in Figs. 6.10(a,b) were 27 and 15 hours respectively. Here we used 5.16 g of the same powder batch used at MERLIN and the sample was placed in a flat disk-shaped can at 45° incidence.

6.4.2 Measurements and Results

The INS data from MERLIN was collected with E_i = 7 meV and 15 meV at both 1.5 K (base temperature) and 150 K are shown in Figs. 6.8(a-d). In Fig. 6.8a), the inelastic signal was detected at the magnetic Bragg peaks position $Q \sim 0.41$ Å^{-1} and was clearly visible up to 3.5 meV with an increase intensity onset at about 2.5 meV.

This excitation continues up to at least 8 meV as shown in Fig. 6.8c) with possibly a flat mode near 6 meV connecting the low-Q scattering with inelastic signal from a magnetic Bragg peak position at about 2.0 Å^{-1}. This observed signal was completely suppressed at 150 K as seen in Figs. 6.8(b,d). The magnetic signal continues up to at

least 12 meV as can be seen in Fig. 6.8e), so the equivalent temperature of 150 K is deliberately selected in Fig. 6.8f) to dampen out completely the magnetic scattering, otherwise spin-wave-like excitations, still persist above the transition temperature, up to $k_BT \sim J$. To show the relative ratio of the magnetic signal compared to the paramagnetic background, energy scan in the MERLIN data is shown in Fig. 6.9.

The lower-energy excitation was also observed at IN6 as shown in Fig. 6.10. Very weak magnetic excitations were observed down to 1.5 meV in Fig. 6.10a) and the results were consistent with the higher quality MERLIN data in Fig. 6.8a). The excitations could be followed down to 0.7 meV as shown in Fig. 6.10c). These excitations damped out in the paramagnetic phases of 150 K as revealed in Figs. 6.10(a,c). No clear signature for a spin gap was detected in this experiment.

As can be seen in the MERLIN data, this vertically dispersing excitation originating from the low Q wavevector is qualitatively different from the magnetic spectra observed in Na_2IrO_3. Also, the detected ordering wavevector (Q $\sim$ 0.41 Å^{-1}) is incompatible with the zigzag magnetic order found in Na_2IrO_3.

Such small Q-vector could be accommodated in the phase diagram of the J_1-J_2-J_3 Heisenberg model in the form of spiral order, H1 and H3 phases with a zero and π phase difference between the two sublattices of the honeycomb lattice, and the magnetic propagation wavevectors for both phases along the $\boldsymbol{a}$-axis, or an H2 phase, where there is finite phase difference, α, between the two spirals propagating along $\boldsymbol{b}$-axis.

Positions of magnetic Bragg peaks are illustrated in Fig. 6.6c) for the H1 and H2 spiral magnetic orders. The phase H3 does not predict a finite magnetic Bragg peaks peak at Q $\sim$ 0.41 Å^{-1} due to an exact cancellation of the phases from the two spirals, thus it can be ruled out for the further analysis.

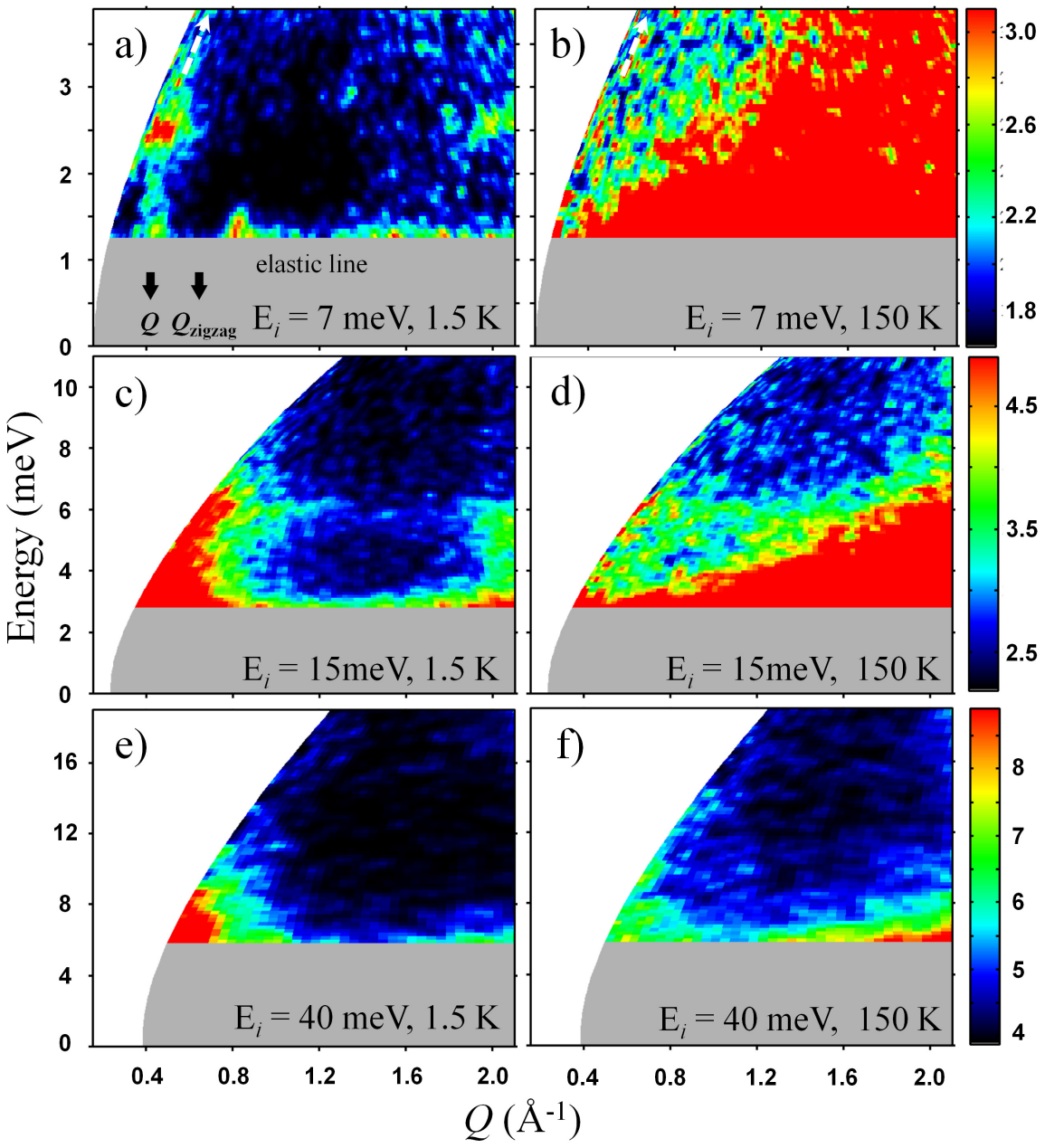


Figure 6.8: Powder Inelastic Neutron Scattering on Li_2IrO_3 from MERLIN. The data with E_i = 7 meV measured at a) 1.5 K, b) 150 K, and with E_i = 15 meV at c) 1.5 K, d) 150 K, and with E_i = 40 meV at e) 1.5 K, f) 150 K. The notable well-defined feature is the strongly dispersive signal at low Q which becomes damped out in the paramagnetic phase in b), d) and f). Thick dashed arrow in a) shows the scan direction in Fig. 6.9. Gray shading marks the inaccessible region close to the elastic line dominated by incoherent elastic scattering.

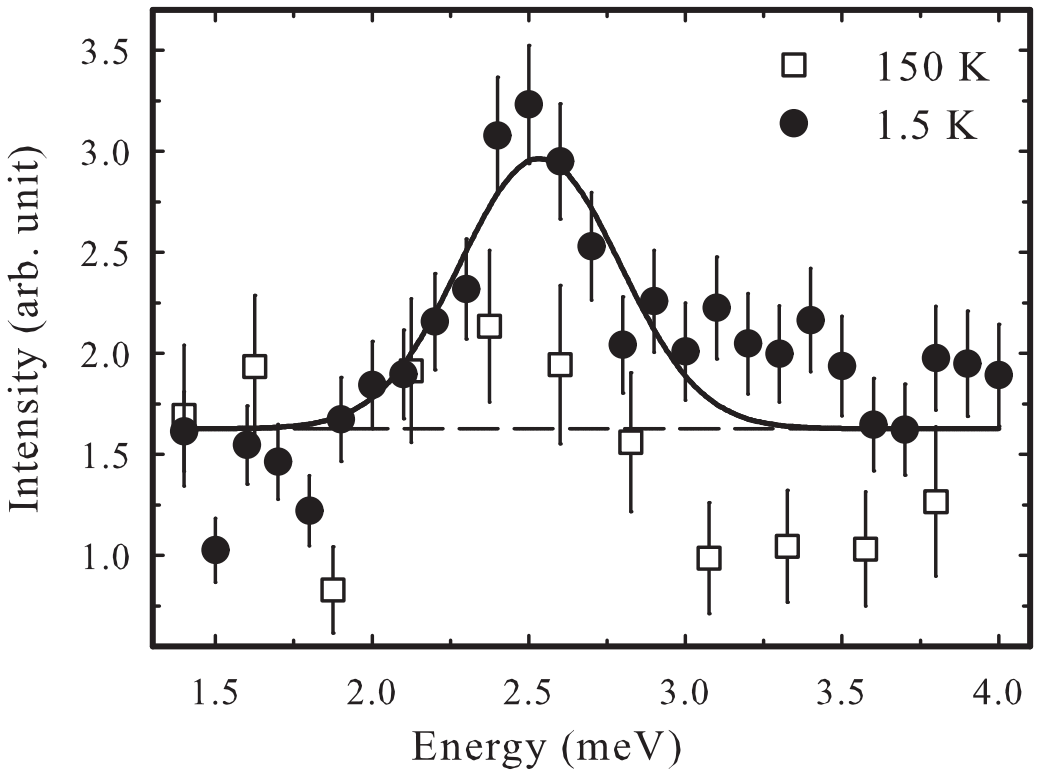


Figure 6.9: Energy Scan through the Magnetic Excitation in the MERLIN Data. The cut is through the scan direction illustrated with a slanted thick dashed arrow in Figs. 6.8(a-b).

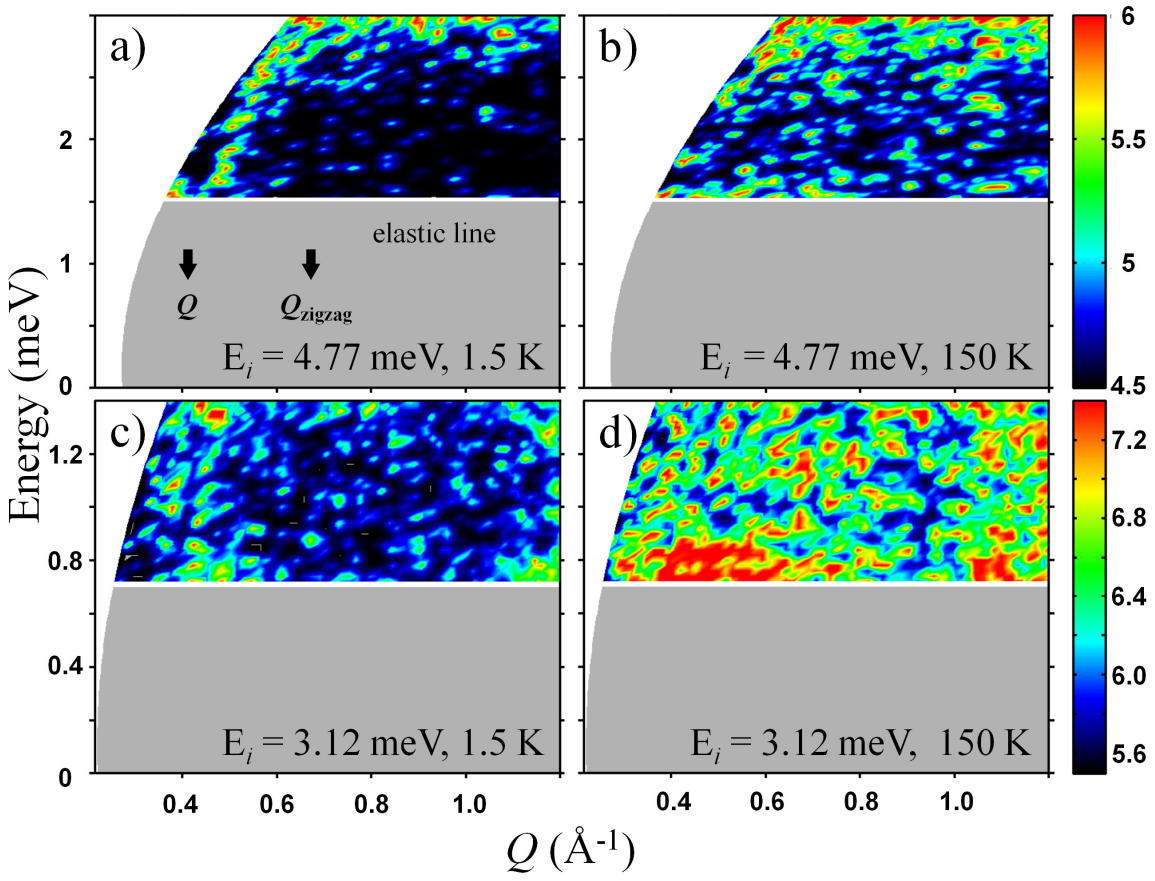


Figure 6.10: Powder Inelastic Neutron Scattering on Li_2IrO_3 using IN6. The data corresponds to $E_i = 4.77$ meV measured at a) 1.5 K, b) 150 K, and $E_i = 3.12$ meV at c) 1.5 K, d) 150 K.

To summarize this Section, powder inelastic measurements on Li_2IrO_3 were successfully made using MERLIN, observing strongly dispersive magnetic excitations with a softening wavevector corresponding to a large magnetic unit cell that is not accounted for by the current theories of the Kitaev-Heisenberg model [3, 45]. The observed magnetic wavevector of Li_2IrO_3 is not compatible with a zigzag phase detected for Na_2IrO_3, but two spiral phases (H1 and H2) in the Heisenberg J_1-J_2-J_3 model could be consistent with the observed magnetic Bragg peak and the softening point of the excitation spectra. The other H3 phase can be ruled out since it does not give the correct magnetic Bragg peak due to the cancellation of the magnetic structure factor. Thus, the spiral phases of H1 and H2 can be candidates for the magnetic ground state of Li_2IrO_3, whose magnetic excitations are examined in the next Section 6.5 using linear spin-wave theory.

6.5 Linear Spin-Wave Analysis of Two Spiral Phases in the Heisenberg J_1-J_2-J_3 Model

This section presents linear spin-wave theory for two spiral phase candidates in the Heisenberg J_1-J_2-J_3 model to describe the magnetic excitations in Li_2IrO_3. The exchange paths in this model are illustrated in Fig. 6.11 with nearest neighbour interaction, J_1 and second, and third nearest neighbour couplings J_2 and J_3. The corresponding spin Hamiltonian is

$$\mathcal{H} = \sum_{1\text{NN}} J_1 \boldsymbol{S}_i \cdot \boldsymbol{S}_j + \sum_{2\text{NN}} J_2 \boldsymbol{S}_i \cdot \boldsymbol{S}_k + \sum_{3\text{NN}} J_3 \boldsymbol{S}_i \cdot \boldsymbol{S}_l, \tag{6.3}$$

where 1NN, 2NN and 3NN indicate the first, second and third nearest neighbours with each interaction counted once.

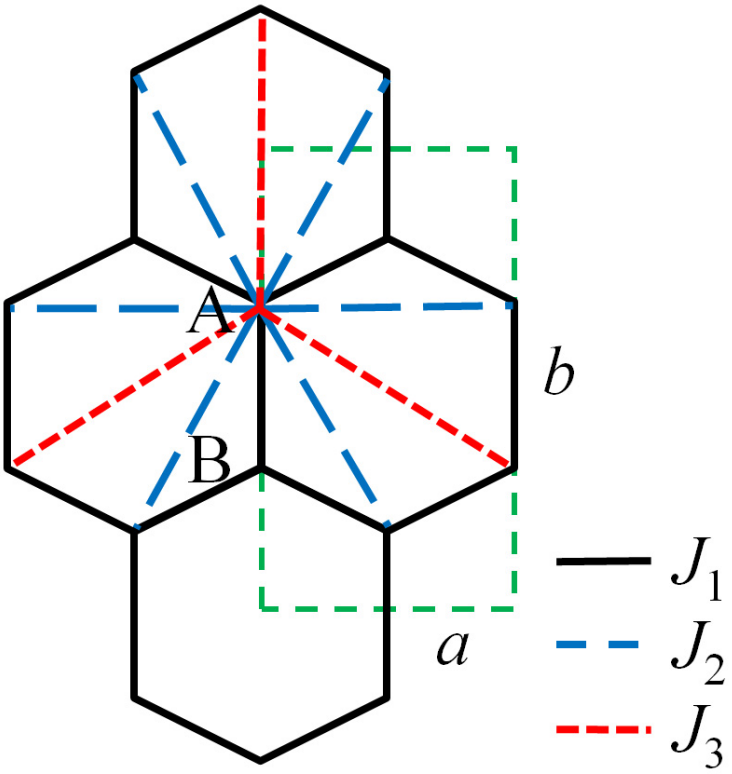


Figure 6.11: Exchange Interaction Paths in the Honeycomb Lattice up to Third Nearest Neighbour. Bi-partite sublattices are indicated by A and B with a dotted rectangle for the in-plane chemical unit cell.

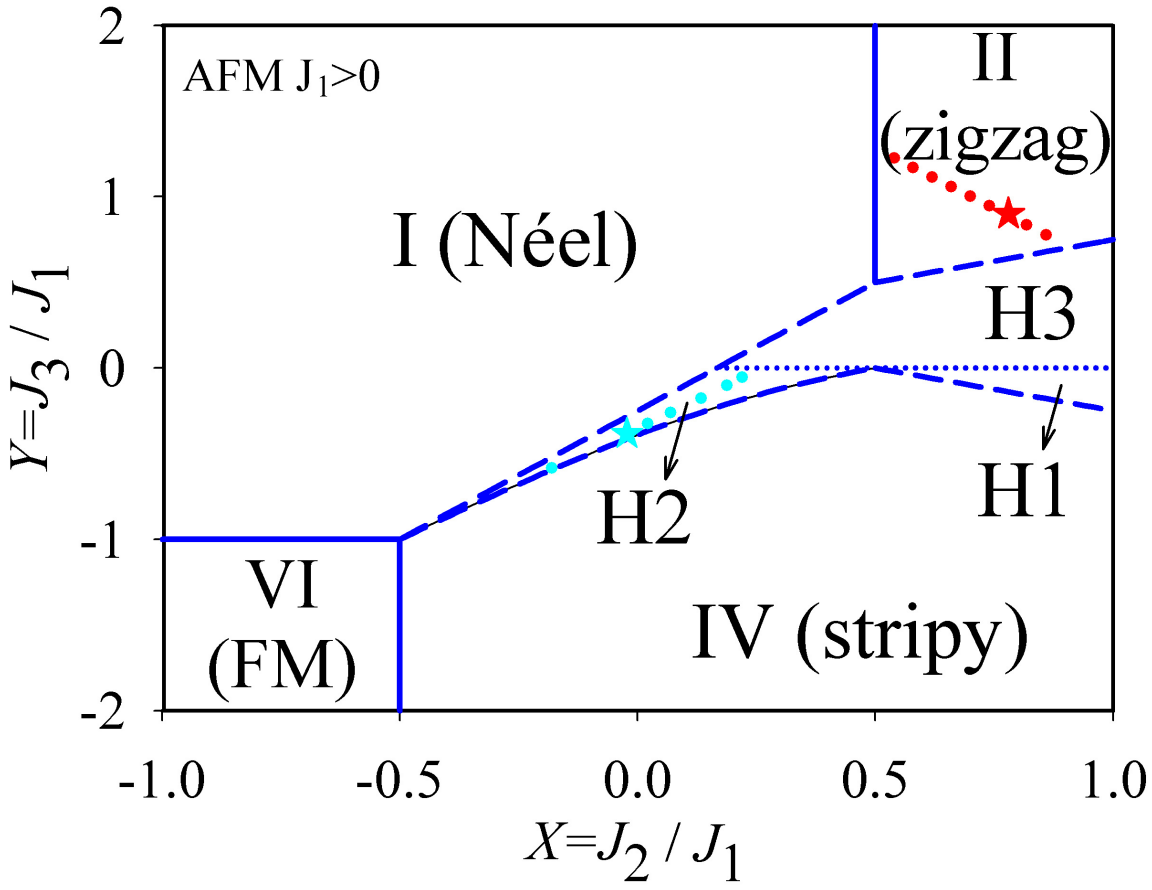


Figure 6.12: Mean-Field Phase Diagram of in the Heisenberg J_1-J_2-J_3 Model. First-order transitions are indicated by the solid blue lines, and second-order transition by dashed blue lines, and disorder transitions by dotted lines. This phase diagram is obtained when the nearest neighbour interaction is antiferromagnetic ($J_1 > 0$), same as the sign of the antiferromagnetic CWT. The scattered solid dots represent a set of parameters for the H2 candidate spiral phase for Li_2IrO_3, whereas the red dots show parameters for Na_2IrO_3. The star symbol in each case is the parameter set which best reproduce features of the observed excitation spectrum, and are used in this thesis as representative values.

The effect of the competition between exchange interactions between the first and second nearest neighbour exchanges in a triangular lattice have been studied in neutron experiments of the cycloidal phase in triangular lattice Cs_2CuCl_4 [64]. The frustration leads to spiral order with an incommensurate magnetic ordering wavevector, and an asymmetric shape for the dispersion relation along the (0K0) direction.

The mean-field phase diagram of the Hamiltonian in Eq. (6.3) [7] has collinear as well as the spiral phases as shown in Fig. 6.12. Here the relative ratio of competing exchange interactions, $X = J_3/J_1$ and $Y = J_2/J_1$, gives rise to the different magnetic orders with the ordering wavevector expressed as a function of X and Y. For the H1 phase (See Fig.6.6a)), there is a zero angle between the A and B sublattices with the spiral wavevector $\boldsymbol{Q} = (Q_x, 0, 0)$ in the reciprocal lattice units where [7]

$$Q_x = \frac{1}{\pi} \arccos \left[-\frac{(1+2X)}{4(X+Y)} \right] \tag{6.4}$$

For the H2 phase (See 6.6b)), the ordering wavevector is $\boldsymbol{Q}$=$(0, Q_y, 0)$ with

$$Q_y = \frac{1}{\pi} \arccos \left\{ -\frac{1}{2Y(1+2Y)} \left[(1+3Y) - 2X(1+Y) \sqrt{\frac{(1+Y)(1-2Y)}{4X^2 - Y(1+2Y)}} \right] \right\} \tag{6.5}$$

with a finite angle (α) between the A and B sublattices, which is also a function of the magnetic ordering wavevector Q, and can be expressed by [7]

$$\alpha = -\frac{\pi}{3} Q_y + \arctan \left[\frac{(1+Y)\sin(\pi Q_y)}{2 + (1+\pi Q_y)\cos(\pi Q_y)} \right] + \pi. \tag{6.6}$$

The mean-field phase diagram in Fig. 6.12 and relevant equations were derived by following Ref. [7] based on the definition of ferromagnetic $J_1 > 0$, and the derivation was also repeated for antiferromagnetic $J_1 < 0$, then further applicable for antiferromagnetic $J_1 > 0$. The mean-field ground state energy for a single exchange interaction in the rotated frame was reproduced, and was generalised for three exchange interactions for the case of Eq. (6.3). Then for the case of the planar spiral phases, where the magnetic moments are confined in the plane, the mean-field ground state energies for all seven phases were analytically reproduced and all phase boundaries of them were obtained in an analytical way, except those adjacent to the H2 phase that were

confirmed by a numerical method. Conditions from Eq. (6.4) to Eq. (6.6) that minimise the mean-field ground state energies at a given set of X and Y, were obtained analytically by using the first partial derivative of the mean-field energies of the H1 and H2 phases with respect to their variables. The relevant equations were then checked for the antiferromagnetic $J_1 > 0$ case, the definition used in this thesis. Note that there are typos in Q_y and α in Ref. [7] given as

$$Q_y = \frac{1}{\pi}\arccos\left\{-\frac{1}{2Y(1+2Y)}\left[(1+3Y)+2X(1+Y)\sqrt{\frac{(1+Y)(1-2Y)}{4X^2-Y(1+2Y)}}\right]\right\}, \quad (6.7)$$

and

$$\alpha = -\frac{\pi}{3}Q_y + \arctan\left[\frac{(1+Y)\sin(\pi Q_y)}{2+(1+\pi Q_y)\cos(\pi Q_y)}\right]. \quad (6.8)$$

They were found when the imaginary eigenvalues of dispersions of some exchanges candidates for the antiferromagnetic $J_1 < 0$ were fixed. When converting a sign of J_1 from ferromagnet to antiferromagnet, the ground state energy changes its sign. The sinusoidal ground state energy curve with a 2π periodicity turns upside down, so a α value for the antiferromagnetic J_1 should be shifted by π to give a correct minimum ground state energy. The other Q_y solution (among two solutions due to a square root in Eq. (6.7)) should also be chosen to prevent the imaginary eigenvalues in the spin-wave dispersion. This is not the case for other six phases including the H1 phase, where the same form of Q_x solution as shown in Eq. (6.4) (with the constant α) is derived for both ferromagnetic and antiferromagnetic J_1.

Unlike the collinear phase, the conventional way to derive the spin-wave spectra in non-collinear ordered magnets is to express the spin components in a local frame (x', y', z'), where spins are ferromagnetically aligned along their equilibrium z'-axis. For a spiral ordered structure, the local reference frame rotates between neighbouring sites by the angle θ between consecutive spins along the rotational direction, while the out-of-plane spin components are unchanged. Then the in-plane magnetic excitations in the global frame (x, y, z), where the experiment is performed, is obtained by translating the in-plane spectrum by the ordering wavevector $\pm\boldsymbol{Q}$, whereas the out-of-plane spectrum is unchanged compared to the local frame as this spin component is not participating in the rotation of axes.

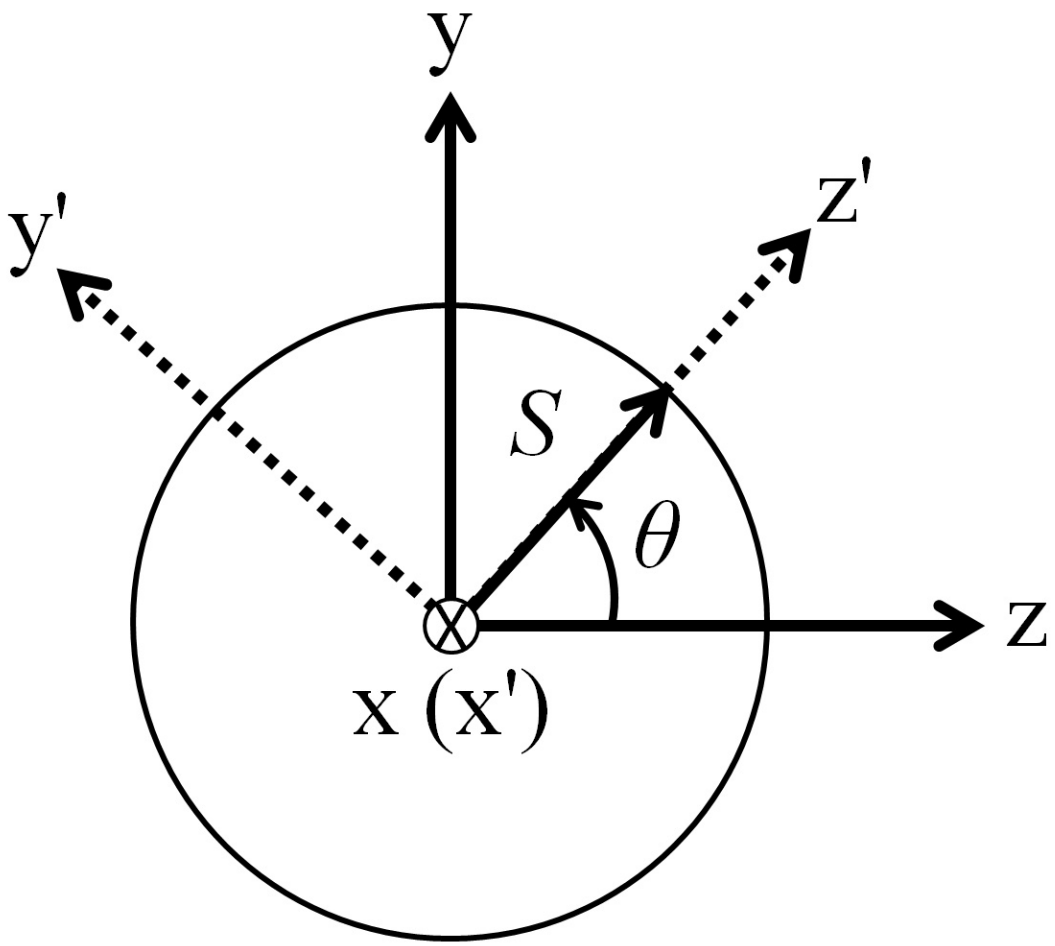


Figure 6.13: Schematic Diagram of the Transformation from Global to Local Axes in the Spiral Structure. (x, y, z) axes corresponds to the global frame where the experiments happen whereas (x', y', z') axes are for the local frame for the linear spin-wave calculation explained in the text. The ordered spin points towards the z'-axis at equilibrium.

As illustrated in Fig. 6.13, the relations between spin components in the global frame (x, y, z) and the local frame (x', y', z') are determined by the rotation of equilibrium the spin vector such as

$$\begin{aligned} S^z &= \cos\theta S^{z'} - \sin\theta S^{y'}, \\ S^y &= \sin\theta S^{z'} + \cos\theta S^{y'}, \\ S^x &= S^{x'}. \end{aligned} \tag{6.9}$$

where $\theta_i = \boldsymbol{Q}\cdot\boldsymbol{r}_i$, defines the equilibrium spin direction at site i. The spin Hamiltonian in Eq. (6.3) is then expressed in terms of spin operators in the local frame. To generate the low-energy spin-wave excitation, spins are treated as harmonic oscillators, and the departure from the fully ordered state is described using spin deviation operators in the Holstein-Primakoff formulism. The spin operators in the rotated frame are given by

$$\begin{aligned} S_i^{z'} &= S - a_i^\dagger a_i & S_j^{z'} &= S - b_j^\dagger b_j \\ S_i^{+} &= S_i^{x'} + iS_i^{y'} \simeq \sqrt{2S}a_i & S_j^{+} &= S_j^{x'} + iS_j^{y'} \simeq \sqrt{2S}b_j \\ S_i^{-} &= S_i^{x'} - iS_i^{y'} \simeq \sqrt{2S}a_i^\dagger & S_j^{-} &= S_j^{x'} - iS_j^{y'} \simeq \sqrt{2S}b_j^\dagger. \end{aligned} \tag{6.10}$$

where a_i (b_i) is an annihilation operator which removes a spin deviation and $\mathrm{a}_i^\dagger$ ($\mathrm{b}_i^\dagger$) is a creation operator which generates a spin deviation in the spin system in the real space in the a (b)-sublattice in the bipartite honeycomb lattice. The spin quantization axis is assumed to be z' and (x', y', z') are defined as a right-handed local coordinate in reference frame.

The exchange interaction in the spin Hamiltonian Eq. (6.3) can be decomposed into

$$\begin{aligned} \boldsymbol{S}_i \cdot \boldsymbol{S}_j =& S_i^x S_j^x + S_i^y S_j^y + S_i^z S_j^z \\ =& S_i^{x'} S_j^{x'} + \cos(\theta_i - \theta_j)[S_i^{y'} S_j^{y'} + S_i^{z'} S_j^{z'}], \end{aligned} \tag{6.11}$$

which is expressed in the local frame (x', y', z') using Eq. (6.9), and written in terms of a bosonic Hamiltonian with annihilation and creation operators using Eq. (6.10). The linear terms including $\sin(\theta_i - \theta_j)$ in the expansion of the spin Hamiltonian are

related to the torque of spins, which is zero in the equilibrium state, so it gives the stable condition of the spiral order in terms of exchange couplings. This means that the linear terms do not contribute the generation of the spin-wave excitation.

The Fourier transformation of the corresponding operators is given by

$$\begin{aligned} a_i &= \frac{1}{\sqrt{N}} \sum_{\boldsymbol{k}} a_{\boldsymbol{k}} e^{-i\boldsymbol{k}\cdot\boldsymbol{r}_i} \qquad b_j = \frac{1}{\sqrt{N}} \sum_{\boldsymbol{k}} b_{\boldsymbol{k}} e^{-i\boldsymbol{k}\cdot\boldsymbol{r}_j} \\ a_i^\dagger &= \frac{1}{\sqrt{N}} \sum_{\boldsymbol{k}} a_{\boldsymbol{k}}^\dagger e^{+i\boldsymbol{k}\cdot\boldsymbol{r}_i} \qquad b_j^\dagger = \frac{1}{\sqrt{N}} \sum_{\boldsymbol{k}} b_{\boldsymbol{k}}^\dagger e^{+i\boldsymbol{k}\cdot\boldsymbol{r}_j} \end{aligned} \tag{6.12}$$

where N is the total number of spins on each sublattice, a_i ($a_i^\dagger$) annihilates (creates) one magnon in the a-sublattice and similarly for the b-sublattice. Excluding higher-order terms beyond bilinear, the spin Hamiltonian becomes a quadratic form of magnon operators

$$\mathcal{H} = \sum_{\boldsymbol{k}} \mathsf{X}^\dagger \mathsf{H} \mathsf{X} + 2N(1 + 1/S) E_{MF}, \tag{6.13}$$

where E_{MF} is the mean-field ground state energy (per spin) and $2N$ is the total number of spin sites on the two sublattices. The sum extends over all wavevectors $\boldsymbol{k}$ in the first Brillouin zone of the chemical unit cell.

For the H1 order as illustrated in Fig. 6.6a), the defined operator basis in the local axes is

$$\mathsf{X}^\dagger = \left[a_{\boldsymbol{k}}^\dagger \ , \ b_{\boldsymbol{k}}^\dagger \ , \ a_{-\boldsymbol{k}} \ , \ b_{-\boldsymbol{k}} \right], \tag{6.14}$$

where a and b label operators on two inequivalent sublattice A and B. The Hamiltonian matrix in Eq. (6.13) is obtained as

$$\mathcal{H} = \frac{1}{2} \sum_{\boldsymbol{k}} \left[\ a_{\boldsymbol{k}}^\dagger \ , \ b_{\boldsymbol{k}}^\dagger \ , \ a_{-\boldsymbol{k}} \ , \ b_{-\boldsymbol{k}} \ \right] \begin{bmatrix} A & B & C & D^* \\ B^* & A & D & C \\ C & D^* & A & B \\ D & C & B^* & A \end{bmatrix} \begin{bmatrix} a_{\boldsymbol{k}} \\ b_{\boldsymbol{k}} \\ a_{-\boldsymbol{k}}^\dagger \\ b_{-\boldsymbol{k}}^\dagger \end{bmatrix} + \text{constant} \tag{6.15}$$

$$= \sum_{\boldsymbol{k}} A a_{\boldsymbol{k}}^\dagger a_{\boldsymbol{k}} + B a_{\boldsymbol{k}}^\dagger b_{\boldsymbol{k}} + C a_{\boldsymbol{k}}^\dagger a_{-\boldsymbol{k}}^\dagger + D^* a_{\boldsymbol{k}}^\dagger b_{-\boldsymbol{k}}^\dagger + \ldots \ , \tag{6.16}$$

where

$$
\begin{aligned}
A &= S\ \{J_2(1+Q_0)\cos(2\pi h) - (J_1 + 2J_1P_0 + 2J_2Q_0 + 4J_2P_0 + J_3 + 2J_3Q_0) \\
&\qquad +J_2(1+P_0)\{\cos[\pi(h+k)] + \cos[\pi(h-k)]\}\} \\
B &= S\ \{J_1\eta^{-2} + J_1(1+P_0)\eta\cos(\pi h) + J_3\eta^4 + J_3(1+Q_0)\eta^{-2}\cos(2\pi h)\} \\
C &= S\ \{J_2(1-Q_0)\cos(2\pi h) + J_2(1-P_0)\{\cos[\pi(h+k)] + \cos[\pi(h-k)]\}\} \\
D &= S\ \{J_1(1-P_0)\eta^{-1}\cos(\pi h) + J_3(1-Q_0)\eta^2\cos(2\pi h)\} \\
\eta &= e^{k\pi i/3} \\
P_0 &= \cos(\theta/2) \\
Q_0 &= \cos(\theta).
\end{aligned}
$$

Here $\theta = 2\pi Q_x$, the magnetic ordering wavevector is $\boldsymbol{Q} = (Q_x, 0, 0)$, and (h, k) are components of the scattering wavevector $\boldsymbol{k}$ in units of the reciprocal lattice of the $a \times b$ rectangular unit cell shown in Fig. 6.19a). By periodicity the above expressions are valid for any momentum, not necessarily restricted to the first chemical Brillouin zone.

For the H2 order as shown in Fig. 6.6b), the spin-wave Hamiltonian can be brought to the same form as in Eq. (6.15) with

$$
\begin{aligned}
A &= S\ \{2J_2\cos(2\pi h) - (J_1Q_0 + 2J_1P_0 + 2J_2 + 4J_2R_0 + J_3T_0 + 2J_3Q_0) \\
&\qquad +J_2(1+R_0)\{\cos[\pi(h+k)] + \cos[\pi(h-k)]\}\} \\
B &= S\ \{(J_1/2)(1+Q_0)\eta^{-2} + J_1(1+P_0)\eta\cos(\pi h) + (J_3/2)(1+T_0)\eta^4 \\
&\qquad +J_3(1+Q_0)\eta^{-2}\cos(2\pi h)\} \\
C &= S\ \{J_2(1-R_0)\{\cos[\pi(h+k)] + \cos[\pi(h-k)]\}\} \\
D &= S\ \{(J_1/2)(1-Q_0)\eta^2 + J_1(1-P_0)\eta^{-1}\cos(\pi h) + (J_3/2)(1-T_0)\eta^{-4} \\
&\qquad +J_3(1-Q_0)\eta^2\cos(2\pi h)\} \\
\eta &= e^{k\pi i/3} \\
P_0 &= \cos(\theta/6 + \alpha) \\
Q_0 &= \cos(-\theta/3 + \alpha) \\
R_0 &= \cos(\theta/2) \\
T_0 &= \cos(2\theta/3 + \alpha),
\end{aligned}
$$

where $\theta = 2\pi Q_y$ and the magnetic ordering wavevector is $\boldsymbol{Q} = (0, Q_y, 0)$.

Diagonalisation of the Hamiltonian by standard techniques [12, 41] to obtain the normal magnon modes gives two dispersion relations

$$\begin{aligned}(\omega_{\boldsymbol{k}}^{\pm})^2 &= A^2 + BB^* - C^2 - DD^* \\ &\pm\sqrt{4|AB - CD^*|^2 - |B^*D^* - BD|^2},\end{aligned} \tag{6.17}$$

where the two modes come from the two sublattices. The in-plane dispersions in the global frame are obtained by translating by $\pm\,\boldsymbol{Q}$ the dispersion relation from the local frame in Eq. (6.17) giving $\omega^{\pm}_{\boldsymbol{k}+\boldsymbol{Q}}$, $\omega^{\pm}_{\boldsymbol{k}-\boldsymbol{Q}}$ for the in-plane spin fluctuation. For the out-of-plane spin fluctuation, two modes are expected in the global frame with dispersions $\omega^{\pm}_{\boldsymbol{k}}$. The expression for the spin-wave dispersions were analytically derived, reproducing earlier results in Ref. [7] for both the H1 and H2 phases.

The intensity of the spin-wave excitation in neutron scattering is proportional to the dynamical structure factor, expressed as $S^{x'x'}(\boldsymbol{k},\omega)$ for the out-of-plane spin fluctuations and $S^{y'y'}(\boldsymbol{k},\omega)$ for the in-plane spin-spin correlations. The spin-spin correlation for the out-of-plane correlation, which is obtained based on Eq. (3.39) at $\alpha = x$, is given as

$$S^{xx}(\boldsymbol{k},\omega) = \sum_{\lambda} |\langle\lambda|S^{x}(\boldsymbol{k})|0\rangle|^2 \delta(\hbar\omega + E_0 - E_\lambda), \tag{6.18}$$

where the sum runs over the normal magnon modes excited from the ground state $|0\rangle$. $S^x(\boldsymbol{k})$ is the Fourier transformed magnetic moment directional to the x-axis

$$S^x(\boldsymbol{k}) = \frac{1}{\sqrt{N}}\sum_i S_i^x e^{i\boldsymbol{k}\cdot\boldsymbol{r}_i} + \frac{1}{\sqrt{N}}\sum_j S_j^x e^{i\boldsymbol{k}\cdot\boldsymbol{r}_j}, \tag{6.19}$$

where i, j indicates two sublattices in the honeycomb lattice. Using the relation $S_i^x = \frac{S_i^+ + S_i^-}{2}$, $S_j^x = \frac{S_j^+ + S_j^-}{2}$ and the Holstein-Primakoff transformation given in Eq. (6.10), Eq. (6.19) becomes

$$\begin{aligned}S^x(\boldsymbol{k}) &= \sqrt{\frac{S}{2}}\frac{1}{\sqrt{N}}\left(\sum_i e^{i\boldsymbol{k}\cdot\boldsymbol{r}_i}(a_i + a_i^\dagger) + \sum_j e^{i\boldsymbol{k}\cdot\boldsymbol{r}_j}(b_j + b_j^\dagger)\right) \\ &= \sqrt{\frac{S}{2}}\left(a_{\boldsymbol{k}} + b_{\boldsymbol{k}} + a_{-\boldsymbol{k}}^\dagger + b_{-\boldsymbol{k}}^\dagger\right),\end{aligned} \tag{6.20}$$

where the Fourier transformation in Eq. (6.12) is used in the last step. The out-of-plane correlation function is

$$S^{xx}(\boldsymbol{k},\omega) = S^{x'x'}(\boldsymbol{k},\omega), \tag{6.21}$$

as x-axis is unaffected by the rotation. The transformation matrix $\mathcal{S}$ to the normal operator basis $\mathsf{X}' = \mathcal{S}^{-1}\mathsf{X}$ is given in Appendix A with the analytical expression for the dynamic correlation factor $S^{xx}(\boldsymbol{k},\omega)$.

In a similar manner, the in-plane correlation in the global frame is

$$S^{yy}(\boldsymbol{k},\omega) = \sum_{\lambda} |\langle\lambda|S^{y}(\boldsymbol{k})|0\rangle|^2 \delta(\hbar\omega + E_0 - E_\lambda), \tag{6.22}$$

where $S^y(\boldsymbol{k})$ is given by

$$S^{y}(\boldsymbol{k}) = \frac{1}{\sqrt{N}}\sum_i S_i^y e^{i\boldsymbol{k}\cdot\boldsymbol{r}_i} + \frac{1}{\sqrt{N}}\sum_j S_j^y e^{i\boldsymbol{k}\cdot\boldsymbol{r}_j}, \tag{6.23}$$

and the Fourier transforms of the magnetic moment along y-axis are

$$S_i^y = -i\sqrt{\frac{S}{2}}(a_i - a_i^\dagger)\cos\theta_i, \quad S_j^y = -i\sqrt{\frac{S}{2}}(b_j - b_j^\dagger)\cos\theta_j, \tag{6.24}$$

which were obtained by using Eq. (6.9), the relation $S_i^{y'} = \frac{S_i^+ - S_i^-}{2i}$, $S_j^{y'} = \frac{S_j^+ - S_j^-}{2i}$ and Eq. (6.10) subsequently. The combination of Eq. (6.23) and Eq. (6.24) leads to

$$S^{y}(\boldsymbol{k}) = -i\sqrt{\frac{S}{2}}\frac{1}{\sqrt{N}}\left(\sum_i e^{i\boldsymbol{k}\cdot\boldsymbol{r}_i}(a_i - a_i^\dagger)\cos\theta_i + \sum_j e^{i\boldsymbol{k}\cdot\boldsymbol{r}_j}(b_j - b_j^\dagger)\cos\theta_j\right). \tag{6.25}$$

With the Fourier transformation in Eq. (6.12) and using $\cos\theta_i = \frac{1}{2}(e^{i\boldsymbol{Q}\cdot\boldsymbol{r}_i} + e^{-i\boldsymbol{Q}\cdot\boldsymbol{r}_i})$, $\cos\theta_j = \frac{1}{2}(e^{i\boldsymbol{Q}\cdot\boldsymbol{r}_j} + e^{-i\boldsymbol{Q}\cdot\boldsymbol{r}_j})$, Eq. (6.25) becomes

$$\begin{aligned} S^{y}(\boldsymbol{k}) &= -i\frac{1}{2}\sqrt{\frac{S}{2}}\left(a_{\boldsymbol{k}+\boldsymbol{Q}} - a^\dagger_{-\boldsymbol{k}-\boldsymbol{Q}} + b_{\boldsymbol{k}+\boldsymbol{Q}} - b^\dagger_{-\boldsymbol{k}-\boldsymbol{Q}} + a_{\boldsymbol{k}-\boldsymbol{Q}} - a^\dagger_{-\boldsymbol{k}+\boldsymbol{Q}} + b_{\boldsymbol{k}-\boldsymbol{Q}} - b^\dagger_{-\boldsymbol{k}+\boldsymbol{Q}}\right) \\ &= \frac{1}{2}\left(S^{y'}(\boldsymbol{k}+\boldsymbol{Q}) + S^{y'}(\boldsymbol{k}-\boldsymbol{Q})\right), \end{aligned} \tag{6.26}$$

where

$$S^{y'}(\boldsymbol{k}+\boldsymbol{Q}) = -i\sqrt{\frac{S}{2}}\left(a_{\boldsymbol{k}+\boldsymbol{Q}} + b_{\boldsymbol{k}+\boldsymbol{Q}} - a^\dagger_{-(\boldsymbol{k}+\boldsymbol{Q})} - b^\dagger_{-(\boldsymbol{k}+\boldsymbol{Q})}\right). \tag{6.27}$$

The in-plane correlation functions are then

$$\begin{aligned} S^{yy}(\boldsymbol{k},\omega) &= S^{zz}(\boldsymbol{k},\omega) \\ &= \frac{1}{4}\left(S^{y'y'}(\boldsymbol{k}+\boldsymbol{Q},\omega)+S^{y'y'}(\boldsymbol{k}-\boldsymbol{Q},\omega)\right), \end{aligned} \tag{6.28}$$

where the in-plane correlation function $S^{yy}(\boldsymbol{k},\omega)$ in the global frame is now expressed by two in-plane correlation functions, $S^{y'y'}(\boldsymbol{k}+\boldsymbol{Q},\omega)$ and $S^{y'y'}(\boldsymbol{k}-\boldsymbol{Q},\omega)$ in the local frame, which can be obtained by the analytical expressions in the 4×4 Hamiltonian of the form in Eq. (6.15), as given explicitly in the Appendix A based on Ref. [41] [Eq. (A3)]. A close inspection of Eq. (6.28) shows that the rotation of spins induces the satellite modes in the in-plane correlations, which are shifted by $\pm\boldsymbol{Q}$ in the momentum space.

For the comparison of the calculated linear spin-wave spectrum with the measured INS data, we imposed the additional constraint that the parameters should reproduce the Curie-Weiss temperature and the observed magnetic ordering wavevector value.

$$\begin{aligned} \theta_{CW} &= -S(S+1)(J_1+2J_2+J_3)/k_{\mathrm{B}} \\ &= -S(S+1)J_1(1+2X+Y)/k_{\mathrm{B}} \\ &= -33 \text{ K}. \end{aligned} \tag{6.29}$$

Since the H1 phase could not reproduce an antiferromagnetic CWT, only the H2 phase was considered in the further analysis. In the H2 phase, the candidates that satisfy the observed magnitude of the magnetic ordering wavevector are located on a line in the phase diagram in Fig. 6.12, then using Curie-Weiss temperature form in Eq. (6.30), the magnitude J_1 was extracted for each (X, Y) set. By comparing the simulated powder-averaged INS spectrum with the data, the representative set of exchange interactions ($X = J_2/J_1 = -0.022$, $Y = J_3/J_1 = -0.383$, and $J_1 = 6.6038$ meV) was selected, and it is marked as a blue star in Fig 6.12. This condition was used in both the spin-wave dispersion plot in Fig. 6.16 and 6.17, and the powder-averaged spectrum in Fig. 6.14. The magnitude of exchange parameters used were $J_1 = 6.6038$ meV, $J_2 = -0.14528$ meV, $J_3 = -2.5293$ meV. This gives $Q_y = 0.6$, $\alpha = 0.8889\pi$ in Eq. (6.5) and Eq. (6.6), respectively.

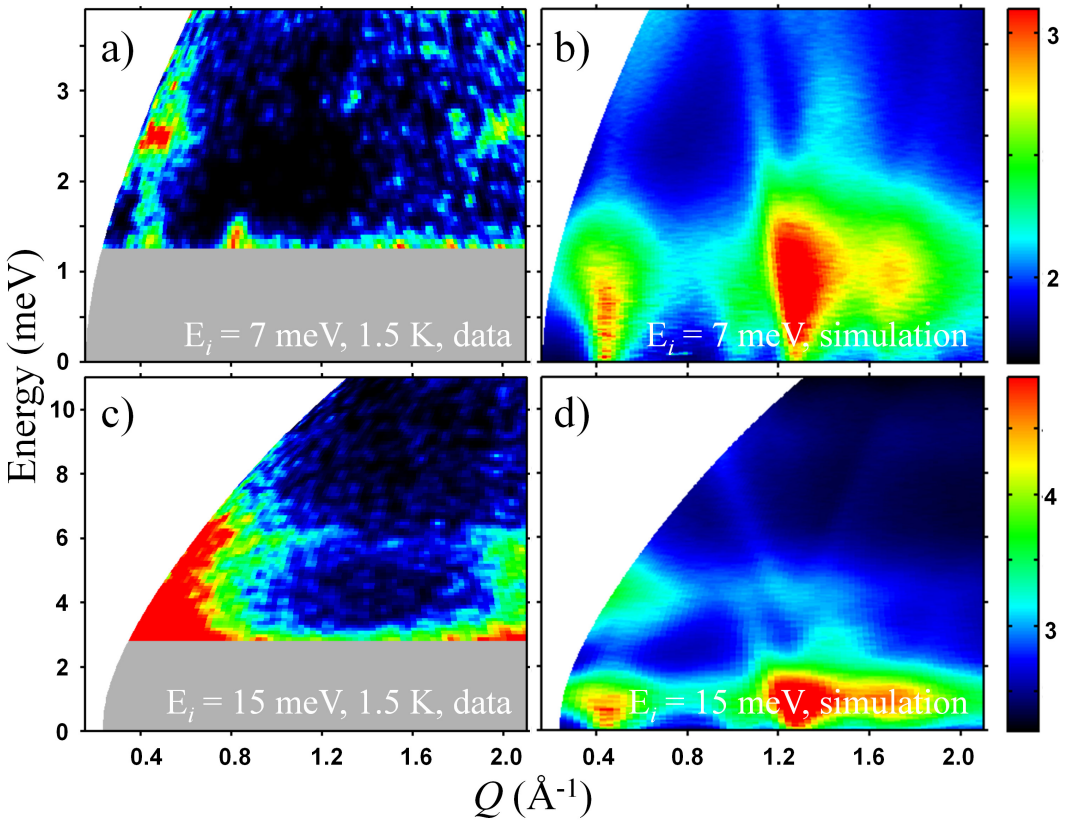


Figure 6.14: Spherically-Averaged Spin-Wave Spectrum for the H2 Phase with Isotropic Exchange Couplings. a) INS data at 1.5 K with an incident neutron energy $E_i = 7$ meV. b) Calculated spherically-averaged spin-wave intensity for the isotropic Heisenberg J_1-J_2-J_3 model with the spiral phase H2 for parameters given in the text. c) INS data at 1.5 K with $E_i = 15$ meV and d) its corresponding simulation. The simulated intensity was convolved with a Gaussian in energy using the experimental energy resolution (FWHM) of 0.58 and 1.1 meV, for b) and d), respectively. The spherical average was done using for each (Q, E) phase space with 500 random Monte-Carlo points (random crystallite orientation with a spherical distribution).

The simulated INS results are compared with the INS data in Fig. 6.14. It shows that the simulated INS spectra does not capture the experimentally observed INS data, such that a stronger intensity at 2.5 meV at $E_i = 7$ meV is not reproduced and the extended scattering to the higher momentum from $\boldsymbol{Q}$ is not reproduced in the simulation at $E_i = 15$ meV. Thus anisotropic interactions in the minimal HB J_1-J_2-J_3 model are considered next. For completeness, the dispersions and intensities of a magnon along the high-symmetry are also shown in Fig. 6.16 and Fig. 6.17.

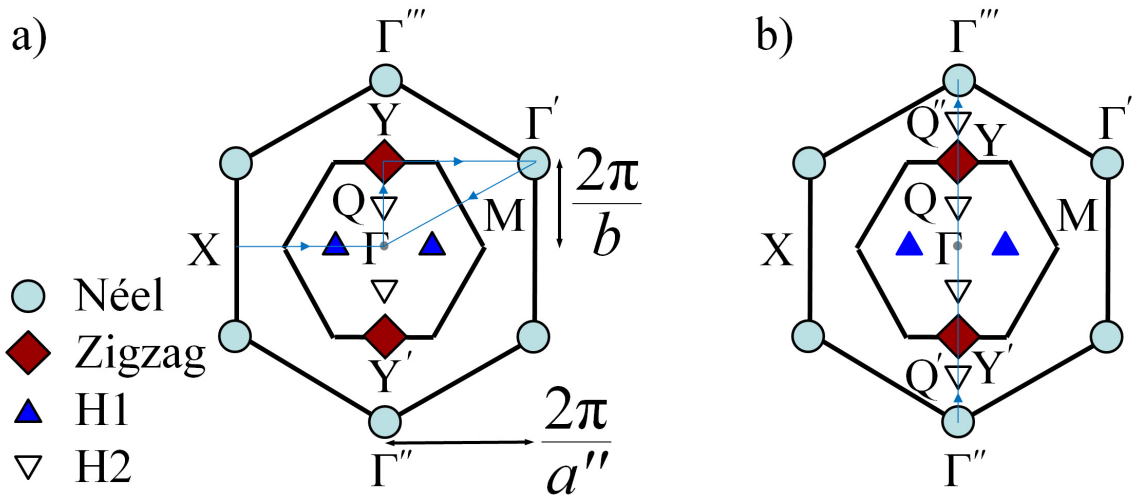


Figure 6.15: Momentum Trajectories along High-Symmetry Direction. a) Reciprocal space diagram showing the high-symmetry direction (arrowed path) along which dispersions are plotted in Fig. 6.16 and 6.19. Inner hexagon is the first Brillouin zone of the honeycomb lattice. b) Same for the dispersion plotted in Figs. 6.17 and 6.20. Note $a'' = a \sin \beta$, where β is a monoclinic angle.

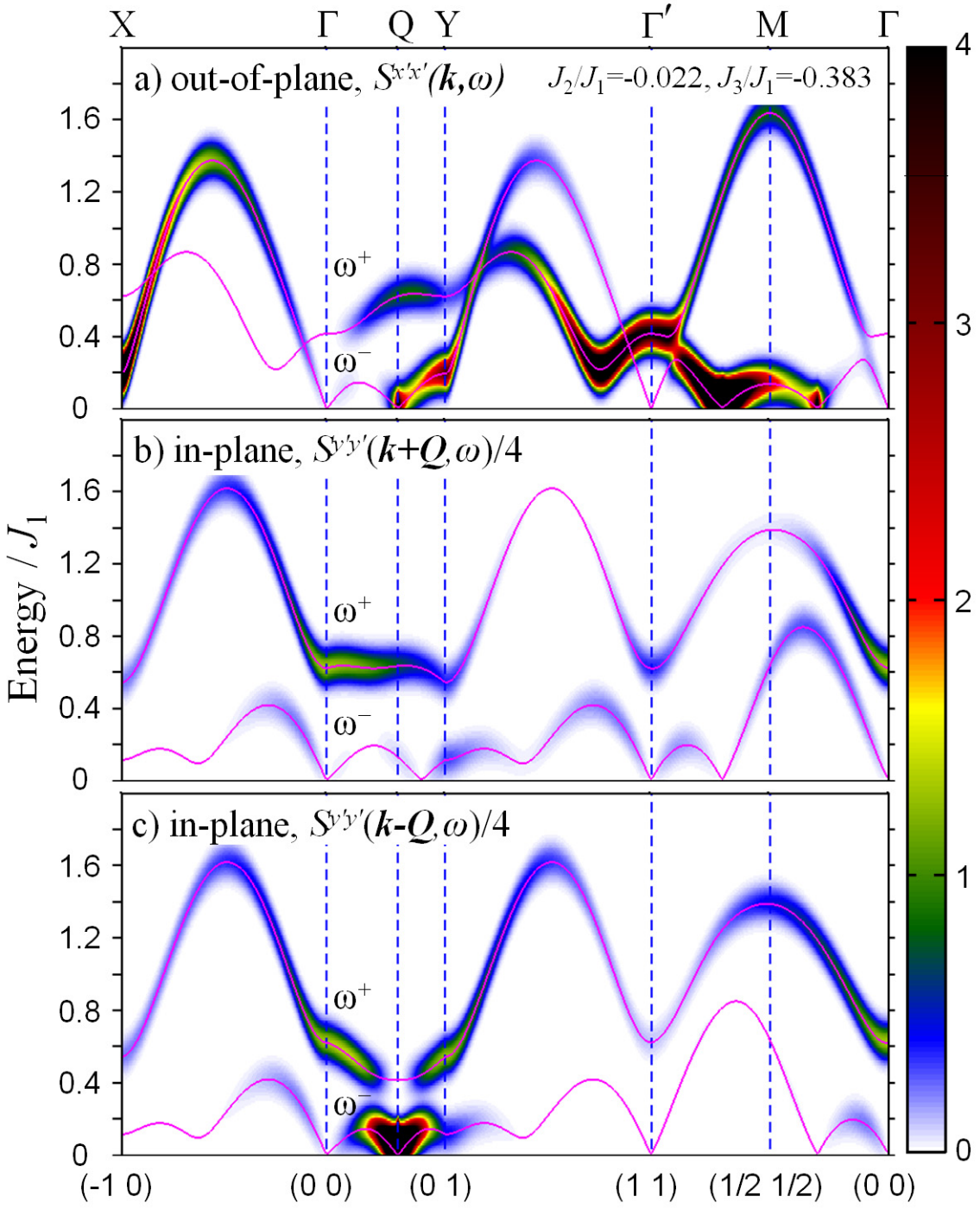


Figure 6.16: Spin-Wave Spectrum of the H2 Spiral Phase of the Isotropic J_1-J_2-J_3 Model along High-Symmetry Directions. Calculated spectrum is visualised in reciprocal space noted by the arrowed path in Fig. 6.15a). Exchange values are listed in the legends. a) Out-of-plane dispersions with colours indicating the spin-spin correlations. b-c) In-plane spectrum observing the $\omega^{\pm}_{\boldsymbol{k}\pm\boldsymbol{Q}}$ dispersions.

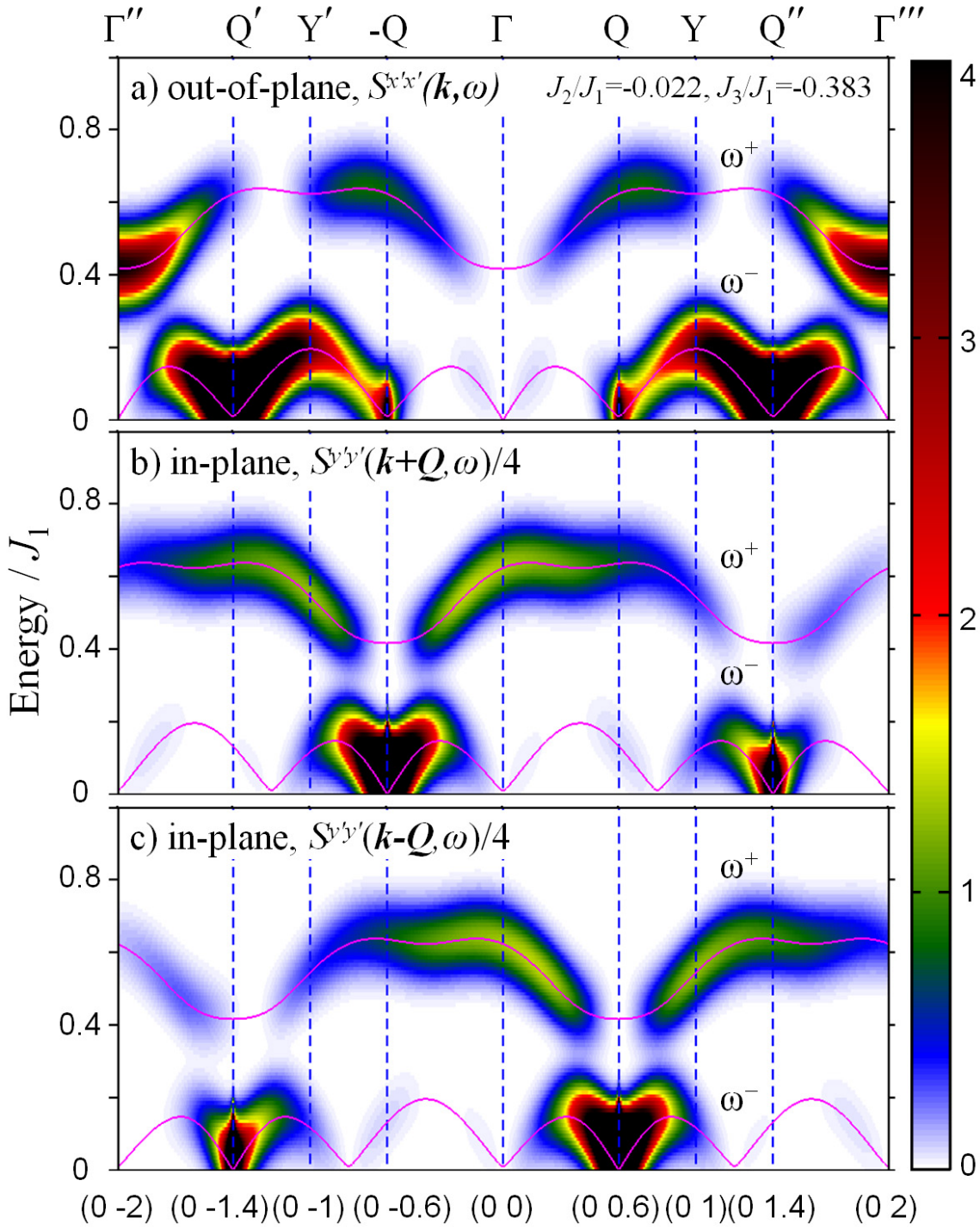


Figure 6.17: Spin-Wave Spectrum in the H2 Phase of the Isotropic J_1-J_2-J_3 Model along the (0K0) Direction. Momentum path is noted in Fig. 6.15b). Exchange couplings are listed in the caption. a) Out-of-plane dispersions with colours indicating the spin-spin correlations. b-c) In-plane dispersion $\omega^{\pm}_{\boldsymbol{k}\pm\boldsymbol{Q}}$.

The most natural anisotropy which could be imposed in the spiral system is the in-plane anisotropy which forces the magnetic moments to rotate in the spiral plane. The isotropic Heisenberg Hamiltonian is given as

$$\mathcal{H} = \sum_{\langle i,j \rangle} J \boldsymbol{S}_i \cdot \boldsymbol{S}_j. \tag{6.30}$$

By implementing an effective exchange anisotropy parameter (ε) leads to

$$\mathcal{H} = \sum_{\langle i,j \rangle} J^x(1-\varepsilon) S_i^x S_j^x + J(S_i^y S_j^y + S_i^z S_j^z). \tag{6.31}$$

where J^x is the exchange coupling along x-direction in the spin space. We introduced the same anisotropic form for all three exchange paths, 1NN, 2NN and 3NN. $\varepsilon > 0$ creates an effective easy in-plane anisotropy in the yz-plane.

In this case, the spin Hamiltonian components in Eq. (6.15) transform to

$$\begin{aligned}
A &= S\ \{(2-\varepsilon)J_2\cos(2\pi h) - (J_1Q_0 + 2J_1P_0 + 2J_2 + 4J_2R_0 + J_3T_0 + 2J_3Q_0) \\
&\quad + J_2(1-\varepsilon+R_0)\{\cos[\pi(h+k)] + \cos[\pi(h-k)]\}\} \\
B &= S\ \{(J_1/2)(1-\varepsilon+Q_0)\eta^{-2} + J_1(1-\varepsilon+P_0)\eta\cos(\pi h) + (J_3/2)(1-\varepsilon+T_0)\eta^4 \\
&\quad + J_3(1-\varepsilon+Q_0)\eta^{-2}\cos(2\pi h)\} \\
C &= S\ \{J_2(1-\varepsilon-R_0)\{\cos[\pi(h+k)] + \cos[\pi(h-k)]\}\} \\
D &= S\ \{(J_1/2)(1-\varepsilon-Q_0)\eta^{2} + J_1(1-\varepsilon-P_0)\eta^{-1}\cos(\pi h) + (J_3/2)(1-\varepsilon-T_0)\eta^{-4} \\
&\quad + J_3(1-\varepsilon-Q_0)\eta^{2}\cos(2\pi h)\} \\
\eta &= e^{k\pi i/3} \\
P_0 &= \cos(\theta/6+\alpha),\ Q_0 = \cos(-\theta/3+\alpha) \\
R_0 &= \cos(\theta/2),\ T_0 = \cos(2\theta/3+\alpha),
\end{aligned}$$

where for $\varepsilon > 0$ the smaller exchange interaction for spin components along the x-axis ensures magnetic moments prefer to be confined in yz-plane.

The spin-wave spectrum (out-of-plane and in-plane) is plotted in Fig. 6.19 in the global frame (directly accessible by the experimental INS measurements). Each correlation has two dispersions modes as the honeycomb lattice contains two Bravais sublattices. The out-of-plane dispersion in Fig. 6.19a) becomes gapped at $\boldsymbol{Q}$ in the presence of anisotropy ε with a gapless feature Γ, whereas one of the four in-plane

modes is gapless at $\boldsymbol{Q}$ as shown in Fig. 6.19c). This is more clearly observed in Fig. 6.20 plotting dispersions along the $(0, K, 0)$ directions.

For $\varepsilon = 0.4$, the calculated spectrum reproduces some of the qualitative features of the observed magnetic excitation spectrum as can be seen in Fig. 6.18. Here the polarization factor was also included assuming that the spiral plane is perpendicular to the b-axis, a natural choice given the monoclinic Li_2IrO_3 unit cell (with a unique axis $\boldsymbol{b}$). The sharply dispersing spectrum in Fig. 6.18a) is well-reproduced in b) although the stronger intensity onset at about 2.5 meV is not captured in the simulation. The overall calculated spectrum in d) in the higher $E_i = 15$ meV is quite similar to the measured one in c) including the "band" of scattering at around 6 meV, linking the magnetic scattering in the next Brillouin zone. However, the model predicts additional scattering above 6 meV, not be detected in the measurements. These discrepancies may be due to the simplified nature of the model considered, and possibly could be reconciliated, for instance, more realistic anisotropic interactions of the Kitaev form are considered and/or the fact that J_1 is not the same for all three bonds of the honeycomb is included.

The powder-averaged spectrum of the H1, H2 phases with a ferromagnetic J_1 coupling were also simulated, but they were qualitatively different from the experimental INS data. Within the parameter of a Heisenberg J_1-J_2-J_3 model, an H2 type ordering can reproduce the sign of the Curie-Weiss temperature, the Q-vector of the first magnetic Bragg peak and several key features of the inelastic spectrum, however this model also predicts sizeable intensity Bragg peaks at higher Q, which are not experimentally observed. The H1 candidate model predicts much weaker intensity Bragg peaks at higher Q, so could be more compatible with the diffraction data, however, with the Heisenberg J_1-J_2-J_3 model no solution could be found that explain the observed antiferromagnetic Curie-Weiss temperature, and the observed Q-vector. However, it may be possible that other microscopic spin Hamiltonians with an H1 ground state could be compatible with the data and it would be interesting to see if the extension of the Kitaev Heisenberg model could potentially account for this behaviour.

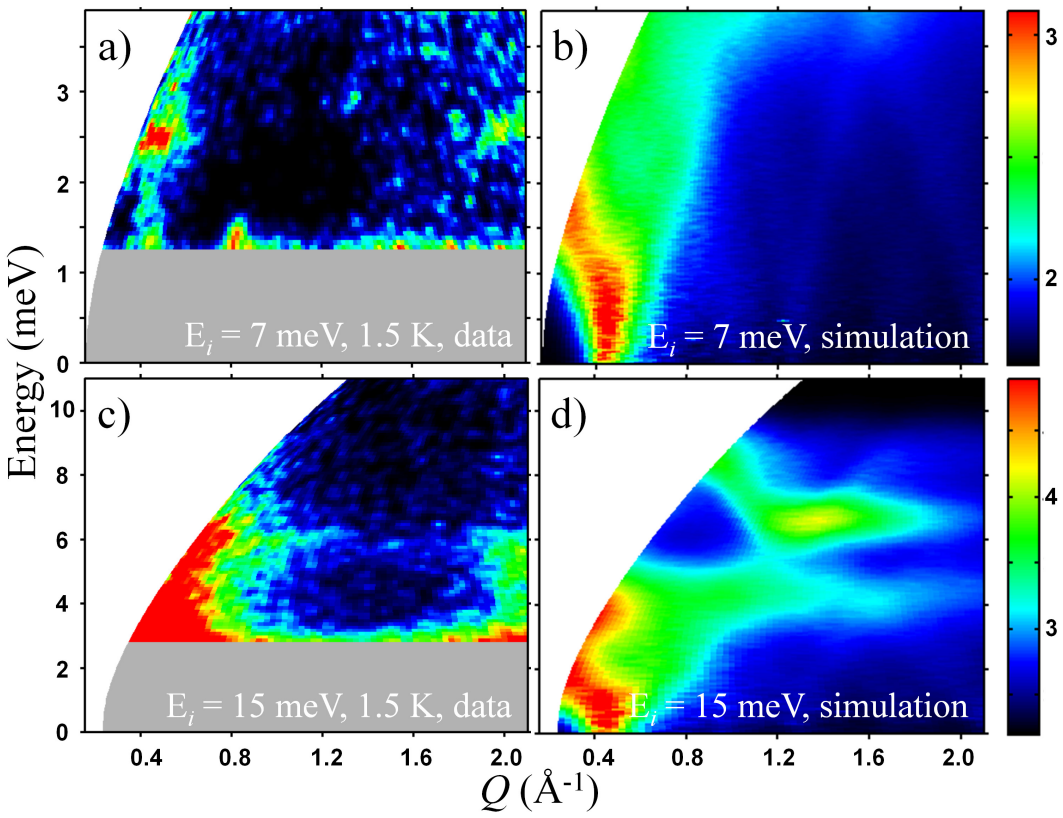


Figure 6.18: Spherically-Averaged Spin-Wave Spectrum in the H2 Phase of the J_1-J_2-J_3 Model with Exchange Anisotropy as in Fig. 6.19 and 6.20. a) INS data at 1.5 K with an incident neutron energy $E_i = 7$ meV. b) Calculated spherically-averaged spin-wave intensity. c) INS data at 1.5 K with $E_i = 15$ meV and d) its corresponding simulation. The simulated intensity was convolved with a Gaussian in energy using the experimental resolution (FWHM) of 0.58, 1.1 meV for b) and d), respectively. The spherical average was done using for each (Q, E) phase space with 500 random Monte-Carlo points (random crystallite orientation with a spherical distribution).

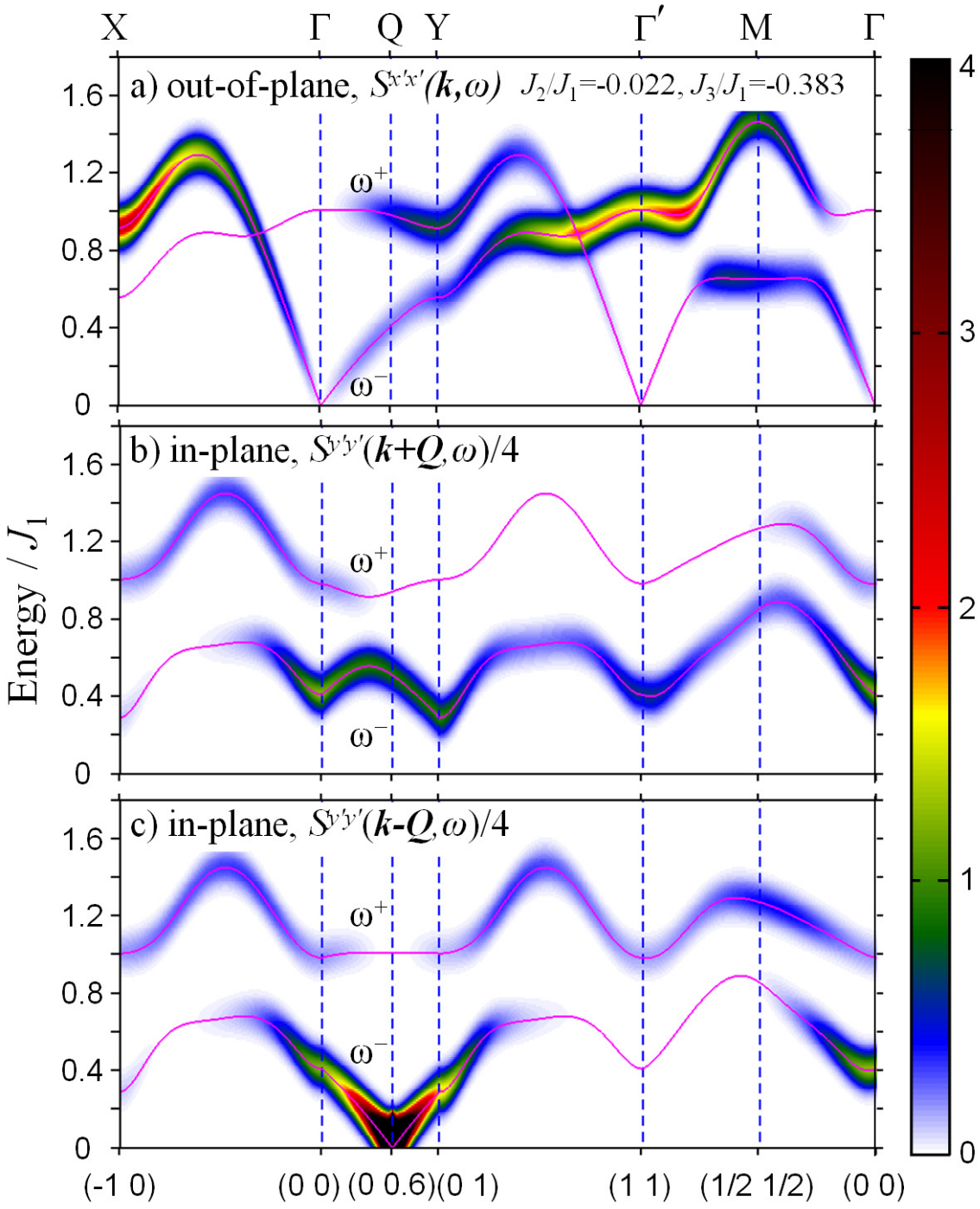


Figure 6.19: Spin-Wave Spectrum in the H2 Phase of the J_1-J_2-J_3 Model with Exchange Anisotropy ($\varepsilon = 0.4$) along High-Symmetry Directions. Spectrum is shown in reciprocal space noted by the arrowed path in Fig. 6.15a). a) Out-of-plane spectrum with colours indicating the spin-spin correlations. b-c) In-plane spectrum showing $\omega^{\pm}_{\boldsymbol{k}\pm\boldsymbol{Q}}$ dispersions.

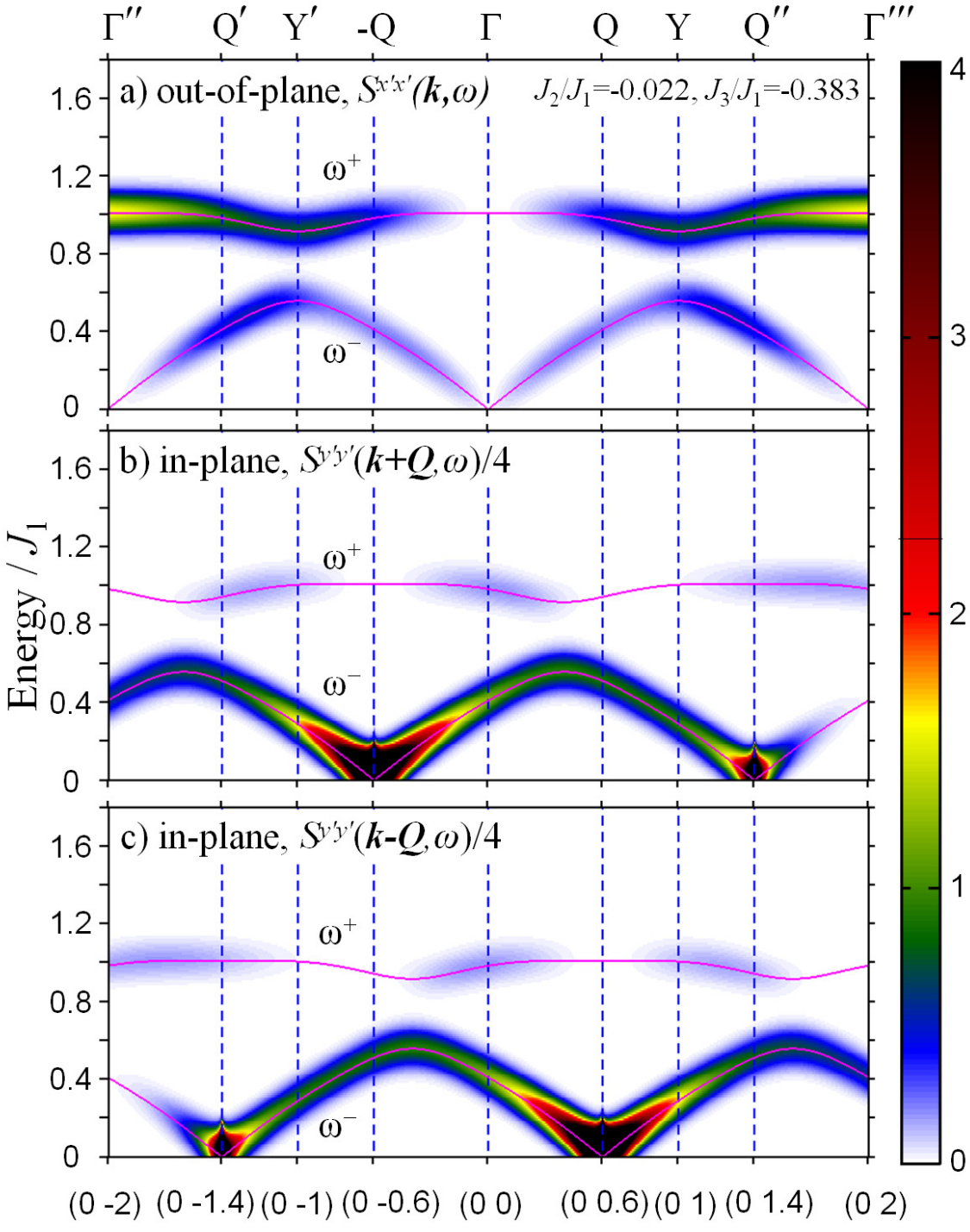


Figure 6.20: Spin-Wave Spectrum in the H2 Phase of the J_1-J_2-J_3 Model with Exchange Anisotropy ($\varepsilon = 0.4$) along the (0K0) Directions. Spectrum is shown in reciprocal space noted by the arrowed path in Fig. 6.15b). a) Out-of-plane spectrum with colours indicating the spin-spin correlations. b-c) In-plane spectrum showing $\omega^{\pm}_{\boldsymbol{k}\pm\boldsymbol{Q}}$ dispersions.

6.6 Discussion

It is surprising that the magnetism of honeycomb Li_2IrO_3 is completely different from the isostructural Na_2IrO_3. Experimental evidence from combined techniques of μ^+SR, neutron diffraction and inelastic neutron scattering supports the long-range spiral magnetic order with a wavevector compatible with a much larger magnetic unit cell than any ground states in the generalised Kitaev Heisenberg model.

Compared to the isostructural Na_2IrO_3, Li^+ ions have smaller ionic radii compared to Na^+ and this could lead to substantial changes in the Ir-O-Ir bond angles, which could modify the exchange interactions, thus potentially stabilising a magnetic order different from the zigzag magnetic phase in Na_2IrO_3.

Although the minimal exchange model considered here based on a Heisenberg J_1-J_2-J_3 model with strong anisotropy and an H2 magnetic order captures some of the basic features of the measured excitation spectrum in Li_2IrO_3, there is some degree of discrepancy such as the position of the stronger scattering at about 2.5 meV and the absence of higher energy scattering in the data. Pulsed-field magnetization experiments found an anomaly indicating a transition in a magnetic field of about 25 T, which could match this 2.5 meV magnetic excitation gap. Moreover, the H2 phase predicts a sizeable intensity of the magnetic Bragg peak at higher Q's, which is however not observed. The alternative H1 phase could be more compatible with the diffraction pattern, but a different spin Hamiltonian (not Heisenberg J_1-J_2-J_3 model) would be needed to explain quantitatively the magnitude of the Q-vector, antiferromagnetic Curie-Weiss temperature and spin-wave spectrum.

6.7 Conclusions

The magnetic properties of Li_2IrO_3 were measured with various experimental techniques such as bulk susceptibility, μ^+SR and elastic and inelastic neutron scattering with a high-quality powder sample. Susceptibility showed dominant AFM interactions with a small Curie-Weiss temperature of -33 K, and an anomaly near 15 K indicative of a transition to long-range magnetic order, which was confirmed by μ^+SR

experiments.

By powder elastic neutron diffraction measurement, one magnetic Bragg peak was detected, which was also seen on the elastic line in powder inelastic neutron scattering experiment. This magnetic wavevector is distinct from those corresponding to the collinear phases, and it is consistent with a spiral phase that could be accommodated in the Heisenberg J_1-J_2-J_3 model (with or without easy-plane exchange anisotropy).

The powder inelastic neutron scattering measurements with an optimised setup revealed sharply dispersive excitations stemming from the softening wavevector of the magnetic Bragg peak at around 0.41 $Å^{-1}$ with a stronger onset near at 2.5 meV, and the low energy scattering continued down to the lowest energy probed (0.7 meV), with no signature for a spin gap in this energy range.

The INS data collected from MERLIN was attempted to be reproduced by linear spin-wave calculation in the spiral phase with in-plane anisotropy in the ***ac***-plane. In the Heisenberg J_1-J_2-J_3 model, since the H1 phase was not compatible with the antiferromagnetic Curie-Weiss temperature and the H3 phase does not provide finite intensity at the observed magnetic Bragg peak, the H2 phase was considered in detail as it satisfied both constraints for AFM Curie-Weiss temperature and the magnetic ordering wavevector. The mean-field energy and the phase diagram were derived following Ref. [7] as a cross-check, and the analytical expressions for spin-wave dispersions in the H1 and H2 phase were also reproduced following Ref. [7]. A set of exchange parameters with the Heisenberg J_1-J_2-J_3 Hamiltonian with the exchange anisotropy was proposed, that could explain several key features of the observed inelastic neutron scattering spectrum. Within a Heisenberg J_1-J_2-J_3 model, the H2 phase is the model that can explain the magnitude of Q and the sign of the CW temperature (AFM), however the H2 phase predicts sizeable intensity Bragg peaks at higher Q which were not observed. An H1 phase could be more compatible with the diffraction pattern, but it would need a different Hamiltonian to explain the Q-vector and CW temperature. It would be intriguing to see if the generalisation of KH model could reproduce the data.

Chapter 7

Crystal Structure of $(Na_{1-x}Li_x)_2IrO_3$

This chapter presents the experimental results of single crystal X-ray diffraction on $(Na_{1-x}Li_x)_2IrO_3$ ($x = 0.05 \sim 0.4$), and the structure determination. The single crystals at the lower dopings ($x = 0.05 \sim 0.2$) show a good sample quality, unlike the higher dopings ($x = 0.3, 0.4$) which reveal an increasing number of multi-grains. The sensitivity of the x-ray diffraction intensity to the precise location of Li ion in the structure and the site-mixing of Na and Ir ions in the honeycomb plane are tested with various models, showing all refined structures are similar especially for the lower doping concentrations, which means only the averaged structure could be extracted. In determining the crystal structure, a degree of site-mixing in the honeycomb layer has to be included for the refinements to converge. The simulated single crystal x-ray diffraction patterns clarify a dominant effect of site-mixing on the Bragg peaks and insensitivity on Li positions in x-ray diffraction experiments. Although only the averaged crystal structures are obtained, the lattice parameters are robustly determined over the whole Li-doping range, showing that a, b-lattice parameters are more sharply contracted than the c-lattice parameter and β angle, and based on this experimental information, ab initio calculations show that Li ions are preferentially occupying the honeycomb layers sites.

7.1 Introduction

The search for exotic magnetic properties such as quantum spin liquids is one of the most active research areas in frustrated magnetism. The research work on iridate system has been ignited by theoretical proposals for possible existence of topological insulators [32] and Kitaev spin liquids in honeycomb $\mathcal{A}_2IrO_3$ ($\mathcal{A}$=Na, Li) [3]. Since Na_2IrO_3 [30, 57, 39, 31, 40] and iso-structural Li_2IrO_3 (See Chapter 6) turned out to be long-range ordered below a Néel temperature near 15 K, another candidate to test for the existence of a quantum spin liquid is the intermediate phase of $(Na_{1-x}Li_x)_2IrO_3$ [65, 66]. The real structure of Na_2IrO_3 showed rather distorted IrO_6 octahedra, which is thought to be less favourable for dominant Kitaev interaction. Thus, the basic idea is to engineer the shape of IrO_6 octahedra in a more idealised way by substituting the smaller Li ions instead of the bigger Na ions, which is expected to release the squeezed IrO_6 octahedra in the parent Na_2IrO_3 [40] compound. In this limit, the system could have dominant Kitaev interactions over the conventional Heisenberg exchange coupling.

The bulk physical properties such as specific heat and susceptibility of these mixed compounds [65] found that the observed T_N showed a significant reduction with increasing Li doping at the low doping regime, reached a minimum at $x = 0.7$, and then increased again towards $x = 1$, the other end compound of Li_2IrO_3 [31]. Based on this observation, it has been suggested that the system could go through a quantum phase transition between different magnetic orders at around $x = 0.7$. At this doping, the material contained the near perfect honeycomb lattice [65], pointing out that the system is closest to the spin liquid at this doping. Also, the magnetic susceptibility measurements revealed their anisotropic characteristics [65], depending on the direction of an applied magnetic field, suggested to be related to the trigonal distortion of IrO_6 octahedra. Thus, the change of anisotropic susceptibilities from lower to higher doping has been considered as evidence of the sign change of the trigonal splitting from Na_2IrO_3 to Li_2IrO_3 [65].

The structural distortion have been considered as an important factor which could

alter the magnetic properties. For instance, *ab initio* calculations [37, 59, 34] predicted that the electronic structure and magnetic properties of Na_2IrO_3 is very sensitive to the crystal electric field determined by the trigonal distortion of IrO_6 octahedra. Therefore it is essential to determine the detailed crystal structures of $(Na_{1-x}Li_x)_2IrO_3$ at various Li-doping to investigate how the lattice parameters and microscopic structure evolve upon Li-dopings. This would be also an important information for *ab initio* calculations to understand the electronic structure, magnetic order and spin dynamics. This motivated the present study to precisely determine the crystal structure of the doped system.

This chapter presents single-crystal x-ray diffraction studies of the doped phases $(Na_{1-x}Li_x)_2IrO_3$ (x = 0.05 to 0.4). It is found that site-mixing between Ir and Na (or Li) ions in the honeycomb lattice is required to make the structural refinement converge. Measurements revealed that for the higher dopings (x = 0.3, 0.4), samples were containing multi-grains, and no common unit cell parameters could index all the grains, which could be consistent with the observation of a miscibility gap above $x > 0.25$ in SEM measurements [66], thus suggests that the samples at the higher Li dopings studied in this thesis were not an uniform solid solution, but were phase separated.

7.2 Experimental Details

To determine the structure, single crystal X-Ray Diffraction (XRD) was performed in the Clarendon Laboratory using a Mo-source Oxford Diffraction Supernova diffractometer on single crystals of $(Na_{1-x}Li_x)_2IrO_3$ (x = 0.05, 0.1, 0.15, 0.2, 0.3, 0.4). This technique proved to work well for Na_2IrO_3, where the diffuse scattering by frequent layering stacking faults (See Sec. 5.3) was well-separated from the main Bragg peaks, and this allowed the quantitative refinement of the crystal structure.

The doped single crystals were grown via the flux method in Philip Gegenwart group at Georg-August-Universität in Göttingen, Germany [66], and the typical size was 70×60×10 μm^3. Preliminary screening experiments were made on over 10 to

20 single crystals for one or two hours, and then the sample quality compared in terms of the number of impurity peaks, grains and the ratio of diffuse scattering intensity to the main Bragg peak intensity. Through this screening process, an optimal single crystal was selected at each doping, and used for collecting x-ray data with good statistics, which was then used for refinements to determine the detailed crystal structure. The data for refinement were usually collected for $10 \sim 22$ hours at room temperature, typically finding more than 1000 peaks indexed with the C2/m model shown in Table 5.1, found for Na_2IrO_3 in Section 5.

7.3 Measurements and Results

The crystals examined showed a good quality at the lower dopings, although samples contained multi-grains especially at higher doping possibly due to the phase separation beyond $x = 0.25$ suggested by SEM measurements [66]. Thus, the experimental results are classified into two subsections: for lower dopings ($x = 0.05$-0.2) in Subsection 7.3.1, and higher dopings ($x = 0.3$, 0.4) in Subsection 7.3.2.

7.3.1 Lower Li-Doped Samples

The selected single crystals of $(Na_{1-x}Li_x)_2IrO_3$ at $x = 0.05$ and $x =0.1$ showed a diffraction pattern consistent with a single monoclinic domain with a minimal level of impurity peaks. In particular, the 5 % doped sample showed the best quality with a small number of impurity peaks and rather weak diffuse scattering. As an illustration of the data quality, typical diffraction patterns in the (HK0) and (0KL) planes for $x = 5$ % Li-doped sample are shown in Fig. 7.1. A well-defined hexagonal diffraction pattern is seen in the (HK0) plane in Fig. 7.1b), and weak diffuse scattering along $\boldsymbol{c}^*$ was observed in Fig. 7.1a).

Structural refinement was carried out within the C2/m space group. The refinement process did not converge well assuming normally occupied atomic positions in Na_2IrO_3 even for the lowest doped sample at 5 %. However, if site occupancy of the nominal Na1 site (site 2a $(0, 0, 0)$ in Table. 5.1), and the centre of the honeycomb

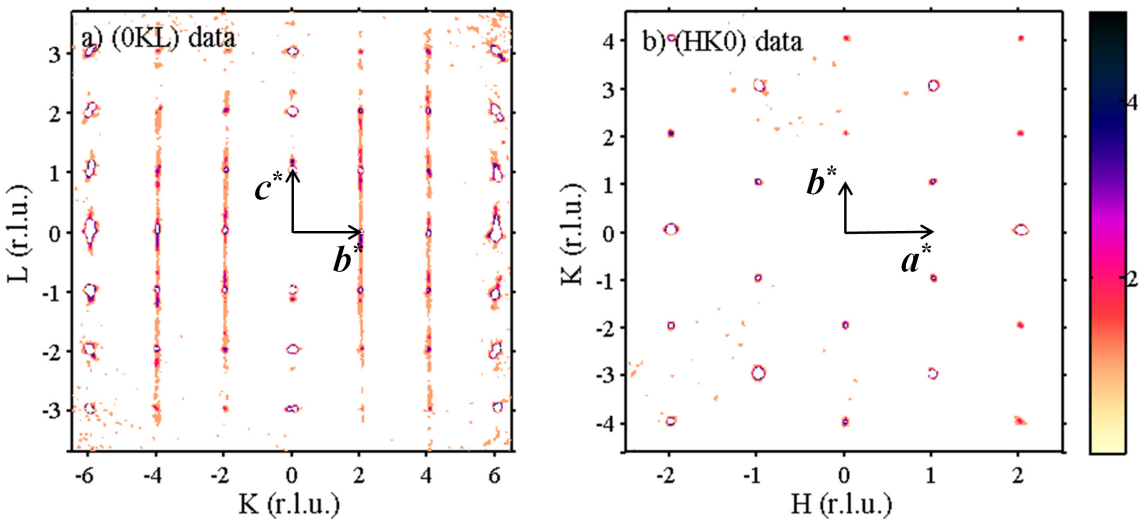


Figure 7.1: X-Ray Diffraction Data for the 5 % Li-doped Sample. a) (0KL) data with the weak diffuse scattering coming from stacking faults considered for Na_2IrO_3 in detail. b) (HK0) data with the clear the hexagonal diffraction patterns, ensuring the single domain of the sample measured. Colorbar represents an arbitrary intensity.

layers is allowed to vary, the refinement can converge with the resulting occupancy, a value larger than unity, which is physically impossible. This suggests the presence of a stronger scatterer at that site, and a natural candidate, in this case would be iridium which scatters x-ray much more strongly (77 electrons for Ir compared to 11 for Na). Then the refinement was done again assuming site-mixing between Ir and Na ions in the centre of the honeycomb, and the refinement converged well. Therefore, a finite site-mixing (f = 15 %) is required in this refinement analysis even for the 5 % Li-doped samples unlike the case of Na_2IrO_3, where only a smaller level of site-mixing (8.6 %) marginally improved the refinement results.

To verify the existence of site-mixing between Ir and Na ions in the honeycomb layer and to also test the sensitivity of the XRD data to Li ions' positions in unit cell, six different crystallographic structural models in the C2/m space group were tested for x = 0.05, 0.1, 0.15 and 0.2 dopings: 1) pure Na_2IrO_3 (x = 0) with no site-mixing, 2) pure Na_2IrO_3 ($x = 0$) but allowing site-mixing between Na and Ir on the nominally Na1 2a and Ir 4g sites, 3) put all doped Li on the Ir site and allow also Ir-Na site-mixing between the Na1 and Ir site, 4) put all doped Li on Na1 site and

allow some Na-Ir site-mixing on this and the Ir site, 5) put all doped Li on Na2 site in the hexagonal NaO_2 layers and allow Na-Ir site-mixing in the honeycomb layer, 6) put all doped Li on Na3 site in the hexagonal NaO_2 layer, and allow Na-Ir site-mixing in the honeycomb layer. It was assumed that the total occupancy on each site is unity and the total atomic count is given by the nominal compositions. Since the total release of occupancy with no constraints lead to a divergence of parameters, refinements did not converge well.

All refinements in the lower dopings did not work well without site-mixing, but improved significantly when site-mixing was allowed, the proportion of the site-mixing f $\sim 14-15$ % was found for $x = 0.05$ and 0.1 Li-doped data, whereas the site-mixing was smaller (f $\sim 4-5$ %) for $x = 0.15$ and 0.2 Li-doped data with, i.e. site Na1 2a $(0, 0, 0)$ was occupied with (1-f)×Na and f×Ir, and site Ir 4g $(0, 1/3, 0)$ was occupied with (1-f)×Ir and f×Na for model 2), and similarly for other models. It was also difficult to identify the unique position of Li atoms, whether on the Ir site 4g or the Na1, 2, 3 sites because models 3-6) refined equally well with very similar refinement results. The final refined atomic positions in the $C2/m$ unit cell in each doping were very close to those in the structure for pure Na_2IrO_3 in Table 5.1 (particularly true for 5 % data). They possibly had a bit more symmetric honeycombs due to the loss of contrast between the honeycomb sites and the centre, but one cannot reliably determine positions of Li atoms to see where Li goes or if it is even present in the sample. This is because Ir is the dominant x-ray scatterer (77 electrons) whereas Li is only very weakly scattering with x-rays (only 3 electrons), thus x-ray diffraction is not a sensitive technique to detect positions of the Li ions.

The results of the x-ray studies on each doping are as follows. The x-ray data was most reliable for $x = 5$ % amongst all dopings. For instance, the sample was a single grain and a vast majority of peaks (84.84 % of the 922 observed peaks) were indexed with a $C2/m$ unit cell. Table 7.1 showed the refined structure for model 4, where Li was assumed to replace Na in the honeycomb layers, position Na1. It gave very similar results for the atomic positions obtained with Li on any of the other sites, or even model 2, where there was no Li at all. The structural

Table 7.1: Structural parameters extracted from 5 % Li-doped single-crystal x-ray data at 300 K. ($C2/m$ space group, $a = 5.379(5)$ Å, $b = 9.314(5)$ Å, $c = 5.594(5)$ Å, $\beta = 108.714(5)^\circ$, $Z = 4$). All sites are fully occupied. U is the isotropic displacement. The goodness-of-fit (S) is 1.269, $wR2 = 0.1684$ and $R1 = 0.0632$ ($R_{\text{int}} = 0.0797$, $R_{\text{sigma}} = 0.051$).

Atom	Site	x	y	z	Occ	U(Å^2)
Ir1	$4g$	0.5	0.16673(8)	0	0.849	0.0074(6)
Na1	$4g$	0.5	0.16673(8)	0	0.151	0.0074(6)
Na2	$2a$	0	0	0	0.498	0.0092(8)
Ir2	$2a$	0	0	0	0.302	0.0092(8)
Li2	$2a$	0	0	0	0.2	0.0092(8)
Na3	$2d$	0.5	0	0.5	1	0.021(4)
Na4	$4h$	0.5	0.3388(11)	0.5	1	0.019(3)
O1	$8j$	0.758(3)	0.1732(11)	0.792(3)	1	0.013(3)
O2	$4i$	0.720(4)	0	0.210(4)	1	0.013(4)

variation between different models (2 to 6) within the doping were minor, only a few percentage in terms of the fractional coordinations of ions and the isotropic thermal parameters. Within the uncertainly of the experimentally determined intensities, the site occupancy of Li ions could not be reliably fitted, resulting in similar outcomes whether Li ions were put on the Na1 or other crystallographic sites. This means that it would be difficult to confidently identify the crystallographic Li sites substituted with this experiment. Thus *ab initio* calculations were performed in the group of Igor Mazin at Naval Research Laboratory, Washington, USA and Roser Valenti at Goethe-Universität Frankfurt, Germany, to identify the most stable structure when Li is doped, which found that at low dopings Li atoms replace Na in the centre of the honeycomb layers [66] as shown in Table. 7.1.

The sample quality and refinement results for the 10 % Li-doped sample were similar to those for the 5 % Li-doped samples. To be specific, a single monoclinic grain was seen in x-ray data and the level of site-mixing necessary for the refinements

Table 7.2: Structural parameters extracted from 10 % Li-doped single-crystal x-ray data at 300 K. (C2/m space group, $a = 5.3819(7)$ Å, $b = 9.315(1)$ Å, $c = 5.580(2)$ Å, $\beta = 108.83(2)°$, $Z = 4$). All sites are fully occupied. U is the isotropic displacement. The goodness-of-fit (S) is 1.467, $wR2 = 0.2143$ and $R1 = 0.0753$ ($R_{\rm int} = 0.053$, $R_{\rm sigma} = 0.0515$).

Atom	Site	x	y	z	Occ	U(Å^2)
Ir1	4g	0.5	0.16684(7)	0	0.8303	0.0065(4)
Na1	4g	0.5	0.16684(7)	0	0.1697	0.0065(4)
Na2	2a	0	0	0	0.2605	0.0171(7)
Ir2	2a	0	0	0	0.3395	0.0171(7)
Li2	2a	0	0	0	0.4	0.0171(7)
Na3	2d	0.5	0	0.5	1	0.022(3)
Na4	4h	0.5	0.3384(7)	0.5	1	0.023(3)
O1	8j	0.757(2)	0.1734(8)	0.791(2)	1	0.014(3)
O2	4i	0.719(3)	0	0.213(3)	1	0.013(3)

($f = 17$ %) is very close to that of the 5 % Li-doped sample data. The detailed structure such as Ir-Ir bond distances and Ir-O-Ir angles were also very similar. The refined crystal structure parameters in model 4, where Li ions were in the Na1 site, for 10 % Li-doped sample is listed in Table. 7.2.

In the samples for doping levels of 15 % or higher, no single grain crystal could be found but the samples always showed multi-grains, where several crystallites were stuck to one another and rotated mostly around the $\boldsymbol{c}^*$-axis normal to the layers. Refinements for those data were successfully performed simultaneously using multiple sets of Bragg peak lists from the separate grains. In the refinements almost of all models converged well, except model 3 for the 15 % data which was unstable. The converged crystal structures were very similar to one another, so it was very hard to extract any definite conclusions about the detailed crystal structure. The fit results only marginally improved when site-mixing of Na atoms on the honeycomb site of f$\sim 4-5$ % was allowed. The atomic positions were fitted the model 4 as in the case of

Table 7.3: Structural parameters extracted from 15 % Li-doped single-crystal x-ray data at 300 K. ($C2/m$ space group, $a = 5.354(11)$ Å, $b = 9.27(13)$ Å, $c = 5.59(3)$ Å, $\beta = 108.7(4)°$, $Z = 4$). All sites are fully occupied. U is the isotropic displacement. The goodness-of-fit (S) is 1.778, $wR2 = 0.2679$ and $R1 = 0.1151$ ($R_{\text{int}} = 0.168$, $R_{\text{sigma}} = 0.105$ for the first grain and $R_{\text{int}} = 0.198$, $R_{\text{sigma}} = 0.157$ for the second grain).

Atom	Site	x	y	z	Occ	U(Å^2)
Ir1	$4g$	0.5	0.16688(15)	0	0.915	0.0086(8)
Na1	$4g$	0.5	0.16688(15)	0	0.085	0.0086(8)
Na2	$2a$	0	0	0	0.2301	0.019(3)
Ir2	$2a$	0	0	0	0.1699	0.019(3)
Li2	$2a$	0	0	0	0.6	0.019(3)
Na3	$2d$	0.5	0	0.5	1	0.025(6)
Na4	$4h$	0.5	0.3394(16)	0.5	1	0.022(4)
O1	$8j$	0.756(4)	0.177(2)	0.792(4)	1	0.016(5)
O2	$4i$	0.709(5)	0	0.204(5)	1	0.005(5)

the 5 % sample, and the refined crystal structure in the model 4 for the 15 % sample is shown in Table 7.3.

X-ray data for the 20 % doping showed even more multi-grains with a larger proportion of impurities peaks than that of the 15 % doping. The best sample was chosen such that it had a minimum number of multi-grains (three) and fewer impurity peaks. The reflection figure-of-merit parameters (R_{int} and R_{sigma}) were quite large, indicating that it was not a very good fit, possibly due to the technical difficulty in calculating Bragg peak intensities when peaks from different grains overlapped. This data is in principle compatible with all six models, thus the refined structural parameters in model 4 shown in Table 7.4 are only indicative. Because the refinement results were close for essentially all of the models considered, there were some systematic uncertainties that were more significant than the errors of the actual fitted positions of the ions. So one can only regard these refined atomic positions as an averaged structure.

Table 7.4: Structural parameters extracted from 20 % Li-doped single-crystal x-ray data at 300 K. ($C2/m$ space group, $a = 5.335(2)$ Å, $b = 9.232(2)$ Å, $c = 5.564(2)$ Å, $\beta = 108.39(4)°$, $Z = 4$). All sites are fully occupied. U is the isotropic displacement. The goodness-of-fit (S) is 2.091, $wR2 = 0.3019$ and $R1 = 0.1237$ ($R_{\text{int}} = 0.245$, $R_{\text{sigma}} = 0.041$ for the first grain, $R_{\text{int}} = 0.147$, $R_{\text{sigma}} = 0.047$ for the second grain and $R_{\text{int}} = 0.301$, $R_{\text{sigma}} = 0.058$ for the third grain).

Atom	Site	x	y	z	Occ	U(Å^2)
Ir1	$4g$	0.5	0.16714(12)	0	0.9038	0.0111(7)
Na1	$4g$	0.5	0.16714(12)	0	0.0962	0.0111(7)
Na2	$2a$	0	0	0	0.0075	0.0152(19)
Ir2	$2a$	0	0	0	0.1925	0.0152(19)
Li2	$2a$	0	0	0	0.8	0.0152(19)
Na3	$2d$	0.5	0	0.5	1	0.027(5)
Na4	$4h$	0.5	0.3377(14)	0.5	1	0.030(4)
O1	$8j$	0.759(5)	0.1780(17)	0.805(5)	1	0.025(5)
O2	$4i$	0.716(5)	0	0.191(5)	1	0.019(5)

In the low dopings, some variation of the quality was found between different samples of the same nominal composition. For example, the best sample for the 15 % doped case showed only a small amount of diffuse rods of scattering along $\boldsymbol{c}^*$-axis, indicating a well-formed three-dimensional structure with only a few stacking faults. However, all other 15 % doped samples screened showed a sizeable degree of diffuse scattering, similar to that of most 5 % and 20 % samples. This indicates that there was a variability in the amount of diffuse scattering from sample to sample (different amount of stacking faults).

The fact that site-mixing was essential in the refinement analysis for the Li-doped sample can imply that the inhomogeneities in the lattice introduced by the Li doping disturb the Ir honeycomb network, such that it makes the system more prone to site-mixing in the honeycomb plane, which will lead to an incomplete ionic order $Na^+ : Ir^{4+} = 1 : 2$ into honeycomb of Ir sites. On the other hand, it has been also

Table 7.5: Structural Information for Lower Li-Doped Samples. Values are from the refined structures at each doping level as shown from Table 7.1 to 7.4, representing a shorter and longer distances and angles. Parameters for undoped Li_2IrO_3 [47] and Na_2IrO_3 [40] are also given for the comparison.

Dopings	Ir-Ir distances (Å)	Ir-O distances (Å)	Ir-O-Ir angles (°)
0 %	3.1298 ∼ 3.1379	2.06 ∼ 2.08	98 ∼ 99.4
5 %	3.105 ∼ 3.106	2.073 ∼ 2.078	96.8 ∼ 97.0
10 %	3.1056 ∼ 3.1083	2.074 ∼ 2.078	96.8 ∼ 96.9
15 %	3.089 ∼ 3.09	2.03 ∼ 2.064	97.4 ∼ 99.2
20 %	3.0751 ∼ 3.0861	1.999 ∼ 2.016	99.9 ∼ 100.2
100 %	2.9787 ∼ 2.9789	1.9671∼ 2.08	94.7 ∼ 95.3

observed that the site-mixing is more frequent for the 5 %, 10 % samples than for the 15 %, 20 % samples although the number of multi-grains was smaller for the 5 %, 10 % samples.

The detailed structural information such as Ir-Ir, Ir-O distances and Ir-O-Ir angles is summarized in Table 7.5 based on the refinement results with the model 4 as given from Table 7.1∼ 7.4. Ir-Ir and Ir-O distances monotonically decreased upon Li-doping, whereas Ir-O-Ir angles had a minimum value at 5 % and 10 % dopings. Thus the octahedra distortion did not show a monotonic behaviour, which made it difficult to understand how the distortion can play a role to modify the exchange interactions and subsequently the magnetic order. Thus, the structural parameters obtained with the current x-ray data can only be taken as representative information.

To summarize, the best single crystals amongst over 10 to 20 samples at each doping were selected, and high-quality x-ray data was collected. For the 5 % and 10 % Li-doped samples, one grain crystals could be found, whereas multi-grain samples were found for the 15 % and 20 % Li-dopings with more overlap of Bragg peaks from different grains, which made the refined structure less reliable. Six crystal structure models have been compared with the data, and almost all models except model 1, where there is no site-mixing, worked equally well for all lower dopings ($x = 0.05-0.2$).

Thus, the existence of Li ions and their positions cannot be distinguished by using the x-ray data alone, and an averaged crystal structure can be only extracted with the samples studied in this project. To identify the Li positions, *ab initio* calculations were performed, revealing that at low dopings ($x < 0.25$) Li ions occupy the Na1 site in the honeycomb layer [66], so Li ions were fixed in the Na1 with the nominal occupancy. The refined representative structures are given in Table 7.1∼7.4. The summary of the detailed structural information is presented in Table 7.5. All five refined models were very similar, and atomic positions were found to be very close to the nominal values of the undoped Na_2IrO_3 $C2/m$ structure. However, a significant distinction in the refinements with the doped structure compared to the undoped case was that the data of the doped system could only be refined with a site-mixing between Ir and Na ions in the honeycomb layer.

The calculation of diffraction intensity is compared later in Section 7.4 for various models to scrutinise the effect of site-mixing and sensitivity to the location of Li ions.

7.3.2 Higher Li-Doped Samples

All samples at higher dopings at $x = 0.3$ and 0.4 showed even more multi-grains and unidentified random peaks, likely due to impurities. Also strong diffuse rods of scattering along $\boldsymbol{c}^*$-axis were seen, similar to what was observed in the $15 - 20$ % Li-doped samples.

Similar to the lower doping cases, the refinement generally gave better results with the site-mixing allowed in the honeycomb layer, and there was a similar ambiguity on the positions of substituted Li ions. Thus, the detailed analysis of the microscopic crystal structure was not improved compared to those from the lower dopings. Also, since Bragg peaks from different grains were sometimes overlapping, particularly for the highest 40 % doping samples, it was difficult to separate the diffraction pattern reliably into contributions from the different grains, which made the refined structure even less reliable than for the lower dopings, thus a detailed structural refinement was not pursued further.

The increased number of multi-grains observed for the $x = 0.3$ and 0.4 samples and

a difficulty to index all peak reliably with a common unit cell parameters for the grains suggests that those samples were likely multi-phases. It is consistent with the scenario of possible phase separation revealed by Scanning Electron Microscope (SEM) study on $(Na_{1-x}Li_x)_2IrO_3$ single crystals at $x = 0.3$ and $x = 0.6$ [66], which identifies two phases and separate micro-domains at each doping respectively interpreted as evidence of phase separation at $x > 0.25$.

Fig. 7.2 shows the systematic trend seen in the evolution of the lattice parameters. The lattice parameters a, b, c and a monoclinic angle β in the C2/m unit cell are plotted as a function of Li-doping for $x = 0.05 \sim 0.4$. At higher dopings, the values correspond to averages over parameters of the main grain. The plotted parameters are the averaged values over between 6 to 17 distinct and reasonably good samples at each nominal doping composition, having good reflection statistics ($R_{\rm int}$, $R_{\rm sigma}$), and a small errors indicates the good distribution of fitted values. The lattice parameters of the end point at $x = 0$ (Na_2IrO_3) are the averaged values for 12 data including the structure in Table 5.1 [40], whereas those of the end system $x = 1$ (Li_2IrO_3) are averaged values over the two published structures [47, 31] by using values converted to the C2/m notation (from the reported C2/c notation in one case).

A noticeable trend in Fig. 7.2 is that the in-plane lattice parameters a and b contract at a similar rate when more Li ions are substituted, whereas c and β remain almost constant up to the maximum nominal doping of 20 %. It could suggest that the interlayer stacking spacing is not significantly affected by the substituted Li ions, but the in-plane lattice parameters shrink as the smaller Li^+ is replaced with the larger Na^+ ions. However, there is also a possibility that Li ions may be substituted mainly in the hexagonal layers, which can also shrink the in-plane lattice parameters. The $x = 0.4$ data seems anomalous in this respect as the a and b values do not agree to have contracted as much as expected by continuing the trend from the lower dopings (dashed lines in Fig. 7.2), this may be because the sample has phase separated and the main grain is representative of the lower doping, $x = 0.25$ suggested by *ab initio* calculation [66].

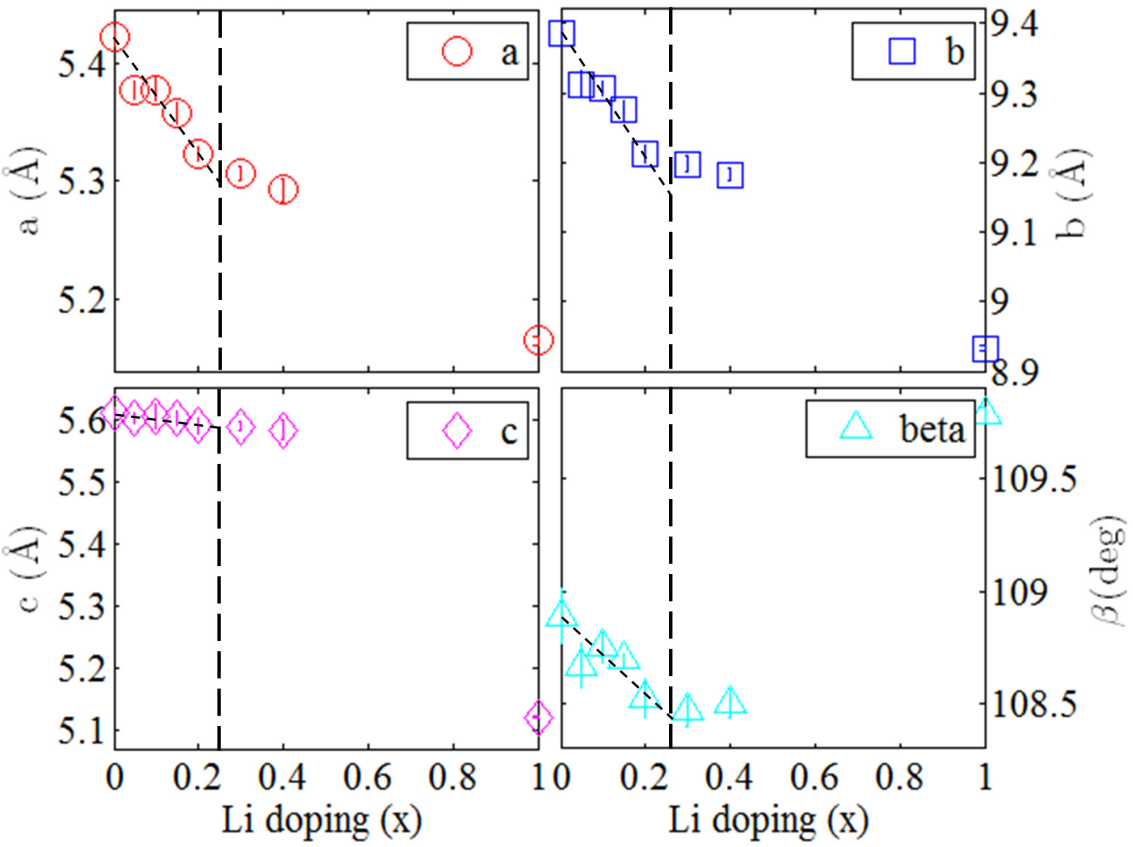


Figure 7.2: Evolution of Lattice Parameters in $(Na_{1-x}Li_x)_2IrO_3$ upon Li-doping. Averages of many crystals studied at the same composition are shown. Note that 10 % Li-doping on the x-axis means $x = 0.1$ in $(Na_{1-x}Li_x)_2IrO_3$. The vertically long-dashed line is for $x = 0.25$ and the inclined dotted lines are the guideline for eyes. Dashed lines show the linear trend in the parameters dependence on dopings for $x < 0.25$.

In order to examine where Li ions could go in the lattice, *ab initio* structural relaxation calculations have been performed with $(Na_{1-x}Li_x)_2IrO_3$ at various dopings [66]. It was found that at small dopings, $x \leq 0.25$, substituting Na by Li in the $Ir_{2/3}Na_{1/3}O_2$ plane is energetically much more favorable than in the NaO_2 plane, in agreement with ionic size considerations, where the smaller Li^+ ions prefer to be placed inside the honeycomb layer at the Na1 position to avoid the higher energy when Li is substituted in the larger Na layer. After the $Ir_{2/3}Na_{1/3}O_2$ planes are completely substituted by Li ions to form $Ir_{2/3}Li_{1/3}O_2$ layers, further Li doping in the interlayers is energetically unfavorable, compared to a phase separation into the $x = 0.25$ and an $x = 1$ phase [66].

The current experiments could be improved in various direction. If other crystals of the $x = 5$ % doping or so with a more complete ionic order, having the well-formed Ir honeycombs, could be synthesized, it might be possible to detect the actual Li positions more sensitively, so determine where Li ions preferentially occupy the hexagonal Na layers or centre of the Ir honeycombs. Another route is if high-purity single crystals of even higher doping such as 70 % become available, the differences in the Bragg peaks intensities between alternative Li positions may become large enough to be detected. Moreover, one can use other experimental tool, for instance neutron diffraction experiments will more sensitively detect the positions of Li ions than the x-ray method because of the larger scattering cross-section of neutrons from Li ions. It will be also interesting to examine the magnetic order of $(Na_{1-x}Li_x)_2IrO_3$ since magnetic ground states of Na_2IrO_3 (discussed in Section. 4) and Li_2IrO_3 (examined in Section. 6) are distinct. This may suggest that the intermediate magnetic ground state is also different from those of the two end compounds, and is possibly close to the proposed quantum spin liquid [65]. This intermediate phase will be intriguing to examine in both contexts of an unusual magnetic structure and its spin dynamics. A recent study [65] showed that single crystal growth at $x = 0.7$ is possible, and suggested a possible quantum phase transition near that critical concentration attributed to the close proximity to a nearby quantum spin liquid phase.

7.4 Structure-Factor Calculations of the Diffraction Pattern

In this Subsection, the simulated x-ray diffraction patterns are discussed to compare effects on the diffraction intensities due to site-mixing and different Li positions. The XRD simulations were done using four structural models with atomic positions and site-mixing described in Table 7.1 (C2/m notation): a) pure Na_2IrO_3 ($x = 0$) without site-mixing, b) pure Na_2IrO_3 ($x = 0$) with $f = 14$ % site-mixing between Na1 and Ir 4g site in the honeycomb plane, c) same as b) with $x = 5$ % Li ions on Na1 2a site and allow 14 % Na-Ir site-mixing, d) same as c) but with $x = 25$ % Li on Na1 site. The comparison between a) and b) will investigate an effect of site-mixing, and b) and c) the effect of 5 % Li doping, and c) and d) the effect of 25 % Li doping on the simulated intensity.

The simulated (0KL) planes of the four models (a-d) are shown in Fig. 7.3 with cuts in Fig. 7.4 so as to directly compare the evolution of the peak intensities of comparative models. The biggest change in the calculated profile intensity is the dramatic decrease in the peak intensities for (02L) and (04L) peaks, L integer compared to those at (00L) and (06L) positions when site-mixing occurs, which is similar to what was observed in Fig. 7.1a). Even with a frequent site-mixing (∼9%) in the undoped sample (See Fig. 5.6a)), the relative intensity ratio of the (020) to (060) peak is 0.13 whereas it is only 0.06 for 5 % Li-doped data from Fig. 7.1a), and the latter ratio is much closer to the calculated value of 0.03 from Fig. 7.3c). Thus this relative feature in the intensity pattern in the 5 % data is well-captured by the model with site-mixing. Note that other experimental factors could also contribute the difference, i.e. such as absorption factor, which was difficult to incorporate very reliably due to the large x-ray absorption of iridium ions.

The calculation in Fig. 7.4 shows that the Ir-Na site-mixing is the dominant factor in determining any change of Bragg peak intensities in the doped structure compared to the nominal pure Na_2IrO_3 structure. Once some site-mixing is taken into account, the change of intensity due to substitution of Na ions by Li ions have a minor effect

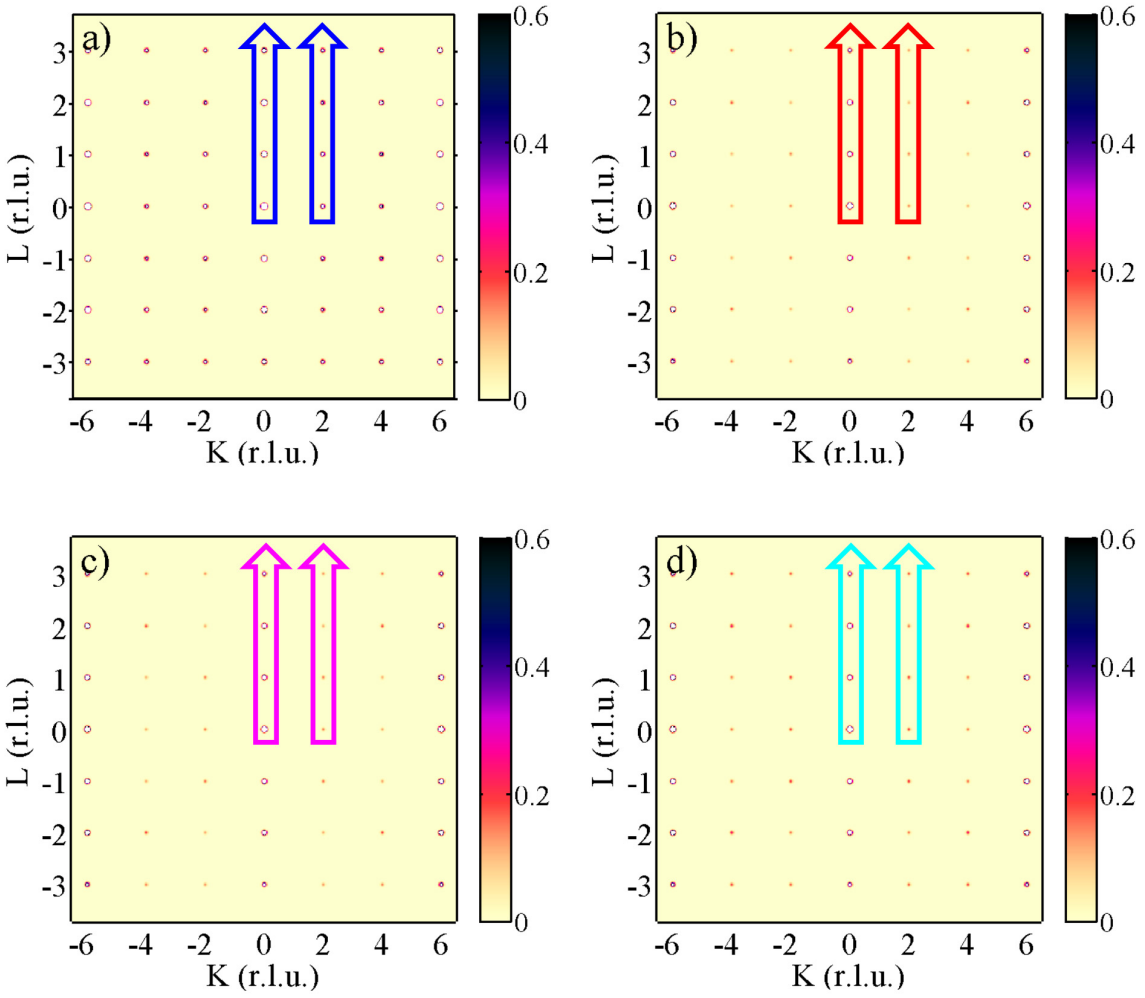


Figure 7.3: Simulated (0KL) Diffraction Planes. a) pure Na_2IrO_3 ($x = 0$) in the C2/m model with no site-mixing (Table 5.1), b) pure Na_2IrO_3 ($x = 0$) in the C2/m model but allowing site-mixing between Na1 and Ir sites, c) put all doped $x = 0.05$ Li on the Na1 2a site and allow some Na-Ir site-mixing on this and the Ir 4g site, d) same as c) but with $x = 0.25$ Li on the same Na1 site. Colorbar indicates the calculated arbitrary intensity.

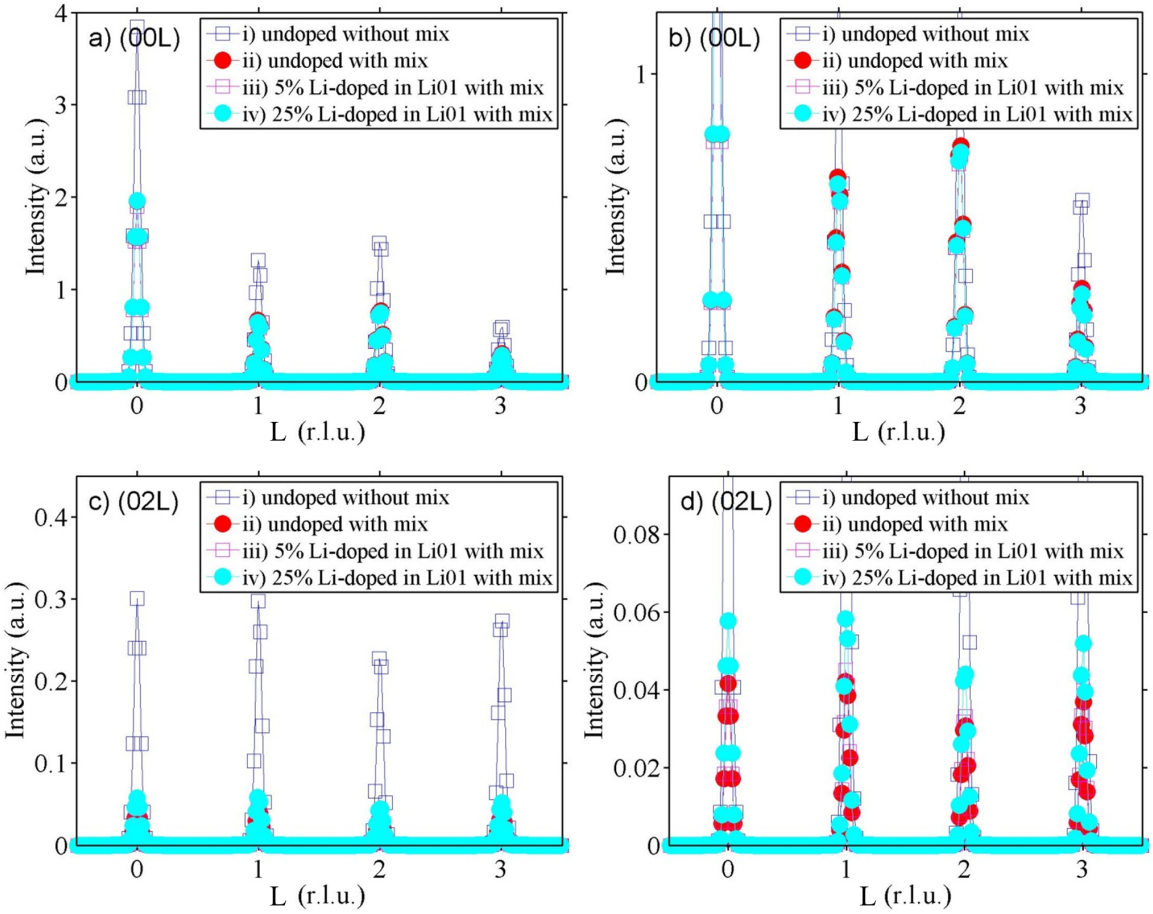


Figure 7.4: Scan along (00L) and (02L) Directions in the Simulated Diffraction Pattern. Scans are indicated by arrows in Fig. 7.3. Right panels are the same as the left panels, but a zoomed-in vertical axis.

as can be seen for both the 5 % and 25 % dopings. For those cases the intensity is not significantly modified, which could be the reason why the positions of Li-ions in the refinement of x-ray data could not be reliably obtained.

In conclusion, the diffraction simulations demonstrate that site-mixing has a much stronger impact on the drop in intensities than the Na substitution by Li ions at least up to a level of doping of 25 %, which explains why similar refined structures were obtained in five models with different Li positions as discussed in Section 7.3.

7.5 Conclusions

The crystal structure of $(Na_{1-x}Li_x)_2IrO_3$ at various dopings, a candidate for a quantum spin-liquid, were investigated by single crystal x-ray diffractometre. For lower dopings ($x = 0.05 - 0.2$), the refinement worked well after allowing for site-mixing between Ir and Na in the honeycomb layer, unlike the parent undoped compound Na_2IrO_3 where no evidence for significant site mixing could be found since the refinement was already working well without any site-mixing. Note that the small amount of site-mixing only marginally improve the agreement with the x-ray data. Six different models were used to test the sensitivity on Li positions and the effect of site-mixing, with the result that all five refined structures with site-mixing were roughly similar with only a few percentage difference in the fractional atomic coordinate within the unit cell. They were also similar to the parent structure of Na_2IrO_3 particularly for 5 % doping result. Structure-factor calculation of the diffraction patterns also supported the necessity to include site-mixing and insensitivity of the x-ray data in detecting the lightest metal ions, Li ions, consistent with refinement results.

Higher Li-doped samples showed many more co-existing crystal grains and an increased overlap of nuclear Bragg peaks from these multi-grains, which made refinements less reliable. Since the current x-ray diffraction does not effectively detect Li positions as proved in both the refinement and simulation, only the averaged structure could be extracted. It does not enable one to perform the more detailed structural analysis such as the change of bond angles or the trigonal distortion in IrO_6 octa-

hedra, which is thought to be an important factor to determine the changes in the exchange couplings, the nature of the magnetic ground state and excitations.

On the other hand, the lattice parameters were robustly determined since they solely depended not on intensities but on the positions of Bragg peaks. The systematic dependence of the averaged lattice parameters on Li doping was extracted from multiple x-ray data, finding a steeper reduction in the a, b-lattice parameters than the c-lattice parameter and monoclinic angle β, which remains constant up to 20 % Li doping. This potentially means that Li ions are preferentially substituted into the honeycomb layer, and as suggested by *ab initio* relaxation calculations which predicted that Li ions preferentially locate in the centre of the honeycomb plane up to 25 % doping and beyond this doping phase separation into $x = 0.25$ and $x = 1$ phases becomes energetically favourable. It will be interesting to study the detailed crystal structures at the higher dopings near $x = 0.7$ where homogeneous solid solution samples have been reported with the $C2/m$ structure even single crystal samples are available [65], in order to find the trend in the distortion of the IrO_6 octahedra, and the magnetic properties and test the proposed scenario for a critical point.

Chapter 8

Concluding Remarks

Throughout this thesis, the cooperative magnetic order and excitation of $5d$ transition metal oxides $\mathcal{A}_2IrO_3$ ($\mathcal{A}$=Na, Li) and the intermediate material (solid solution) $(Na_{1-x}Li_x)_2IrO_3$ have been examined.

For the quasi-two-dimensional honeycomb antiferromagnet Na_2IrO_3, long-range magnetic order was confirmed with muon spin relaxation measurements at low temperature, which was consistent with bulk magnetic susceptibility results. Inelastic neutron scattering measurements have been done successfully using an optimised setup to minimise the strong neutron absorption from iridium nuclei. Measurements observed a clear sinusoidal magnetic dispersion with a softening wavevector, which corresponds to either a zigzag or stripy ordered phases. Using linear spin-wave theory, the magnetic excitation spectrum has been calculated for the stripy phase in the Kitaev-Heisenberg model, finding a qualitatively different spectrum compared to the observed inelastic neutron scattering data. An alternative spin Hamiltonian, the isotropic Heisenberg J_1-J_2-J_3 model, was also used to calculate the linear spin-wave spectrum, in both the zigzag and stripy phases. The best agreement with the data has been achieved with the magnon spectrum of the zigzag order. This result suggests that the further neighbour coupling could have an important role in stabilising the zigzag magnetic structure in Na_2IrO_3. The presence of small antiferromagnetic interlayer interaction was also considered, and showed to have only a minor effect on the calculated spectrum, affecting only on the boundary of the magnetic scattering at low Q, so the level of agreement with the data was similar to a pure 2D model.

An upper bound of a possible Kitaev exchange interaction present in addition to the Heisenberg J_1-J_2-J_3 interaction was also estimated. A recently proposed generalised Kitaev-Heisenberg model was also considered to be consistent qualitatively with the observed data. To unambiguously distinguish between the generalised Kitaev-Heisenberg model and the Heisenberg J_1-J_2-J_3 model, other experimental techniques to directly access the Γ-point ($Q = 0$) excitation would be useful. The magnetic anisotropy was also studied with low-energy higher-resolution inelastic neutron scattering experiments, which observed features consistent with a small spin gap. The observed data was parameterised by using a linear spin-wave spectrum in the zigzag phase assuming an Ising-like exchange anisotropy.

To gain an understanding of the structure and how it may affect the strength of the anisotropic Kitaev interaction, the crystal structure of Na_2IrO_3 was studied in detail using a single-crystal x-ray diffraction technique to improve earlier powder studies. The diffraction pattern observed sharp Bragg peaks as well as a periodic pattern of diffuse rods of scattering along a $\boldsymbol{c}^*$-axis, which was quantitatively explained by a simple model of structural staking faults. The contribution of diffuse scattering was unambiguously separated from the main peaks, which lead to a robust determination of the crystal structure. The obtained unit cell has the C2/m space group with half of the unit cell size of the previously proposed C2/c unit cell. The stability of the C2/m model compared to the C2/c model was proved by *ab initio* structural relaxation calculations, which showed that the latter converged to the former structure. Moreover, via direct structure-factor calculations, it was shown that additional peaks predicted in the C2/c space group were not detected in the experimental data. By comparing four idealised crystal structures with the real structure, the major distortion away from cubic IrO_6 octahedra at 90° Ir-O-Ir bonding is a trigonal squashing along the ⟨111⟩ cubic direction parallel to the $\boldsymbol{c}^*$-axis in the unit cell. This leads to significant deviations from the ideal 90° Ir-O-Ir bonds required for dominant Kitaev interactions. This information may be important for future *ab initio* calculation of the exchange interaction. The asymmetry of IrO_6 and NaO_6 octahedra in the honeycomb plane was attributed to the charge inequality of cations (Ir^{4+} and Na^+), and different ionic

radii, which was also captured by *ab initio* simulations. Several "idealised" crystal structures were explicitly given in this thesis, and this information could be used for theoretical calculations to investigate a route to ensure a dominant Kitaev exchange interaction.

The search for magnetism of isostructural Li_2IrO_3 was motivated by the prediction that it could host a more significant Kitaev interaction than Na_2IrO_3. Magnetic susceptibility measurements showed an antiferromagnetic interaction with an onset of long-range magnetic ordering proved by muon spin relaxation experiments. Powder inelastic neutron experiments observed a strongly dispersive excitation that was qualitatively different from Na_2IrO_3. Powder elastic neutron diffraction measurements found a single magnetic Bragg peak, which was consistent with the peak observed in the elastic line in powder inelastic neutron scattering data. The magnitude of this wavevector corresponds to a larger unit cell than that of the zigzag phase, which implies an incommensurate spiral magnetic order in Li_2IrO_3. The Heisenberg J_1-J_2-J_3 model was considered with three spiral orders, the H1, H2 and H3 structures. Since H3 did not reproduce the observed Bragg peak and H1 did not satisfy the antiferromagnetic Curie-Weiss temperature, the H2 phase was considered in detail. The inelastic neutron scattering data was compared to linear spin-wave calculations for the H2 spiral order. The isotropic J_1-J_2-J_3 Hamiltonian could not explain the observed data, and qualitatively agreement could be obtained by anisotropic interactions in the form of in-plane exchange anisotropy. The spherically-averaged magnetic spectrum with this anisotropy qualitatively reproduced the same key features in the data. Thus, within a Heisenberg J_1-J_2-J_3 model, the H2 phase is the one that can explain the magnetic excitation data, the magnitude of Q and the sign of the CW temperature (AFM). However, the H2 phase predicts sizeable intensity Bragg peaks at higher Q which were not observed. An H1 phase could be more compatible with the diffraction pattern, but it would need a different Hamiltonian to explain the Q-vector and CW temperature. It would be interesting to see if the generalisation of KH model could reproduce the experimental data.

The crystal structures of the intermediate phase $(Na_{1-x}Li_x)_2IrO_3$ materials ($x =$

$0.05 - 0.4$) were considered as a potential route to realise a quantum spin liquid, and the structure was examined using single crystal x-ray diffraction. Lower Li-doped samples ($x = 0.05 - 0.2$) showed a better sample quality with a small number of grains, with fewer impurity peaks, whereas higher Li-doped samples ($x = 0.3, 0.4$) showed much more grains, with large amounts of impurity peaks. Using the best sample at each Li-doping, six different structural models were tested, finding an insensitivity of the refinement results to the Li positions and the existence of some level of site-mixing, which is again supported by structure-factor calculations for the diffraction patterns. Due to this constraint, the refined crystal structures obtained using x-ray data with samples studied in this thesis are representative. On the other hand, the lattice parameters were robustly extracted from the diffraction patterns, showing a systematic dependence upon Li-dopings. It was found that there was a sharper decrease in the a, b-lattice parameters than in the c-lattice parameter and the monoclinic angle β, which remained almost constant up to 20 % Li-doping. *Ab initio* relaxation calculation proposed that Li ions preferentially replace Na in the centre of the honeycomb network up to 25 % Li-doping, and beyond this level of doping it was predicted that the phase separation became energetically more favourable into $x = 0.25$ and $x = 1$ phases. The prediction of phase separation is consistent with the observed evolution of lattice parameters, as the observed decrease in the a, b-lattice parameters became moderate above 20 % doping, possibly due to the mixture of the different Li-dopings resultant from phase separation. The solid-solution samples at higher Li-dopings would be interesting to be studied in a context of a possible quantum phase transition between distinct magnetic orders of the Na_2IrO_3 and Li_2IrO_3 end members of the series.

Appendix A

Dynamical Correlation

An analytical expression of the dynamical structure factor [41] is shown in this Appendix in the case of the 4×4 Hamiltonian such as

$$\mathsf{H} = \begin{bmatrix} A & B & C & D^* \\ B^* & A & D & C \\ C & D^* & A & B \\ D & C & B^* & A \end{bmatrix}. \tag{A.1}$$

The dynamical correlations (per magnetic site) are obtained as

$$\begin{aligned} S^{xx} \quad (\boldsymbol{Q},\omega) = \mathcal{C}\tfrac{S}{8} \Big[& \tfrac{|W(-\omega_+)+X(-\omega_+)+Y(-\omega_+)+Z(-\omega_+)|^2}{N(-\omega_+)} + \\ & \tfrac{|W(\omega_+)+X(\omega_+)+Y(\omega_+)+Z(\omega_+)|^2}{N(\omega_+)} \Big] \; G(\omega-\omega_+) \\ + \mathcal{C}\tfrac{S}{8} \Big[& \tfrac{|W(-\omega_-)+X(-\omega_-)+Y(-\omega_-)+Z(-\omega_-)|^2}{N(-\omega_-)} + \\ & \tfrac{|W(\omega_-)+X(\omega_-)+Y(\omega_-)+Z(\omega_-)|^2}{N(\omega_-)} \Big] \; G(\omega-\omega_-) \end{aligned} \tag{A.2}$$

where $G(\omega-\omega_\pm)$ is a Gaussian with a finite width to model the instrumental resolution, and $\boldsymbol{Q}$ is the scattering wavevector, using the shorthand notation $\omega_\pm = \omega^\pm_{\boldsymbol{Q}}$ and the functions W, X, Y, Z and N are given by

$$\begin{aligned} W(\omega) &= -(A+\omega)(A^2+BB^*-C^2-DD^*-\omega^2)+2ABB^*-C(B^*D^*+BD) \\ X(\omega) &= C(A^2+BB^*-C^2+DD^*-\omega^2)-A(B^*D^*+BD)-\omega(B^*D^*-BD) \\ Y(\omega) &= B^*\left[(A+\omega)^2-BB^*+C^2\right]-2C(A+\omega)D+BD^2 \\ Z(\omega) &= D(A^2+C^2-DD^*-\omega^2)+B^{*2}D^*-2AB^*C \\ N(\omega) &= |-WW^*+XX^*-YY^*+ZZ^*|. \end{aligned} \tag{A.3}$$

The overall intensity prefactor $\mathcal{C}$ in Eq. (A.2) is an unity in liner spin-wave theory and is considered here as a variable parameter in the comparison with the experimental data in a first approximation.

The transformation matrix $\mathcal{S}$ to the normal operator basis $\mathsf{X}' = \mathcal{S}^{-1}\mathsf{X}$, in which the Hamiltonian is diagonal, is obtained as

$$\mathcal{S} = \begin{bmatrix} \overline{W}(\omega_-) & \overline{W}(\omega_+) & \overline{W}(-\omega_-) & \overline{W}(-\omega_+) \\ \overline{Y}(\omega_-) & \overline{Y}(\omega_+) & \overline{Y}(-\omega_-) & \overline{Y}(-\omega_+) \\ \overline{X}(\omega_-) & \overline{X}(\omega_+) & \overline{X}(-\omega_-) & \overline{X}(-\omega_+) \\ \overline{Z}(\omega_-) & \overline{Z}(\omega_+) & \overline{Z}(-\omega_-) & \overline{Z}(-\omega_+) \end{bmatrix},$$

where the shorthand notation $\overline{W}(\omega) = W(\omega)/\sqrt{N(\omega)}$ and so forth is used.

The procedures to diagonalise the quadratic Hamiltonian H in Eq. (6.13) to find the eigenvectors and eigenvalues (dispersion relation $\omega^{\mp}$) is outlined in Ref. [12]. This $\mathcal{S}$ matrix satisfies the eigenvalue equation $\mathsf{gH}\mathcal{S} = \mathcal{S}\mathsf{gH}'$ and the normalization condition $\mathcal{S}\mathsf{g}\mathcal{S}^{\dagger} = \mathsf{g}$, where g is the commutator matrix for the operator basis defined by

$$\mathsf{g} = \mathsf{X}(\mathsf{X}^*)^T - (\mathsf{X}^*\mathsf{X}^T)^T = \begin{bmatrix} 1 & 0 & 0 & 0 \\ 0 & 1 & 0 & 0 \\ 0 & 0 & -1 & 0 \\ 0 & 0 & 0 & -1 \end{bmatrix}$$

and

$$\mathsf{H}' = \begin{bmatrix} \omega_- & 0 & 0 & 0 \\ 0 & \omega_+ & 0 & 0 \\ 0 & 0 & \omega_- & 0 \\ 0 & 0 & 0 & \omega_+ \end{bmatrix}$$

is the Hamiltonian representation in the normal operator basis X' [12].

Appendix B

Spherically-averaged Neutron Scattering Intensity

The one-magnon neutron scattering intensity including the magnetic form factor and neutron polarization factor is proportional to

$$\left(\frac{g}{2}f(Q)\right)^2\left[\left(1-\frac{Q_x^2}{Q^2}\right)S^{xx}(\boldsymbol{Q},\omega)+\left(1-\frac{Q_y^2}{Q^2}\right)S^{yy}(\boldsymbol{Q},\omega)\right] \tag{B1}$$

where $f(Q)$ was used for the Ir^{4+} spherical magnetic form factor [67] and the g-factor was assumed to be equal to 2. Here Q_x (Q_y) are the components of the wavevector transfer $\boldsymbol{Q}$ along the x-axis (y-axis), where z is the ordered spin direction. The precise direction of the ordered moments ($\hat{\boldsymbol{z}}$-axis) with respect to the crystallographic axes has only a small effect on the powder-averaged spectrum via small intensity modulations through the polarization factors $\left(1-\frac{Q_{x,y}^2}{Q^2}\right)$, however for concreteness, a specific moment direction for the comparison with data was included. For the J_1-J_2-J_3 model (in Figs. 4.8(b-c and e), Fig. 4.17d) and Fig. 4.19b)), the moments were assumed to be aligned along the crystallographic $\boldsymbol{a}$-axis (as suggested by resonant xray data [63]) and for the KH model (Figs. 4.8(d,f)) the moment is assumed to be along the cubic $\hat{\boldsymbol{z}}$-axis closest to the $\boldsymbol{a}$-axis (tilted out-of-plane by 35.26° from the $-\boldsymbol{a}$ axis, see Fig. 4.12a) inset). Eq. (B1) was numerically averaged over a spherical distribution of orientations for the wavevector transfer $\boldsymbol{Q}$ and convolved with the instrumental resolution to obtain the plots in Figs. 4.8(b-f), directly comparable with the raw neutron scattering data in Fig. 4.8a). For the KH-J_2-J_3 model the intensity is also given by Eq. (B1) but with the axis labels (x, y, z) replaced by (y', z, x'), where

the x'-axis defines the ordered moment direction (located in the original xy-plane) and y' and z are orthogonal directions to it. For the spiral H2 order (in Fig. 6.14 and Fig. 6.18), the spherically-averaged powder simulations were done assuming the magnetic moments were confined in the crystallographic ac-plane.

Bibliography

[1] S. Blundell. *Magnetism in Condensed Matter*. Oxford University Press, (2001).

[2] H. Gretarsson, J. P. Clancy, X. Liu, J. P. Hill, Emil Bozin, Yogesh Singh, S. Manni, P. Gegenwart, Jungho Kim, A. H. Said, D. Casa, T. Gog, M. H. Upton, Heung-Sik Kim, J. Yu, Vamshi M. Katukuri, L. Hozoi, Jeroen van den Brink, and Young-June Kim. *Physical Review Letters*, 110:076402, (2013).

[3] Jiří Chaloupka, George Jackeli, and Giniyat Khaliullin. *Physical Review Letters*, 105:027204, (2010).

[4] G. Jackeli and G. Khaliullin. *Physical Review Letters*, 102:017205, (2009).

[5] E. Rastelli, A. Tassi, and L. Reatto. *Physica B+C*, 97:1–24, (1979).

[6] J. B. Fouet, P. Sindzingre, and C. Lhuillier. *The European Physical Journal B - Condensed Matter and Complex Systems*, 20:241, (2001).

[7] E. Rastelli. *Statistical Mechanics of Magnetic Excitations*. World Scientific, (2013).

[8] B. Lebechk B. Wildesyz, A.R. Roesslix and K. W. Godfreyy. *Journal of Physics: Condensed Matter*, 10:6417, (1998).

[9] Jens Jensen and Allan R. Mackintosh. *Rare Earth Magnetism: Structures and Excitations*. Clarendon Press, Oxford, (1991).

[10] C. Kittel. *Quantum Theory of Solids*. Wiley, (1987).

[11] T. Holstein and H. Primakoff. *Physical Review*, 58:1098, (1940).

[12] R. M. White, M. Sparks, and I. Ortenburger. *Physical Review*, 139:A450, (1965).

[13] N. D. Mermin and H. Wagner. *Physical Review Letters*, 17:1133, (1966).

[14] G. H. Wannier. *Physical Review*, 79:357, (1950).

[15] Wildes A. R., Roessli B., Lebech B., and Godfrey K. W. *Journal of Physics: Condensed Matter*, 10:6417, (1998).

[16] Hong-Chen Jiang, Zheng-Cheng Gu, Xiao-Liang Qi, and Simon Trebst. *Physical Review B*, 83:245104, (2011).

[17] G. L. Squires. *Introduction to the Theory of Thermal Neutron Scattering*. Dover Publications, (1997).

[18] S. W. Lovesey. *Theory of Neutron Scattering from Condensed Matter, Vols 1 and 2*. Clarendon Press, Oxford, (1987).

[19] W. Marshall and S. W. Lovesey. *Theory of Thermal Neutron Scattering*. Clarendon Press, Oxford, (1971).

[20] Furrer Albert, Mesot Joël, and Strässle Thierry. *Neutron Scattering in Condensed Matter Physics*. World Scientific, (2009).

[21] B.T.M. Willis and C.J. Carlile. *Experimental Neutron Scattering*. Oxford University Press, (2013).

[22] Information on the wish diffractometer is given in the webpage, http://www.isis.stfc.ac.uk/instruments/wish/.

[23] Laurent C. Chapon, Pascal Manuel, Paolo G. Radaelli, Chris Benson, Leigh Perrott, Stuart Ansell, Nigel J. Rhodes, Davide Raspino, D. Duxbury, E. Spill, and Julian Norris. *Neutron News*, 22:22, (2011).

[24] Instrument layout is given in the in6 webpage with explanations how the beamline works, https://www.ill.eu/en/html/instruments-support/instruments-groups/instruments/in6/description/instrument-layout/.

[25] The schematic view is obtained from the supernova manual which can be found in this website, http://www.chem.agilent.com/en-us/products-services/instruments-systems/x-ray-crystallography/supernova-dual-wavelength-diffractometer-platform/pages/default.aspx.

[26] The information for crysalispro software can be found in the website, http://www.chem.agilent.com/en-us/products-services/software-informatics/crysalispro/pages/default.aspx.

[27] C. Giacovazzo A. Guagliardi M. C. Burla G. Polidori A. Altomare, G. Cascarano and M. Camalli. *Journal of Applied Crystallography*, 27:435, (1994).

[28] George M. Sheldrick. *Acta Crystallographica Section A Foundations of Crystallography*, A64:112, (2008).

[29] This figure comes from SQUID manual document.

[30] Yogesh Singh and P. Gegenwart. *Physical Review B*, 82:064412, (2010).

[31] Yogesh Singh, S. Manni, J. Reuther, T. Berlijn, R. Thomale, W. Ku, S. Trebst, and P. Gegenwart. *Physical Review Letters*, 108:127203, (2012).

[32] Atsuo Shitade, Hosho Katsura, Jan Kunes, Xiao-Liang Qi, Shou-Cheng Zhang, and Naoto Nagaosa. *Physical Review Letters*, 102:256403, (2009).

[33] Hosub Jin, Heungsik Kim, Hogyun Jeong, Choong H. Kim, and Jaejun Yu. http://arxiv.org/abs/0907.0743, (2010).

[34] Bhattacharjee Subhro, Lee Sung-Sik, and Kim Yong Baek. *New Journal of Physics*, 14:073015, (2012).

[35] Itamar Kimchi and Yi-Zhuang You. *Physical Review B*, 84:180407, (2011).

[36] Yi-Zhuang You, Itamar Kimchi, and Ashvin Vishwanath. *Physical Review B*, 86:085145, (2012).

[37] Choong H. Kim, Heung Sik Kim, Hogyun Jeong, Hosub Jin, and Jaejun Yu. *Physical Review Letters*, 108:106401, (2012).

[38] I. I. Mazin, Harald O. Jeschke, Kateryna Foyevtsova, Roser Valentí, and D. I. Khomskii. *Physical Review Letters*, 109:197201, (2012).

[39] X. Liu, T. Berlijn, W. G. Yin, W. Ku, A. Tsvelik, Young-June Kim, H. Gretarsson, Yogesh Singh, P. Gegenwart, and J. P. Hill. *Physical Review B*, 83:220403, (2011).

[40] S. K. Choi, R. Coldea, A. N. Kolmogorov, T. Lancaster, I. I. Mazin, S. J. Blundell, P. G. Radaelli, Yogesh Singh, P. Gegenwart, K. R. Choi, S.-W. Cheong, P. J. Baker, C. Stock, and J. Taylor. *Physical Review Letters*, 108:127204, (2012).

[41] E. M. Wheeler, R. Coldea, E. Wawrzyńska, T. Sörgel, M. Jansen, M. M. Koza, J. Taylor, P. Adroguer, and N. Shannon. *Physical Review B*, 79:104421, (2009).

[42] Andrey V. Chubukov and Th Jolicoeur. *Physical Review B*, 46:11137, (1992).

[43] Alexei Kitaev. *Annals of Physics*, 321:2–111, (2006).

[44] G. Del Maestro Adrian and J. P. Gingras Michel. *Journal of Physics: Condensed Matter*, 16:3339, (2004).

[45] Jirí Chaloupka, George Jackeli, and Giniyat Khaliullin. *Physical Review Letters*, 110:097204, (2013).

[46] Julien Bréger, Meng Jiang, Nicolas Dupr, Ying S. Meng, Yang Shao-Horn, Gerbrand Ceder, and Clare P. Grey. *Journal of Solid State Chemistry*, 178:2575–2585, (2005).

[47] Matthew J. O'Malley, Henk Verweij, and Patrick M. Woodward. *Journal of Solid State Chemistry*, 181:1803, (2008).

[48] W. Urland and R. Hoppe. *Zeitschrift fur anorganische und allgemeine Chemie*, 392:23, (1972).

[49] R. J. Kuban. *Crystal Research and Technology*, 18:85, (1983).

[50] R. Wolf and R. Hoppe. *Zeitschrift fur anorganische und allgemeine Chemie*, 556:97, (1988).

[51] The definitaion of refinement parameters are given in the shelxl manual, which is available in the website: http://shelx.uni-ac.gwdg.de/shelx/shelx97.pdf.

[52] G. Kresse and J. Hafner. *Physical Review B*, 47:558, (1993).

[53] G. Kresse and J. Furthmüller. *Physical Review B*, 54:11169, (1996).

[54] Th Proffen and R. B. Neder. *Journal of Applied Crystallography*, 30:171, (1997).

[55] E. Wawrzyńska, R. Coldea, E. M. Wheeler, I. I. Mazin, M. D. Johannes, T. Sörgel, M. Jansen, R. M. Ibberson, and P. G. Radaelli. *Physical Review Letters*, 99:157204, (2007).

[56] E. Wawrzyńska, R. Coldea, E. M. Wheeler, T. Sörgel, M. Jansen, R. M. Ibberson, P. G. Radaelli, and M. M. Koza. *Physical Review B*, 77:094439, (2008).

[57] Feng Ye, Songxue Chi, Huibo Cao, Bryan C. Chakoumakos, Jaime A. Fernandez-Baca, Radu Custelcean, T. F. Qi, O. B. Korneta, and G. Cao. *Physical Review B*, 85:180403, (2012).

[58] Jeffrey G. Rau, Eric Kin-Ho Lee, and Hae-Young Kee. *Physical Review Letters*, 112:077204, (2014).

[59] Vamshi M Katukuri, S Nishimoto, V Yushankhai, A Stoyanova, H Kandpal, Sungkyun Choi, R Coldea, I Rousochatzakis, L Hozoi, and Jeroen van den Brink. *New Journal of Physics*, 16:013056, (2014).

[60] S. J. Blundell. *Contemporary Physics*, 40:175, (1999).

[61] J. Sugiyama, J. H. Brewer, E. J. Ansaldo, B. Hitti, M. Mikami, Y. Mori, and T. Sasaki. *Physical Review B*, 69:214423, (2004).

[62] J. W. Krizan, J. H. Roudebush, G. M. Fox, and R. J. Cava. *Materials Research Bulletin*, 52:162, (2014).

[63] X. Liu, T. Berlijn, W. G. Yin, W. Ku, A. Tsvelik, Young-June Kim, H. Gretarsson, Yogesh Singh, P. Gegenwart, and J. P. Hill. *Physical Review B*, 83:220403, (2011).

[64] R. Coldea, D. A. Tennant, and Z. Tylczynski. *Physical Review B*, 68:134424, (2003).

[65] G. Cao, T. F. Qi, L. Li, J. Terzic, V. S. Cao, S. J. Yuan, M. Tovar, G. Murthy, and R. K. Kaul. *Physical Review B*, 88:220414, (2013).

[66] S. Manni, Sungkyun Choi, I. I. Mazin, R. Coldea, Michaela Altmeyer, Harald O. Jeschke, Roser Valenti, and P. Gegenwart. http://arxiv.org/abs/1312.0815, (2013).

[67] J. W. Lynn, G. Shirane, and M. Blume. *Physical Review Letters*, 37:154, (1976).